Multi-wavelength Study of Star Formation in Nearby Galaxies

A thesis

submitted for the degree of

Doctor of Philosophy

in

The Department of Physics,

Pondicherry University,

Puducherry - 605 014, India

by

Chayan Mondal

Indian Institute of Astrophysics,

Bangalore - 560 034, India

September 2019

Multi-wavelength Study of Star Formation in Nearby Galaxies

Chayan Mondal
Indian Institute of Astrophysics

Indian Institute of Astrophysics
Bangalore - 560 034, India

Title of the thesis	:	**Multi-wavelength Study of Star Formation in Nearby Galaxies**
Name of the author	:	**Chayan Mondal**
Address	:	Indian Institute of Astrophysics II Block, Koramangala Bangalore - 560 034, India
Email	:	chayan@iiap.res.in
Name of the supervisor	:	**Prof. Annapurni Subramaniam**
Address	:	Indian Institute of Astrophysics II Block, Koramangala Bangalore - 560 034, India
Email	:	purni@iiap.res.in

Declaration of Authorship

I hereby declare that the matter contained in this thesis is the result of the investigations carried out by me at the Indian Institute of Astrophysics, Bangalore, under the supervision of Prof. Annapurni Subramaniam. This work has not been submitted for the award of any other degree, diploma, associateship, fellowship, etc. of any other university or institute.

Signed: _____

Date: _____

Certificate

This is to certify that the thesis titled **'Multi-wavelength Study of Star Formation in Nearby Galaxies'** submitted to the Pondicherry University by Mr. Chayan Mondal for the award of the degree of Doctor of Philosophy, is based on the results of the investigations carried out by him under my supervision and guidance, at the Indian Institute of Astrophysics. This thesis has not been submitted for the award of any other degree, diploma, associateship, fellowship, etc. of any other university or institute.

Signed: _____

Date: _____

List of Publications

1. Subramaniam Annapurni et al., including **Mondal Chayan**, 2016, "In-orbit Performance of UVIT on ASTROSAT", *Proceedings of the SPIE*, Volume 9905, id. 99051F 10pp. [arXiv:1608.01073], (Impact factor = 3.50, citation = 13)

2. Subramaniam Annapurni et al., including **Mondal C.**, 2016, "A hot companion to a Blue Stragglers in NGC188 as revealed by the Ultra-violet Imaging Telescope (UVIT) on ASTROSAT", *Astrophys. J. Lett.*, Volume 833, Issue 2, article id. L27, 5 pp. [arXiv:1612.02535], (Impact factor = 8.374, citation = 9)

3. Tandon, S.N. et al. including **Mondal C.**, 2017, "In orbit performance of UVIT and First Results", *J. Astrophys. Astr.*, Volume 38, Issue 2, article id. 28, 14 pp. [arXiv:1612.00612], (Impact factor = 1.217, citation = 16)

4. S. N. Tandon, Annapurni Subramaniam, including **C. Mondal**, 2017, "In-orbit Calibrations of the Ultraviolet Imaging Telescope", *Astron. J.*, Volume 154, Issue 3, aricle id. 128, 14 pp. [arXiv:1705.03715], (Impact factor = 5.497, citation = 22)

5. George, K.; Joseph, P.; **Mondal, C.** et al., 2018, "UVIT observations of the star-forming ring in NGC 7252:Evidence of possible AGN feedback suppressing central star formation", *A&A*, volume 613, id. L9, 5pp. [arXiv:1805.03543], (Impact factor = 5.567, citation = 4)

6. Singh, Avinash; Bhalerao, Varun; Anupama, G. C.; **Mondal, Chayan**; Sahu, Snehalata, "AstroSat UVIT Observations of AT2018cow", 2018, *The Astronomer's Telegram*, No. 11822.

7. **C. Mondal**, A. Subramaniam, K. George, 2018, "UVIT imaging of WLM : Demographics of star forming regions in the nearby dwarf irregular galaxy", *Astron. J.*, Volume 156, Issue 3, article id. 109, 16 pp. [arXiv:1807.07359], (Impact factor = 5.497, citation = 2)

8. K. George, P. Joseph, **C. Mondal** et al., 2019, "Insights on bar quenching from a multiwavelength analysis: The case of Messier 95", *A&A*, Volume 621, id. L4, 5 pp. [arXiv:1812.04178], (Impact factor = 5.567, citation = 4)

9. P. K. Nayak, A. Subramaniam, S. Subramanian, S. Sahu, **C. Mondal**, Maria-Rosa L. Cioni, C. Bell, 2019, "Detection of extended Red Clump in the SMC cluster Kron 3", 2019, *Proceedings IAU Symposium* No. 351.

10. **C. Mondal**, A. Subramaniam, K. George, 2019, "Tracing the outer disk of NGC 300: An ultraviolet view", *J. Astrophys. Astr.*, Volume 40, Issue 4, article id. 35, 17 pp. [arXiv:1907.06366], (Impact factor = 1.217, citation = -)

11. **C. Mondal**, A. Subramaniam, K. George, 2019, "UVIT view of dwarf irregular galaxy IC 2574 : Is the star formation triggered due to expanding H I shells?", *Astron. J.*, revised version submitted.

12. **C. Mondal**, A. Subramaniam, K. George, 2019, "Tracing young star forming clumps in the nearby flocculent spiral galaxy NGC 7793 with UVIT imaging", in preparation.

Presentations

1. Poster presentation in the *Astronomical Society of India meeting 2016 (ASI:2016)*, held at Kashmir University, Kashmir, India, during 10-13 May 2016.

2. Oral presentation in the conference *Star and Planet Formation: Insights and Intricacies*, held at IIST, Thiruvananthapuram, India, during 5-7 December 2016.

3. Poster presentation in the *Astronomical Society of India meeting 2017 (ASI:2017)*, held at B. M. Birla Auditorium, Jaipur, India, during 6 - 10 March, 2017.

4. Oral presentation in the conference *Galaxy Evolution and Dynamical Structures (GEDS-I)*, held at IUCAA, Pune, India, during 22 - 24 January, 2018.

5. Poster presentation in the *Astronomical Society of India meeting 2018 (ASI:2018)*, held at Osmania University, Hyderabad, India, during 5 - 9 February 2018.

6. Poster presentation in the international conference *15th Potsdam Thinkshop : The role of feedback in galaxy formation: from small scale winds to large-scale outflows* held at Potsdam, Germany, during 3 - 7 September 2018.

7. Oral presentation in the *Astronomical Society of India meeting 2019 (ASI:2019)*, held at Christ (Deemed to be University), Bengaluru, India, during 18 -22 February 2019.

Acknowledgements

Firstly, I want to deeply thank my supervisor Prof. Annapurni Subramaniam at Indian Institute of Astrophysics for her immense encouragement, positive guidance and support throughout my PhD. Her knowledge, dedication, sincerity and love for the subject have always motivated me in my work. The scientific discussions, we had throughout my PhD, have enriched me a lot and inspired me to think more openly. Most importantly, She gave me all the freedom to explore my research to the extent I enjoy it. She was also equally supportive in other aspects outside research, which helped me to move forward in some of my tough times. She has a unique personality, which taught me many valuable things. I heartily thank her for being a perfect guide as well as a symbol of inspiration throughout this journey.

I am grateful to Dr. Koshy George, Dr. Smitha Subramanian, Dr. Joseph Postma and Prof. Ram Sagar for all the enriching discussions. They helped me a lot to understand many basic things related to my work. I also want to thank all the teachers of our JAP course for their enriching lectures, which helped me to understand the basics of astrophysics. I am also thankful to the members of my Doctoral Committee - Prof S. Sivaprakasam and Prof. Mousumi Das for their valuable feedback and suggestions.

I am grateful to the Director, the Dean and the Board of Graduate Studies (BGS) of IIA for providing me the platform and all required facilities to pursue my research work. I am equally thankful to the Administrative Officer and other administrative staff of IIA for their help in administrative related work. I also thank the members of the library and Data centre for their activeness and constant support throughout the time. I also thank all the staff of Bhaskara guest house for their constant support and help.

I want to thank my research group mates Snehalata, Prasanta, Sindhu, Samyaday and others for all the help, related and unrelated to my work. I am thankful to Avinash for helping me with many tools and techniques for data analysis. A big thanks to my dear batchmates Dipanweeta, Snehalata, Samrat, Anirban, Megha and Tridib for their love and friendship, which meant a lot for me. I want to thank Subham, my senior cum hostel roommate, and Sajal, my senior for helping me with many academic and non-academic things, which make my journey more enjoyable. I am extremely thankful to all the seniors, friends and juniors, whom I came across during my stay at Bhaskara. You people have made my time memorable in many ways. Thanks for all the support.

I am grateful to all my teachers from School (Srichanda M.N.M. Institution), College (RKMRC, Narendrapur) and IIT Kharagpur for their encouragement and inspiration. A special thanks to Prof. Somnath Bharadwaj, Prof Sayan Kar and Prof Anushree Roy from IIT Kharagpur.

The journey to the IIA has only become possible for the love and support of all my dear friends from Narendrapur and Kharagpur. I thank all of them for playing their part.

A special thanks to Ritwika, for being there from the very beginning to the end in all ups and downs. I want to thank Sujoy da, my cousin, who first time introduced me to the beauty of the night sky. Those stories under the dark sky in my village still inspire me to think about the unknown unknown. Last but not the least, I am extremely grateful to my parents, my brother and all other family members for their constant support and love, which made me reach here.

Data usage

We have used data from various telescopes, covering a large wavelength range from ultra-violet to radio, in this thesis. I acknowledge and thank the members of each of these teams for making the data available.

The primary part of the analysis has been done with the UV imaging data from the Ultra-Violet Imaging Telescope (UVIT). UVIT project is a result of collaboration between IIA, Bengaluru, IUCAA, Pune, TIFR, Mumbai, several centres of ISRO, and Canadian Space Agency. The Mission Group (ISAC) and ISTRAC (ISAC) continue to provide support in making observations with, and reception and initial processing of the data. I gratefully thank all the individuals involved in various teams of this mission.

We have also used images as well as source catalogue from the observations of the Galaxy Evolution Explorer (GALEX). GALEX is a National Aeronautics and Space Administration (NASA) mission led by the California Institute of Technology. The data products of GALEX was made available by the Mikulski Archive for Space Telescopes (MAST), a NASA funded project. We thank both the GALEX and MAST team for providing science ready data products to the public.

This study has used H I 21 cm radio data from the observations of the Very Large Array (VLA) of National Radio Astronomy Observatory (NRAO). The NRAO is a facility of the National Science Foundation operated under cooperative agreement by Associated Universities, Inc. We have also acquired H I data from the Australian Telescope Compact Array (ATCA), operated by CSIRO, Australia's national science agency. We thank members of both VLA and ATCA teams.

Apart from these, we have also used other multi-wavelength data from various telescopes, found in the literature. The infra-red images used in this study are

observed by Spitzer, which is operated by the Jet Propulsion Laboratory, California Institute of Technology under a contract with NASA. The Hα data utilised in this thesis are observed with CTIO 4.0 meter and KPNO 0.9m telescopes. We have used optical image from the U.K. Schmidt telescope, operated by the UK Science Research Council (SRC) in this study. The molecular data utilised in this study are observed with Atacama Large Millimeter Array (ALMA). We thank the members related to each of these telescopes for providing the science products.

Some of the data, discussed above, are downloaded from the NASA/IPAC Extragalactic Database (NED), which is operated by the Jet Propulsion Laboratory, California Institute of Technology, under contract with the NASA. We acknowledge and thank the whole team of NED.

Dedicated to

my family

Abstract

The galaxies in the Universe are changing constantly through secular evolution, mergers and interactions. Recent star forming activities in galaxies convey important message about the current evolutionary state of these systems. The study of star formation can be explored well in galaxies, which are nearby, where star forming regions are resolved up to smaller scales. This thesis is aimed to understand the nature of star formation and young star forming regions in four nearby galaxies, which are part of the Local Volume. Among the four selected galaxies, two (WLM and IC 2574) are dwarf irregular and two (NGC 7793 and NGC 300) are spiral galaxies. We primarily used FUV and NUV imaging observations to identify and characterise young star forming regions in each galaxy, supplemented with multi-wavelength data. The major part of the UV data is acquired using the Ultra-Violet Imaging Telescope (UVIT). In order to explore the properties of neutral interstellar medium (ISM) and its connection with the active star forming regions, we used H I intensity maps. We also used other multi-wavelength data, such as Hα, optical, infra-red and molecular CO in specific cases, to understand the properties of star forming regions in more detail.

Using UVIT data, we identified several possible OB associations with sizes between 4 - 50 pc in the galaxy WLM. The UV, Hα and H I multi-wavelength data together helped to infer a vigorous recent star formation in the western part of the galaxy. Our study concludes that being a dwarf system, WLM is forming stars quite efficiently in the recent times. In the galaxy IC 2574, we found 28.6% of the identified FUV bright star forming regions to be located in H I shells, 12.6% inside H I holes and 60.1% to be away from any H I hole. Cross-matching with Hα emission, we found that 23 H I holes have both FUV and Hα emission in their shells signifying very recent trigger. Therefore, star formation in IC 2574 has been partly triggered due to the expanding H I holes, whereas in majority of the sites, it is driven by other mechanisms.

Both the spiral galaxies, NGC 7793 and NGC 300, studied in this thesis are members of the nearby sculptor group. Utilising multi-band data, we found that the disk of both the galaxies are more extended towards the shorter wavelengths. The young star forming clumps identified in the galaxy NGC 7793 have radii between 12 - 70 pc, which is similar to the size of giant molecular clouds identified in the galaxy. The clumps younger than 10 Myr are specifically found along the flocculent arms, which signifies the enhancement of recent star formation along the arms in NGC 7793. In the galaxy NGC 300, we studied the stellar populations in the outer disk of the galaxy between the radii 5.3 kpc and 10 kpc ($1 \sim 2$ R_{25}) and noticed an enhancement of star formation during the last 25 Myr. The UV emission beyond the R_{25} radius has contribution from most of the low mass sources and is extended up to $\sim 2R_{25}$ radius. We conclude that NGC 300 has an extended UV disk, mainly populated by young low mass sources.

Our study brings out the importance of UV images in tracing the recent star formation in galaxies. It highlights the unique capability of the UVIT to resolve star forming regions up to size $\sim$ 10 pc for a distance up to 4 Mpc and study their properties. Our study also demonstrated how it can be useful to identify the triggering mechanism, if we combine the UV images with Hα images and H I and CO maps.

Contents

Abstract **i**

List of Figures **vii**

List of Tables **xvii**

Abbreviations **xix**

1 Introduction **1**
1.1 Study of galaxies 6
1.2 Importance of nearby galaxies 8
1.3 Star formation in nearby galaxies 15
1.4 Importance of multi-wavelength observations 22
1.5 Motivation and Aim of the study 26
1.6 Overview of the Thesis 28

2 Data and Observation **31**
2.1 Data 31
2.2 Ultra-violet 32
2.2.1 Ultra-Violet Imaging Telescope (UVIT) 33
2.2.2 Galaxy Evolution Explorer (GALEX) 42
2.2.3 HST/WFPC2-F170W 45
2.3 21 cm H I data 46
2.3.1 Very Large Array (VLA) 46
2.3.2 Australia Telescope Compact Array (ATCA) 47
2.4 Hα - Optical images 47
2.5 Infra-red images 48
2.6 Molecular CO data 48
2.7 Summary 48

3 Methodology **51**
3.1 Introduction 51

3.2 Theoretical models . . . 52
3.2.1 Starburst99 Simple Stellar Population model . . . 52
3.2.2 Stellar spectral model . . . 56
3.3 Tools for data analysis . . . 58
3.3.1 Contour maps with DS9 . . . 58
3.3.2 Photometry . . . 60
3.3.3 Identifying parent-child structure : *Astrodendro* . . . 62
3.4 Summary . . . 64

4 Star formation in WLM **65**
4.1 Introduction . . . 65
4.2 Theoretical models . . . 69
4.3 Effect of Extinction and Metallicity . . . 69
4.4 Data and Analysis . . . 72
4.4.1 Extent of UV emission . . . 73
4.4.2 Luminosity density profile . . . 75
4.4.3 UV colour maps . . . 79
4.4.4 (F148W−N263M) colour map . . . 81
4.4.5 (F148W−N245M) colour map . . . 84
4.4.6 Correlating with Hα and H I maps . . . 85
4.4.7 Correlating with HST detected hot stars . . . 87
4.4.8 Mass estimation of compact star forming regions . . . 88
4.4.9 Correlating with CO observations . . . 92
4.4.10 Star Formation Rate . . . 92
4.5 Results and Discussion . . . 96
4.6 Summary . . . 101

5 Star formation in IC 2574 **103**
5.1 Introduction . . . 103
5.2 Extinction in UV . . . 106
5.3 Data and Analysis . . . 107
5.3.1 Distribution of FUV emission and H I gas . . . 107
5.3.2 H I shells . . . 109
5.3.3 FUV bright star forming regions . . . 111
5.3.4 Structure of star forming regions . . . 119
5.3.5 FUV Luminosity density profile of IC 2574 . . . 127
5.3.6 Remnant cluster of Super Giant Shell . . . 128
5.4 Results and Discussion . . . 130
5.5 Summary . . . 135

6 Star formation in NGC 7793 **137**
6.1 Introduction . . . 137
6.2 Theoretical models . . . 140

6.3 Extinction in UV . . . 141
6.4 Data and Analysis . . . 142
6.4.1 UV disk profile of NGC 7793 . . . 143
6.4.2 Correlation with H I column density . . . 144
6.4.3 Identification of young star forming clumps . . . 145
6.4.4 Age estimation . . . 149
6.4.5 Age distribution . . . 150
6.4.6 Mass estimation . . . 152
6.4.7 Mass distribution . . . 155
6.4.8 Nuclear star cluster . . . 157
6.5 Results and Discussion . . . 158
6.6 Summary . . . 164

7 XUV disk of NGC 300 **167**
7.1 Introduction . . . 167
7.2 Theoretical models . . . 170
7.3 Data and Analysis . . . 170
7.3.1 Background and foreground sources . . . 173
7.3.2 Reddening and Metallicity . . . 176
7.3.3 FUV Disk of NGC 300 . . . 179
7.3.4 Correlation with optical image . . . 180
7.3.5 Correlation with H I . . . 181
7.3.6 Correlation with 24 μm infrared image . . . 183
7.3.7 Luminosity density profile . . . 184
7.3.8 Star formation rate . . . 186
7.3.9 Age estimation of UV sources . . . 187
7.3.10 Spatial age distribution of UV sources . . . 189
7.3.11 Mass estimation of UV sources . . . 191
7.3.12 Spatial mass distribution of UV sources . . . 192
7.4 Results and Discussion . . . 193
7.5 Summary . . . 198

8 Conclusions and Future Work **201**
8.1 Summary . . . 202
8.2 Conclusion . . . 205
8.3 Future Work . . . 208

Bibliography **211**

List of Figures

1.1 The Hubble Ultra Deep field observed with multiple bands of HST starting from ultra-violet to infra-red. Image credit - NASA, ESA, H. Teplitz and M. Rafelski (IPAC/Caltech), A. Koekemoer (STScI), R. Windhorst(ASU), Z. Levay (STScI) 4
1.2 The Hubble tuning fork diagram which shows the morphological classification scheme of galaxies. Image credit - NASA & ESA . . . 6
1.3 Distribution of Local volume galaxies in the galactic coordinate system. Image credit - Kaisina et al. (2012) 10
1.4 Images of two nearby galaxies are shown. The upper one is the dwarf galaxy DDO 68 and the bottom one is the spiral galaxy M83. Image credit - Subaru Telescope (NAOJ), NASA/ESA Hubble Space Telescope, European Southern Observatory. Processing & Copyright: A. Aloisi (DDO68) & Robert Gendler (M83) 14
1.5 This figure shows the tracers which are primarily used to identify young stellar population in galaxies. The age corresponding to each tracer signifies that 90% of that emission is contributed by stellar population younger than the given age. This figure is constructed as per the data provided in Kennicutt & Evans (2012). 23

2.1 The layout of UVIT instrument housed in AstroSat satellite. Image courtesy : UVIT webpage of Indian Institute of Astrophysics. . . . 32
2.2 The effective area profiles of UVIT in the filters available in FUV, NUV and Visible channels of UVIT. Image courtesy : Tandon et al. (2017) 35
2.3 The photon counting detector system of UVIT. Image courtesy : Hutchings et al. (2007) 36
2.4 The layout of CCDLAB software (Postma & Leahy 2017) used for UVIT data reduction. 37
2.5 The UVIT FUV image of the galaxy NGC 7793. Left : Image before drift correction, Right : Image after drift correction. 39
2.6 An example of typical drift pattern of UVIT field during the course of observation. 39
2.7 Flow chart for UVIT data reduction procedure using CCDLAB. . . 40
2.8 The layout of GALEX instrument. Image courtesy : GALEX webpage maintained by the instrument science team. 43

2.9 The effective area profiles of GALEX FUV and NUV filters. 45

3.1 The upper panel shows Starburst99 model generated integrated spectrum for six different ages. The parameters chosen are mentioned in the figure. In the lower panel, the UV part of the above spectrum are shown along with the scaled effective area profiles of five different UVIT filters. 53

3.2 Starburst99 model generated diagnostic plots for simple stellar population. The upper panel shows the variation of (F148W−N242W) colour as a function of cluster age. The parameters are mentioned in the figure. The lower panel shows F148W magnitude as a function of (F148W−N242W) colour (i.e. age of cluster). Different curves signify five different total cluster masses ($10^7 M_\odot$, $10^6 M_\odot$, $10^5 M_\odot$, $10^4 M_\odot$, $10^3 M_\odot$). The points shown in each curve are for different ages starting from 1 Myr to 900 Myr with the same interval as shown in upper panel. 55

3.3 Flux ratios in UVIT filters F148W & N245M (blue) and F148W & N263M (red) are plotted as a function of temperature with the help of Kurucz stellar model. 58

3.4 A representation of dendrograms and the algorithm of *astrodendro*. Image courtesy : Astrodendro official website. 63

4.1 False colour composite image of the galaxy WLM. The galaxy is observed in three different UVIT filters F148W, N245M and N263M which are represented by blue, green and red colours respectively. . 67

4.2 The relation between UV flux ratio and temperature, estimated using Kurucz spectra, for log(g) = 5.0 and log(Z) = −0.5 . The F148W/N263M and F148W/N245M flux ratios are shown in Figure (a) and (b) respectively. The blue curves in both the figures are without extinction correction. The other curves are generated by applying extinction on blue curve for different extinction laws mentioned in the figure. 68

4.3 Starburst99 model generated colour-magnitude plots for simple stellar population. The Figure shows F148W magnitude with (F148W−N263M) colour. Different curves (continuous line) signify four different total cluster masses ($10^6 M_\odot$, $10^5 M_\odot$, $10^4 M_\odot$, $10^3 M_\odot$). The dashed lines show the extinction and reddening corrected values for each model curve. The points shown in each curve are for different ages starting from 1 Myr to 900 Myr (increasing along the colour axis) with age interval 10 Myr for 1 to 100 Myr range and 100 Myr for 100 to 900 Myr. The value of other parameters adopted for this figure is listed in Table 7.2. 70

4.4 The variation of extinction coefficient (R_λ, i.e. $A_\lambda/E(B-V)$) with wavelength for different extinction laws. The solid lines of different colours represent different laws mentioned in the figure. The scaled effective area curves for three UVIT filters are also shown by the dashed lines. 73
4.5 The flux ratio $Flux_{F148W}/Flux_{N263M}$ is plotted with temperature for two different metallicity log(Z)=−1.0 and −0.5. 74
4.6 The background figure is the 512×512 F148W band image of WLM with contours plotted for different limits of F148W flux values as mentioned in Table 4.4. The blue contours represent the brightest (hence most massive) regions of the galaxy. The overall extent of FUV emission of WLM is traced by the yellow contours. 76
4.7 The background figure is the 512×512 N263M band image of WLM. The blue, green and red contours shown in the figure are generated for pixels brighter than 23 magnitude in F148W, N245M and N263M filter images respectively. The FUV emission (blue contours) is seen to be enveloped by both green and red contours representing the NUV emission of WLM. 77
4.8 The background figure is the 512×512 N263M band image of WLM. The blue, green and red contours shown in the figure are generated for pixels brighter than 23.80, 23.69 and 23.58 magnitude (adding the effect of extinction) respectively in F148W, N245M and N263M filter images. The extent of NUV emission as traced in N263M filter is found to be more than that of Figure 4.7. 78
4.9 The profile for surface luminosity density (erg/sec/pc^2) with galactocentric distance in kpc for three UVIT filters. The UV emission of WLM is found to be extended at least up to a radius 1.7 kpc. The shaded region corresponding to each curve shows the 5σ photometric error whereas the error bars (bottom right) represents 5σ error due to the present uncertainty of adopted zero point magnitudes. . 80
4.10 The variation of (F148W−N245M) and (F148W−N263M) colour is shown with galactocentric distance in kpc. Both the profiles remain nearly flat in the inner 1 kpc whereas an upturn is noticed for the outer part beyond 1 kpc. The photometric errors are shown in the profile and the error bars displayed in the bottom right corner signify the error due to the uncertainty in zero point magnitudes. . 81

4.11 The (F148W−N263M) colour map of the galaxy is shown with different plotted contours. Figure (a) shows the whole galaxy along with the specified position of five regions R1, R2, R3, R4 and R5. The blue, red and green contours are generated for different flux limits signifying different temperature ranges as mentioned in Table 4.5. The background image shown here is smoothed and the grey scale denotes the logarithmic value of the CPS ratio for the smoothed image. We have shown zoomed in images for regions R1, R2, R3, R4 and R5 in Figure (b), (c), (d), (e) and (f) respectively. The blue contoured regions denote the hotter regions of the galaxy. 83
4.12 The (F148W−N245M) colour map of the galaxy is shown with different plotted contours. Figure (a) shows the whole galaxy along with the specified position of five regions R1, R2, R3, R4 and R5. The blue, red and green contours are generated for different flux limits signifying different temperature ranges as mentioned in Table 4.6. The background image shown here is smoothed and the grey scale denotes the logarithmic value of the CPS ratio for the smoothed image. We have shown zoomed in images for regions R1, R2, R3, R4 and R5 in Figure (b), (c), (d), (e) and (f) respectively. The blue contoured regions are found to be more fragmented than those in Figure 4.11. 86
4.13 Hα image of the galaxy WLM, covering regions R1, R2, R3 and R4, is shown in the background where the grey scales signifies the logarithmic value of CPS. The cyan contours signify the Hα emitting regions of the galaxy. The plotted blue and red contours are same as shown in Figure 4.11a. The UV detected hot regions show a good spatial correlation with the Hα emitting regions of the galaxy. . . . 88
4.14 The background image shows the H I density distribution of the galaxy WLM. The hook like magenta contour is the over density pattern reported by Kepley et al. (2007). The plotted blue, red and green contours are same as shown in Figure 4.11a. R1 has several UV detected hot star forming regions with less H I density. Other regions (R2, R3, R4 and R5) are found to have dense H I gas. . . . 89
4.15 F148W/N263M smoothed image is shown with same blue and red contours as plotted in Figure 4.11. The HST detected massive stars (cyan box) are overlaid on the regions R1, R2, R3 and R4 as shown in figures (a), (b), (c) and (d) respectively. 90
4.16 The F148W and N263M band magnitude and corresponding error of 590 identified point sources in the galaxy WLM. 91
4.17 The identified compact star forming regions are over plotted (grey filled circles) on starburst99 model curves. 91

4.18 The smoothed F148W/N263M image is shown in the background with the logarithmic grey scale. The blue and red contours signify the hot regions of the galaxy as in Figure 4.5a. Two black squares (one in north-west (NW) and another in south-east (SE)) are the two 1 arcmin^2 ALMA fields observed by Rubio et al. (2015) for detecting CO clouds. The green circles shown inside the boxes are the position of detected CO clouds. 93
4.19 Figure (a) and (b) show the zoomed in view of the regions (inside two black boxes of Figure 4.18) where CO detection is found in north-west (NW) and south-east (SE) field respectively. The background image and contours are same as mentioned in Figure 4.18. The CO clouds are shown in green circles where the size of the circles signifies the size of the cloud with respect to the 1 pc reference circle shown in each figure. The clouds are labelled as per Rubio et al. (2015). The numbers shown near each green circle signify its virial mass in $M_\odot$. 94
4.20 The radial profile for SFR density ($M_\odot/yr/kpc^2$) with 3σ error bar is shown in the figure. 95
4.21 The figure shows all five regions (R1, R2, R3, R4 and R5) with F148W band image in the background. The black arrows show the position angle along four different directions. The blue and red ellipses represent 1 kpc and 2 kpc galactocentric distance respectively. 96
4.22 The azimuthal variation of radially averaged (up to 2 kpc) SFR density ($M_\odot/yr/kpc^2$) with 3σ error bar is shown in the figure. Two peaks at PA $\sim 0^o$ and 180^o signify the contribution of star forming regions from northern and southern half of the galaxy respectively. . 97

5.1 UVIT F148W band image of the galaxy IC 2574. 106
5.2 The background image is the UVIT FUV image of the galaxy IC 2574 observed in F148W filter. The H I holes, as identified by Walter & Brinks (1999), are shown by black circles/ellipses. The number corresponding to each hole is same as assigned by these authors. The green and blue contours signify pixels with FUV flux more than 2.14×10^{-18} and 3.21×10^{-19} $erg/sec/cm^2/\mathring{A}$ respectively. The red contours denote regions with H I column density greater than $1.0 \times 10^{21} cm^{-2}$. 108
5.3 The H I column density map of the galaxy is shown along with the 48 H I holes (black circles/ellipses) as identified by Walter & Brinks (1999). The grey scale shows flux in JY/B*M/S. 110
5.4 A smaller part of the galaxy IC 2574 is shown. The brown contour signifies parent structure and the yellow contour is for child structures. 112
5.5 This is a cartoon image of an H I hole of radius R. The grey annular region is the shell of width R/3. The cyan clumps represent star forming regions in three different scenarios as discussed in the study. 113

5.6 The figure shows some selected holes along with the identified FUV bright regions. The background image is UVIT FUV image of IC 2574. The black solid circles/ellipses show the holes of radius R, where the shells are defined by black dashed lines of width R/3 between radii (R−R/6) to (R+R/6). A length scale of 100 pc is shown in each image. The brown contours denote the FUV bright regions identified for a threshold flux of 1.07×10^{-18} $erg/sec/cm^2/\mathring{A}$. The numbers shown in blue and black respectively signify the ID for holes and identified regions as given in Table 5.2. 115
5.7 The histogram of the size of identified parent clumps. 117
5.8 The background image is H I moment 0 map of IC 2574. The grey scale signifies flux in JY/B*M/S. The red contours signify regions having H I column density more than $10^{21}cm^{-2}$. The identified FUV bright star forming regions are shown as blue circles. 119
5.9 The measured value of FUV surface luminosity density and H I column density of 419 identified FUV bright regions are shown. The inset shows the zoomed in part for FUV luminosity density between $1-5\times10^{35}$ $erg/sec/pc^2$. 122
5.10 The figure shows 9 selected parent structures, along with their dendrograms, identified for a threshold flux $1.07\times10^{-18}erg/sec/cm^2/\mathring{A}$ (green dashed line). The red dashed lines represent flux value of $2.14\times10^{-18}erg/sec/cm^2/\mathring{A}$. The largest parent structure and its dendrogram are shown in the upper panel of the figure. A length scale of 100 pc is shown for each region in solid black line. The Y axis of dendrogram shows the flux in terms of counts per second while the X axis denotes unique identification number of each structure which is not related to their ID presented in the paper. . . 123
5.11 The radial surface luminosity density ($erg/sec/pc^2$) profile of the galaxy. 126
5.12 The FUV image of the galaxy IC 2574. The regions highlighted as S1, S2, S3, S4, S5 and S6 are the active star forming regions of the galaxy. 126
5.13 The FUV image of H I shell 35 (red ellipse) along with the remnant cluster (blue circle) is shown in the left. The zoomed in view of the cluster is shown in right where two resolved components are clearly noticed. 129

6.1 False colour composite image of the galaxy NGC 7793. The galaxy is observed in two UVIT filters F148W and N242W which are represented by blue and yellow colours respectively. 139

6.2 The Figure shows F148W vs (F148W−N242W) colour-magnitude plot, simulated with the data from starburst99 SSP model. Different curves (continuous line) signify four different total cluster masses ($10^6 M_\odot$, $10^5 M_\odot$, $10^4 M_\odot$, $10^3 M_\odot$). The dashed lines are plotted by considering the extinction and reddening of the galaxy. The points shown in each curve are for different ages starting from 1 Myr to 900 Myr (increasing along the colour axis) with age interval 10 Myr for 1 to 100 Myr range and 100 Myr for 100 to 900 Myr. The values of model input parameters are listed in Table 6.2. 140
6.3 The FUV and NUV radial luminosity density profiles of NGC 7793 are respectively shown in solid blue and red lines. Each profile is normalised with respect to the maximum of the respective curve. The dashed lines are the exponential fits for each observed profiles. The values of the estimated disk scale-length in FUV and NUV are 2.64±0.16 kpc and 2.21±0.21 kpc respectively. 142
6.4 The figure shows the H I moment 0 map of the galaxy NGC 7793. The grey scale is in Jy/B*M/S. The yellow contours show regions with H I column density more than $10^{21} cm^{-2}$. The blue and red contours respectively represent FUV and NUV emission profile. These are generated for a threshold flux of 5 times the average background value measured in each respective band. The black dashed ellipse shows the R_{25} boundary of the galaxy. 144
6.5 A selected star forming region of the galaxy is shown along with the contour of parent (brown) and child (yellow) structures. The background shows UVIT F148W band image. The value of the adopted threshold flux is $\log[\text{flux}(erg/sec/cm^2/\mathring{A})] = -17.80$. . . . 146
6.6 The number of identified parent and child structures are shown as a function of varying threshold flux. The black line shows the ratio of the number of child and parent structures. The vertical green dashed line represents the threshold flux ($\log(\text{flux}) = -17.80$) selected for our analysis. 148
6.7 The histogram shows the size of identified clumps (child structure) for the selected values of threshold flux and minimum number of pixel. 149
6.8 The histogram of (F148W−N242W) colour of the clumps brighter than 21 mag in F148W band is shown in the upper panel. In the lower panel, we have shown their distribution as a function of radial distance from the galaxy centre. 151
6.9 The identified star forming clumps are over plotted (grey filled circles) on the simulated model curves as shown in Figure 6.2. 152
6.10 The age histogram of the identified star forming clumps. 153

6.11 Spatial distribution of clumps (red points) as a function of their estimated age between the range 1 - 400 Myr. The figures represent four different age groups as mentioned in the text. The age range of the group is mentioned in the corresponding panel. 154
6.12 The mass histogram of the identified star forming clumps. 155
6.13 Spatial distribution of clumps (red points) as a function of their estimated mass between the range $3 \times 10^2 - 10^6 M_\odot$. The figures represent four different mass groups as mentioned in the text. The mass range of the group is mentioned in the corresponding panel. . 156
6.14 The upper panel (a) shows the nuclear star cluster as seen in the UVIT FUV image. The red circles represent five different apertures with radius starting from 1.5 pixel to 13.5 pixel. The lower panel (b) shows the extinction and background corrected (F148W−N242W) colour profile of the object as measured from the annuli displayed above. 159

7.1 False colour composite GALEX image of the galaxy NGC 300 where FUV and NUV are represented by blue and yellow colour respectively. Image courtesy : NED Database. 169
7.2 Starburst99 model generated (FUV−NUV) colour as a function of age (Myr). Different curves are for five different metallicities (Z). For 1-100 Myr range, age interval is 10 Myr and after that interval is 100 Myr for age up to 900 Myr. The cluster mass considered is $10^6 M_\odot$. 171
7.3 Starburst99 model generated FUV vs (FUV−NUV) CMD for simple stellar population. Different curves signify five different total cluster mass ($10^7 M_\odot$, $10^6 M_\odot$, $10^5 M_\odot$, $10^4 M_\odot$, $10^3 M_\odot$). The points shown in each curve are for different ages starting from 1 Myr to 900 Myr (increasing along the colour axis) with the same age interval chosen in Figure 7.2. 172
7.4 The identified sources (detected in both FUV and NUV bands) are over plotted on GALEX image of NGC 300. The inner circular region, containing the blue points, is considered as the galaxy and outer annular region with red points is assumed as field region. . . . 174
7.5 Figure (a) shows the FUV vs (FUV−NUV) CMD for galaxy region (blue points in Figure 7.4) and Figure (b) shows the CMD for outer field region (red points in Figure 7.4). 175
7.6 Figure (a) shows the FUV vs (FUV−NUV) CMD of sources remaining in the galaxy region after performing background subtraction. Figure (b) shows the CMD of 742 UV sources (reddening and extinction corrected) which are finally considered as part of the galaxy. The sources marked with red star are present in the outer disk between radius 5.3 kpc to 10 kpc. 177

7.7 The background figure is the binned 960 × 960 pixel FUV image of NGC 300 with different contours plotted for different limits of FUV flux value as mentioned in Table 7.3. The blue contours represent the brightest (hence massive) regions of the galaxy. The grey scale of the image denotes counts per second per pixel. The ellipses shown in the figure signify R_{25}, $1.5R_{25}$ and $2R_{25}$ galactocentric distance respectively. Two extended structures (ES) are also shown by arrow. 180

7.8 The background figure shows the DSS optical image of NGC 300. The yellow contoured region represents the main optical disk of the galaxy. Blue and green contours are same as shown in Figure 7.7. . 181

7.9 The H I density contours are shown in white on the background H I density map of NGC 300 in both figures. The unit of the grey scale is Jy/beam. The blue, green and red contours shown in Figure (a) are the same as Figure 7.7. In Figure (b) we have shown the distribution of UV sources (blue points) present in the outer disk (between 5.3 kpc and 10 kpc) of NGC 300. 182

7.10 The MIPS 24 μm image of NGC 300 is shown in the background with red contours indicating regions with intense infrared emission. The same blue contours of Figure 7.7 are also shown. The unit of the grey scale is MJy/sr. 184

7.11 The normalised surface luminosity density profiles of NGC 300 in different wavebands are shown in different colours. The solid lines denote the observed profiles whereas dashed lines of the same colour show the fitted exponential profiles. Three vertical black dashed lines are plotted to show the FUV scale-length (R_d) (our study), optical radius (R_{25}) and the extend of optical disk of the galaxy from Bland-Hawthorn et al. (2005). The horizontal dotted green line represents the FUV background. In inset, we have shown all the observed and fitted profiles in logarithmic scale up to radial distance of 6 kpc. 185

7.12 The radial profile of SFR density ($M_\odot/yr/kpc^2$) is shown up to a radius 10 kpc (blue curve). The red curve shows the scaled value of SFR density ($M_\odot/yr/kpc^2$) as calculated through an HST study by Gogarten et al. (2010). The radial profile of SFR density between radii 5.3 kpc and 10 kpc is shown in the inset. 188

7.13 Age histogram of all the selected UV sources between radius 5.3 kpc and 10 kpc. 189

7.14 The selected UV sources (blue square) in the outer disk are over-plotted on the GALEX FUV image of the galaxy. Figure (a) shows the spatial position of younger sources (Age $<$ 25 Myr) and the relatively older sources (Age $>$ 25 Myr) are shown in Figure (b). The reference PA is shown in the top left corner. 190

7.15 The selected UV sources are shown on the simulated plot presented in Figure 7.3. The sources present in the outer disk between radii 5.3 kpc to 10 kpc are shown in brown circles whereas grey diamonds represent the sources in the inner disk within radius 5.3 kpc. 191
7.16 Mass histogram of the detected UV sources present between radius 5.3 kpc and 10 kpc is shown. Sources with mass below $10^3 M_\odot$ are not displayed in the figure. 192
7.17 The figures show the mass distribution of UV sources in the outer disk of the galaxy. Figure (a) shows the high mass (M$> 10^5 M_\odot$) sources, Figure (b) shows intermediate mass ($10^3 M_\odot <$M$< 10^5 M_\odot$) sources and low mass sources (M$< 10^3 M_\odot$) are shown in Figure (c). 194

List of Tables

2.1 Details of FUV and NUV filters of UVIT as obtained from Tandon et al. (2017) . . . 36
2.2 Log of UVIT observations. . . . 43
2.3 Details of GALEX filters. . . . 45
2.4 Log of Data used in this study . . . 48

3.1 Starburst99 model parameters . . . 57

4.1 Properties of WLM . . . 67
4.2 Starburst99 model parameters . . . 71
4.3 Extinction parameters for average LMC law (Gordon et al. 2003) . 72
4.4 Details of flux and magnitudes for contours in the F148W map shown in Figure 4.6. . . . 76
4.5 Details of flux ratio and temperature for the (F148W−N263M) colour map, as shown in Figure 4.11. . . . 77
4.6 Details of flux ratio and temperature for the (F148W−N245M) colour map, as shown in Figure 4.12. . . . 80

5.1 Properties of IC 2574 . . . 105
5.2 Connection between FUV bright star forming regions and the H I holes. This table helps to capture the location of the FUV bright regions with respect to the H I holes. In the second column we listed the regions present in the shell. The regions present inside each hole are shown in column 3. Each region number signifies its ID, listed in Table 5.5. The numbers given within parentheses are the ID of Hα cross-identified region from the catalogue of Miller & Hodge (1994). The age of each hole and their types are given in columns 4 and 5 respectively from Walter & Brinks (1999). . . . 120
5.3 Table5.2 continued . . . 121

5.4 Summary of Table 5.2. Column 2 shows the total number for holes (along with three different types) and identified regions. Columns 3 and 4 respectively show the number of holes with FUV emission in shell and inside it. Column 5 lists the number of holes with no related FUV emission. The bottom row of the table denotes the similar statistics with respect to the identified regions. The numbers shown in parenthesis denote the numbers after cross-match with Hα emission. 124
5.5 Properties of FUV bright star forming regions as defined in Figure 5.6. The full table containing all 419 regions is available in electronic format. 125
5.6 Starburst99 model parameters 128
5.7 Properties of the remnant cluster 129

6.1 Properties of NGC 7793 139
6.2 Starburst99 model parameters 141

7.1 Properties of NGC 300 170
7.2 Starburst99 model parameters 171
7.3 Details of flux and magnitudes for contours in the FUV map shown in Figure 7.7. 178

Abbreviations

NASA	**N**ational **A**eronautics and **S**pace **A**dministration
UVIT	**U**ltra-**V**iolet **I**maging **T**elescope
GALEX	**GAL**axy Evolution **EX**plorer
VLA	**V**ery **L**arge **A**rray
ATCA	**A**utralian **T**elescope **C**ompact **A**rray
NED	**N**ASA/IPAC **E**xtra-galactic **D**atabase
HST	**H**ubble **S**pace **T**elescope
KPNO	**K**itt **P**eak **N**ational **O**bservatory
CTIO	**C**erro **T**ololo **I**nter-American **O**bservatory
IRAC	**I**nfra-**R**ed **A**rray **C**amera
ALMA	**A**tacama **L**arge **M**illimeter **A**rray
MIPS	**M**ulti-band **I**maging **P**hotometer for **S**pitzer
THINGS	**T**he **H** I **N**earby **G**alaxy **S**urvey
GASS	**G**alactic **A**ll **S**ky **S**urvey
DSS	**D**igitized **S**ky **S**urvey
SSM	**S**canning **S**ky **M**onitor
MCP	**M**icro **C**hannel **P**late
CMOS	**C**omplementary **M**etal-**O**xide-**S**emiconductor
PC	**P**hoton **Counting**
FWHM	**F**ull **W**idth **H**alf **M**axima
PSF	**P**oint **S**pread **F**unction
FITS	**F**lexible **I**mage **T**ransport **S**ystem

CCD	**C**harge **C**oupled **D**evice
SSP	**S**imple **S**tellar **P**opulation
IRAF	**I**mage **R**eduction and **A**nalysis **F**acility
IMF	**I**nitial **M**ass **F**unction
$M_{\odot}$	Solar **M**ass
RA	**R**ight **A**scension
DEC	**D**eclination
SFR	**S**tar **F**ormation **R**ate
SGS	**S**uper **G**iant **S**hell
ISM	**I**nter-**S**tellar **M**edium
GMC	**G**iant **M**olecular **C**loud
SFH	**S**tar **F**ormation **H**istory
BCD	**B**lue **C**ompact **D**warf
LSB	**L**ow **S**urface **B**rightness **G**alaxies
IUE	**I**nternational **U**ltra-violet **E**xplorer
CMD	**C**olour **M**agnitude **D**iagram
LEGUS	**L**egacy **E**xtra-galactic **U**V **S**urvey
ISRO	**I**ndian **S**pace **R**esearch **O**rganisation

Chapter 1

Introduction

The branch of extra-galactic astronomy started with the famous discovery by one of the celebrated astronomers, Edwin Hubble, when he realised that some of the luminous nebulae he was working with are not part of the Milky Way and termed them as 'extra-galactic nebulae' (Hubble 1926). This was later confirmed as individual galaxies present outside our galaxy. Since then the field of extra-galactic astronomy has evolved extensively and enriched our understanding of the universe in a completely different way. Galaxies can be considered as gravitationally bound systems of both dark matter and baryonic matter. The baryonic components visible to us mainly constitute stars, gas and dust. Whereas dark matter is an invisible component and it forms the major part of the galaxy mass. It also has gravitational influence on the baryonic matter. The formation and evolution of galaxies during the early time of the universe as well as in the present era have been studied extensively in literature (Blumenthal et al. 1984; Bromm et al. 2009; Mo et al. 2010). According to the ΛCDM cosmological model, galaxies are formed due to the accretion of primordial gas cloud into the potential well of dark matter

halo. The collapsing cloud becomes denser with time and also starts cooling radiatively. Within a certain radius, the cloud density reaches a point, where the mass of the dense gas cores crosses the Jeans mass limit (Jeans 1928). This induces star formation across the cloud and sets up the stage to form a galaxy. These primordial galaxies later evolve and merge hierarchically to form larger structures. The massive galaxies observed in the present time are thus formed from the continuous merging of such smaller systems (Blumenthal et al. 1984). It is thus important to study galaxies in different red-shift to explore their evolution. This helps us to understand galaxies in a range of epoch, spanning from the early universe to present era.

Our observable universe consists of more than 100 billion galaxies. The images of Hubble Ultra Deep field (Beckwith et al. 2006) shown in Figure 1.1 conveys that each small piece of the sky is actually populated with numerous galaxies which can be seen with deep imaging observations. These galaxies have different shapes and sizes.

With the discovery of different types of galaxies, astronomers classified galaxies into several groups as per their appearance. The galaxy classification was first performed by Hubble and later expanded by de Vaucouleurs (1959), Sandage (1961), Morgan & Osterbrock (1969), van den Bergh (1976) and many others. The classification scheme of Hubble is represented by a diagram as shown in Figure 1.2, which is known as the famous Hubble tuning fork diagram. According to the morphology, Hubble primarily classified these systems into two categories, i.e. elliptical and spiral galaxies. Elliptical galaxies have a smooth shape with no specific structure. They are classified into various sub-classes on the basis of ellipticity. Some ellipticals appear to be almost round whereas some have elongated shape. Whereas, spiral galaxies have specific features in their structure. They usually have a thin disk with an extended stellar halo around it. The spiral features are distributed on the disk. Many spirals show a spheroidal concentration of light at the centre called

bulge, which has a profile, similar to an elliptical galaxy (Athanassoula 2005).

In the Hubble classification scheme, spirals are mainly classified into two categories based on the presence of a bar, another ellipsoidal component located at the centre (Kormendy & Kennicutt 2004). Galaxies without a bar are called normal spirals and galaxies with a bar are named as barred spirals. In the case of barred spirals, the arms are found to originate from the ends of the bar. Both the normal and barred spiral galaxies are again classified into multiple sub-classes on the basis of tightness and openness of spiral arms. It has been found that about 50 -70 % of observed bright spiral galaxies have a bar feature (Eskridge et al. 2000; Marinova & Jogee 2007). Galaxies with well defined strong spiral arms are called grand design spiral galaxy whereas there are galaxies with loosely defined arms and therefore named as flocculent spirals. The galaxies which fall at the conjunction of spiral and elliptical galaxies are named as lenticular galaxies. They are morphologically classified as SO galaxies, as shown in the Hubble tuning fork diagram in Figure 1.2. They have a central bulge similar to the profile of an elliptical galaxy and a featureless smooth extended disk. Lenticulars are also classified into sub-classes based on the presence and absence of a bar. Apart from these, there are galaxies which do not have any definite shape and hence they are classified as irregular galaxies. The presence of these types of galaxies was later highlighted by de Vaucouleurs, and expanded the galaxy classification to include an elaborate classification of the spirals.

This whole spectrum of galaxies also has a wide range in their total stellar mass. Galaxies with mass more than $10^9 M_\odot$ are massive galaxies whereas those with mass less than $10^9 M_\odot$ are termed as dwarf galaxies. For example, an irregular galaxy with mass less than $10^9 M_\odot$ is called a dwarf irregular galaxy.

The whole diversity of galaxy morphology opens an obvious question about the origin and evolution of these objects. The simple way to address this is to study the

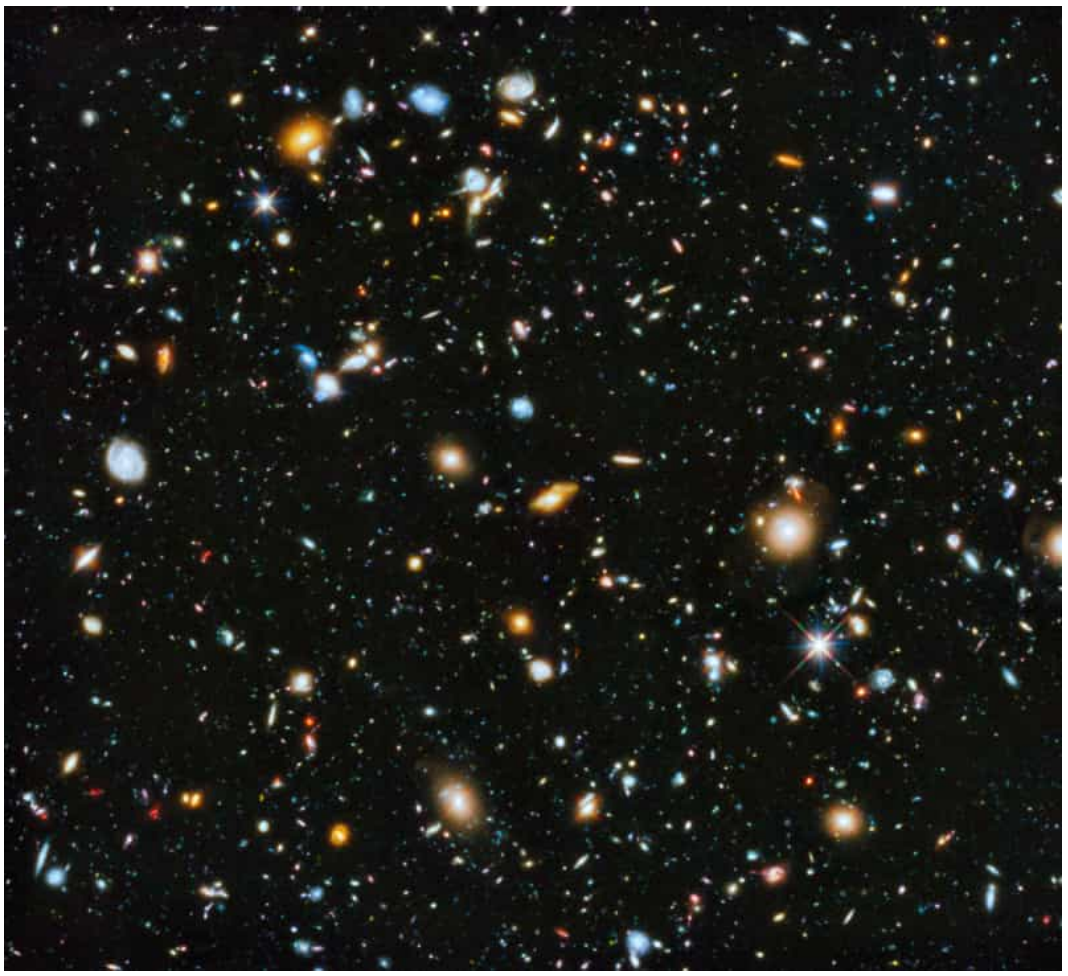

FIGURE 1.1: The Hubble Ultra Deep field observed with multiple bands of HST starting from ultra-violet to infra-red. Image credit - NASA, ESA, H. Teplitz and M. Rafelski (IPAC/Caltech), A. Koekemoer (STScI), R. Windhorst(ASU), Z. Levay (STScI)

external and internal environments of different types of galaxies. The evolutionary path of a galaxy is believed to be strongly impacted by the environment where it is present. It has been noticed that the massive elliptical and lenticular galaxies are mostly found in the inner part of galaxy groups and clusters, whereas spiral and irregular galaxies are mostly seen in less dense environments like the outer part of galaxy clusters or field region (Hubble & Humason 1931; Oemler 1974; Melnick & Sargent 1977; Dressler 1980). This observation suggests that the environment plays an important role in the evolution of galaxies and therefore to decide their morphological class.

The important implication of the Hubble sequence was revealed by a pioneering review by Roberts & Haynes (1994). They observed a correlation for several galaxy parameters along the Hubble sequence from early type elliptical to late type spiral and irregular galaxy. Though the total mass to light ratio of galaxies shows a constant value along the sequence, the value of H I gas mass to light ratio increases monotonically from elliptical to spiral and further to irregular galaxies. A strong correlation is also seen in the (B−V) colour, which progressively becomes more bluer from elliptical to spiral and irregular galaxy. Roberts & Haynes (1994) argued that the variation of star formation rate (SFR) to be the main reason for these correlations. The redder colour and low gas fraction in elliptical galaxies signify a lower star formation rate in the recent time. In the other case, spiral and irregular galaxies have higher gas fraction with bluer (B−V) colour, which conveys a higher rate of recent star formation.

A more comprehensive work is carried out by Larson & Tinsley (1978), where they used (U−B) and (B−V) two colour diagram to distinguish between galaxies with monotonically decreasing SFR and galaxies having several recent bursts in star formation. This leads to the classification of galaxies into two primary groups called red sequence and blue sequence. Blanton et al. (2003) studied 183,487 galaxies between red-shift 0.02 to 0.22 from SDSS sample and reported a bi-modal distribution as a function of (g−r) colour. With a similar approach, Baldry et al. (2004) used (u−r) colour, which distinguished red and blue populations for a large sample of nearby galaxies between red-shift 0.008 to 0.04. These together established the presence of two different groups, i.e. star-forming active and non-star-forming passive galaxies, in the galaxy population. It has been noticed that the red sequence is mostly populated by dead massive elliptical and lenticular galaxies whereas the spirals and irregular galaxies are generally found in the blue sequence. Therefore, both spiral and irregular galaxies are ideal to study the nature of recent star formation in external galaxies.

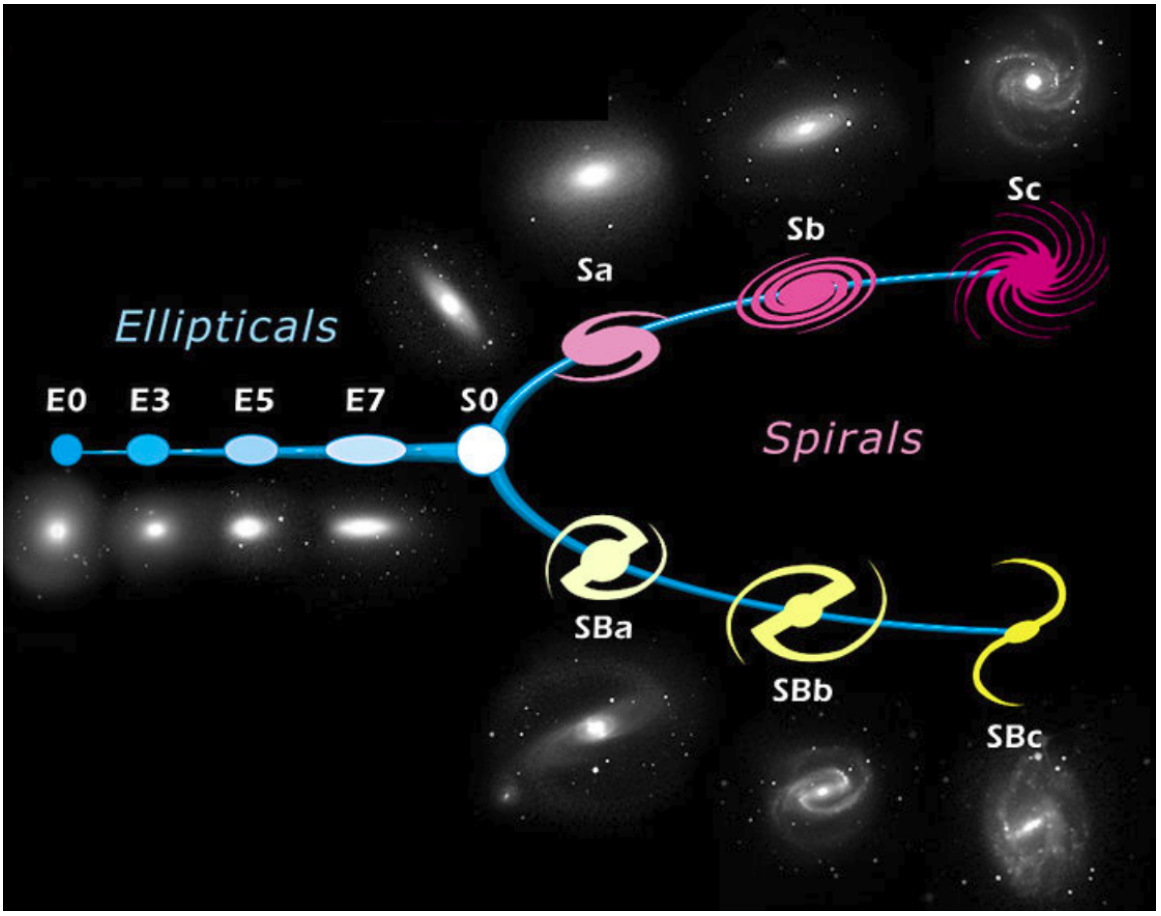

FIGURE 1.2: The Hubble tuning fork diagram which shows the morphological classification scheme of galaxies. Image credit - NASA & ESA

1.1 Study of galaxies

The study of external galaxies covers a range of different aspects depending on the distance. Galaxies, which are present far away, mostly appear like an unresolved extended source. Study of these high red-shift systems is important to explore the formation and evolution of galaxies during the early phase of the universe. This also helps to understand the processes through which galaxies build up their mass with time, although the internal properties of such galaxies are yet to be explored in detail. In the other hand, nearby galaxies offer a unique opportunity to resolve individual clumps (or even up to individual stars) and study their properties. With the advent of new technologies, the spatial resolution of telescopes has improved

considerably to enhance the areas of exploration in the field extra-galactic study, specifically for nearby galaxies.

Physical properties of any galaxy depend on its kinematics and its building blocks, such as, gas, star and dust present in it. The primary luminous component of a galaxy is stars. A galaxy can host stars of different ages with different chemical abundances. Stars formed in the earlier epochs are old and have low metal abundance, whereas stars formed later or accreted during mergers have a range of age and chemical abundance. Galaxies with ongoing star formation contain young massive OB stars, which primarily emit in the ultra-violet wavelength. The location of these stars points to the sites of recent star formation in a galaxy, whereas the old stellar populations are usually more bright in optical and infra-red.

The other two baryonic components, i.e. gas and dust, together form a large proportion of the interstellar medium (ISM) in a galaxy. Interstellar gas can have three different forms, i.e. atomic, molecular and ionised. Atomic gas, the primary component of ISM, has two main phases i.e. cool and warm atomic hydrogen (H I). Both of these are traced by 21 cm H I spectral lines in the radio band. The cooler phase has a temperature and density around 100 K and 30 cm^{-3} respectively whereas it is around 5000 K and 0.6 cm^{-3} for the warmer phase (Draine 2011). Again, the molecular gas of a galaxy primarily contains molecular hydrogen. This is much denser ($\sim 10^3 - 10^6 cm^{-3}$) and cooler ($\sim$10 - 50 K) phase of the ISM (Draine 2011) and thus provides the ideal atmosphere to induce star formation in galaxies. As H_2 molecules do not emit in this temperature, the sub-millimetre emission from CO molecules (Young et al. 1995) is used as a proxy to trace molecular hydrogen in galaxies. The molecular gas is usually distributed in the form of clouds or filaments in a galaxy. The larger clouds have a typical size of $\sim$ 20 pc and known as Giant Molecular Cloud (GMC). Inside the larger clouds and filaments, there are smaller clumps of size $\sim$ 2 pc which further have dense, cold cores of sub-parsec size (Bodenheimer 2011). These cloud cores are the sites where individual stars

form (Williams et al. 2000). The star clusters or the stellar associations are born from the GMCs, which have enough mass to produce groups of stars.

Another component of the interstellar gas is ionised hydrogen known as H II gas. The far-ultraviolet (FUV) emission from the young and massive O/B type stars ionises the neutral atomic hydrogen to create H II gas. This has a range of density from $0.1 - 10^4 cm^{-3}$ (Draine 2011). Tracing each component of the interstellar gas, therefore, provides important clues about the physical nature of ISM across a galaxy. Another important component of ISM is the interstellar dust, which originates from the material ejected from stars. This dust is primarily composed of carbon, silicate and graphite grains and other complex molecules (Rowan-Robinson 1986, 1992). The presence of interstellar dust reduces the apparent intensity of an emitting source by absorbing a part of the emitted radiation. The dust grains absorb high energy UV photons and gets heated up to further re-emit thermal radiation in the lower energy infra-red band. Emission in far-infrared bands is used to trace the distribution of dust across a galaxy (Li & Draine 2001). Therefore, a complete understanding of all the components in a galaxy requires observation in multiple wavebands. Again, galaxies with different morphological types show a notable difference in terms of available gas, star and dust content. Therefore, morphological classes have equal importance in contributing to our understanding of the pathway of galaxy formation and evolution.

1.2 Importance of nearby galaxies

In order to understand the physics internal to a galaxy, it is essential to probe each detectable component of the galaxy up to a smaller length scale. This, in turn, helps to disentangle the underlying connection between stars, gas and dust. The lower limit of this length scale primarily depends on two parameters. One is

the distance to the galaxy and another is the spatial resolution of the telescope. In this context, the sample of nearby galaxies offer an ideal platform to carry out studies for exploring small scale characteristics of star forming regions and ISM in external galaxies.

The galaxies, present within $\sim$ 1 Mpc from the Milky Way, are considered to be part of a group called the Local group (van den Bergh 2000; Karachentsev 2005). It has around 50 detected members, where the majority are dwarf galaxies. The most massive members of the group are Milky Way and M31, both being spirals. More recently, it has been found that the Local group is, in fact, a combination of two groups, each formed around these two massive spiral galaxies (Tully 2015). Due to the closer distance of these Local group members, it has been possible to identify individual stars in these galaxies with many of the available observing facilities.

Apart from the Local group, the galaxies which are present within 11 Mpc from the Milky way and have a corrected radial velocity (V_{LG}, i.e. velocity with respect to the centroid of the Local Group) less than 600 km/sec, are considered as members of the Local volume (Kraan-Korteweg & Tammann 1979; Karachentsev 2005). The Local volume also has several galaxy groups, such as Centaurus A, M81, Maffei and sculptor. Each of these groups is composed of a number of galaxies with different morphological types. The first attempt to make a distance limited catalogue of nearby galaxies was made by Kraan-Korteweg & Tammann (1979). They listed 179 galaxies, complete up to the brightness limit -18.5 mag in B band, within a distance 10 Mpc. Many of these galaxies are small dwarf galaxies. Due to the faintness of dwarf galaxies, improvements in the observing facilities result in the detection of more number of such systems. In 2004, Karachentsev et al. (2004) updated the catalogue of nearby galaxies with 451 objects. Later in 2013, Karachentsev et al. (2013) published a catalogue of 869 galaxies within a distance of 11 Mpc. At present, the Local volume has a total of 1209 members as per the

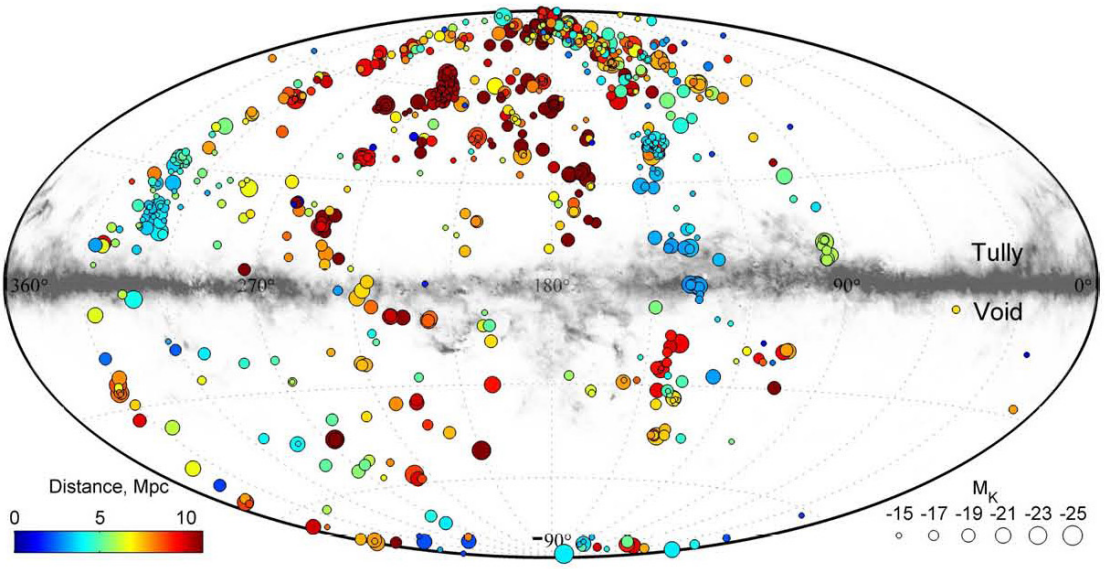

FIGURE 1.3: Distribution of Local volume galaxies in the galactic coordinate system. Image credit - Kaisina et al. (2012)

updated database constructed earlier by Kaisina et al. (2012). The distribution of these galaxies is shown in Figure 1.3. This large number of galaxy sample in the Local volume has provided immense scope to explore star formation history (SFH), impact of galaxy environments and galaxy mass function more accurately with the help of observations (Koribalski et al. 2018).

Among the several kinds of galaxies, dwarf galaxies are observed to be the most abundant type of galaxy present in the universe. The luminosity function of galaxies as proposed by Schechter (1976) shows a gradual increase in galaxy number from brighter to fainter absolute magnitudes. This highlights the richness of low mass systems with respect to massive brighter galaxies. This is also true for the Local group and Local volume sample. The other morphological type, which is also seen in good number in the nearby universe is the star forming spiral galaxies. It is thus important to study these two types of galaxies in the nearby universe to better understand their high red-shift counter parts. Below we introduce the dwarf galaxies and star forming spiral galaxies. Examples of such two galaxies are shown in Figure 1.4.

Dwarf galaxies

Dwarf galaxies, in general, have small intrinsic size and low absolute luminosity (Hodge 1971). These objects are generally less massive, metal poor, gas rich and also contain a lesser amount of dust (Hunter 1997). They are the building blocks of the galaxy formation and evolution and formed when the universe was very young. In the hierarchical merging ΛCDM paradigm, the stellar halos of the massive galaxies in the local universe are thought to have accumulated from the continuous merging of dwarf galaxies (Blumenthal et al. 1984). Despite their numbers and proximity, they are still among the least understood objects. Understanding the factors that allow these dwarf galaxies to survive to the present day may explain the discrepancies between observed and predicted distribution of such galaxies in and around the Milky Way. This requires an understanding of how internal and environmental effects shape the evolution of low-mass systems like dwarf galaxies.

Around 85% of the total identified galaxies in the local volume are reported to be dwarf galaxies (Kaisina et al. 2012; Karachentsev & Kaisina 2019). A majority of these dwarf galaxies are identified to be the satellites of massive galaxies. Karachentsev & Kaisina (2019) reported that around 52% of the dwarf populations are found to be present around massive spirals or in denser environment of galaxy groups. Rest of the objects are distributed in relatively less dense environments. Not surprisingly, the dwarf galaxies are also sub-classified. Dwarf spheroidal galaxies are very less luminous, gas poor and mostly seen around massive spirals (Grebel et al. 2003). It is more probable that the tidal interactions with the massive galaxy have stripped the gas from these systems in the course of their evolution (Mayer et al. 2001). As a result, they do not show any signature of star formation at present. The kinematics of dwarf spheroidal galaxies present around massive spirals provide important clues regarding the mass of the central massive galaxy. In contrast, dwarf irregular galaxies are gas rich system and mostly identified in sparse regions (Hunter 1997). As the gravitational influence of massive

galaxies has not impacted these objects much, they still contain enough gas and show signatures of star formation. Apart from these two types, there are also dwarf ellipticals and blue compact dwarf (BCD) galaxies. Dwarf elliptical galaxies are significantly less bright than the normal compact ellipticals and known to be very metal poor systems (Ferguson & Binggeli 1994), whereas BCDs are smaller dwarf systems with (B−V) colour bluer than the ellipticals. Their spectra show signatures of H II regions, similar to those seen in spiral galaxies (Thuan & Martin 1981; Thuan & Izotov 2005).

Spiral galaxies

Spiral galaxies can be defined as disk galaxies with ongoing star formation (Blanton & Moustakas 2009). They are comparatively larger, massive and more metal rich systems than the typical dwarf galaxies. Following the discovery of external galaxies by Hubble (1926), astronomers started to compile a list of these objects along with their brightness and morphological types. Shapley & Ames (1932) published a catalogue of 1246 bright galaxies with 701 of them classified as spirals. A more updated catalogue of brighter galaxies was published by de Vaucouleurs et al. (1964), which also contains galaxy size and radial velocity along with revised morphological types. Later in 1981, Sandage & Tammann (1981) utilised various available galaxy catalogues and presented a more comprehensive list of nearby bright galaxies. This list contains nearby spiral galaxies with designated morphological type of spiral sub-classes. More recently, Karachentsev et al. (2013) published a complete list of galaxies of the Local volume, including the nearby spirals.

The disk component of spiral galaxies has an exponential brightness profile. Spiral galaxies roughly cover a mass range between $10^9 - 10^{12} M_{\odot}$. The presence of gravitational instability in the disk of these galaxies produce density waves, which manifest as spiral arms (Lin & Shu 1966; Roberts et al. 1975). The spiral arms

have implications on star formation and related characteristics, which make them different in terms of the star forming environments in dwarf galaxies. The presence of disk in spiral galaxies also motivates to study the disk growth with time (Roškar et al. 2008) and explore the formation pathways of galaxies with extended disks. The nearby spiral galaxies, with more face on orientation, are ideal to study the distribution and properties of star, gas and dust in much detail. The flux from the underlying stars of these systems is less obstructed by the dust and therefore provides scope to explore the characteristics of stellar population across the disk. On the other hand, the nearby edge on spirals are perfect to study the galaxy rotation curve, which provides valuable clues to the dark matter content of the galaxy. The larger angular extent in the sky is also utilised to study the radial variation of metallicity, SFR, flux density etc in nearby spirals. Recent studies have also detected signature of star formation in the extended disk of several nearby spiral galaxies which are named as XUV disk galaxies (Thilker et al. 2005a,b, 2007; Gil de Paz et al. 2005).

Spiral galaxies of different sub-classes have specific characteristics. The bulge to disk light ratio is found to decrease gradually from early type to late type spirals for both bared and non-bared categories. The bulge dominated early type systems are also noticed to have spiral arms with smoothly distributed stars, whereas spiral arms in late type spirals are filled with many bright knots of stars and appear more patchy (Longair 2008). Spiral galaxies with strong bar experience re-distribution of angular momentum of stars and gas. This perturbation makes the gas to flow inward and induce star formation in the nucleus (Athanassoula 1992; Sheth et al. 2005; Coelho & Gadotti 2011). Apart from these, there exists a type of disk galaxies with sufficiently low surface brightness called Low Surface Brightness (LSB) galaxies (Impey & Bothun 1997). Due to the level of faintness, their identification is more limited in the nearby universe.

FIGURE 1.4: Images of two nearby galaxies are shown. The upper one is the dwarf galaxy DDO 68 and the bottom one is the spiral galaxy M83. Image credit - Subaru Telescope (NAOJ), NASA/ESA Hubble Space Telescope, European Southern Observatory. Processing & Copyright: A. Aloisi (DDO68) & Robert Gendler (M83)

1.3 Star formation in nearby galaxies

Star formation in a galaxy can be triggered due to multiple reasons. The primary condition to induce star formation is to compress and cool the molecular gas to the extent where it crosses the Jeans mass limit (Jeans 1928) and start collapsing under its own gravity. This can be achieved by the impact of multiple drivers on both small and large scales. On smaller scales, one of the most dominant mechanisms is the feedback from supernova shock waves. There are several studies done with observation and simulation which show shock waves to trigger star formation (Cameron & Truran 1977; Lee et al. 1977; Boss 1995; Stone & Norman 1992; Preibisch et al. 2002; Nagakura et al. 2009). This again depends on several factors, such as shock propagation velocity, density of the cloud before and after the impact of the shock, cooling time scale etc. Depending upon these factors there can be two different consequences. In one case the shock wave can act as a positive feedback and induce star formation while in other cases it can also function as a negative feedback to destroy the cloud (Dale et al. 2012; Rogers & Pittard 2013).

Another way to trigger star formation is the expansion of H II regions around massive stars (Elmegreen & Lada 1977; Whitworth et al. 1994). The huge radiation pressure of massive stars produces a shock and powers it to expand supersonically. This shock front sweeps up the circumstellar material and starts accumulating mass in a shell. The material in this shell gradually becomes more dense and cool to induce star formation at some point. Observational evidences of this phenomena are presented by Deharveng et al. (2003); Zavagno et al. (2006). The other mechanism which can also cause star formation in a galaxy is the cloud-cloud collision (Tan 2000). This again depends on several factors such as the mass ratio of the colliding clouds, their temperature and relative velocity.

Mechanisms which drive star formation in larger scale are mostly driven by galaxy interactions or global density wave. Large scale star formation can be produced

by merging of two galaxies (Hopkins et al. 2013; Powell et al. 2013) or due to their tidal interaction (Woods et al. 2006; Di Matteo et al. 2007). Either of these events causes strong gravitational instability which induces a global star formation across the galaxy. This can also be achieved in spiral galaxies by the spiral density wave. The strong density wave can also produce instability and trigger star formation in the disk, specifically along the spiral arms (Roberts 1969). Regardless of these triggering mechanisms, there are two primary factors which control the details of star formation in a galaxy. These are the magnetic field and the turbulence of the ISM (Bodenheimer 2011). The effect of ambipolar diffusion can make magnetically supported sub-critical cloud to cross its Jeans mass and start collapse to form stars (Basu & Mouschovias 1994). This way star formation is controlled by magnetic fields in low-mass cloud cores. Again, turbulence of ISM is considered to be the key driver which controls star formation globally in a galaxy (McKee & Ostriker 2007). The supersonic shock wave generated by turbulence can randomly make molecular cloud to become dense and collapse to form stars. The same phenomena can also support a molecular cloud against its self-gravity and inhibit the collapse. This way turbulence controls star formation and dictates the hierarchy of star forming regions (Larson 1981).

Evolution of galaxies over a time scale is dictated by its star formation. Therefore, understanding recent star formation in a galaxy is important for exploring the present stage of its evolution. The impact of star formation can significantly alter both the dynamical and chemical evolution of a galaxy. In order to decipher the detailed characteristics of star formation and the star forming regions, it is essential to probe the galaxies with high spatial resolution. It has been possible to resolve the star forming knots or even the individual star in clusters present in the nearby galaxies with the available observing facilities, particularly the HST (Calzetti et al. 2015). In the case of a far away galaxy, the same task becomes difficult due to the limit of instrumental resolution.

There are several methods adopted in the literature to decipher the star formation history of nearby galaxies. One of the earliest attempts was taken by Searle et al. (1973), who evaluated U, B, V colours for a sample of late-type galaxies and compared them to the model values to draw information about the star forming characteristics of each galaxy. They found a declining nature in the SFR with time and also noticed that the majority of the galaxy have similar SFR in the last 10 billion years. In a similar study, Larson & Tinsley (1978) found that normal galaxies show decreasing SFR with time whereas peculiar galaxies carries signature of shorter burst in star formation. Kennicutt (1983) used Hα flux along with the UBV colours to estimate SFR of a large number of spiral and irregular galaxies. They also reported a correlation between SFR and gas density for the studied galaxy sample. During the same time, Huchra et al. (1983) used UV data from the International Ultra-violet Explorer (IUE) and constructed UV-optical-IR energy distribution for some selected observed regions in the galaxy NGC 4214 and NGC 4670. They found signatures of a younger burst with several features corresponding to O type stars. Gallagher et al. (1984) considered a different method to estimate the rate at which a galaxy has formed stars in different epochs during its lifetime. They used galaxy total mass, blue band luminosity and Lyman alpha continuum flux to estimate SFR for different time spans, from the whole lifetime of the galaxy to the last 100 Myr. This approach helped to understand the active nature of nearby galaxies as a function of their age.

In 1991, Tosi et al. (1991) presented a new method to study SFH in nearby galaxies. They imaged the Local group galaxy Sextans B in B, V and R band and constructed colour-magnitude diagram (CMD) with around 2500 detected objects. They compared the observed CMD with the synthetic one simulated using stellar evolutionary model to understand the SFH of the galaxy. A similar work was also done by Gallart et al. (1996) for the galaxy NGC 6822.

Later, the launch of Hubble Space Telescope (HST) has particularly transformed

our understanding of the star forming regions in nearby galaxies. The superior spatial resolution with the suit of multiple wavebands of HST have together helped to identify individual stars and then construct CMDs to explore the age and other properties of the stellar populations. One of the first studies with the HST observations was done by Dohm-Palmer et al. (1997) for the galaxy Sextans A. Later on Dolphin (2002); McQuinn et al. (2010a); Cignoni & Tosi (2010); Weisz et al. (2014) and many others have studied a good sample of nearby dwarf galaxies with HST observations. More recently, the Legacy Extra-galactic UV Survey (LEGUS) based on the observations with HST has specifically targeted 50 nearby galaxies within distance 12 Mpc and explored the nature of stellar population with multi-band imaging observations (Elmegreen et al. 2014; Calzetti et al. 2015).

Another breakthrough happened in the field of extra-galactic astronomy with the launch of the Galaxy Evolution Explorer (GALEX) UV space telescope. The larger field of view of the GALEX helped to image the nearby galaxies with a single pointing and thus provided scope to explore radial and azimuthal UV properties of galaxies (Thilker et al. (2005a); Gil de Paz et al. (2007); Muñoz-Mateos et al. (2007); Hunter et al. (2010); Bianchi (2011)). GALEX observations also helped to estimate age and mass of unresolved star forming knots of nearby galaxies from their measured FUV and near-UV (NUV) fluxes (Melena et al. 2009; Goddard et al. 2010). The integrated FUV flux of galaxies further helped to estimate the recent SFR.

There have been several attempts made with the help of optical spectra of star forming regions to explore the SFH of galaxies. González Delgado et al. (2016, 2017) used spectroscopic data from the Calar Alto Legacy Integral Field Area (CALIFA) survey to study the spatially resolved SFH of galaxies of different Hubble type. In recent times, a similar attempt is made with the Multi Unit Spectroscopic Explorer (MUSE) integral-field spectroscopic data (Bacon et al. 2010) to study the emission line properties of star forming regions in nearby galaxies.

The data from MUSE, HST and Atacama Large Millimeter Array (ALMA) are combined together to understand the interplay between young stars and gas at smaller length scales (Leroy et al. 2017; Sun et al. 2018a; Kreckel et al. 2018).

Several studies are also performed with Hα observation which indirectly traces the stellar population of age $<\sim$ 10 Myr and hence provides an estimation of current SFR of a galaxy (Hunter & Elmegreen 2004; Massey et al. 2007; Barnes et al. 2011; Karachentsev & Kaisina 2013a). The combination of UV and infrared observations acquired from GALEX and Spitzer space telescopes have together helped to estimate the SFR of galaxies more accurately (Gordon et al. 2000; Kennicutt et al. 2007; Calzetti et al. 2007). Also, the huge volume of photometric and spectroscopic optical data from the Sloan Digital Sky Survey (SDSS) have uncovered the SFH of a large number of galaxies of different red-shifts (Gallazzi et al. 2006; Panter et al. 2007).

Dwarf irregular galaxies

Dwarf galaxies show a wide variety of star formation history in terms of SFR and recent star forming activity (Cignoni et al. 2018). They also have low metallicity and shallow potential well. Due to the low potential, the metals ejected through stellar evolution and supernovae are thrown out of these systems instead of enriching the ISM. These properties have made dwarf galaxies important in the cosmological perspective. Among the several types, dwarf irregular galaxies have a good amount of gas remaining to form new stars. This metal poor and gas rich environment of dwarf irregular galaxies closely match with the environment of galaxies in the early universe. Therefore, understanding how star formation proceeds in such regimes is crucial to study their counterparts in the early universe (Weisz et al. 2011; Bianchi et al. 2012). The other exceptional characteristic of these dwarf systems are the shallow gravitational potential which suppresses the growth of gravitational instability in these systems. Leaman et al. (2012)

presented a detailed discussion on the possible mechanisms which keep the star formation alive in dwarf galaxies, despite their shallow potential well. Therefore, a star forming dwarf galaxy offers to explore the mechanisms which could trigger star formation in the absence of a substantial impact of the large scale gravitational instabilities.

Another cosmological importance of understanding the chemical properties as well as star formation history of dwarf galaxies is to know the formation path of massive galaxies. Again, the absence of spiral density waves in dwarfs have made them an ideal laboratory to study the effect of internal triggering mechanisms, such as feedback from massive stars (Hunter 1997). Perturbations due to stellar feedback, ram pressure stripping or tidal interaction can significantly affect the evolution of a dwarf galaxy (Revaz & Jablonka 2018). Many dwarfs are known to undergo bursts of star formation, with the duration of starbursts extending up to 1000 Myr in some cases. These local starbursts play a deciding role in the evolution of the galaxy in different ways. Ionising radiation, stellar wind and supernova explosion resulting from massive stars formed in the burst, can disrupt the available gas and also alter the chemical composition of the host galaxy (McQuinn et al. 2010b,c). There are different mechanisms which can trigger a local burst of star formation in a dwarf galaxy. While the massive galaxies formed most of their stars in the first few Gyr, the dwarf galaxies are found to form stars over the entire cosmic time, resulting in a wide variety of star formation histories (Cignoni et al. 2018; Tolstoy et al. 2009; McQuinn et al. 2015) and specific star formation rates, ranging from nearly inactive dwarfs to very active BCDs.

Spiral galaxies

Spiral galaxies show signatures of recent star formation in their disk. Among different classes, the late type spirals (Sc or Sd) are found to be more blue and less luminous whereas the early types (Sa and Sb) are more luminous and redder

in nature (Courteau et al. 2007). According to the theoretical models, the self-gravitating and differentially rotating disk of spiral galaxies produces spiral density wave, which acts as one of the dominant mechanisms to trigger star formation along the spiral arms (Roberts 1969). Although, the efficiency of star formation locally depends on several factors such as, gas density, gravitational potential, shear as well as coriolis forces due to disk rotation, ambient pressure and metallicity of the ISM (Leroy et al. 2008). The spiral structure in a galaxy can also affect the GMCs in the local scale to alter their properties (Schinnerer et al. 2013). Toomre (1964) discussed the conditions which decide the large scale stability of a disk to collapse and form stars. A similar investigation was done by Schaye (2004) for the outer part of disk galaxies, where the gas density is relatively low. The inner disks of spiral galaxy have much denser molecular gas than the outer disk. Leroy et al. (2008) reported a constant SFE of H_2 gas in the inner disk. The active star formation therefore primarily happens in the inner disk and enriches the ISM with more metals. This is also reflected in the observed radial metallicity profile of spirals, which show an increasing gradient towards the centre from outside (Phillipps & Edmunds 1991; Kewley et al. 2010; Sánchez-Blázquez et al. 2011; Pilkington et al. 2012).

The disk formation of spiral galaxy supports an inside-out growth scenario, where the inner part of the disk form much earlier than the outer part (White & Frenk 1991; Mo et al. 1998; Brook et al. 2006). This has been tested in several studies with the help of radial colour profiles produced with multiple bands from UV to infra-red (de Jong 1996; Taylor et al. 2005; Muñoz-Mateos et al. 2007). It has been observed that the star formation efficiency (SFE) has a declining nature in the outer part of the galaxy disk where atomic gas becomes more dominant over molecular. Bigiel et al. (2008) found that SFR in the inner disks of spirals follows a single power law relation with the density of molecular gas. Although, they noticed no such relation in the case of atomic gas. As the ISM in the outer disk of spirals are mostly H I dominated and also have relatively less density, it presents

challenges to our understanding of the cloud/star formation processes. The star formation in the outer disks of galaxies has pulled in a great deal of consideration recently, where these studies are centred around the nearby galaxies (Thilker et al. 2005a,b, 2007; Gil de Paz et al. 2005). Deciphering the star formation histories of outer stellar disks also provide information on the growth of galaxy disks with time and tests current models of disk growth (see, for example, Azzollini et al. (2008)). This is also crucial for understanding the chemical enrichment as well as the impact of stellar feedback into the low density ISM (Thilker et al. 2005b). The study of star formation in the outer disk of spiral galaxies has got attention after the phenomenal discovery of extended UV disk (XUV) by Thilker et al. (2005b). This was possible due to the high sensitive UV observation by GALEX. XUV disks are classified into two categories by Thilker et al. (2007); those with structured, filamentary UV emission with spiral patterns were classified as XUV I disks and those with large UV emission in the outer disk were classified as XUV II disks. Several studies are done on the nature of star formation in the XUV disk of spiral galaxies by Thilker et al. (2005a, 2007); Gil de Paz et al. (2005); Zaritsky & Christlein (2007); Wilsey & Hunter (2010). Goddard et al. (2010); Zaritsky & Christlein (2007); Barnes et al. (2011) studied XUV disk of several nearby galaxies with GALEX observations and characterised the star forming regions located in the outer part.

1.4 Importance of multi-wavelength observations

To study the recent star formation activities in a galaxy, the primary step is to trace the young stellar population in it. The photospheric emission of young massive stars peak in the ultra-violet wavelength. For a standard IMF value, the bulk of the far-UV flux of a young star cluster is contributed by OB type stars. The FUV emission can directly trace stellar population of age between 1 - 100

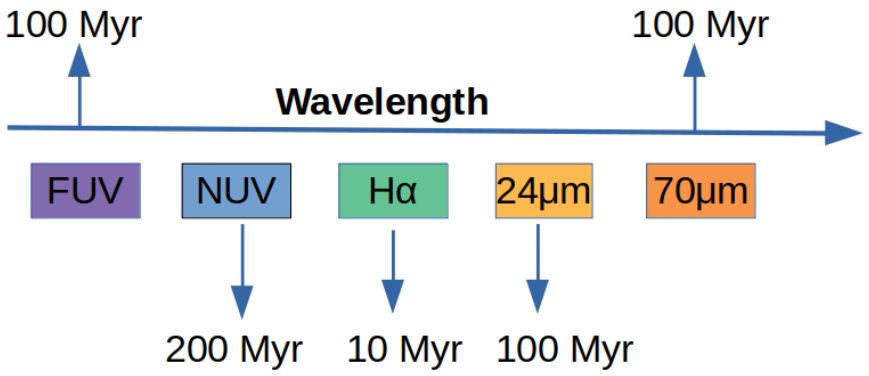

FIGURE 1.5: This figure shows the tracers which are primarily used to identify young stellar population in galaxies. The age corresponding to each tracer signifies that 90% of that emission is contributed by stellar population younger than the given age. This figure is constructed as per the data provided in Kennicutt & Evans (2012).

Myr in galaxies (Kennicutt & Evans 2012), whereas NUV emission is primarily contributed by stars of age up to 200 Myr. Therefore, (FUV−NUV) colour works as an excellent parameter to estimate the age of a star cluster up to a few hundred Myr. Apart from this advantage of directly tracing the younger stars, the study of UV properties of star forming regions has one major disadvantage. This arises due to the high sensitivity of UV photons on the interstellar extinction. The behaviour of extinction in UV shows characteristic variation from galaxy to galaxy or even within a galaxy. Therefore, in order to make an accurate estimation of stellar parameters using UV fluxes, it is essential to have a correct understanding of the underlying dust properties in that region. In order to overcome this drawback and also to achieve a clearer view of the star forming regions, one conventional approach adopted in the literature is to utilise the multi-wavelength data of the galaxy.

One of the powerful proxies used to trace the young massive stars in a galaxy is the Hα emission line of wavelength 6563$\mathring{A}$ (Kennicutt 1998). This line originates due to the transition of electron from orbit 3 to 2 in hydrogen atom. The high energy FUV photons originating from massive stars (M $>$ 15 $M_{\odot}$) can excite the

electron to the 3rd orbit which further drops down to orbit 2 by emitting a photon of wavelength 6563 $\mathring{A}$. The detection of Hα emission in regions within a galaxy thus indirectly confirms the presence of stellar population younger than 10 Myr (Kennicutt & Evans 2012). The other important diagnostic used to trace the young stellar population is emission in far-infrared (FIR). The interstellar dust absorbs some part of the high energy photons emitted by young stars and further re-emit in FIR (Helou 1986; Hunter et al. 1986). The wavelength of this reprocessed light depends on the properties of the dust. The measured FIR flux thus plays a crucial role to estimate the amount of UV photons absorbed by the dust. This, in turn, helps to estimate the value of SFR in regions across the galaxy. It has been noticed that the 24 μm infra-red emission peaks around the youngest star forming regions and thus used as a useful proxy to locate active regions in a galaxy (Helou et al. 2004; Calzetti et al. 2007).

Apart from the emission from stars or dust, the other possible way to locate the sites which are more prone to have star formation is to trace the gas. As the stars form in molecular clouds, the detection of molecular gas will point to the most possible location to have recent star formation in a galaxy. Kennicutt (1998); Bigiel et al. (2008) reported a good correlation between the density of molecular hydrogen and the SFR in galaxies of different types. Also, several studies have shown that the young star clusters forming in the galaxy have a connection with their natal molecular clouds (Leisawitz et al. 1989; Grasha et al. 2018, 2019). Both of these convey a strong clue for molecular clumps to trace sites of recent star formation. The sub-millimeter emission from CO molecules is used as a proxy to trace the molecular hydrogen, which does not have any characteristics emission features at lower temperature. But the detection of molecular gas below a certain density is not an easy task in the case of external galaxies. Therefore, in extreme environments, such as the outer part of disk galaxies, where the gas density is relatively low, it is difficult to trace molecular gas. In contrary, atomic hydrogen gas in a galaxy can be traced directly from the 21 cm emission feature in the radio

band. According to Schmidt (1959); Kennicutt (1998), the SFR within a galaxy is found to correlate with the available H I gas density. But recently Bigiel et al. (2008) studied a sample of spiral and dwarf galaxies and found no such correlation. Still the presence of H I gas in a region hints to the possible presence of molecular hydrogen also. This indirectly traces the sites which have favourable condition to induce star formation (Kennicutt & Evans 2012). A description of these different emissions used to trace star formation is shown in Figure 1.5.

Therefore, the characteristics of star forming regions in a galaxy is best revealed with the utilisation of multi-wavelength observations. This altogether helps to understand the nature of star formation along with the properties of interstellar gas and dust. In order to understand the evolution and overall star formation history of galaxies, astronomers have performed a number of legacy survey programs with the available telescopes. These surveys are mainly of two types, wide field surveys and targeted surveys. The wide field surveys compiled with GALEX (ultra-violet, (Martin et al. 2005)), SDSS (optical, (York et al. 2000)), Two-Micron All Sky Survey (2MASS : near infrared, (Skrutskie et al. 2006)) and H I Parkes All Sky Survey (HIPASS : 21-cm radio, (Meyer et al. 2004)) have uncovered important information about a large number of galaxies. The measurements extracted from these images provide several parameters, such as size, luminosity, stellar mass, star formation history, velocity dispersion etc. of galaxies. On the other hand, the targeted survey like HST programs (Calzetti et al. 2015), Spitzer Infrared Nearby Galaxy Survey (SINGS, (Kennicutt et al. 2003)), The H I Nearby Galaxy Survey (THINGS, (Walter et al. 2008)), The Local Volume H I Survey (LVHIS, (Koribalski et al. 2018)) supplied more detailed observations of some selected nearby galaxies. The observations acquired from all of these surveys have opened a new window of multi-wavelength astronomy in the field of nearby galaxies. Altogether, it helps to understand the nature of different components, such as the young and old stellar populations, the atomic, molecular and ionised gas and also the dust present in a galaxy.

1.5 Motivation and Aim of the study

Young and massive OB stars produce copious amounts of far-UV (FUV) radiation, which can trace star formation up to a few hundred Myr in galaxies, whereas, Hα emission traces star formation only up to a few Myr (Kennicutt & Evans 2012). Imaging studies in UV broad bands can identify young and massive groups of stars, whereas optical bands include contribution from low mass stars as well. There have been several attempts made earlier also to use both photometric and spectroscopic UV observations as the primary tracer of star formation.

The UV telescopes which played an important role in this prospect are Orbiting Astronomical Observatory (OAO, Rogerson (1963), International Ultraviolet Explorer (IUE, Boggess et al. (1978)), XMM Optical Monitor (Mason et al. 2001), Ultraviolet Imaging Telescope (UIT, Stecher et al. (1997)), Far Ultraviolet Spectroscopic Explorer (FUSE, Moos et al. (2000)) and Swift UV/Optical Telescope (Roming et al. 2005). On the other hand, GALEX and HST have played major roles towards our understanding of nearby galaxies. The UV images of nearby star forming galaxies from GALEX mission have made a phenomenal contribution in the last decade (Gil de Paz et al. 2007; Karachentsev & Kaisina 2013a; Thilker et al. 2007). GALEX observations, which covered almost two-thirds of the sky in FUV and NUV, have helped to study spatially resolved star formation in many nearby galaxies. The FUV and NUV fluxes, measured for bright to very faint star forming knots, are utilised to estimate age and mass of those knots across the host galaxy. On the other side, the observations from the HST have helped to identify individual stars in these nearby systems and study the star formation history from the resolved stellar population (Dolphin 2002; McQuinn et al. 2010a; Cignoni & Tosi 2010; Weisz et al. 2014). The HST Legacy ExtraGalactic UV Survey (LEGUS, (Calzetti et al. 2015)) is targeted to image 50 nearby galaxies in different filters including NUV. These have provided valuable insights about clustering of star formation in space and time, cluster evolution, impact of environment on star

formation, connection between young clusters and their parent molecular cloud in galaxies etc.

In summary, the observations from GALEX and HST have made a huge contribution in the field of extra-galactic UV study. Although GALEX imaged in both FUV and NUV with a wide field of view (1.25°), the spatial resolution (∼4.5″ - 6″) is not good enough to resolve star forming clumps in the dense region (especially in the inner part of the galaxy). HST has around 50 times better resolution than GALEX, but it mainly observes up to NUV wavelength with a very small field of view. Therefore, a telescope, which can observe in FUV and NUV bands with a much better spatial resolution than GALEX, can improve the present understanding of nearby star forming galaxies. In this context, the multi-band FUV and NUV observation by Ultra-Violet Imaging Telescope (UVIT) (Kumar et al. 2012) with superior spatial resolution (∼ 1.4″) will give more insights on star forming regions of nearby galaxies.

The resolution of both UVIT and GALEX is not enough to resolve individual stars in nearby galaxies. Therefore, the point like sources, identified in both UVIT and GALEX, are actually star clusters or stellar associations. To characterise these sources, We used starburst99 SSP model which deals with the integrated light of star cluster. One of the great advantages to apply SSP model in UVIT identified star forming clumps, is that the clumps are resolved up to much smaller length scale (i.e. ∼1.4″ ≈ 6.8 pc at the distance of 1 Mpc) and hence it is more probable that they are actually single entity. This motivates us to utilise UVIT data for studying younger clumps throughout a galaxy from inner to outer part.

In this thesis, we have studied four nearby star forming galaxies with the help of UVIT/GALEX images in combination with other multi-wavelength observations. Our sample contains two dwarf irregular galaxies (WLM and IC 2574) and two spiral galaxies (NGC 300 and NGC 7793). Each of the selected galaxy is located

within a distance 4 Mpc and offer a wide range of environment for exploring the nature of star formation. The aims of the study can be summarised as

1. To detect the sites of recent star formation and connect it to possible drivers of star formation.

2. Map the structure (sizes and locations) and hierarchy among the star forming regions, to study their correlation with the galactic environment.

3. To understand the connection between atomic hydrogen gas, Hα emission and the properties of identified young stellar clumps.

4. To compare the nature of star forming regions detected in various types of galaxies studied here.

In order to detect young star forming regions in galaxies, we used the FUV images from UVIT and GALEX. With the spatial resolution of UVIT, we could resolve star forming clumps smallest up to $\sim$ 10 pc. We used FUV magnitude and (FUV$-$NUV) colour of the clumps to estimate their age and mass. This helped us to understand the spatial distribution of star forming clumps as a function of age and mass throughout a galaxy. In the case of GALEX observation, we followed the same method to study stellar population only in the outer disk, where crowding is less. The hierarchy in the structure of star forming regions is studied with the help of *astrodendro* python package. We utilised neutral hydrogen column density map of each galaxy to understand the connection between the distribution of ISM and star forming regions. This helped us to decipher the possible mechanisms which can trigger star formation in the galaxy. The Hα and other multi-wavelength data are used to explore the properties of the identified clumps in more detail.

1.6 Overview of the Thesis

- **Chapter 1:** A general introduction to galaxies, their properties and the nature of star formation in different types are presented. We discussed the

importance of the nearby galaxies, with specific description on dwarf irregular and spiral galaxies, and the usefulness of multi-wavelength study to understand recent star formation. We also explained the motivation and aim of our study.

- **Chapter 2:** Details of various observations, data and the corresponding telescopes/instruments/observatories used in this study are presented in this chapter.

- **Chapter 3:** This chapter discusses the theoretical models and the data analysis techniques adopted for the study.

- **Chapter 4:** We present a study of a nearby dwarf irregular galaxy WLM to understand the demographics of young star forming regions as a function of temperature. We used multi-band UVIT data along with observations from other wavebands and studied the properties of younger star forming clumps and also the neutral and ionised ISM.

- **Chapter 5:** In this chapter, we present a UVIT imaging study of a nearby dwarf irregular galaxy IC 2574. We identified young star forming regions in the galaxy and explore their connection with the H I holes and shells. We estimated several parameters of these regions and studied their hierarchical nature.

- **Chapter 6:** This chapter presents the study of a nearby flocculent spiral galaxy NGC 7793. We identified young star forming clumps with UVIT imaging data and studied their properties. The nuclear star cluster and the overall disk emission profile of the galaxy in UV and H I are also discussed.

- **Chapter 7:** In this chapter, we present a study of a nearby spiral galaxy NGC 300. We studied the nature of star formation in the extended UV disk of the galaxy with GALEX observations. Other multi-wavelength data are used to study the nature of the disk emission in different bands.

- **Chapter 8:** The results of the study are summarised in this chapter along with the conclusions. We also discussed a few projects which are planned for the future.

Chapter 2

Data and Observation

2.1 Data

The primary objective of this thesis is to understand the nature of star forming regions in nearby galaxies using multi-wavelength observations. In order to achieve the goal, we obtained data from different telescopes operating in different wavebands. The key analysis of this study is performed with ultra-violet data acquired from UVIT (Kumar et al. 2012) and GALEX (Martin et al. 2005). As FUV emission traces stellar population of ages up to a few 100 Myr (Kennicutt & Evans 2012), we used FUV images of galaxies to locate young star forming regions. The combination of NUV with FUV helped further to characterise these identified regions in terms of their age and mass. The results obtained from UV data are compared with other multi-wavelength observations, such as optical, infra-red, Hα, H I and molecular CO, for further inferences. The H I column density maps of the galaxies are obtained from the Very Large Array (VLA)(Thompson et al. 1980)

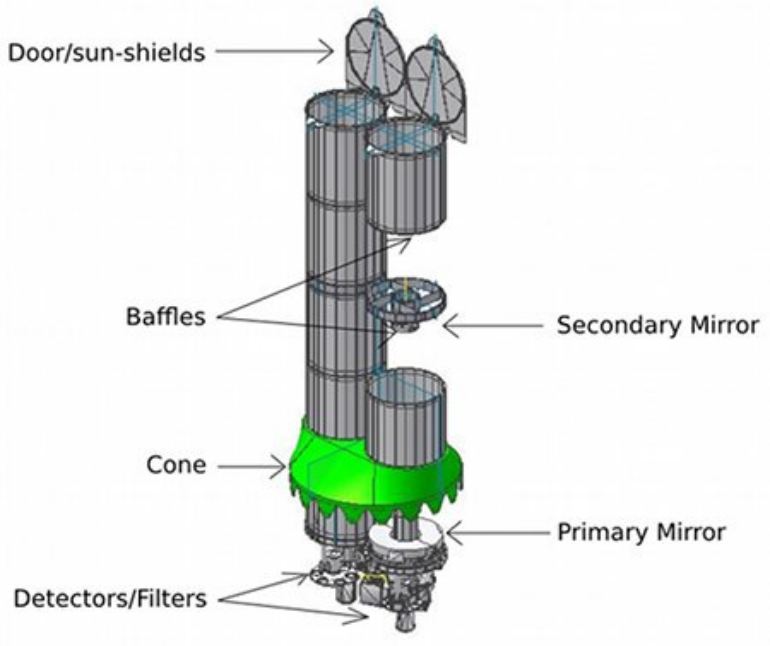

FIGURE 2.1: The layout of UVIT instrument housed in AstroSat satellite. Image courtesy : UVIT webpage of Indian Institute of Astrophysics.

and the Australia Telescope Compact Array (ATCA) (Frater et al. 1992) observations. The optical, Hα, infrared and molecular data, used for specific galaxies, are mainly acquired from NASA/IPAC Extra-galactic Database (NED). In this chapter, we discuss the data and observations used in this study.

2.2 Ultra-violet

In order to trace the locations of young star forming regions in galaxies, we used ultra-violet imaging data from the observation of UVIT and GALEX. Among the four galaxies discussed in this work, three (WLM, IC 2574 and NGC 7793) are observed with UVIT and one (NGC 300) with GALEX.

2.2.1 Ultra-Violet Imaging Telescope (UVIT)

UVIT is a part of India's first multi-wavelength space observatory AstroSat (Singh et al. 2014), launched on 28 September 2015 by the Indian Space Research Organization (ISRO). The satellite is placed at an orbit of 600 km with a period of 90 minutes around the earth. AstroSat is also equipped with three X-ray telescopes which all can observe simultaneously along with UVIT. UVIT is a twin-telescope, where one observes in FUV and another in both NUV and Visible (Figure 2.1). The Visible channel is used to track the drift pattern of source on the detector in the course of observation, though tracking can also be done using FUV and NUV observations in case there are enough UV bright stars in the field. Each of FUV, NUV and Visible channels of UVIT consists of multiple photometric filters of different band-widths. The effective area profiles for these band-widths are shown in Figure 2.2. The band-width, mean wavelength, unit conversion factor and zero point magnitudes are listed in Table 2.1. These values are adopted from the calibration paper of the instrument by Tandon et al. (2017). The instrument is also equipped with two gratings in FUV and one in NUV. These enable UVIT to perform a low resolution slit-less spectroscopy in both the channels.

Both the telescopes of UVIT have f/4.5 Ritchey-Chertian configuration with a focal length of $\sim$ 4750 mm and a circular field of view of diameter $28'$ (Kumar et al. 2012). The primary and secondary mirrors of the two telescopes are hyperbolic in nature and have optical diameters of $\sim$ 375 mm and 140 mm respectively. After the primary and secondary mirrors, the incoming light enters into the filter/grating system in the FUV telescope, whereas the light is split into NUV and optical beams with the help of a dichroic beam splitter before feeding to the filter/grating system. The light beam coming out from the filter/grating is then directed to the detector system. All the three channels of UVIT have intensified Complementary Metal Oxide Semiconductor (CMOS) detector which can work either in photon counting (PC) or integration mode. The FUV and NUV detectors work in the PC

mode while the Visible detector works in the integration mode.

The photon counting detectors of the UVIT (Hutchings et al. 2007) are composed of five primary components, i.e. a photo cathode, micro-channel plate (MCP), phosphor, fiber optic taper and a CMOS image sensor (Figure 2.3). A UV/optical photon enters through the detector window and first hits the photo-cathode which in response ejects an electron. This primary electron is directed towards the MCP, kept in a high voltage of gain $\sim 10^7$. The MCP produces a large number of secondary electrons which are further directed towards the phosphor anode. As the secondary electrons hit the phosphor plate, it emits light. The emitted light is mapped on to the CMOS detector with the help of fiber optic taper connected between them.

The FUV and NUV detector systems work in centroiding mode to read out the photon pulse (Hutchings et al. 2007). The on-board hardware system of the telescope uses a local mean algorithm for the centroiding. In each frame, the centroids of the photon events are recorded across the CMOS detector which has a 512×512 pixel array. For the full field of the detector, the frames are read at a frequency of 28.7 Hz. A smaller window size provides higher frequency for read out (for example, 600 Hz for a 100×100 sub-window). Though a single CMOS-pixel subtends $3.3''$ of the sky, the utilisation of centroiding technique provides a sub-CMOS-pixel spatial resolution which improves the Full Width at Half Maximum (FWHM) of the Point Spread Function (PSF) up to $\sim 1.4''$ (plate scale $\sim 0.4''$). The spatial resolution of $\sim 1.4''$, a field of view of $28'$ along with the suit of multiple filters have made UVIT a unique instrument for imaging in UV.

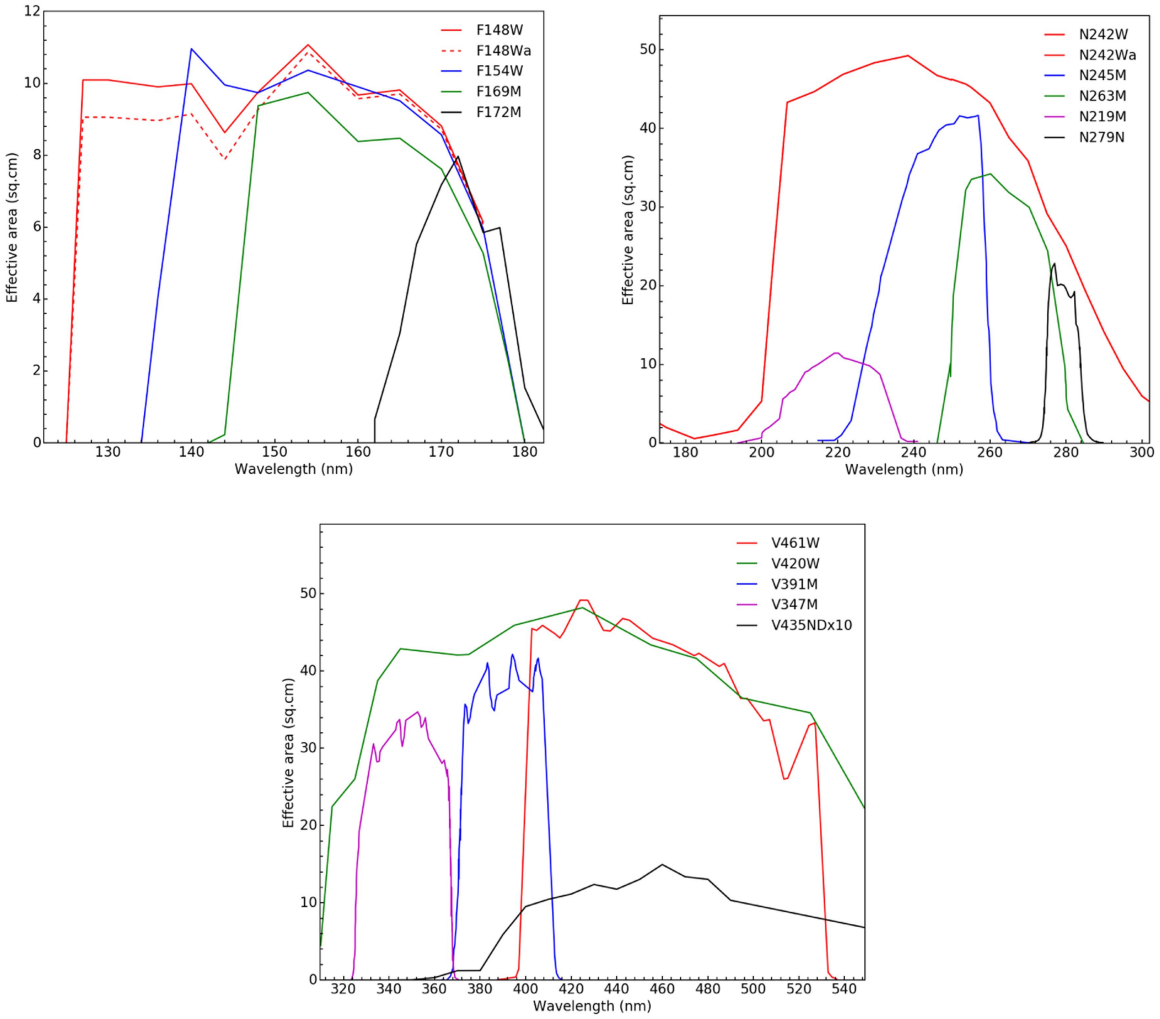

FIGURE 2.2: The effective area profiles of UVIT in the filters available in FUV, NUV and Visible channels of UVIT. Image courtesy : Tandon et al. (2017)

2.2.1.1 Data Processing

The effective observing time of UVIT ranges from 15 - 25 minutes in a single orbit of the satellite. The data recorded in each orbit contain the centroid information of every photon event in each observed frame along with many secondary information such as operating voltages, filter identification, detector window size etc. These are downloaded from the orbit. The data in this raw format are called Level 0 (L0) data. The acquired data from each instrument are reformatted and extracted as Flexible Image Transport System (FITS) table, which is called as Level 1 (L1)

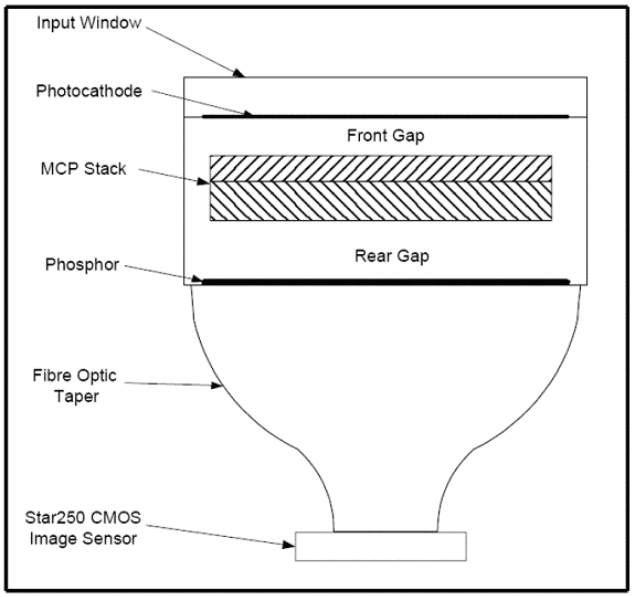

FIGURE 2.3: The photon counting detector system of UVIT. Image courtesy : Hutchings et al. (2007)

TABLE 2.1: Details of FUV and NUV filters of UVIT as obtained from Tandon et al. (2017)

Filter	λ_{mean} ($\mathring{A}$)	$\triangle\lambda$ ($\mathring{A}$)	ZP magnitude (AB)	Unit conversion (erg/sec/cm^2/$\mathring{A}$)
F148W	1481	500	18.016	3.09E-15
F148Wa	1485	500	17.994	3.28E-15
F154W	1541	380	17.778	3.55E-15
F172M	1717	125	16.342	1.074E-14
F169M	1608	290	17.455	4.392E-15
N242W	2418	785	19.81	2.22E-16
N245M	2447	280	18.50	7.25E-16
N263M	2632	275	18.18	8.44E-16
N219M	2196	270	16.59	5.25E-15
N279N	2792	90	16.50	3.50E-15

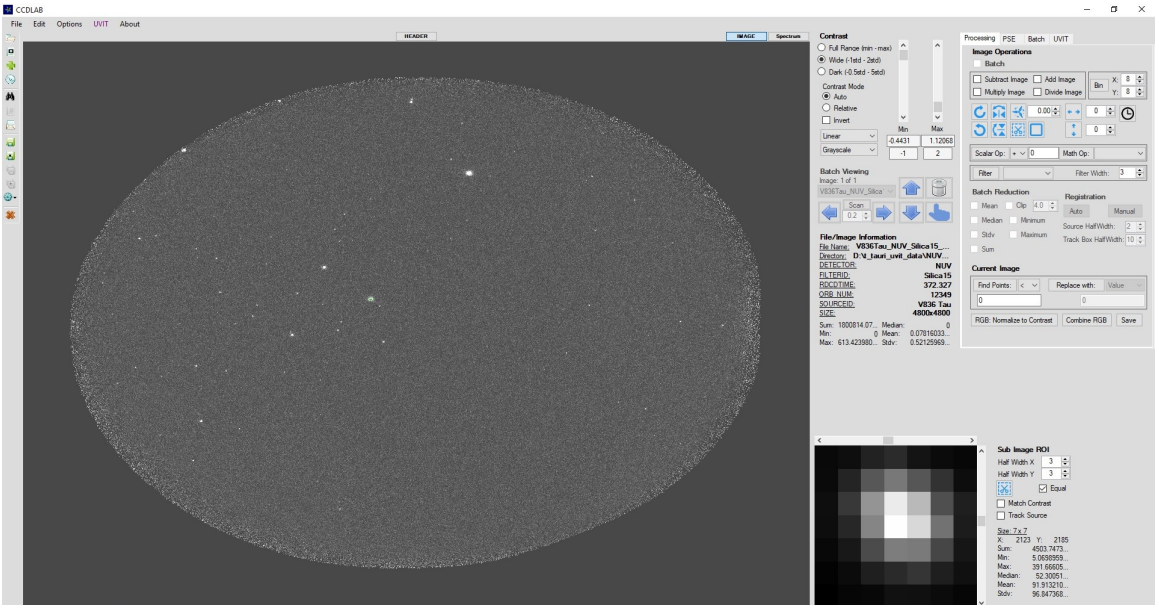

FIGURE 2.4: The layout of CCDLAB software (Postma & Leahy 2017) used for UVIT data reduction.

data. These L1 data are used to produce science ready images (i.e. L2 data) following several corrections related to the detector and the observation. We used CCDLAB software (Postma & Leahy 2017), specifically designed for UVIT, to produce L2 data from L1 following these corrections. In Figure 2.4, we have shown a snapshot of the CCDLAB window.

Detector-specific corrections

The L1 data downloaded for each orbit can have data duplication, whereas the merged L1 data are corrected for data duplication. CCDLAB software checks the timestamp for each observed frame and then discards the duplicate frames accordingly. The time difference between the last and the first unique frame is considered as the integration time for each single observation, after accounting for frames removed in-between, due to any artefact, such as cosmic ray showers, missing frames etc.

The observed frames are corrected for distortion, which is intrinsic to the detector.

The distortion appears due to the imperfection in the fiber-taper bundle connected to the CMOS detector (Girish et al. 2017). This results in a variation of the PSF shape across the detector. The nature of distortion is calibrated in the ground and also tested on-board with observed field of the Small Magellanic Cloud (SMC). This calibration file is used in the CCDLAB to correct distortion in images in order to achieve an astrometric accuracy of rms less than 0.5″.

The software also corrects each frame for the bias in centroiding. A photon pulse taken through the optical fiber-taper falls on 3×3 pixels of the detector. The centroiding, calculated with weighted mean algorithm, is performed on this 3×3 box, which is not large enough for good a sampling. This creates a bias in the centroid position by generating a fixed-pattern noise (FPN) in observed images. The centroid bias list, provided in UVIT calibration database, is used to correct this in each observed frame.

We also performed flat field correction for the distortion and bias corrected images with CCDLAB. Flat is performed to account for the non-uniform sensitivity of the pixels across the detector. The variation in sensitivity appears due to combined modulation of photo-cathode, MCP, phosphor, optical fiber-taper and the CMOS detector across the field. Each image is corrected for this sensitivity variation with the help of FUV and NUV flat field file available in the UVIT calibration database.

Drift correction

The observations taken with UVIT as well as other space telescopes experience drift of sources on the detector during the course of observation. There are three different reasons which induce drift in the UVIT observed images (Postma & Leahy 2017). A low frequency ordered drift appears in the image due to the guided oscillation of the AstroSat satellite. This is done to spread the charge depletion across the MCP. Two other sources which produce random drift are

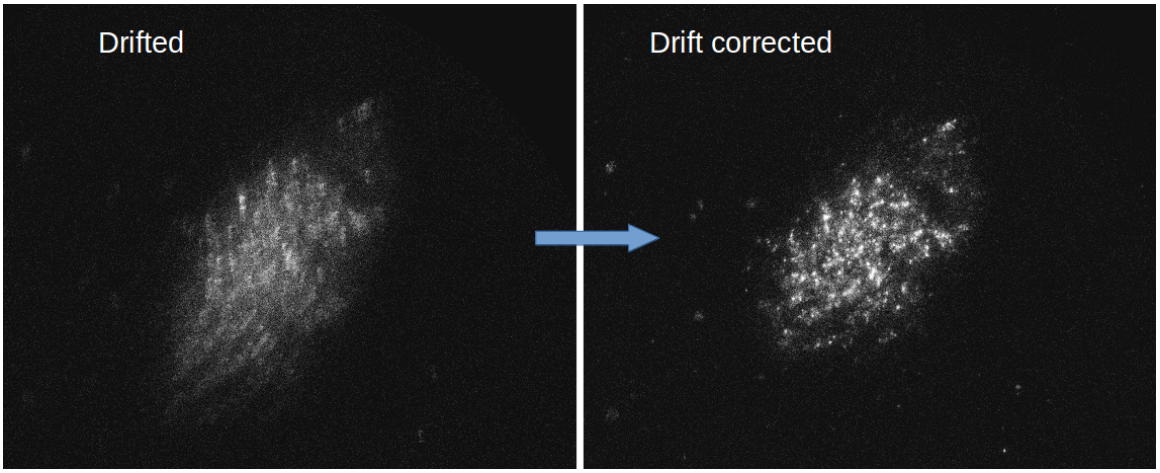

FIGURE 2.5: The UVIT FUV image of the galaxy NGC 7793. Left : Image before drift correction, Right : Image after drift correction.

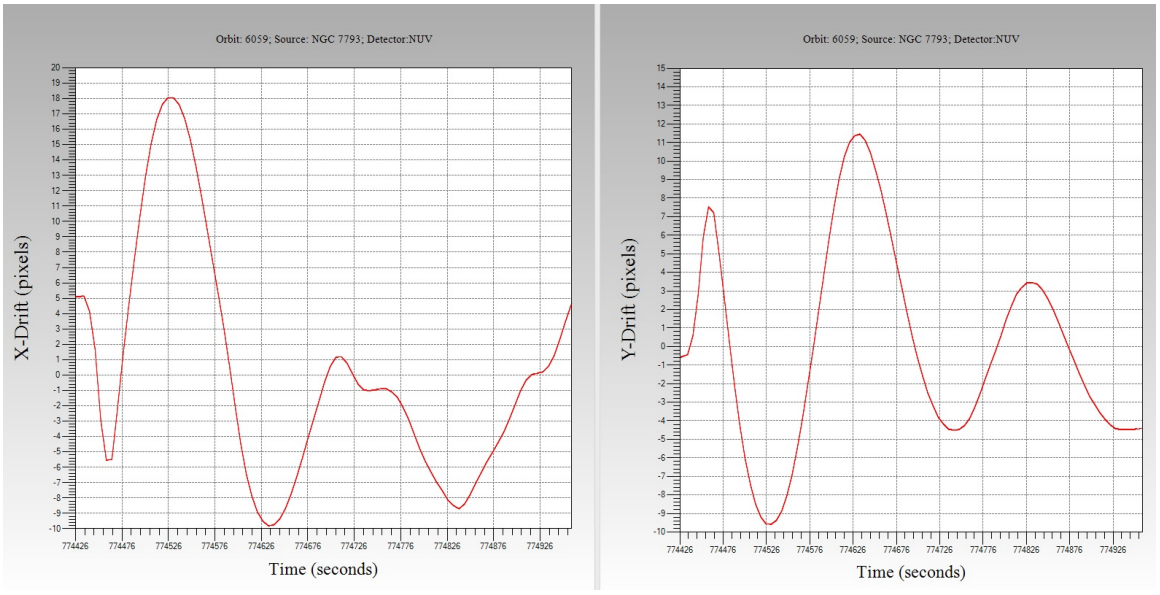

FIGURE 2.6: An example of typical drift pattern of UVIT field during the course of observation.

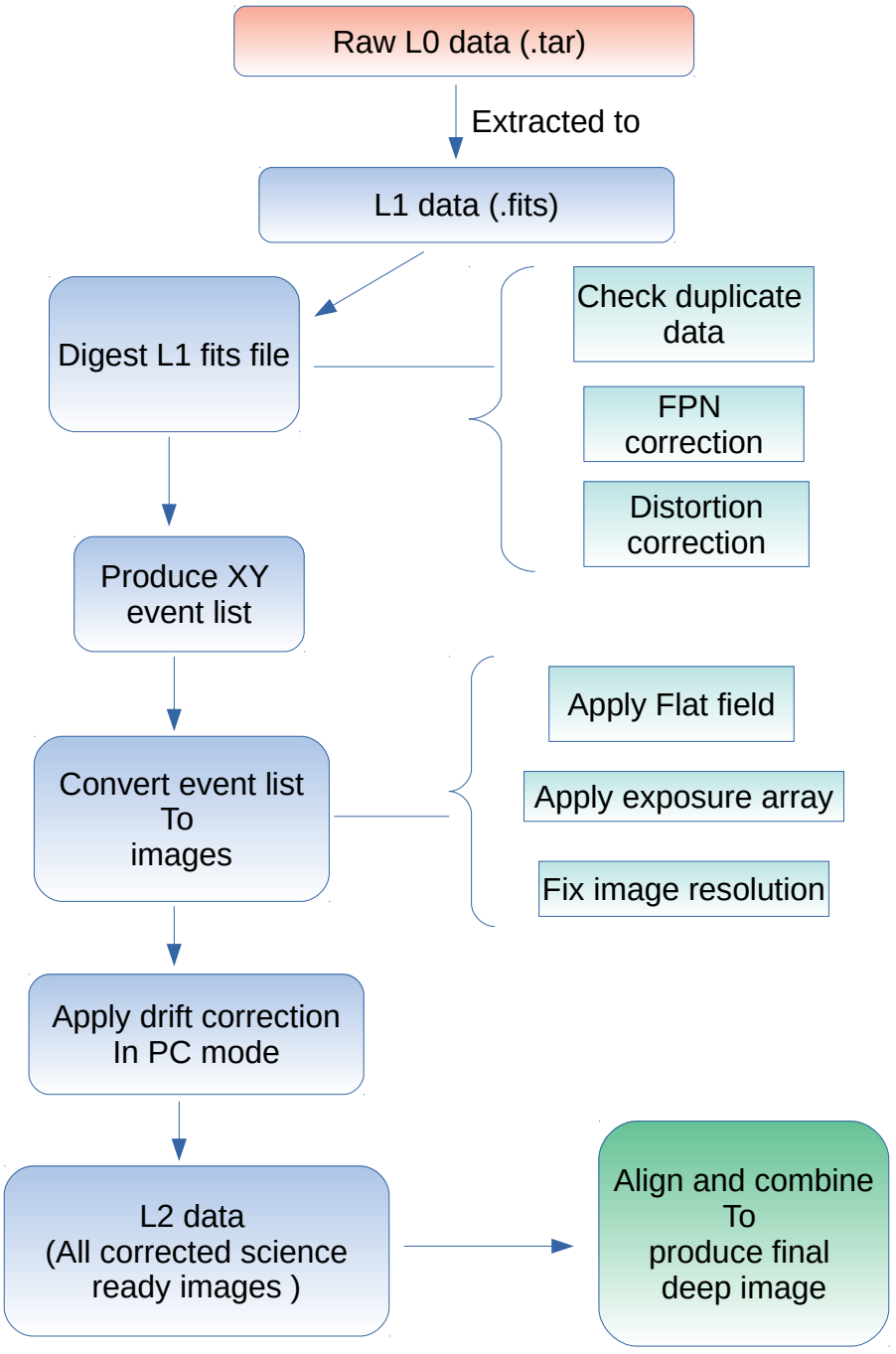

FIGURE 2.7: Flow chart for UVIT data reduction procedure using CCDLAB.

the motion of satellite in the orbit and the movement of the telescope due to the rotation of Scanning Sky Monitor (SSM), another component of AstroSat. CCDLAB calculates the combined drift in each frame. The centroid of the same point source in different frames are merged together with this calculated drift series to produce the final drift corrected image. In Figure 2.5, we show one image of the galaxy NGC 7793 before and after drift correction. A typical drift pattern in the XY pixel coordinate is also shown in Figure 2.6. Due to this drift of the satellite, the sources present near the edge of the detector sometimes go outside the field. As a result, these sources are not exposed throughout the total integration time. CCDLAB also corrects the image for this effect with the help of an exposure array map.

Following these corrections, the science ready images are produced for each orbit. In case the same object is imaged in multiple orbit, CCDLAB also provides the scope to stack them in easy interactive way. The centroid lists of all these images are registered first and then co-aligned with respect to one reference image. The aligned images are then summed up to produce the final science ready image of the object. The images used in this study have 4096×4096 pixel dimension which were built by dividing each pixel of the detector into 8×8 pixels. This has been possible due to the centroiding technique adopted in the detector (Hutchings et al. 2007). The end-to-end procedure of UVIT data processing is shown as a flow chart in Figure 2.7. We have followed these steps to produce science ready images for the galaxy WLM, IC 2574 and NGC 7793 in multiple bands of UVIT.

2.2.1.2 UVIT observations of nearby galaxies

The galaxy WLM is observed in two FUV filters (F148W & F169M) and two NUV filters (N242W, N245M & N263M). The data obtained in F169M filter had a very

low S/N value and hence we could not use it. The work presented in this study on WLM uses the data in three filters F148W, N245M and N263M.

The galaxy IC 2574 was proposed to observe in two broad band filters F148W and N242W. We acquired the data in F148W filter but the data in the NUV channel were not made available due to payload related problems. The work presented on IC 2574 in this study uses the data only in F148W filter.

We used two broad band filters F148W and N242W to image the galaxy NGC 7793. In order to avoid bright UV stars coming in the UVIT field of view, the galaxy was offset by a few arcmin in this observation.

The UVIT images of each galaxy have 4096×4096 pixel dimension with 1 pixel corresponding to 0.4″. At the distance of the galaxy, one pixel corresponds to 2 pc, 7.6 pc and 6.8 pc respectively for WLM, IC 2574 and NGC 7793. The observation ID, date of observation, filters used and exposure time of each final image for these three galaxies are listed in Table 2.2.

2.2.2 Galaxy Evolution Explorer (GALEX)

GALEX is a space telescope dedicated for all-sky imaging in the ultra-violet band (Martin et al. 2005). It was launched on 28 April 2003 from the Kennedy Space Centre by the NASA. The satellite was stationed at an orbit of 690 km with an inclination of 29°. It has an orbital period of 96 minutes with an effective eclipse time between 25 - 30 minutes. The instrument had a 50 cm f/6 Ritchey-Chertian telescope with a circular field of view of diameter 1.25°. GALEX has two imaging bands, FUV (1344-1786 $\mathring{A}$) and NUV (1771 - 2831 $\mathring{A}$) along with grisms to perform low resolution slit-less spectroscopy in both the bands (Figure 2.8). The light from the secondary mirror proceeds through a wheel equipped with selectable grism or

TABLE 2.2: Log of UVIT observations.

Galaxy	Observation ID	Date of observation	Filters	Image exposure time (sec)
WLM	G05_222T01_9000000520	2016-06-30	F148W	2634
			F169M	-
			N245M	1926
			N263M	2370
	G07_005T01_9000001430	2017-08-03	F148W	3378
			N242W	2824
IC 2574	G07_005T02_9000001214	2017-05-10	F148W	10375
			N242W	-
NGC 7793	G06_024T01_9000000780	2016-11-10	F148W	6543
			N242W	8919

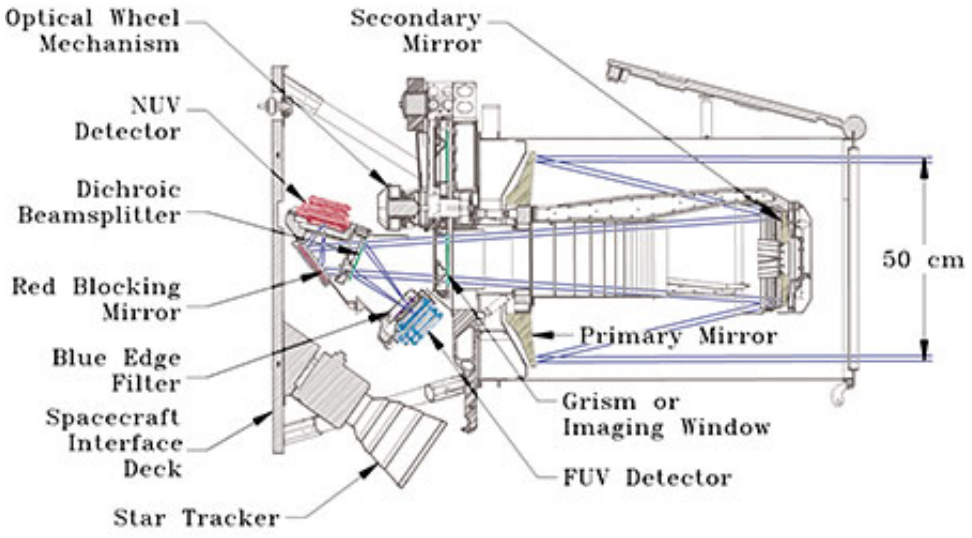

FIGURE 2.8: The layout of GALEX instrument. Image courtesy : GALEX webpage maintained by the instrument science team.

imaging window. A multilayer dichroic coating is used to separate out FUV and NUV light from the incoming beam. The split beams are then directed through the FUV/NUV channel and further collected by the respective detectors. The effective area profiles for the two bands are shown in Figure 2.9 and other related information are given in Table 2.3.

Each detector of the instrument consists of a cathode, micro-channel plate and double layer anode. Both the detectors work in photon counting mode with simultaneous observations in FUV and NUV. The image resolution (FWHM) of the instrument is $4.2''$ in FUV and $5.3''$ in NUV. The key advantage of the instrument is its wide field of view along with the sensitivity to detect sources up to 25 magnitude. The primary objective of the mission was to image a large sample of galaxies from nearby universe to high red-shift in UV. This is to explore the evolution of different types of galaxies and also to understand their recent star forming activities. Several survey programs were performed with GALEX which all together have covered around 2/3 of the sky.

As the detector works in photon counting mode, the primary level of the data contains a list of photon positions on the detector and their arrival time. These lists are corrected for satellite motion and other detector related effects, flat-fielded and background subtracted with the help of a ground based pipeline to produce science ready images (Morrissey et al. 2007). These images are again compiled with SExtractor program (Bertin & Arnouts 1996) to produce a catalogue of point sources present in the observed field. The pipeline generated catalogue contains several information including source position (RA and Dec), their FUV and NUV magnitudes and respective errors etc.

We used images as well as the catalogue of sources produced by GALEX data pipeline for the galaxy NGC 300 in this study. The galaxy was observed as a part of Guest Investigator (GI) survey program between 2004-10-26 to 2004-12-15, and

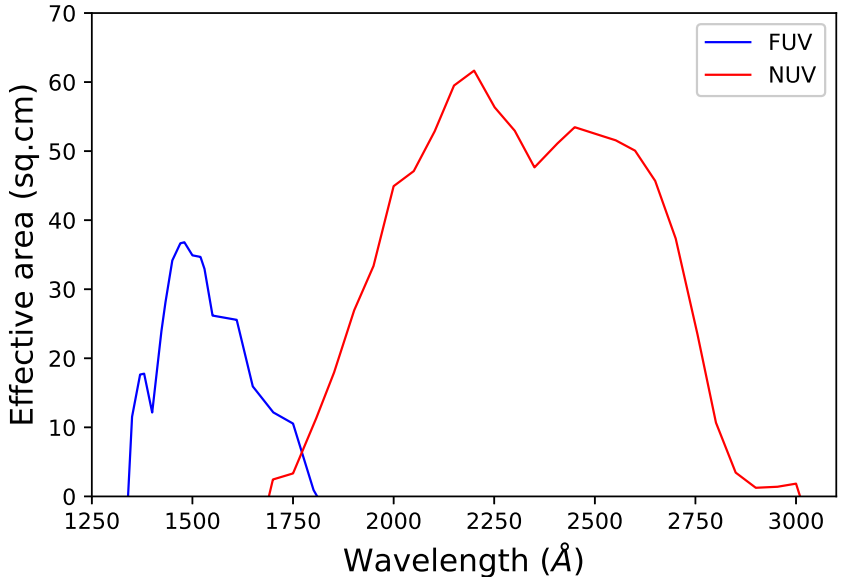

FIGURE 2.9: The effective area profiles of GALEX FUV and NUV filters.

TABLE 2.3: Details of GALEX filters.

Filter	λ_{mean} ($\AA$)	$\triangle\lambda$ ($\AA$)	ZP magnitude (AB)	Unit conversion (erg/sec/cm^2/$\AA$)
FUV	1538	442	18.82	1.40E-15
NUV	2315	1060	20.08	2.06E-16

the Image ID is 3073040579138954826 (tile name GI1_061002_NGC0300). The FUV and NUV images have an exposure time of 12987 sec.

2.2.3 HST/WFPC2-F170W

We have used the star catalogue of the galaxy WLM observed in the FUV F170W filter of HST/WFPC2. The data, containing the positions and F170W band magnitudes of stars, were obtained from Bianchi et al. (2012).

2.3 21 cm H I data

We have used H I column density maps from two radio telescopes. For the galaxy WLM, IC 2574 and NGC 7793, the moment 0 H I maps are acquired from VLA observations whereas we used data from ATCA for the galaxy NGC 300.

2.3.1 Very Large Array (VLA)

VLA is a radio interferometer array of the National Radio Astronomy Observatory (NRAO)(Thompson et al. 1980). It is situated in New Mexico, USA. The array contains 28 antennae each of size 25 meter. The telescope operates within the frequency range from 1 GHz to 50 GHz. The telescope array has four different configurations (A, B, C & D), which cover different baseline. VLA has been utilised to perform various surveys which also include the observation of nearby galaxies in 21 cm wavelength. Two such surveys are Very Large Array - ACS Nearby Galaxy Survey Treasury (VLA-ANGST) and The H I Nearby Galaxy Survey (THINGS). We obtained H I column density map (moment 0) of the galaxy WLM, IC 2574 and NGC 7793 from VLA observations. Each pixel of the obtained VLA images corresponds to $1.5''$ with an image unit of Jy beam^{-1} m s^{-1}. We used equation 2.1 given in Ott et al. (2012) to estimate the H I column density $N_{H\ I}$ (number/cm^2) from the pixel value. In equation 2.1, b_{maj} and b_{min} signify the major and minor axes of beam in arcsecond and $\sum S_i \Delta v$ is the pixel value of moment 0 map in Jy beam^{-1} km s^{-1} unit.

$$N_{H\ I} = 1.104 \times 10^{24} \frac{1}{b_{maj} b_{min}} \sum S_i \Delta v \tag{2.1}$$

The H I data of the galaxy WLM was obtained from NED whereas for IC 2574 and NGC 7793 the data was downloaded from the THINGS database (Walter et al. 2008).

2.3.2 Australia Telescope Compact Array (ATCA)

ATCA is an array of six 22 meter radio antennae located in the Paul Wild Observatory near Narrabri, Australia (Frater et al. 1992). The telescope works in the frequency range between 1.1 to 105 GHz. Five antennae are movable and the sixth one is fixed which together provide different baseline for observation. We obtained the moment 0 H I data of the galaxy NGC 300 from the combined observation of ATCA & Galactic All Sky Survey (GASS). The data were made available by Westmeier et al. (2011) in the form of data cube which we combined using Interactive Data Language (IDL) to produce the integrated column density map of NGC 300. The observations were carried out at a frequency 1420 MHz with a bandwidth of 8 MHz. The pointing covered a large area ($\sim 2^\circ \times 2^\circ$) around the galaxy NGC 300 to map both H I line and continuum emission.

2.4 Hα - Optical images

We have used Hα observations for the analysis of galaxy WLM and IC 2574. The Hα image of WLM was obtained from NED. The observations were obtained from the Cerro Tololo Inter-American Observatory (CTIO) 4.0 meter telescope for an exposure time of 300 sec, by Massey et al. (2007). The image has 2048×4096 pixel array with 1 pixel corresponding to 0.27″. For IC 2574, we used the catalogue of Hα emitting regions given in Miller & Hodge (1994). The observations were performed at the Kitt Peak National Observatory (KPNO) 0.9m telescope for both Hα line and continuum emission. The catalogue contains position, size and flux information of 289 H II regions in the galaxy IC 2574. The Digitized Sky Survey (DSS) blue band image of NGC 300, obtained from NED, was also used in our analysis.

TABLE 2.4: Log of Data used in this study

Galaxy	Ultra-violet	Optical	Hα	Infra-red	21 cm H I	Molecular
WLM	UVIT (F148W, N245M, N263M), HST F170W	-	CTIO 4.0m	-	VLA	ALMA
IC 2574	UVIT (F148W)	-	KPNO 0.9m	-	VLA	-
NGC 7793	UVIT (F148W, N242W)	-	-	-	VLA	-
NGC 300	GALEX (FUV, NUV)	DSS B band	-	IRAC 3.6 μm, MIPS 24 μm	ATCA-GASS	-

2.5 Infra-red images

We used 3.6μm and 24μm infra-red images of the galaxy NGC 300 in our analysis. The observations in 3.6μm mid-infrared band were obtained using Infra-red Array Camera (IRAC) (Fazio et al. 2004), while 24μm far-infrared observations were obtained using Multi-band Imaging Photometer for Spitzer (MIPS) (Rieke et al. 2004). Both the IRAC and MIPS are instruments in Spitzer space telescope. The images were obtained from NED database. A single pixel of the images in 3.6μm and 24μm bands respectively subtends 0.75″ and 1.5″.

2.6 Molecular CO data

The catalogue of CO molecular clouds observed by ALMA in the galaxy WLM, presented by Rubio et al. (2015), was used in our analysis. The catalogue contains position, size, flux density, virial mass and dispersion velocity of 10 CO clouds.

2.7 Summary

The data and observations presented in this chapter are summarised below.

1. Here we present the details of the multi-wavelength data used in this thesis.

2. We acquired multi-band UVIT data for the galaxies WLM, IC 2574 and NGC 7793. Details of observation are presented. For the galaxy NGC 300, we used GALEX images as well as identified source catalogue.

3. We described the details of UVIT instrument and data processing technique along with a flow chart.

4. The data from other bands, such as 21 cm H I, optical, Hα, infra-red and molecular CO data and the sources are discussed briefly.

Chapter 3

Methodology

3.1 Introduction

The observed and processed data need to be compared/interpreted/analysed using theoretical models. In this chapter, we present the models and techniques adopted in our study for analysing the data.

The galaxies studied here are located between 1 - 4 Mpc. The spatial resolution of either the UVIT or the GALEX is not sufficient to resolve individual stars at these distances. On the other hand, a star cluster or a stellar association in these galaxies would appear as a point source or a clump in the UVIT or GALEX images. Therefore, the flux corresponding to such point sources signifies the amount of integrated light contributed by a group of stars which are likely to be part of a single entity. In order to characterise these, we used starburst99 simple stellar population (SSP) model (Leitherer et al. 1999). This model provides synthetic spectra for the integrated light of star clusters. We exploit the model data to

produce diagnostic diagrams which help us in characterising the detected point sources in these galaxies. We also use Castelli & Kurucz (2004) stellar models to decipher the temperature of star forming regions. Depending on the properties of each galaxy and related science goal, we adopted appropriate techniques for analysis. For identifying star forming clumps we used *daofind* package of IRAF and *astrodendro* package of Astropy (Hunter 2007). The photometry of the sources are performed using either IRAF *daophot* or *photutils* astropy packages.

3.2 Theoretical models

3.2.1 Starburst99 Simple Stellar Population model

We used starburst99 model (Leitherer et al. 1999) to estimate age and mass of the identified star forming clumps. Starburst99 is a spectrophotometric SSP model for an actively star forming galaxy. The model provides integrated spectrum of star clusters of different ages within the wavelength range between 91 $\mathring{A}$ to 160 μm. Six such model spectra of different ages are shown in Figure 3.1. There are several free input parameters which can be varied to generate the required model spectrum. Among these the important parameters are star formation law, total cluster mass, initial mass function (IMF), mass boundaries for IMF, metallicity and the type of stellar evolutionary track (Table 7.2). The star formation law can be fixed as either continuous or instantaneous. In case the star formation rate is constant over a larger time scale, the continuous law is chosen while instantaneous law is applied for regions undergoing variable star formation with changing stellar birth and death rate. For galaxies with active star formation or enhancement in recent star formation, the instantaneous star formation law is considered as the suitable choice. The total mass of the cluster can also be fixed for instantaneous

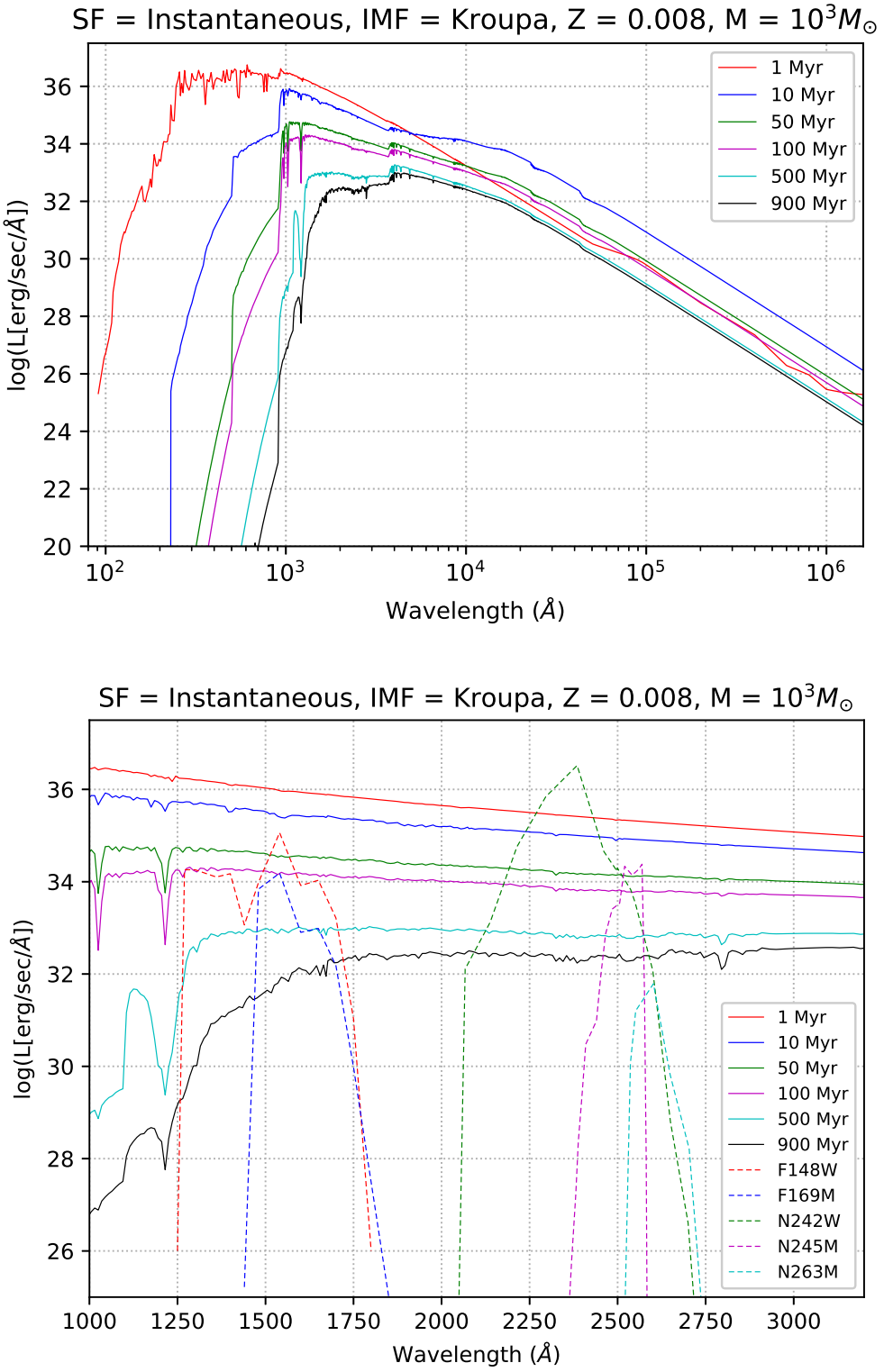

FIGURE 3.1: The upper panel shows Starburst99 model generated integrated spectrum for six different ages. The parameters chosen are mentioned in the figure. In the lower panel, the UV part of the above spectrum are shown along with the scaled effective area profiles of five different UVIT filters.

law of star formation. This is generally fixed within a range between $10^3 - 10^7 M_\odot$. The flux level of the spectrum increases with increasing cluster mass.

The type of IMF and the associated stellar mass limits are selected on the basis of observed environment. The exponents of IMF can be fixed with stellar mass boundaries for multiple intervals. For example, Salpeter IMF has a single exponent ($\alpha = 2.35$) whereas Kroupa IMF has two exponents ($\alpha = 1.3, 2.3$) for two different mass intervals. Another important parameter is the metallicity. Starburst99 offers five different values (Z = 0.001, 0.004, 0.008, 0.02, 0.04) for the metallicity. The model uses Padova and Geneva stellar evolutionary tracks for the evolution of a star cluster. There are six different options available for evolutionary tracks. This is selected primarily based on the age range of cluster one is interested to study.

Apart from these parameters, one can also vary the cut-off mass for supernova and black hole which have default values of 8 $M_\odot$ and 120 $M_\odot$ respectively. One can also change the stellar wind model for specific needs. The model also provides supernova rate, the number of Wolf-Rayet (WR) and O type stars with the evolutionary time of a cluster. The bolometric luminosity and mass-loss rate of a cluster are also estimated as a function of age. Starburst99 also provides many important information related to the FUV emission of a cluster, which include the stellar continuum, FUV line spectra, measure of Lyman alpha discontinuity, Hα and Hβ equivalent width etc. A personalised simulation can be run in this *web interface*[*] to produce necessary output files.

In our study, we assumed the star formation law to be instantaneous for the estimations. IMF value is taken to be 1.3 (for 0.1 $M_\odot$ to 0.5 $M_\odot$), 2.3 (for 0.5 $M_\odot$ to 120 $M_\odot$) (Kroupa IMF, (Kroupa 2001)) with stellar mass limit as $M_{low} = 0.1 M_\odot$ and $M_{up} = 120 M_\odot$, which are appropriate for studying SSP up to a few 100 Myr. For a fixed metallicity (as per the metallicity of each galaxy), we selected

[*]http://www.stsci.edu/science/starburst99/docs/parameters.html

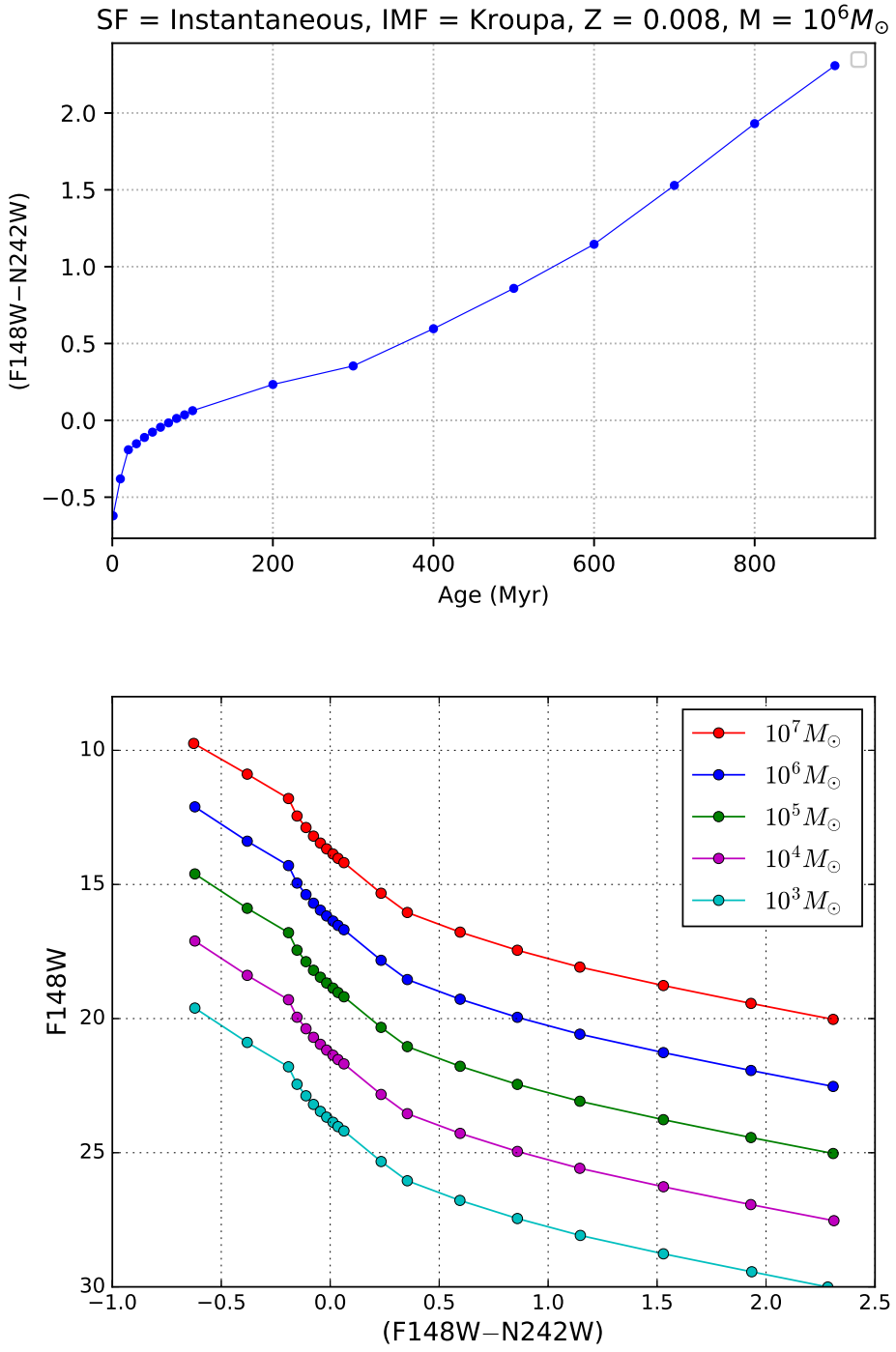

FIGURE 3.2: Starburst99 model generated diagnostic plots for simple stellar population. The upper panel shows the variation of (F148W−N242W) colour as a function of cluster age. The parameters are mentioned in the figure. The lower panel shows F148W magnitude as a function of (F148W−N242W) colour (i.e. age of cluster). Different curves signify five different total cluster masses ($10^7 M_\odot$, $10^6 M_\odot$, $10^5 M_\odot$, $10^4 M_\odot$, $10^3 M_\odot$). The points shown in each curve are for different ages starting from 1 Myr to 900 Myr with the same interval as shown in upper panel.

19 spectra of different ages within the range 1 to 900 Myr. In the lower panel of Figure 3.1, six such spectra are shown along with five different UVIT filters. Each spectrum is convolved with the effective area profile of the filters used for observation. The output of the convolution gives the expected flux value in each filter. These fluxes are converted to magnitudes by considering the distance of that galaxy into account. We then produced model grids of (FUV−NUV) colour as a function of age. One example is shown in the upper panel of Figure 3.2 for the galaxy NGC 7793 observed with two broad band filters of UVIT. The (F148W−N242W) colour becomes redder with increasing cluster age. This figure is used to estimate the age of identified clumps (with Z = 0.008) from their observed (F148W−N242W) colour. Similar figures are generated for other galaxies as well, for relevant filters and related input parameters. We further considered five different values for the total cluster mass ($10^7 M_\odot$, $10^6 M_\odot$, $10^5 M_\odot$, $10^4 M_\odot$, $10^3 M_\odot$) and follow the same method to generate diagnostic colour magnitude diagram (CMD) for a range of age between 1 - 900 Myr. One such CMD is shown in the lower panel of Figure 3.2. The colour of an SSP entity remains unchanged with varying cluster mass. Again for a fixed age, FUV magnitude becomes brighter with increasing cluster mass. The plot conveys that the age and mass of an SSP can be traced by (FUV−NUV) colour and FUV magnitude respectively. Similar diagnostic diagrams are generated for different metallicity and filter combinations relevant to the galaxy studied. We used these model CMDs to estimate the age and mass of star forming clumps identified in each galaxy.

3.2.2 Stellar spectral model

In order to identify hot star forming regions based on the UV colours, we constructed a relation between the UV colours (i.e., the flux ratio between UVIT filters) and temperatures of stars. We used Castelli & Kurucz (2004) stellar models that offer stellar spectra for a range of effective temperatures (3500 - 50000 K,

TABLE 3.1: Starburst99 model parameters

Parameter	Value
Star formation	Instantaneous
Stellar IMF	Kroupa (1.3, 2.3)
Stellar mass limit	0.1, 0.5, 120 $M_{\odot}$
Cluster mass range	$10^3 M_{\odot}$-$10^7 M_{\odot}$
Stellar evolution track	Geneva (high mass loss)
Metallicity	Z=0.04, 0.02, 0.008, 0.004, 0.001
Age range	1-900 Myr
Supernova cut-off mass	8 $M_{\odot}$
Black hole cut-off mass	120 $M_{\odot}$

with an uneven spacing), for deriving the above relation. For a fixed temperature, stellar spectra are available for different surface gravity (log(g)) and metallicity (log(Z)). The given log(g) values range from 0.0 to 5.0 with an interval of 0.5. The available metallicity values range from -2.5 to 0.5 with an interval 0.5, including the Solar value. We fixed the metallicity as per the requirement and selected 13 spectra of log(g) = 5.0 in the temperature range 3,500 - 50,000 K. The fluxes of the spectra are given in surface flux unit, $erg/sec/cm^2/\mathring{A}$. These spectra are convolved with the effective area profiles of UVIT filters to calculate the expected flux in each filter. Thus for each selected temperature, we estimated the expected flux values in different UVIT filters. We created diagnostic plots (Figure 3.3) by taking the ratio of fluxes for two different combinations of filters (i.e. $Flux_{F148W}/Flux_{N263M}$ and $Flux_{F148W}/Flux_{N245M}$) as function of temperature. These curves are used to estimate the temperature distribution of star forming regions as well as to identify the potential locations of OB associations in a galaxy from the observed value of the flux ratio. We adopted this technique to map the demographics of star forming regions as a function of temperature in WLM galaxy.

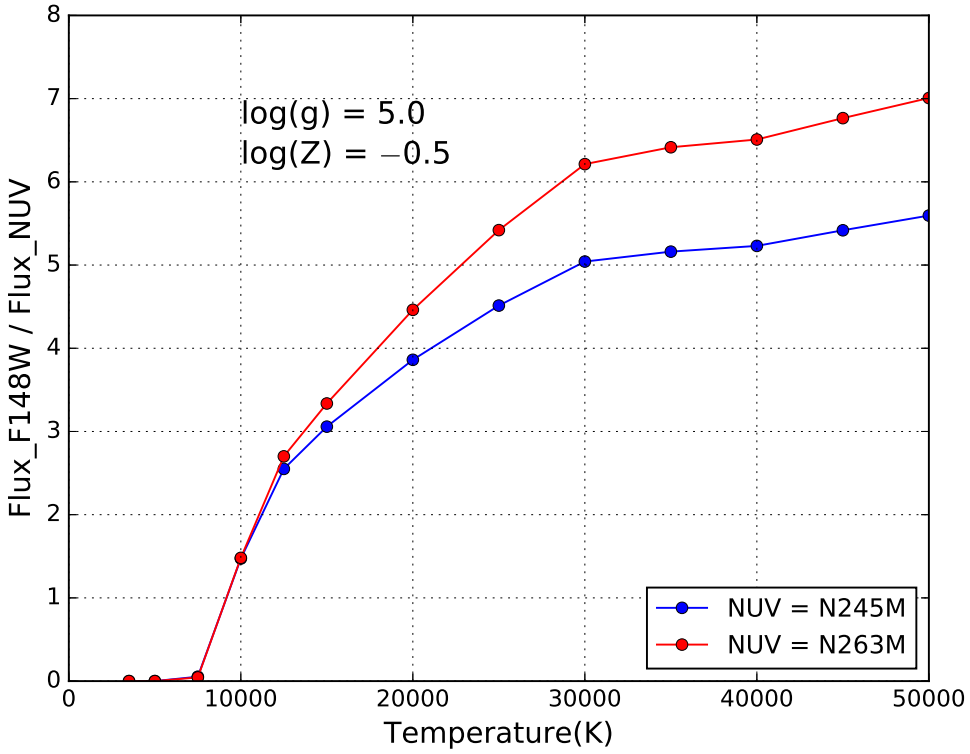

FIGURE 3.3: Flux ratios in UVIT filters F148W & N245M (blue) and F148W & N263M (red) are plotted as a function of temperature with the help of Kurucz stellar model.

3.3 Tools for data analysis

3.3.1 Contour maps with DS9

One of the techniques adopted in this study to understand the emission profile of a galaxy in different wavebands is by creating and comparing contour maps. A contour, plotted on an image, effectively signifies a region where the pixels have value more than a defined threshold. We used SAOimage ds9 (Joye & Mandel 2003), an astronomical imaging and data analysis software, to generate and overlay contours on FITS images.

Flux maps

In order to trace regions of different flux levels within a galaxy in a specific waveband, we created contours for different ranges of flux value. In the contour parameters window of ds9, the lower and upper limits are fixed in terms of image pixel unit for a corresponding flux range. We also fixed the value of both contour level and smoothness. The value of contour level and smoothness are varied according to the region of interest and the image resolution. With these parameters, contours are plotted on the image for each particular flux range. Different colours are used to highlight contours signifying different flux levels. This method is primarily used to understand the UV emission profile of a galaxy. We also produced contours for images in other wavebands (such as optical, Hα, infra-red and H I) to compare and correlate results obtained from UV filters.

Colour maps

We also generated UV colour map for tracing the temperature of star forming regions. The images, used to create colour maps, are first co-aligned (using CCDLAB) and normalised (using *imarith* package of IRAF) with respect to their exposure time. Using the same IRAF package, the image in one filter (f1) is divided by the image in another filter (f2) to create a new f1/f2 image. In order to retain correct information in the resultant image, this technique demands for same psf size in both the operated images. As the FWHM of psf is almost same in different FUV and NUV filters of UVIT, this technique is performed with UVIT images. The pixel value of the resultant image is the ratio of counts per second (cps i.e. flux) in the respective filters. The flux ratio is equivalent to a colour index, which again is a measure of temperature. Therefore, the colour maps produced with UVIT images are utilised to decipher the temperature of star forming regions with the help of simulated plot generated using Kurucz stellar models (for example Figure 3.3). We used multi-band UVIT observation of the galaxy WLM and applied

this method to map the temperature morphology of star forming regions in the galaxy.

3.3.2 Photometry

Photometry is defined as the measurement of photons (i.e. flux) from any astronomical object. This measurement is usually done in specific waveband with a definite bandwidth. In the photon counting mode, the number of photons collected per second (i.e. cps) in a waveband is used to calculate flux in that band using equation 3.1. The unit conversion factor in the equation signifies the amount of flux contributed by a single photon in that particular band. The estimated photon rate is also used to calculate magnitude of that source with the help of equation 3.2. The value of unit conversion factor and zero point magnitude in each available band of a telescope are determined with the help of a standard celestial source. In this study, two different techniques are used to count the photon rate of any observed source. One is aperture photometry and another is PSF photometry.

$$Flux = CPS \times Unit\ Conversion\ (erg/sec/cm^2/\mathring{A}) \tag{3.1}$$

$$Magnitude = -2.5 \log(CPS) + Zero\ point \tag{3.2}$$

Aperture Photometry

The basic idea of aperture photometry is to measure the number of photons enclosed within a particular aperture centred on a source. In the case of point sources, the aperture size is decided on the basis of FWHM of isolated bright stars present in the same field. Generally, the aperture is considered as circular, with a

radius of around 4-5 times the average FWHM value. This encloses around ∼99% of the flux contributed by the source, as demonstrated by a growth curve analysis. Aperture photometry for point sources is performed with the *daophot* package of IRAF. Sources are first identified with *daofind* package by fixing three primary parameters. These are the average value of FWHM of bright stars, average background flux and a lower threshold to identify faint sources. The *phot* package is then used to estimate flux values for different apertures. This flux is corrected for background/sky flux, which is measured locally for each source.

For extended sources, the shape and size of aperture changes from one source to another. The star forming regions present in a galaxy have different sizes. Therefore, implementation of a constant aperture size for all these clumps will not be ideal to do aperture photometry. In order to consider an aperture size proportionate with the size of the identified clump, we used *Photutils*, an affiliated package of *Astropy* (community-developed core Python package, (Astropy Collaboration et al. 2013, 2018)). In this package, the aperture shape can be fixed as circular or elliptical or annular as per the need. Here, the star forming clumps are identified with the help of *astrodendro* python package, discussed later in this section. We used the area of each identified irregular shaped star forming clumps to calculate the equivalent radii which are then used as aperture sizes. The background subtraction in this case is performed with an average value estimated from the observed field.

PSF photometry

In the case of crowded fields, the estimation of flux using aperture photometry for point sources is inaccurate. This arises due to an additional amount of light contributed from nearby sources, as the flux profile of a point source could overlap with profiles of sources which are located within a few FWHM. In order to get a correct estimation of the flux in such cases, it is essential to exclude the extra flux

contributed by neighbouring sources. The flux profile of a star on the detector can be approximated to a Gaussian profile. Depending on the optics, plate scale and pixel sampling, the flux profile could also resemble Lorentian or Moffat profiles. In the case of psf photometry, one tries to build a model psf profile from a set of bright isolated stars present in the same frame and then fit that profile to estimate flux of point sources present in the crowded field. The fit radius is considered as $\sim$ FWHM of the model psf. The complete procedure is performed with multiple tasks in IRAF. The tasks *pstselect* and *psf* are respectively used to select appropriate stars and building the model psf from their flux profiles. The model psf is fitted to the identified point sources with the task *allstar*. At the final stage, two source catalogues and a residual image are created. One catalogue contains point sources which are selected for fitting the model profile and another is for sources which are rejected in the fitting procedure. The residual image is created by subtracting the fitted sources from the actual image. The residual image is checked for verifying the goodness of PSF fitting visually, while fit error as a function of magnitude quantifies the goodness of fit.

3.3.3 Identifying parent-child structure : *Astrodendro*

Astrodendro[†] is a Python package to compute dendrograms of astronomical data. This tool is employed in the UV imaging data of galaxies to identify bright star forming regions. Dendrograms are structure trees used to highlight the parent-child connection between identified structures of different flux levels (Figure 3.4). Each tree present in a dendrogram signifies a parent structure whereas the leaves connected to that tree represent child structures present within the parent structure. The package helps to identify structures formed by a minimum number of pixel (m_p), each having a value more than a defined threshold flux (m_f). It

[†]http://www.dendrograms.org/

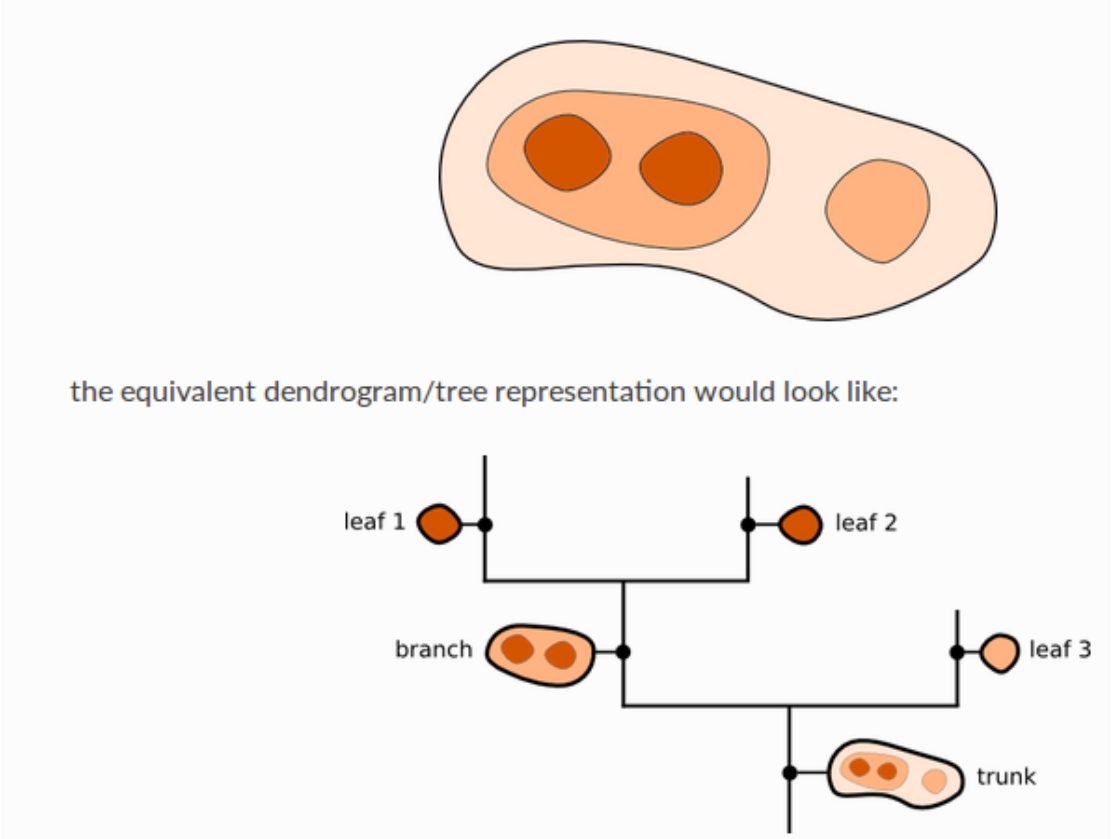

FIGURE 3.4: A representation of dendrograms and the algorithm of *astrodendro*. Image courtesy : Astrodendro official website.

identifies both parent and child structure on the basis of selected value of the parameters. The way how the algorithm works is shown in Figure 3.4.

The code first identifies the brightest pixel in the image and starts building a structure obeying the input values of m_p and m_f. Each child structure (leaf) is defined as a local intensity peak (maxima) in the image. The boundary of a child structure is decided when there is a local minima identified between the other nearest maxima. The difference between this maxima and minima should be greater than $m_{\Delta f}$ which is another input parameter. The value of $m_{\Delta f}$ is so chosen that it can exclude the smaller local intensity peaks which may be noise and not actual source. Branches are structures which enclose multiple leaves inside it. Each tree contains multiple leaves and branches (sub-structures) inside it. The boundary

of a parent structure is defined when the pixel value falls below the input threshold flux. In a similar way the algorithm identifies multiple parent structures (trees) in a given image. This tool provides position, flux and area for each identified parent and child structure. We used this tool to identify both large complexes and smaller individual star forming clumps in a galaxy. We also explored the hierarchical nature of star forming regions with the help of dendrograms.

3.4 Summary

The summary of this chapter is given below

1. We discussed starburst99 SSP model and related diagnostic diagrams used in this study.
2. We briefly discussed Kurucz stellar model used to simulate relation between temperature and UV flux ratio.
3. We described the technique to produce contour for flux and UV colour maps using ds9 software.
4. The method of aperture and psf photometry are discussed.
5. We described astrodendro python package used to identify and study the structure of star forming regions in galaxies.

Chapter 4

UVIT imaging of WLM : Demographics of star forming regions in the nearby dwarf irregular galaxy[†]

4.1 Introduction

WLM is a faint dwarf irregular galaxy of the Local group, located at a distance of 995 kpc (Urbaneja et al. 2008). It has an integrated absolute magnitude of $M_V = -14.1$ (van den Bergh 1994). This galaxy was first discovered by Wolf (1909) and later confirmed by Lundmark and Melotte (1926) and thus got the name as WLM (Wolf-Lundmark-Melotte) (Dolphin 2000). The nearest neighbour of WLM, located 175 kpc away, is a small dSph galaxy, Cetus (Whiting et al. 1999),

[†]Results of this chapter are published in Mondal et al. (2018)

whereas the massive spirals (MW, M31, M33) are about 1 Mpc away (Minniti & Zijlstra 1997). Due to its isolated location in the sky, it is believed that the galaxy has not interacted with other galaxies, which is demonstrated in the figure 1 of Leaman et al. (2012). The metal poor environment ($logZ = -0.87$, Urbaneja et al. (2008)) of WLM has made it an ideal sample to study such isolated systems. Parameters of WLM are presented in Table 4.1.

The photometric studies done by Ferraro et al. (1989); Minniti & Zijlstra (1997); Dolphin (2000) showed that this galaxy contains stellar populations of varying ages ranging from a few Myr to more than 10 Gyr. Several studies also reported this galaxy to have a relatively metal rich younger disk with an old metal poor halo (Ferraro et al. 1989; Minniti & Zijlstra 1997; Dolphin 2000; Rejkuba et al. 2000). Melena et al. (2009) studied the UV bright regions in 11 dwarf irregular galaxies including WLM. They detected 165 bright UV regions of the galaxy using GALEX data and estimated their age and mass, assuming them to be star clusters. The cluster formation was found to show a constant rate which stopped 22 Myr ago. They found the UV disk to be extended more than the Hα disk of the galaxy. A recent HST study by Bianchi et al. (2012) covered the galaxy in three HST pointings, and detected a rich population of young and hot stars in the 1 - 10 Myr age range. H I disk of the galaxy is also well studied and found to be extended than the optical or UV disk. Kepley et al. (2007) used VLA observation to map the H I density distribution of the galaxy and found a hook like structure near the centre. They concluded that the star formation, that is propagating out from the centre of the galaxy created this pattern. Using ALMA observations, Rubio et al. (2015) identified several CO cloud cores in the galaxy. The presence of these low mass clouds were a new insight in such a metal poor environment, but revealed the possibility of low mass cluster formation in the galaxy. In this context, it is therefore important to study the nature of recent star formation in this galaxy. As it offers a good opportunity to look into the star forming regions up to much smaller length scales, we observed this galaxy with AstroSat/UVIT in

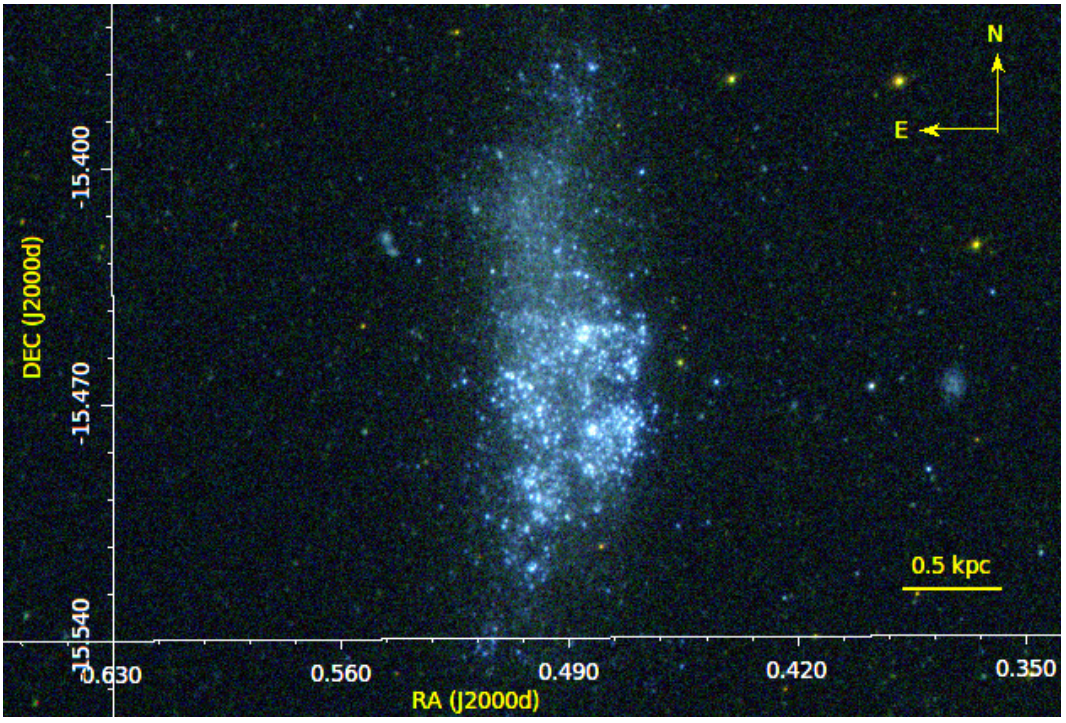

FIGURE 4.1: False colour composite image of the galaxy WLM. The galaxy is observed in three different UVIT filters F148W, N245M and N263M which are represented by blue, green and red colours respectively.

TABLE 4.1: Properties of WLM

Property	Value	Reference
Right Ascension (RA)	00:01:57.8	Gallouet et al. (1975)
Declination (DEC)	-15:27:51.0	Gallouet et al. (1975)
Morphological type	IB(s)m	de Vaucouleurs et al. (1991)
Distance	995 ± 46 kpc	Urbaneja et al. (2008)
M_V	−14.1	van den Bergh (1994)
Metallicity ($log(Z/Z_\odot)$)	-0.87 ± 0.06	Urbaneja et al. (2008)
Inclination	69°	de Vaucouleurs et al. (1991)
PA of major axis	181°	de Vaucouleurs et al. (1991)

multiple bands (Image - Figure 4.1). The UVIT images are used to decipher the characteristics of young star forming regions of the galaxy in detail. The details of this study are presented in this chapter.

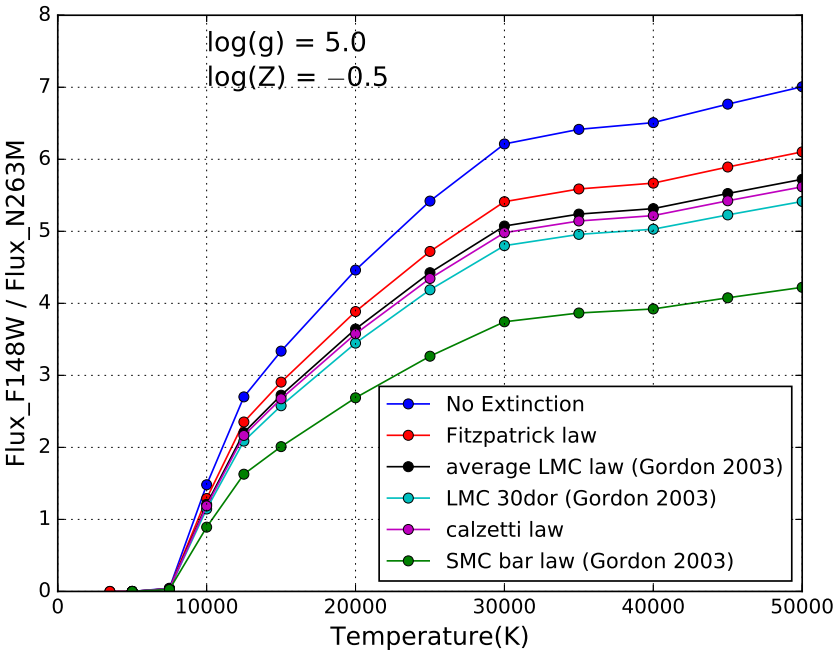

(a)

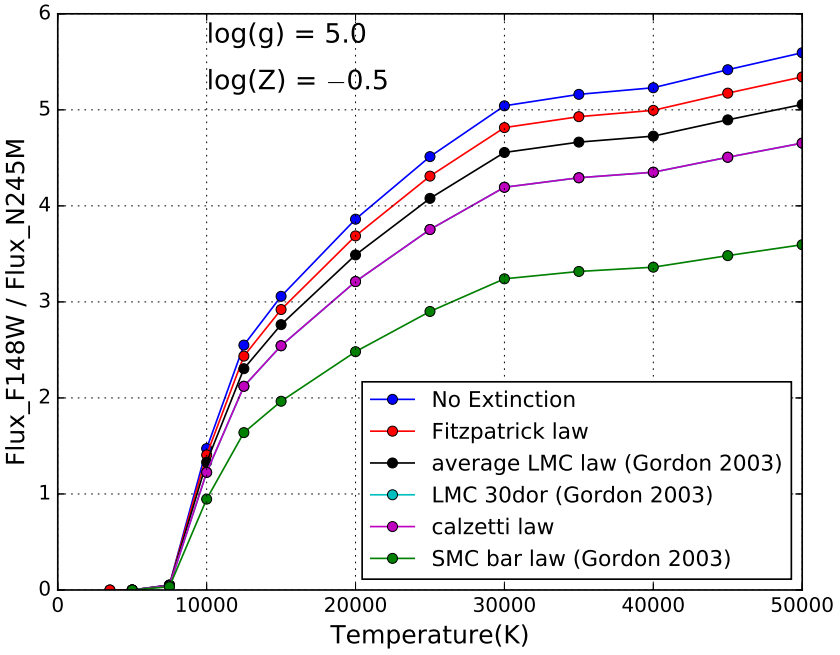

(b)

FIGURE 4.2: The relation between UV flux ratio and temperature, estimated using Kurucz spectra, for log(g) = 5.0 and log(Z) = −0.5 . The F148W/N263M and F148W/N245M flux ratios are shown in Figure (a) and (b) respectively. The blue curves in both the figures are without extinction correction. The other curves are generated by applying extinction on blue curve for different extinction laws mentioned in the figure.

4.2 Theoretical models

In order to identify hot star forming regions based on the UV colours, we used the diagnostic plots as shown in Figure 3.3. The red and blue curves respectively signify flux ratios $Flux_{F148W}/Flux_{N263M}$ and $Flux_{F148W}/Flux_{N245M}$ as a function of temperature. To apply these relations in the observed colour maps, we need to consider the effect of extinction. In Figure 4.2, we showed two plots for two different flux ratios and also highlighted the change in the derived laws by considering five different types of extinction laws, which are discussed in the next section. The upper and lower panel respectively show $Flux_{F148W}/Flux_{N263M}$ and $Flux_{F148W}/Flux_{N245M}$ flux ratios. These curves are used to identify the potential location of OB associations and also to explore the temperature distribution of star forming regions in WLM.

We further used starburst99 model (Leitherer et al. 1999) to characterise the identified compact star forming regions. Following the method discussed in Section 3.2.1, we produced model grids for F148W magnitude as a function of (F148W−N263M) colour (Figure 4.3). In order to convert the model generated fluxes to magnitude values, we adopted a distance of 995 kpc (Urbaneja et al. 2008) for WLM. We considered four different values for the total cluster mass ($10^6 M_\odot$, $10^5 M_\odot$, $10^4 M_\odot$, $10^3 M_\odot$) and a fixed metallicity of Z=0.004, to generate Figure 4.3. The dashed lines are plotted by considering the extinction and reddening to each of the actual model curves (continuous lines) shown for different masses.

4.3 Effect of Extinction and Metallicity

The behaviour of extinction curve in the UV region shows a noticeable variation for different external galaxies. It is observed that the extinction coefficient

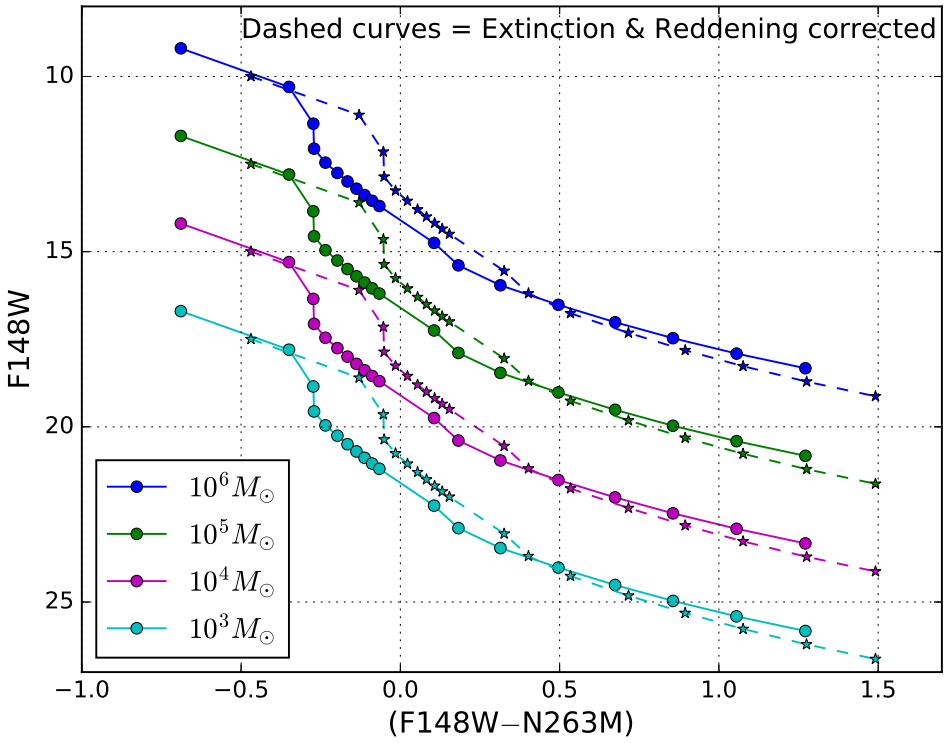

FIGURE 4.3: Starburst99 model generated colour-magnitude plots for simple stellar population. The Figure shows F148W magnitude with (F148W−N263M) colour. Different curves (continuous line) signify four different total cluster masses ($10^6 M_\odot$, $10^5 M_\odot$, $10^4 M_\odot$, $10^3 M_\odot$). The dashed lines show the extinction and reddening corrected values for each model curve. The points shown in each curve are for different ages starting from 1 Myr to 900 Myr (increasing along the colour axis) with age interval 10 Myr for 1 to 100 Myr range and 100 Myr for 100 to 900 Myr. The value of other parameters adopted for this figure is listed in Table 7.2.

in FUV and NUV changes from galaxy to galaxy or even within a galaxy. The 2175 $\mathring{A}$ bump is an important feature of the Galactic extinction curve and it also shows characteristic variation for external galaxies. Gordon et al. (2003) reported the differential nature of extinction curve in UV for the galaxy Large Magellanic Cloud (LMC), SMC and Milky way. Therefore it is important for us to first understand the nature of extinction law which applies for the star forming regions of WLM and second to understand how the flux in UVIT filters are affected by the extinction law. In Figure 4.4 we show the behaviour of different extinction

TABLE 4.2: Starburst99 model parameters

Parameter	Value
Star formation	Instantaneous
Stellar IMF	Kroupa (1.3, 2.3)
Stellar mass limit	0.1, 0.5, 120 $M_{\odot}$
Total cluster mass	$10^3 M_{\odot}$-$10^6 M_{\odot}$
Stellar evolution track	Geneva (high mass loss)
Metallicity	Z=0.004
Age range	1-900 Myr

laws such as Fitzpatrick law (for Milky Way) (Fitzpatrick 1999), Calzetti law (for starburst regions) (Calzetti et al. 1994), average LMC, LMC 30 Dor and SMC bar (Gordon et al. 2003) along with the UVIT filter profiles. The data for the extinction curves are obtained from the extinction calculator (McCall 2004) available in NED website. It is quite clear that the N245M filter profile partially overlaps with the 2175 $\mathring{A}$ bump of the extinction curve. Assuming the average value of R_{λ} within the bandpass of each filter, and adopting E(B−V) = 0.082 (Gieren et al. 2008), we estimated the extinction value (A_{λ}) for different extinction laws using the general transformation law given in equation 4.1. The extinction corrected flux ratios after incorporating different extinction laws are shown in Figure 4.2. Since the behaviour of extinction in UV for extra-galactic study is highly debated, the simulated plots in Figure 4.2 highlights the possible uncertainty in the estimated temperature for a fixed flux ratio.

In their study of the properties of HST identified stars, Bianchi et al. (2012) concluded that the most suitable extinction law for the star forming regions of WLM is the average LMC type (Gordon et al. 2003). In our study we adopted the UV extinction of WLM to be average LMC type and calculated the value of R_{λ} and A_{λ} for all three UVIT filters which are given in Table 4.3.

TABLE 4.3: Extinction parameters for average LMC law (Gordon et al. 2003)

Filter	R_λ	A_λ
F148W	9.78	0.80
N245M	8.40	0.69
N263M	7.07	0.58

Considering the possibility of a spread in the metallicity across the star forming regions, we explored the effect of metallicity in the estimated temperature. It turns out that as log(Z) changes from -0.5 to -1.0, the corresponding change in the flux ratio for different temperature is found to be negligible (Figure 4.5). The metallicity of WLM, measured from a spectroscopic study of blue supergiants present in the galaxy, is reported to be -0.87 by Urbaneja et al. (2008). As the effect of metallicity is not very sensitive on the derived temperature, we consider log(Z) $= -0.5$ for the Kurucz model spectra.

$$A_\lambda = R_\lambda E(B-V) \tag{4.1}$$

4.4 Data and Analysis

In this study, we used UVIT observations in three filters F148W, N245M and N263M of the galaxy WLM. The combined UVIT image and the observation details are discussed in Section 2.2.1. This study also uses data from other wavebands, like 21 cm radio, Hα, HST FUV and molecular CO. The details of these observations are also given in Chapter 2.

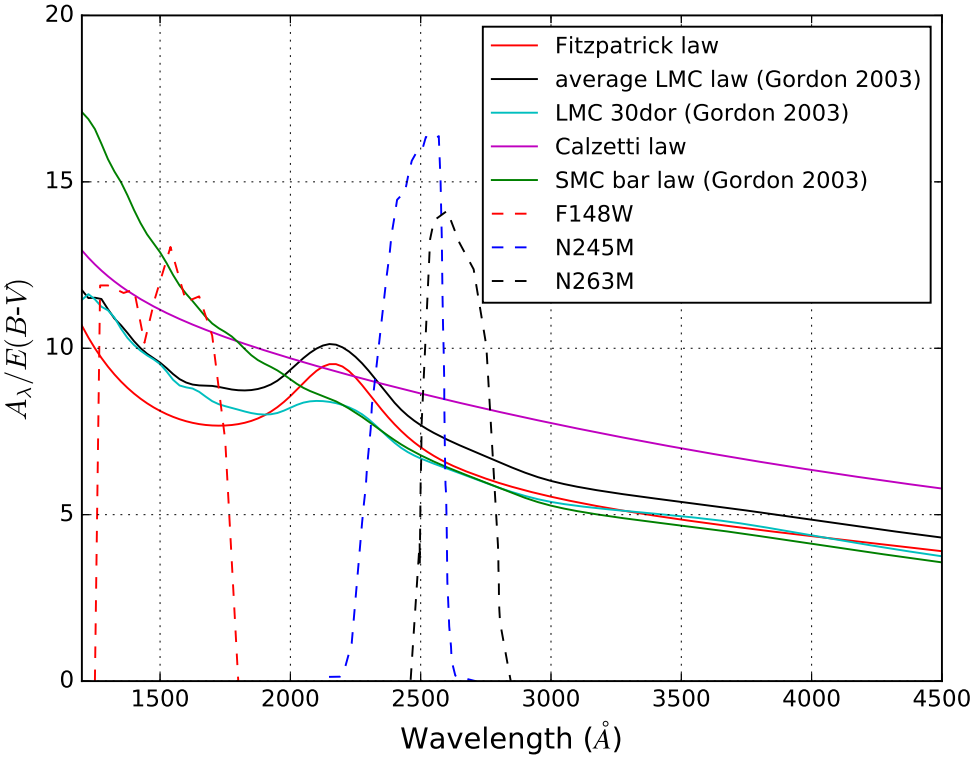

FIGURE 4.4: The variation of extinction coefficient (R_λ, i.e. $A_\lambda/E(B-V)$) with wavelength for different extinction laws. The solid lines of different colours represent different laws mentioned in the figure. The scaled effective area curves for three UVIT filters are also shown by the dashed lines.

4.4.1 Extent of UV emission

We consider the F148W band image to study the extent of UV emission in WLM, which in turn traces the expanse of hot and young massive stars. The FUV emitting regions as shown in Figure 4.1 are found to be highly structured. Many regions could be massive complexes comprising of a large number of smaller groups, which are not resolved in our images, while some are found to be much smaller, suggestive of smaller groups, and in a few cases individual association of OB stars. In order to locate the brightest and hence massive complexes, we created a low-resolution map of size 512×512, where each pixel corresponds to 3.3″ which is equivalent to ∼ 16 pc at the distance of WLM. Each pixel value of the image

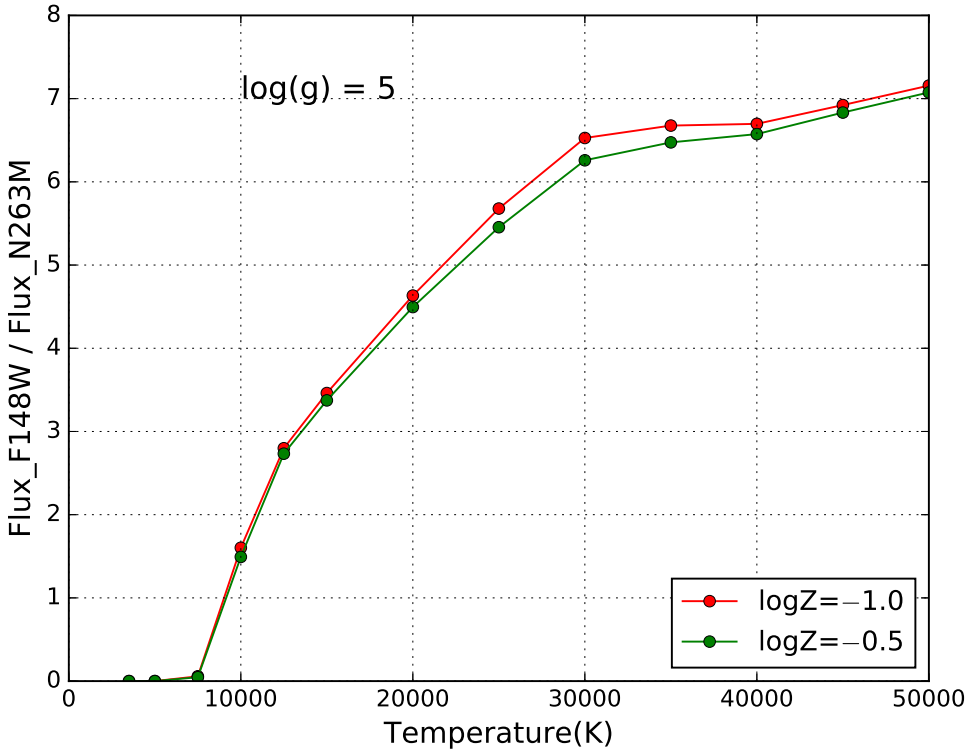

FIGURE 4.5: The flux ratio $Flux_{F148W}/Flux_{N263M}$ is plotted with temperature for two different metallicity log(Z)=−1.0 and −0.5.

denotes the integrated count of a stellar group having size $\sim$ 16×16 pc^2. As we target to locate large complexes and their sizes, we created contours by fixing the lower and upper limit of flux values which are given in Table 4.4 (shown in Figure 4.6). The blue contours show pixels brighter than 20 magnitude. These are the most luminous star forming complexes present in the galaxy. We find that at this FUV magnitude, the contributing compact star forming regions are likely to be more massive than 10^3 M$_\odot$ (see Figure 4.3). The CPS corresponding to this FUV magnitude is 0.16 and there are only a few regions which have CPS more than this value (see figure 4.6). We are able to identify three luminous (extended) regions which are shown in blue. The green and red contours, which signify relatively less bright regions, are found to be present around these regions, suggestive of a hierarchical structure. The yellow contours generated for pixels fainter than 22

magnitude and brighter than 23 magnitude portray the overall extend of the FUV emission.

We further studied the structure of emission in two NUV images (N245M and N263M). Using similar 512×512 images, we generated contours for pixels brighter than 23 magnitude for both the NUV images. For comparison, the blue, green and red contours generated for images in F148W, N245M and N263M band respectively are over laid on the N263M image (Figure 4.7). It is clearly seen that the extent of UV emission gradually increases as we go towards longer wavelengths. The red contours, signifying the emission in NUV N263M filter, are found to be stretched more outward than the green (N245M) and blue (F148W) contours. The FUV emission, traced by the blue contours, is found to be present inside the extent of both the NUV emission (green and red contours). As the contours shown above are likely to be affected by extinction, we apply the extinction correction and reproduce the contours. Applying the average LMC law for extinction (Gordon et al. 2003), the extinction corrected magnitudes are 23.80, 23.69 and 23.58 magnitudes, for F148W, N245M and N263M filters, respectively. The blue, green and red contours shown in Figure 4.8 are generated for the above magnitudes in F148W, N245M and N263M filter images respectively. Again the morphology of FUV and NUV emission are found to be similar to Figure 4.7. The NUV emission as traced by N263M filter is found to be more extended in Figure 4.8 than in Figure 4.7. As the FUV traces hotter and massive population, when compared to the NUV, it is clear that these are located in the inner part of the galaxy, whereas relatively cooler less massive stellar populations are present in the outer regions.

4.4.2 Luminosity density profile

The radial variation of luminosity density in UV conveys the characteristic distribution of star forming regions in any active galaxy. Since WLM is observed in one

TABLE 4.4: Details of flux and magnitudes for contours in the F148W map shown in Figure 4.6.

$log(Flux_{F148W})$ range $[erg/sec/cm^2/\AA]$	Magnitude range (extinction uncorrected)	Contour colour
> -15.3	< 20	Blue
-15.7 to -15.3	> 20 & < 21	Green
-16.1 to -15.7	> 21 & < 22	Red
-16.5 to -16.1	> 22 & < 23	Yellow

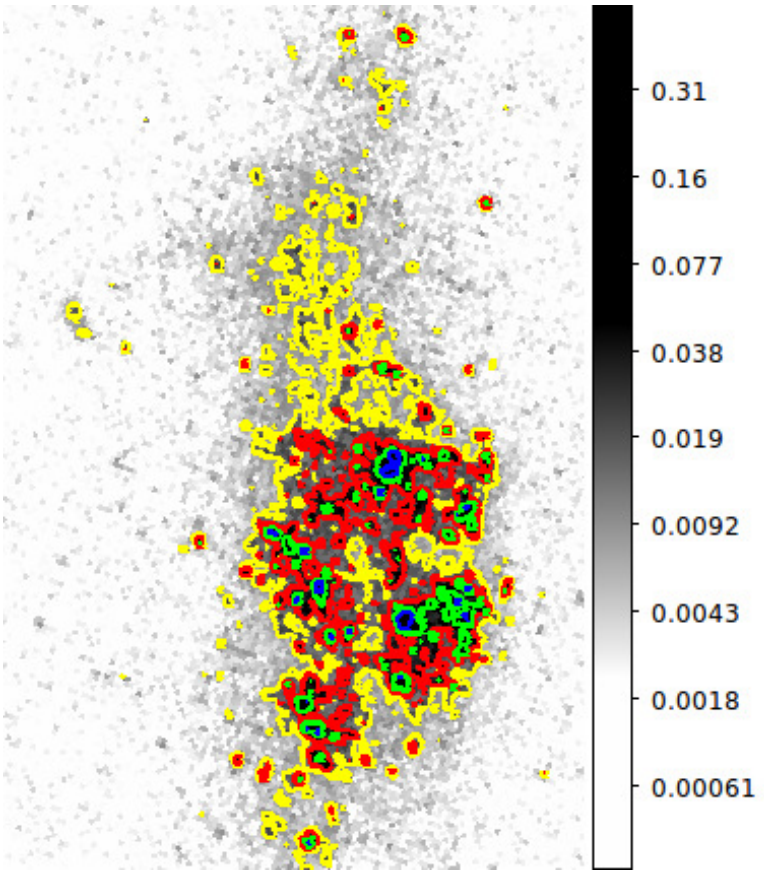

FIGURE 4.6: The background figure is the 512×512 F148W band image of WLM with contours plotted for different limits of F148W flux values as mentioned in Table 4.4. The blue contours represent the brightest (hence most massive) regions of the galaxy. The overall extent of FUV emission of WLM is traced by the yellow contours.

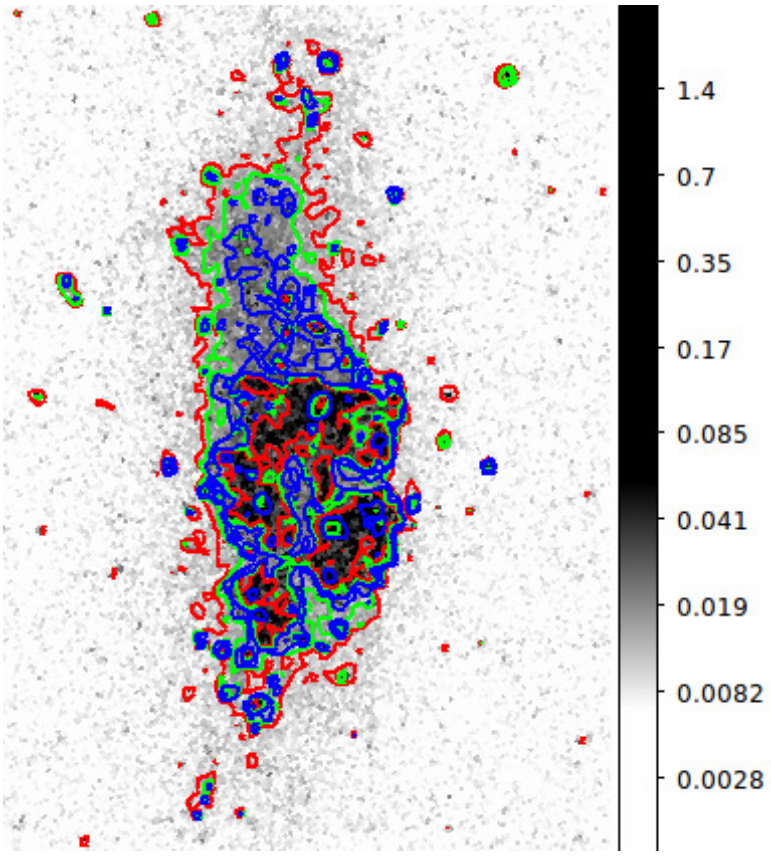

FIGURE 4.7: The background figure is the 512 × 512 N263M band image of WLM. The blue, green and red contours shown in the figure are generated for pixels brighter than 23 magnitude in F148W, N245M and N263M filter images respectively. The FUV emission (blue contours) is seen to be enveloped by both green and red contours representing the NUV emission of WLM.

TABLE 4.5: Details of flux ratio and temperature for the (F148W−N263M) colour map, as shown in Figure 4.11.

$(Flux_{F148W}/Flux_{N263M})$ range	Temperature range (K)	Contour colour
>5.23	> 35000	Blue
4.43 to 5.23	> 25000 & < 35000	Red
3.18 to 4.43	> 17500 & < 25000	Green

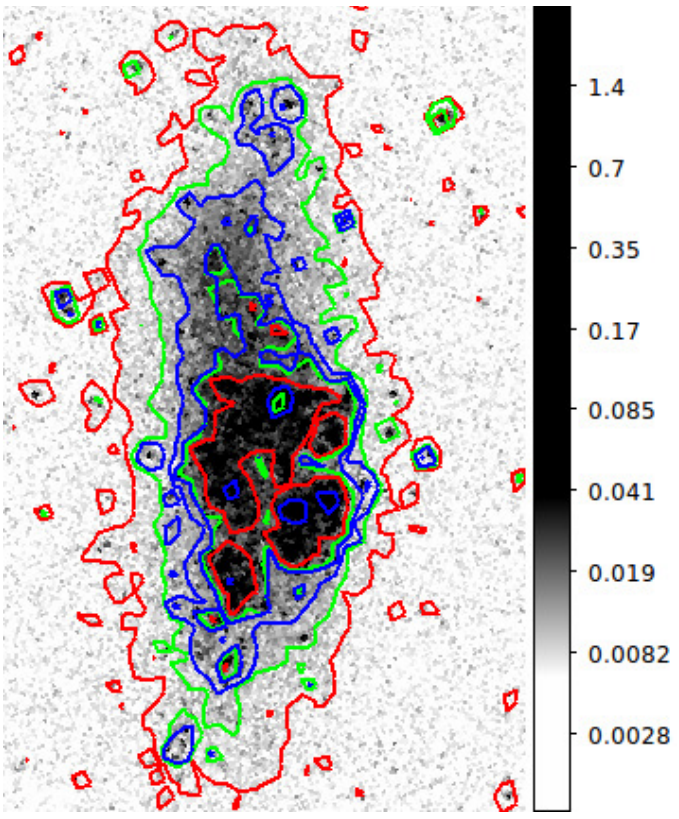

FIGURE 4.8: The background figure is the 512 × 512 N263M band image of WLM. The blue, green and red contours shown in the figure are generated for pixels brighter than 23.80, 23.69 and 23.58 magnitude (adding the effect of extinction) respectively in F148W, N245M and N263M filter images. The extent of NUV emission as traced in N263M filter is found to be more than that of Figure 4.7.

FUV and two NUV filters of UVIT, we constructed the radial surface luminosity density profile in all the filters. Assuming the inclination and position angle of the galaxy (Table 4.1), we estimated the galactocentric distance to each pixel in all the three images, using the relation given in van der Marel & Cioni (2001) . Starting from the galaxy centre (RA and Dec given in Table 4.1), we considered annuli of width 0.1 kpc and measured the total CPS in each individual annuli, up to a radius 2 kpc. The total CPS value is then corrected for background and extinction. The average background in CPS/kpc^2 in all the three images are calculated by considering three similar annuli of width 0.1 kpc from radius 2.5 kpc to 2.8 kpc. The luminosities in each annuli are then estimated by assuming the

distance to WLM as 995 kpc, and considering respective value of unit conversion factor and bandwidth of each filter from Table 2.2. The surface luminosity density (erg/sec/pc^2) as a function of radius is shown in Figure 7.11. The luminosity density in all three filters shows a dip in the central part of the galaxy and peaks around 0.4 kpc (in F148W it is $\sim$ 0.5 kpc) from the centre, which signifies that the star formation is relatively less active near the centre of WLM. Beyond 0.4 kpc it decreases again towards the outer part of the galaxy. In order to investigate the relative flux variation between the far and near UV, we further plotted (F148W − N245M) and (F148W − N263M) radial colour profile in Figure 4.10. From centre to 0.5 kpc, both the colours become bluer with radius. After 0.5 kpc the trend changes and the colours start becoming redder with respect to the value at 0.5 kpc. Beyond 1 kpc the colours become redder, than the average value in the inner 1 kpc. Again (F148W − N263M) colour is found to be bluer than (F148W − N245M) in the inner 1 kpc region whereas it becomes almost similar outside 1 kpc. This fact can be interpreted as the outer part beyond 1 kpc has a relatively large extinction and/or less number of massive stars when compared to the inner part.

4.4.3 UV colour maps

We use the FUV and NUV images to create UV colour maps, to trace the temperature profiles of star forming regions. The method to produce colour map is explained in Section 3.3.1. The image in F148W filter is divided by the images in N263M and N245M filter to create F148W/N263M and F148W/N245M images respectively. The pixel value of each of these resultant images is actually the CPS ratio in the respective filters. We infer the temperature corresponding to each pixel of F148W/N263M (or F148W/N245M) image with the help of Figure 4.2. We consider the black curve, which is generated according to average LMC type extinction law (Gordon et al. 2003), of both Figure 4.2a & b.

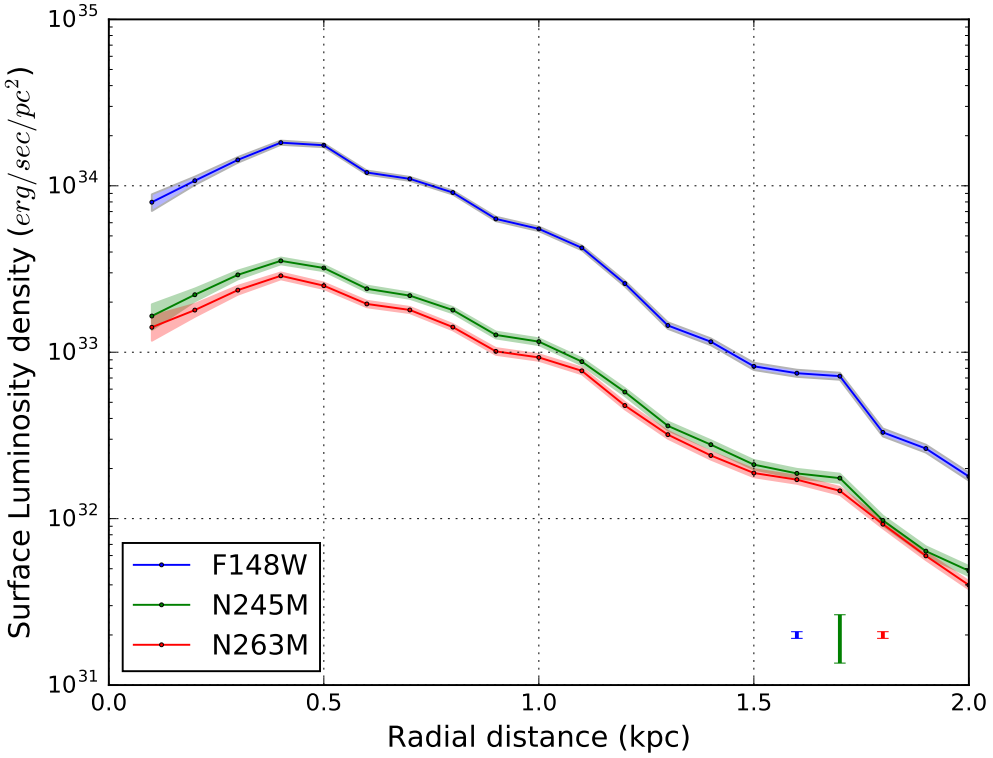

FIGURE 4.9: The profile for surface luminosity density (erg/sec/pc^2) with galactocentric distance in kpc for three UVIT filters. The UV emission of WLM is found to be extended at least up to a radius 1.7 kpc. The shaded region corresponding to each curve shows the 5σ photometric error whereas the error bars (bottom right) represents 5σ error due to the present uncertainty of adopted zero point magnitudes.

TABLE 4.6: Details of flux ratio and temperature for the (F148W−N245M) colour map, as shown in Figure 4.12.

$(Flux_{F148W}/Flux_{N245M})$ range	Temperature range (K)	Contour colour
> 4.64	> 35000	Blue
4.09 to 4.64	> 25000 & < 35000	Red
3.15 to 4.09	> 17500 & < 25000	Green

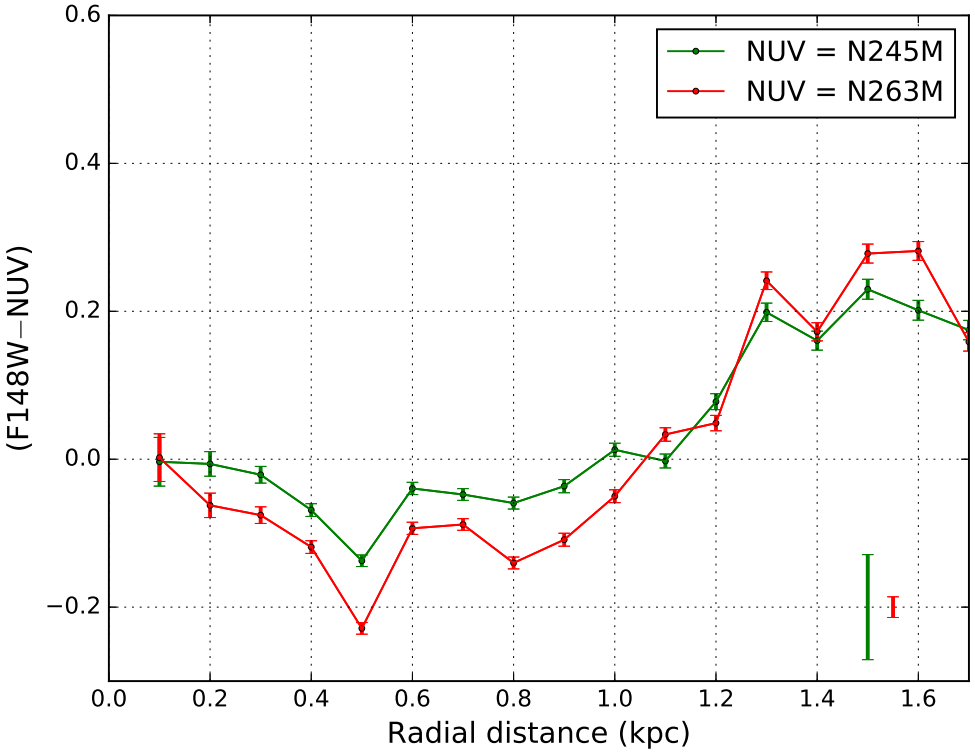

FIGURE 4.10: The variation of (F148W−N245M) and (F148W−N263M) colour is shown with galactocentric distance in kpc. Both the profiles remain nearly flat in the inner 1 kpc whereas an upturn is noticed for the outer part beyond 1 kpc. The photometric errors are shown in the profile and the error bars displayed in the bottom right corner signify the error due to the uncertainty in zero point magnitudes.

4.4.4 (F148W−N263M) colour map

We first considered (F148W−N263M) colour map to investigate the temperature profiles of the star forming regions. Considering the black curve of Figure 4.2a, we fixed different upper and lower limits of flux ratio for creating different sets of contour signifying different ranges of temperature which are listed in Table 4.5. We adopted a smoothness of 2 pixels ($\sim$ 4 pc), which helps to trace smaller regions as well. We divided the galaxy in five different regions and designated them as R1, R2, R3, R4 and R5. Their locations are shown in Figure 4.11a. We adopt the same temperature used by Bianchi et al. (2012) to classify the regions. The blue

contours signify regions with very high temperature (T > 35000 K, corresponding to early O type stars) while red contour indicates an intermediate temperature (25000 K < T < 35000 K, late O type stars) and relatively low temperature (17500 K < T < 25000 K, early B type stars) regions are shown in green contour (Table 4.5). Regions which are not covered by any of these three contours are suggestive to have temperatures less than 17500 K. The regions R1 to R5, with overlaid contours are shown in Figure 4.11b to 4.11f. Thus the regions covered by these contours are occupied by OB stars. The high temperature regions (blue contour) are found to be enveloped by relatively lower temperature regions (red and green contours) throughout the galaxy. These show the hierarchical structure of actively star forming regions.

The south-western part (R1) is found to have several high temperature regions (blue contour) of different sizes. Though the regions have irregular shape, an approximate size can be assigned by measuring their longest dimension. The largest high temperature complex identified in R1 is L-shaped, with a north-south extend of $\sim$ 50 pc, and an east-west extend of $\sim$ 40 pc. The width of the region is in the range, $\sim$20-30 pc. This is the largest massive complex in WLM. We also found nearly 10 regions of size > 20 pc. The smaller regions (< 10 pc) are more scattered and large in number, with smallest of them with sizes $\sim$ 4 pc. The red contours signifying intermediate temperature are found to connect several hot regions (blue contour) and form knotted structures. It is also noticed that the number of smaller ($\sim$4 pc) low temperature regions are more than similar size hotter regions. The nature of temperature gradient around each hot star forming region (blue contour) is clearly depicted by the red and green contours present around them.

The region R2 is assigned to the southern part of the galaxy. We identify three high temperature regions of size $\sim$ 30 pc, and a large number of smaller regions with sizes < 10 pc. One clumpy hot region is identified at the extreme south of the galaxy, which appears to be almost detached from the main body of the galaxy.

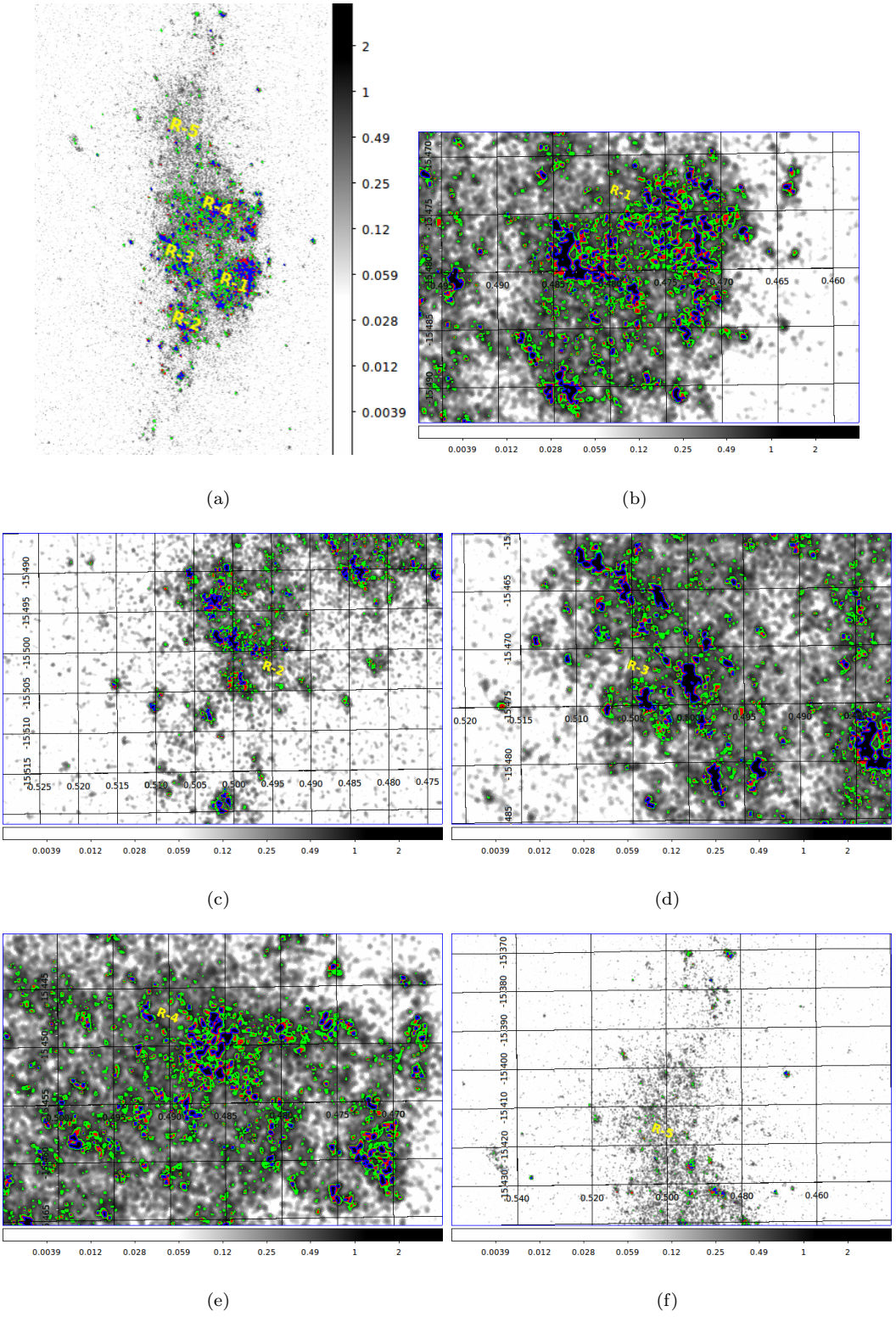

FIGURE 4.11: The (F148W−N263M) colour map of the galaxy is shown with different plotted contours. Figure (a) shows the whole galaxy along with the specified position of five regions R1, R2, R3, R4 and R5. The blue, red and green contours are generated for different flux limits signifying different temperature ranges as mentioned in Table 4.5. The background image shown here is smoothed and the grey scale denotes the logarithmic value of the CPS ratio for the smoothed image. We have shown zoomed in images for regions R1, R2, R3, R4 and R5 in Figure (b), (c), (d), (e) and (f) respectively. The blue contoured regions denote the hotter regions of the galaxy.

The eastern part of the galaxy (R3) is found to have more number of larger-sized high temperature regions, with 8 complexes of size larger than 20 pc and one region extending up to $\sim$ 50 pc in length. These 8 complexes are spatially isolated from each other and distributed along the south-west to north-east direction. Around some of these large complexes, we noticed smaller ($<$ 10 pc) hot regions which are connected by red contours. The scenario of R4 (north and north-western part) region is a little different. Though the region has a larger spatial extent than the rest, we do not detect any large structure with very high temperature, rather an abundance of structures scattered all around. We also identify two locations (one along north and another along west) with increased number of scattered structures. The extreme northern part of the galaxy (R5) does not show any high temperature region except two or three isolated hot star forming clumps.

Therefore the star forming regions of WLM are found to have an overall hierarchical structure with hottest cores surrounded by relatively less hotter regions. It is also clear that the young star forming regions are fragmented and clumpy in nature.

4.4.5 (F148W−N245M) colour map

In order to explore the effect of differential extinction inside the galaxy and to study the detected hot star forming regions further, we performed the same exercises for colour map (F148W−N245M) (i.e. F148W/N245M image). The model generated diagram for tracing the temperature in (F148W−N245M) colour map is shown in Figure 4.2b (blue curve). The UV colour image with the overlaid contours are shown in Figure 4.12a. The expanded view of R1, R2, R3, R4 and R5 regions are shown in Figure 4.12b to 4.12f. It is natural to expect the shape and distribution of the identified hot star forming regions to be similar in nature in both the colour maps. We notice that, though the overall distribution of hot star forming

regions in both the colour maps matches in general, a closer look reveals a more fragmented structure in the (F148W−N245M) colour map. The larger complexes detected in (F148W−N263M) colour maps are noticed to split into smaller regions in (F148W−N245M) colour map. This could happen because of two reasons. The differential behaviour of 2175 $\AA$ bump inside the galaxy can change the effective extinction value which affects the observed flux value in N245M filter. This in turn can produce the structural differences of star forming regions between the two colour maps. The same effect can also be produced by a clumpy distribution of hot stars, which have more flux in N245M filter. Thus, we conclude that either the young and hot stellar groups or the dust or both of them present in WLM have a clumpy distribution.

4.4.6 Correlating with Hα and H I maps

We correlate the spatial distribution of UV detected high temperature regions in the colour map (i.e. (F148W−N263M)) with Hα and H I image of the galaxy. Since Hα radiation mainly comes from gas ionised by massive and hot OB type stars, it is expected that the UV detected high temperature regions will show a good spatial correlation with Hα emitting regions. In Figure 4.13, along with the contours (blue and red) created in (F148W−N263M) colour map, we have shown the Hα emitting regions of the galaxy in cyan contours. Almost all of the high temperature regions detected in R1, R2, R3 and R4 appear inside the cyan contours, which indeed signifies a good spatial correlation between them. In the R1 region, we notice a hole in the Hα map which does not have any detected UV hot region near its centre, though we detect a few smaller hot regions within the hole. We identify a large number of hot regions located to the north of the hole, with reduced number of such regions in the southern side. We identify several clumpy and knotted hot regions towards west of R1 region with very less Hα emission. In R2, there are two major hot clumps which also show Hα. All the hot regions

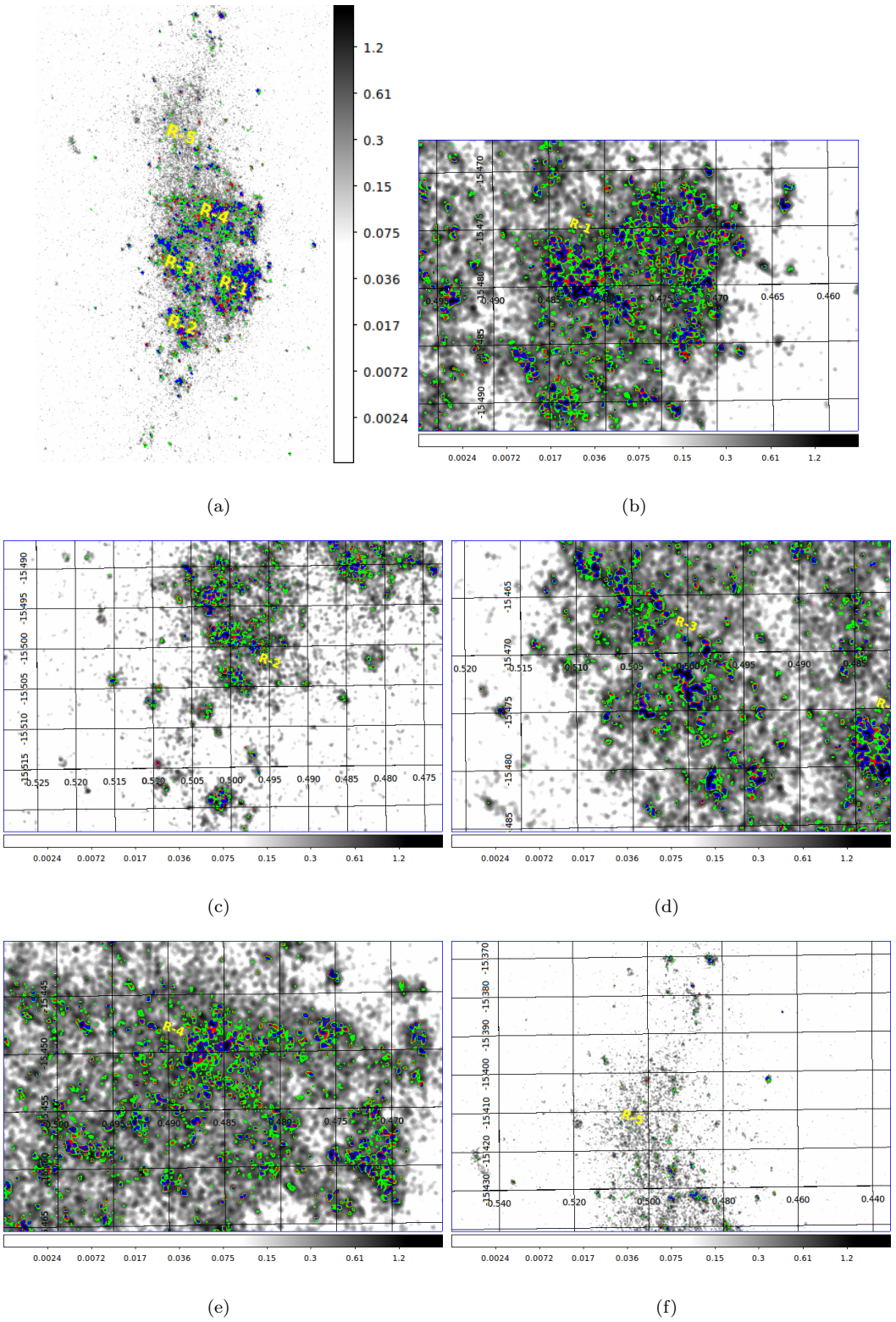

FIGURE 4.12: The (F148W−N245M) colour map of the galaxy is shown with different plotted contours. Figure (a) shows the whole galaxy along with the specified position of five regions R1, R2, R3, R4 and R5. The blue, red and green contours are generated for different flux limits signifying different temperature ranges as mentioned in Table 4.6. The background image shown here is smoothed and the grey scale denotes the logarithmic value of the CPS ratio for the smoothed image. We have shown zoomed in images for regions R1, R2, R3, R4 and R5 in Figure (b), (c), (d), (e) and (f) respectively. The blue contoured regions are found to be more fragmented than those in Figure 4.11.

detected in R3 region correlate well with Hα emitting regions. The shapes of the Hα contours also match with the overall distribution pattern of high temperature regions. In R4 region, the detected clumps of hot regions are enveloped by Hα emission. The elongation of the central Hα contour in R4 along west and south is also traced well by the hot regions. The overall good spatial correlation between Hα emitting regions and UV detected hot complexes confirms the presence of massive O and early B type stars in these complexes.

Further, we spatially correlate these hot star forming regions with neutral hydrogen (H I) density map of the galaxy. Since stars are mainly formed from molecular clouds, the presence of hydrogen gas would support the possibility of recent star formation. Kepley et al. (2007) identified a hook like over density pattern in the H I distribution as shown in Figure 4.14. The hook shaped magenta contour is found to cover almost all the high temperature regions except those in R1. Therefore, R1 region is found to have many UV detected hot star forming clumps showing Hα emission, (except some part in west - Figure 4.13) but with a relatively low H I density. This may be the result of a vigorous recent star formation in R1, where the H I gas is ionised/driven away after the star formation. Other hot regions in R2, R3 and R4 are found to have a high column density of H I along with Hα emission.

4.4.7 Correlating with HST detected hot stars

Bianchi et al. (2012) observed the galaxy WLM with six HST broadband filters (F170W, F255W, F336W, F439W, F555W, F814W) and noticed a richness of stars with age younger than 10 Myr. The bluest band used in their observation is F170W with a bandwidth of 1200 - 2400 $\mathring{A}$. Stars which are bright in F170W band are expected to be hot, young and relatively massive. We spatially correlated the hot regions detected in our study with stars that are brighter than 19 magnitude

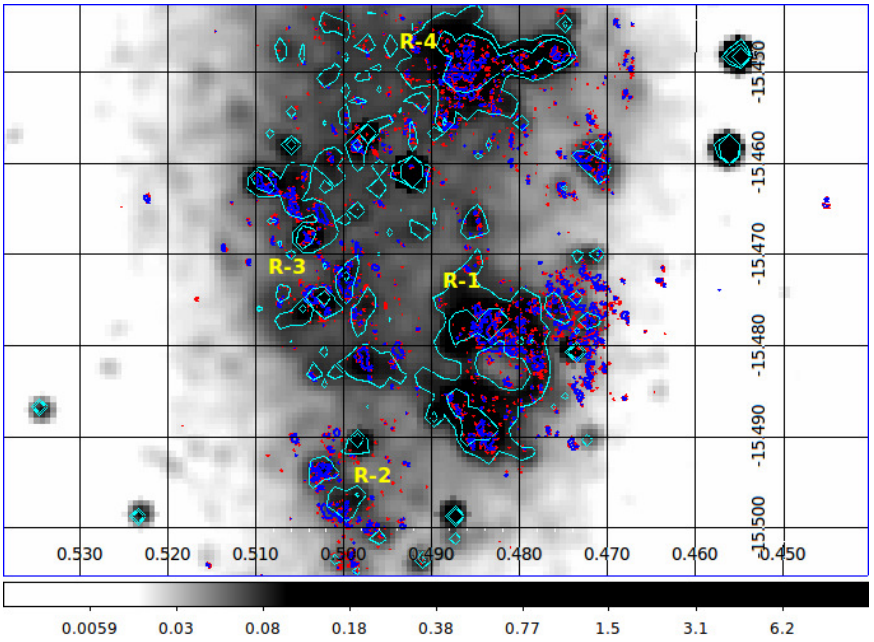

FIGURE 4.13: Hα image of the galaxy WLM, covering regions R1, R2, R3 and R4, is shown in the background where the grey scales signifies the logarithmic value of CPS. The cyan contours signify the Hα emitting regions of the galaxy. The plotted blue and red contours are same as shown in Figure 4.11a. The UV detected hot regions show a good spatial correlation with the Hα emitting regions of the galaxy.

in F170W band from their photometric catalogue. Excluding some part of R3, the regions R1, R2, R3 and R4 are almost fully covered by the three HST fields observed in their study. In Figure 4.15 we have overlaid these stars on top of (F148W−N263M) colour map. The detected stars (cyan box) show a good spatial correlation with the hot star forming regions (blue and red contour) of the galaxy. This confirms that massive young stars are co-located with the high temperature star forming regions identified in our study.

4.4.8 Mass estimation of compact star forming regions

In the UVIT images, some of the star forming regions were found to appear like point sources, due to their small sizes. As these are a good number of them, many

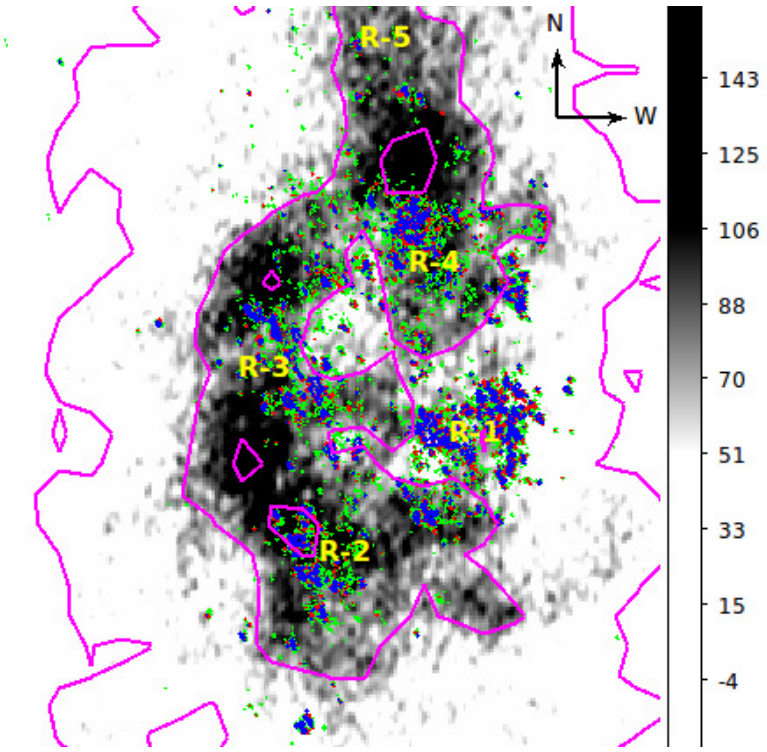

FIGURE 4.14: The background image shows the H I density distribution of the galaxy WLM. The hook like magenta contour is the over density pattern reported by Kepley et al. (2007). The plotted blue, red and green contours are same as shown in Figure 4.11a. R1 has several UV detected hot star forming regions with less H I density. Other regions (R2, R3, R4 and R5) are found to have dense H I gas.

of these are likely to be part of WLM, though a small fraction could belong to the background. We assumed all the detected point sources to be the compact star forming regions of the galaxy and performed PSF photometry (as explained in Section 3.3.2) to estimate their magnitudes. The photometry is done separately for all the three images of the galaxy. The catalogues of identified point sources in different filters are cross-matched with the help of *Topcat* (Taylor 2005) to identify the common sources. We considered images in F148W and N263M filter and identified 590 point sources in the galaxy. In Figure 4.16, we showed the photometric magnitudes and their corresponding errors in both F148W and N263M bands.

In order to estimate mass, we considered the simulated model diagram shown in Figure 4.3. In Figure 4.17, we plotted the identified star forming regions (grey

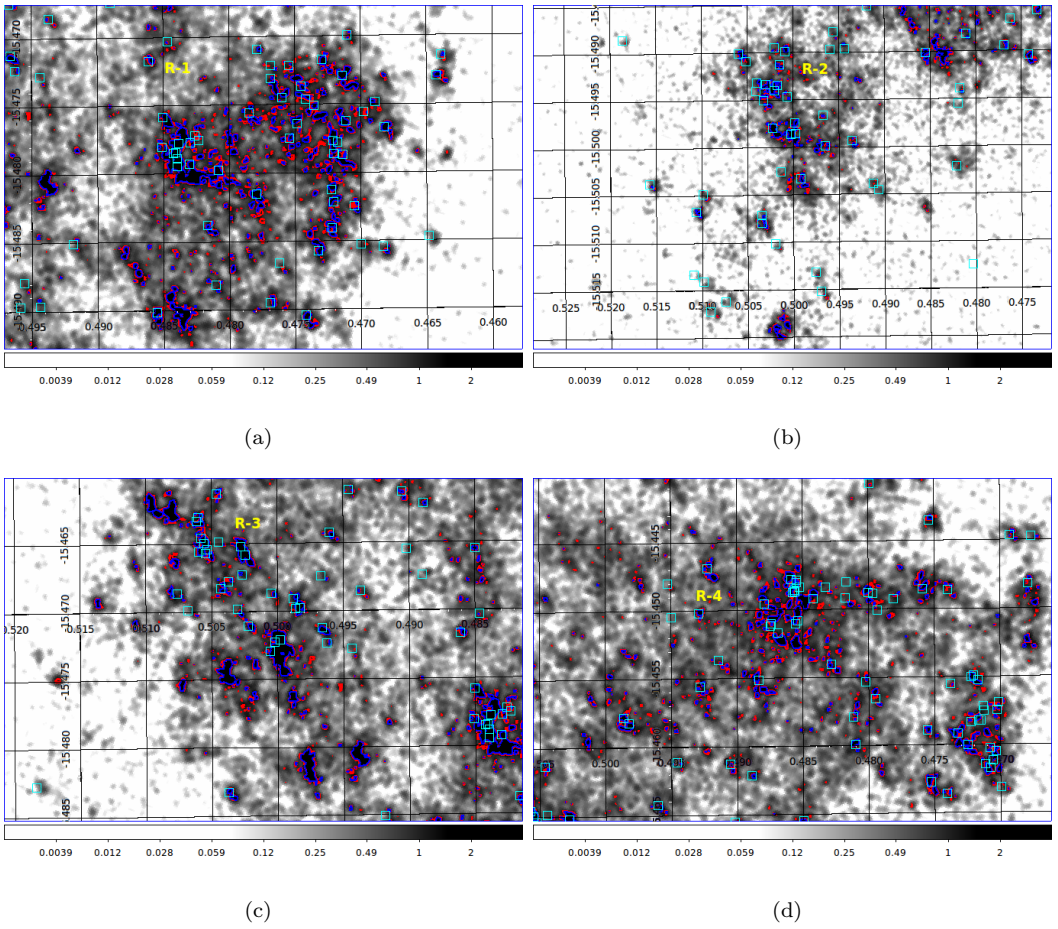

(a) (b)

(c) (d)

FIGURE 4.15: F148W/N263M smoothed image is shown with same blue and red contours as plotted in Figure 4.11. The HST detected massive stars (cyan box) are overlaid on the regions R1, R2, R3 and R4 as shown in figures (a), (b), (c) and (d) respectively.

points) along with the model curves as previously shown in Figure 4.3 to estimate the mass of these regions. Most of the detected star forming regions have colours within the model range, whereas we do detect a significant number of sources with bluer colours. These may be due to background sources and hence we consider only those which appear within the model limit. The majority of the compact star forming regions are found to have mass M $< 10^3 M_\odot$ with some of them between $10^3 M_\odot$ and $10^4 M_\odot$. A few regions are found to have M $> 10^5 M_\odot$, but could be older as indicated by their colour. Therefore the galaxy WLM is found to have a large number of young low mass compact star forming regions with M $< 10^3 M_\odot$.

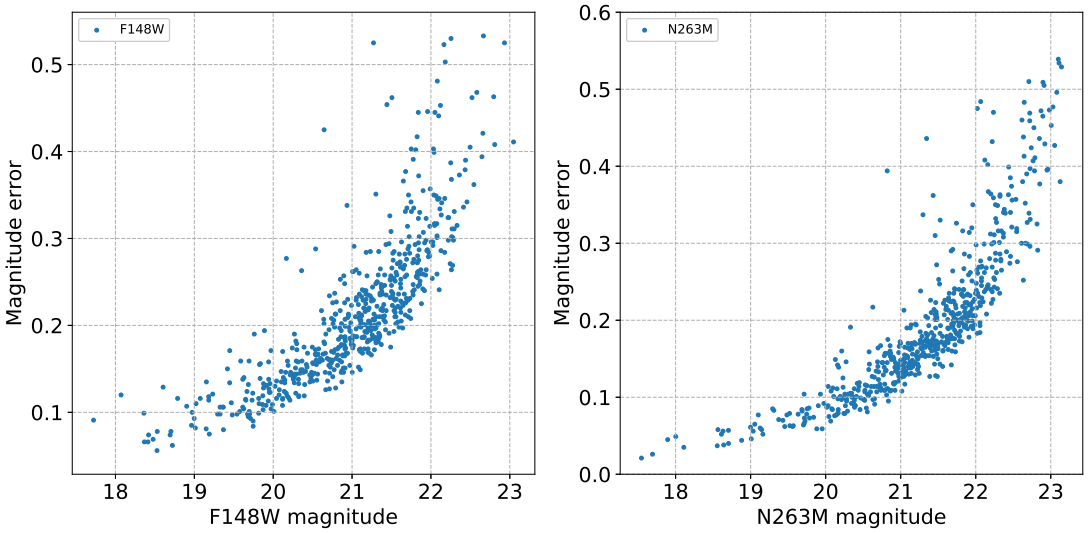

FIGURE 4.16: The F148W and N263M band magnitude and corresponding error of 590 identified point sources in the galaxy WLM.

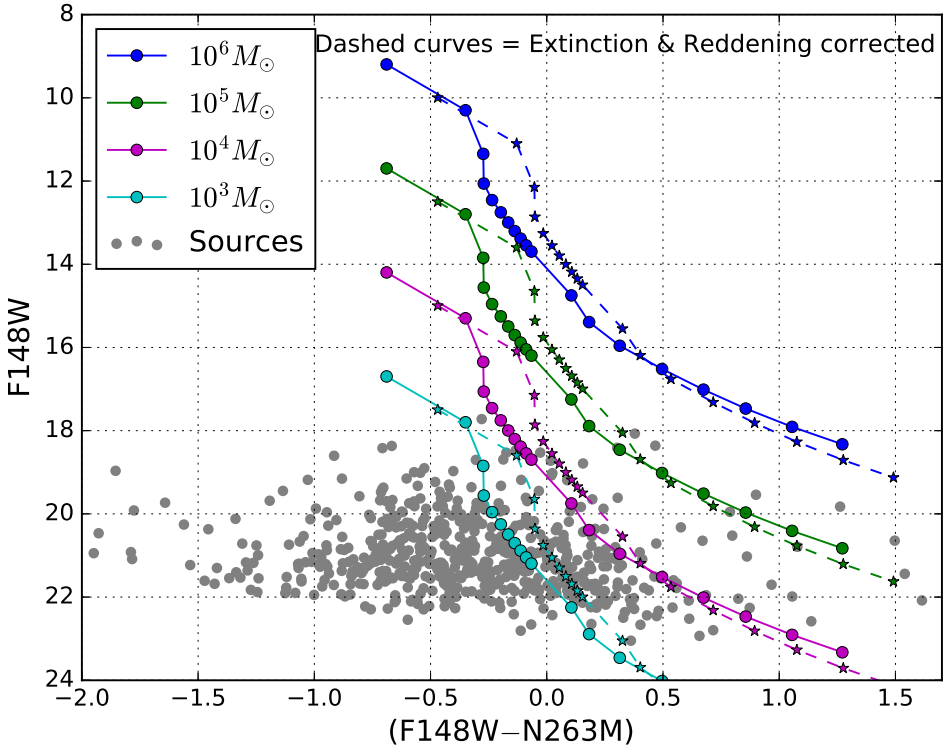

FIGURE 4.17: The identified compact star forming regions are over plotted (grey filled circles) on starburst99 model curves.

4.4.9 Correlating with CO observations

Since molecular clouds are the sites of star formation, we correlate our results with a recent CO observations of WLM. With the help of ALMA, Rubio et al. (2015) observed two 1 arcmin^2 field in WLM with a spatial resolution of 6.2 pc × 4.3 pc which is comparable with UVIT. They identified 10 CO clouds with an average radius of 2 pc and an average virial mass of $2{\times}10^3$ $M_\odot$. In Figure 4.18, we have shown the positions of detected CO clouds (green circles) in the two targeted fields (north-west (NW) and south-east (SE)) shown in black square boxes. The same blue and red contours of Figure 4.11 are also shown to correlate the position of detected molecular clouds with respect to the hot star forming regions. In Figure 4.19, we zoom in to these regions where CO clouds are detected (black box of Figure 4.18). Along with the spatial position, we show the size and virial mass of each cloud as estimated by Rubio et al. (2015). The majority of the detected clouds are of low mass ($\sim 10^3$ $M_\odot$), which in principle supports our finding of a large number of low mass compact star forming regions in WLM. Again the absence of higher mass molecular clouds could be the reason for the absence of massive compact star forming regions in this galaxy. We further find that eight of the detected CO clouds are found to be present away from the hot star forming regions. The only two clouds which are found to be co-located (there could also be a projection effect) with the hot star forming regions are NW-1 and SE-4, where SE-4 is the most massive cloud detected.

4.4.10 Star Formation Rate

In order to estimate the SFR of WLM, we used the F148W band (FUV) exposure normalised image of the galaxy. We summed up the flux (CPS) within a galacto-centric distance of 1.7 kpc, which is the extent of WLM's outer disk as found in

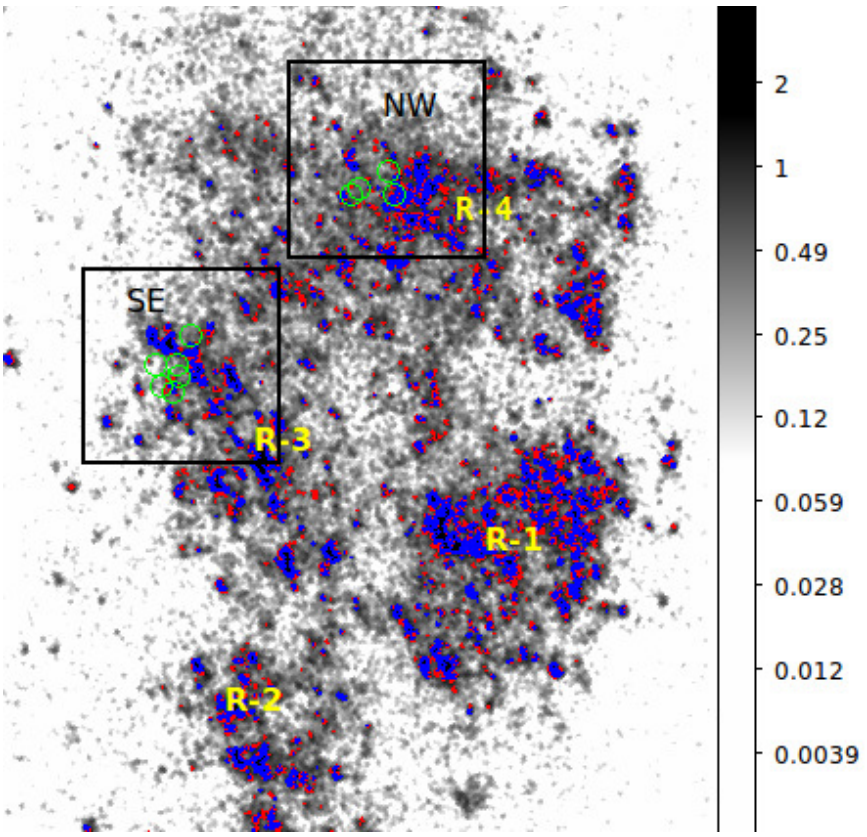

FIGURE 4.18: The smoothed F148W/N263M image is shown in the background with the logarithmic grey scale. The blue and red contours signify the hot regions of the galaxy as in Figure 4.5a. Two black squares (one in north-west (NW) and another in south-east (SE)) are the two 1 arcmin^2 ALMA fields observed by Rubio et al. (2015) for detecting CO clouds. The green circles shown inside the boxes are the position of detected CO clouds.

section 4.4.2. The background corrected total flux is converted to magnitude and further corrected for extinction. The background and extinction corrected magnitude is used to calculate the total SFR of the galaxy ($M_{\odot}/yr$). The corrected FUV flux is found to be $7.0{\times}10^{-13} \pm 3.6{\times}10^{-15} erg/sec/cm^2/\mathring{A}$ and the corresponding magnitude to be 12.12±0.01. We used the scaling relation, given in equation 7.4 (Karachentsev & Kaisina 2013a), to estimate the SFR, where mag_{FUV} is the corrected FUV magnitude and D is the distance to the galaxy in Mpc. Karachentsev & Kaisina (2013a) used this relation to estimate the SFR of a large sample of galaxies in the local volume using GALEX FUV observation. Since F148W filter of UVIT has bandpass similar to GALEX FUV, we used this relation to estimate

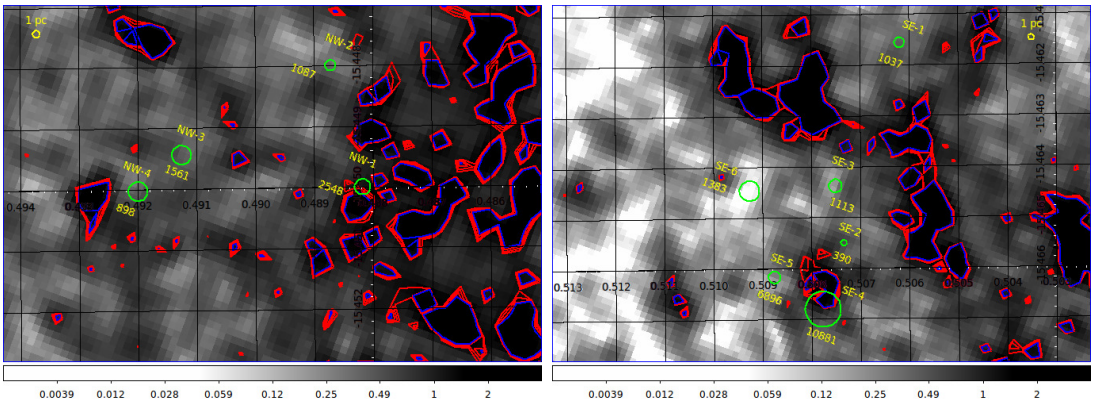

(a) (b)

FIGURE 4.19: Figure (a) and (b) show the zoomed in view of the regions (inside two black boxes of Figure 4.18) where CO detection is found in north-west (NW) and south-east (SE) field respectively. The background image and contours are same as mentioned in Figure 4.18. The CO clouds are shown in green circles where the size of the circles signifies the size of the cloud with respect to the 1 pc reference circle shown in each figure. The clouds are labelled as per Rubio et al. (2015). The numbers shown near each green circle signify its virial mass in $M_{\odot}$.

SFR. The total SFR up to a radial distance 1.7 kpc is found to be 0.008±0.0001 $M_{\odot}/yr$. This value of SFR could change if we adopt a different scaling relation. For example, if we adopt the empirical relation modelled by McQuinn et al. (2015), we estimate the SFR of WLM in the range 0.002 - 0.006 $M_{\odot}/yr$.

In order to explore radial variation of SFR within WLM, we generated the radial profile of SFR density (i.e. $M_{\odot}/yr/kpc^2$). The radial variation of SFR density is shown in Figure 7.12. The SFR density is found to increase with radius up to 0.4 kpc, resulting in a peak at this radius. The SFR density decreases after 0.4 kpc in the outer part, where the profile is shown up to 2 kpc. The profile also suggests that the SFR density is dominated by regions within a radius of 1 kpc. The relative positions of all the regions (R1, R2, R3, R4) along with the position angle is shown in Figure 4.21. This figure shows that most of these regions are located within the 1 kpc radius. We further explored the azimuthal variation of SFR density by taking the radially averaged value up to 2 kpc in Figure 4.22. The

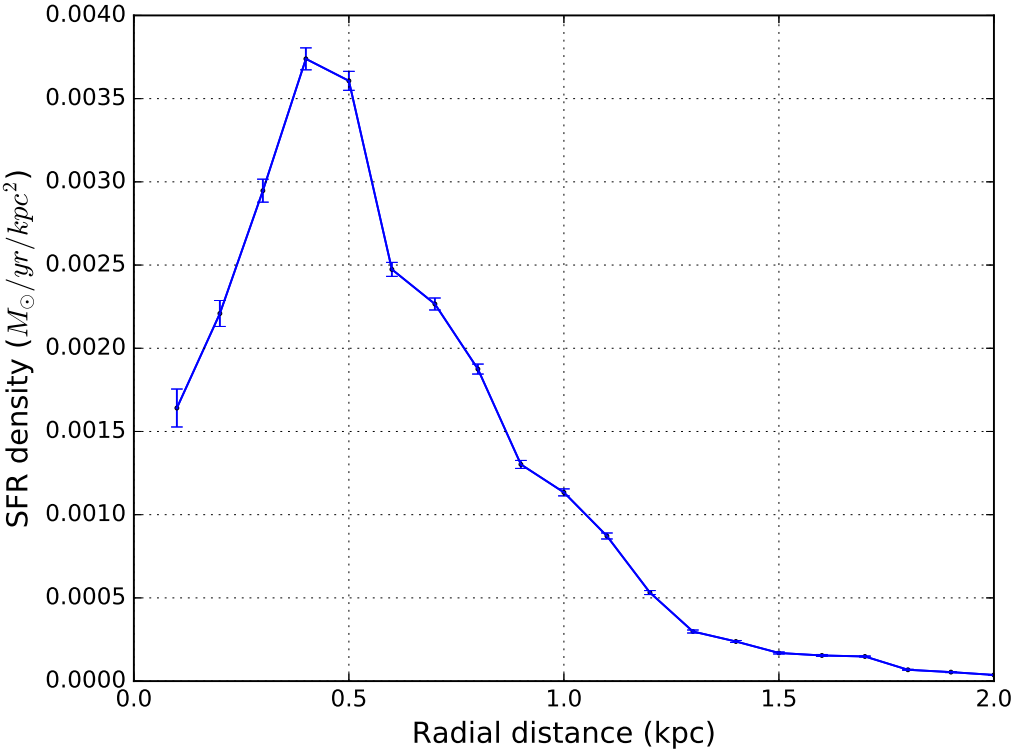

FIGURE 4.20: The radial profile for SFR density ($M_\odot/yr/kpc^2$) with 3σ error bar is shown in the figure.

profile shows two peaks at diametrically opposite values of position angle ($\sim 0^o$ and 180^o). The peak near PA $\sim 0^o$ has contribution from the northern regions R4 and R5, whereas the peak at PA $\sim 180^o$ has contributions from R1, R2 and R3. Figure 4.22 and 4.21 suggest that the southern half of the galaxy has a slightly higher SFR density when compared to the northern half.

$$log(SFR_{FUV}(M_\odot/yr)) = 2.78 - 0.4 * mag_{FUV} + 2log(D) \tag{4.2}$$

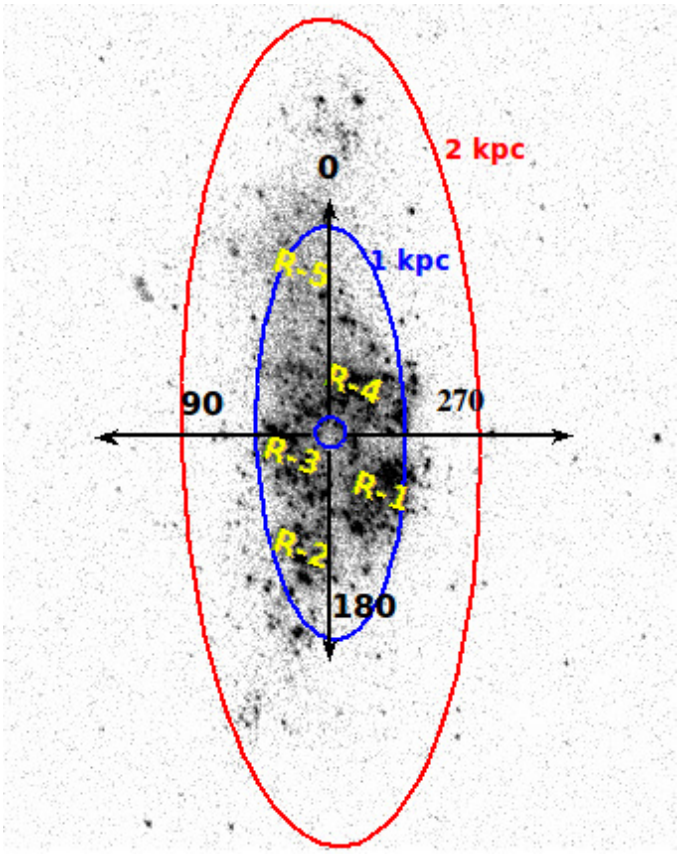

FIGURE 4.21: The figure shows all five regions (R1, R2, R3, R4 and R5) with F148W band image in the background. The black arrows show the position angle along four different directions. The blue and red ellipses represent 1 kpc and 2 kpc galactocentric distance respectively.

4.5 Results and Discussion

The primary objective of this study is to identify hot star forming regions of the dwarf irregular galaxy WLM and map its demographics. We used the UV images of the galaxy acquired from UVIT having a spatial resolution $\sim 1.5''$. The hot star forming regions are identified from the UV colour maps with the help of temperature - flux ratio relation derived from Kurucz spectra. We point out that this relation may change for any corresponding change in the assumed value of metallicity, extinction and surface gravity of stars. We demonstrate that the change of metallicity value between 0.002 to 0.006 has negligible effect on the flux ratio,

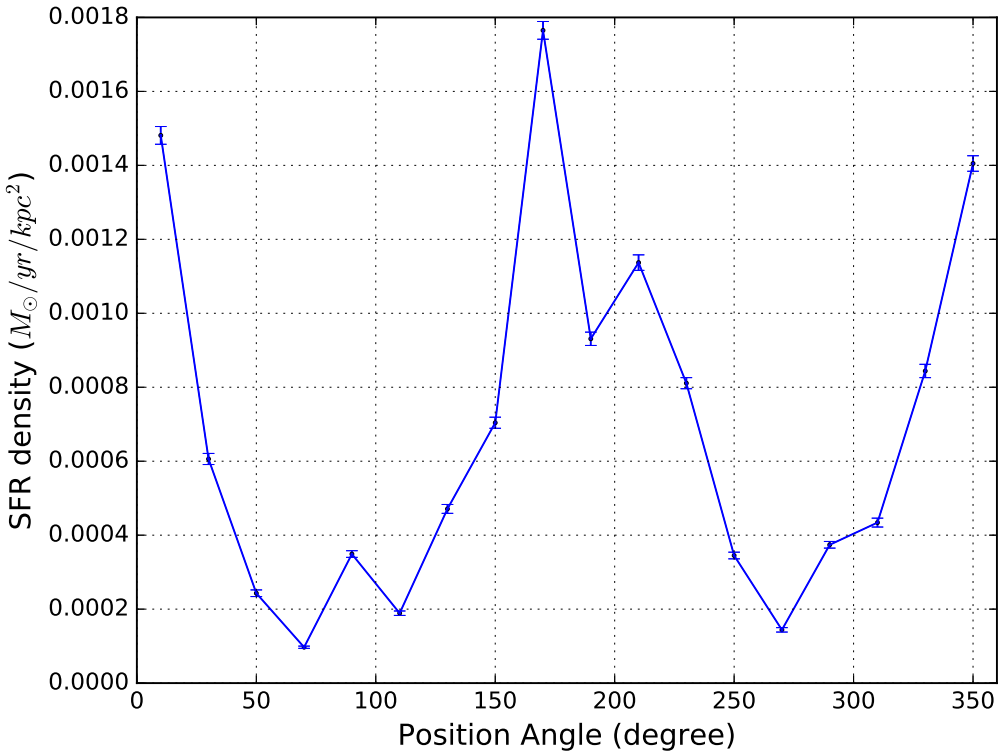

FIGURE 4.22: The azimuthal variation of radially averaged (up to 2 kpc) SFR density ($M_\odot/yr/kpc^2$) with 3σ error bar is shown in the figure. Two peaks at PA $\sim 0^o$ and 180^o signify the contribution of star forming regions from northern and southern half of the galaxy respectively.

hence on the measured temperature. On the other hand, the estimated parameters will have a dependence on the assumed extinction and its variation. Figure 4.2a shows the range of temperature for a given flux ratio, for various extinction laws. It also suggests that the uncertainty in temperature due to extinction is more for a higher temperature.

For any dwarf galaxy, feedback from massive stars act as one of the dominant mechanisms for driving star formation. According to the study of Dolphin (2000), WLM formed half of its stars, 9 Gyr ago and shows a reduction in star formation rate after that. They also found the star forming activity to increase around 1 to 2.5 Gyr, which continued till now. Bianchi et al. (2012) found the galaxy to

undergo a vigorous star formation during the last 10 Myr. They found 531 stars with temperature T > 18000 K and 721 stars having M > 9 $M_{\odot}$. In this study, we detect several hot regions with T > 35000 K, which are likely to be populated by O type stars. As the life time of these stars are $\sim$ 10 Myr, this would suggest that WLM has undergone a recent star formation activity with the production of massive stars. We also notice the hot regions to be surrounded by relatively cooler regions, suggestive of hierarchical structure. These are in agreement with the findings of Bianchi et al. (2012). We identified around 20 hot complexes with a size of 20 - 50 pc and more than 50 complexes with a size of 10 - 20 pc. Regions with size < 10 pc are found to be large in number (up to a few hundred) and scattered over a larger area of the galaxy. The smaller regions have less masses and are likely to be populated by a few OB stars, whereas the larger ones are likely to be complexes consisting of two or more associations of the galaxy. Our study finds that WLM is dominated by small sized regions, with the largest complex not exceeding 50 pc.

It is well known that the star formation creates hierarchical structures comprising of star clusters, OB associations, and complexes (Efremov & Elmegreen 1998; Bastian et al. 2007; Sun et al. 2018b). These structures are found to have various sizes and density in various environments (Elmegreen et al. 2014; Grasha et al. 2017). Bresolin et al. (1998) studied OB associations in 7 nearby spiral galaxies using HST-WFPC2 data and found a size range of $\sim$ 70 - 100 pc. For nearby irregular galaxies, the size of OB associations are reported to be $\sim$ 80 pc by Ivanov (1996). Mel'Nik & Efremov (1995) found relatively smaller size ($\sim$ 10 - 80 pc, with a peak around 30 pc) for galactic OB association whereas for LMC and SMC, it is around 60 pc (Bresolin et al. 1996). Bastian et al. (2007) noticed the star formation in M33 to be hierarchical in nature with a size distribution of young stellar complexes between 10 - 100 pc. Garcia et al. (2010) studied IC 1613, a similar nearby dwarf irregular galaxy like WLM, and concluded the star formation to be hierarchical with no specific length scale. The identified OB associations in

their study show a size $\sim$ 14 - 42 pc which is quite similar to our findings in WLM. Garcia et al. (2010) also found 44% of the total associations are smaller in size. Several studies conclude that the size of these detected associations is highly dependent on the resolution of telescope and the distance to the galaxy (Garcia et al. 2010; Bastian et al. 2007). Due to the better spatial resolution of UVIT we are able to detect smaller substructures of the star forming regions present in the galaxy, when compared to GALEX. The overall sizes of OB associations in WLM, detected through UVIT are found to be quite similar to those in IC 1613 (nearby dwarf irregular), but smaller than those in M33 (nearby spiral) and the Milky Way.

Around most of the larger hot complexes we detect the presence of several smaller regions connected together by low temperature contours. This brings out the clumpy nature of star forming regions in WLM. The feedback from the massive stars (large hot complex) may have triggered further star formation near to them which results in these clumpy distribution of young star forming regions. It is also noticed that relatively low temperature regions are much more spread than the hot regions which is also mentioned in the study by Bianchi et al. (2012). The star forming regions also show several knotted structures, specifically in R1. The overall distribution of detected hot star forming regions throughout the galaxy clearly reveals that the southern part of the galaxy is much more active than its northern part. The hot star forming regions detected in (F148W−N245M) colour map are found to be more fragmented than those seen in (F148W−N263M) colour map. A clumpy distribution of either the young stellar objects or the dust or both of them present in the galaxy can result in these observed structural differences.

We also studied the extent of UV emission in WLM. It is noticed that the NUV emission as traced by N245M and N263M filters is more extended than the FUV emission. Since the FUV emission mainly comes from the younger stellar populations, it is probable that the populations present in the outer part of the galaxy

are relatively older than those of inner part. The luminosity density profile clearly shows that the UV emission of the galaxy is present at least up to a radius 1.7 kpc.

A high resolution H I study by Kepley et al. (2007) revealed the presence of a hook like structure in H I distribution. They speculated that an expanding ring like structure has broken in the western part and generated this hook like pattern. They concluded that this structure is likely to be the result of star formation propagating outside from the centre of the galaxy. The hot regions detected in our study delineate this hook structure except in the western part (i.e. in R1). The H I density shows an overall reduction in R1 whereas we see intense Hα emission with a central hole in the same region. On the basis of this scenario Kepley et al. (2007) concluded that H I is likely to be used up or ionised or destroyed due to high rate of star formation in this part of the galaxy. In our study we detected several knotted structures of hot star forming regions in R1 which signify the presence of several OB stars. This region also has one of the three most luminous star forming complexes (see Figure 4.6). This L-shaped complex is located to the north and is suggestive of intense recent star formation. We also notice the presence of hot star forming regions forming an arc like shape, located to the west of the H-alpha ring (see Figure 4.13). This might suggest that the H-alpha emission is shrinking towards the inner hole, in the eastern side. The western arc like structure could be relatively older with respect to the northern complex. The radiation from these OB stars has probably driven/consumed the H I gas present there, which supports the scenario of Kepley et al. (2007).

In a recent study with ALMA observations, Rubio et al. (2015) detected several CO clouds with sizes ranging from 3 to 12 pc in diameter. The smaller hot star forming regions (i.e. clusters or OB associations) identified in our study have an average size from 4 - 20 pc, with most of them with sizes < 10 pc. The comparable size of CO clouds and hot star forming regions suggest that star formation

happens in smaller molecular clouds in this galaxy. The masses estimated for the compact star forming regions detected in this study also match well with the mass of the CO clouds, confirming the formation of low mass stellar clumps.

We estimated the total FUV magnitude to be 12.12±0.01 magnitude, corresponding to a SFR of ∼0.008±0.0001 $M_{\odot}/yr$. As mentioned earlier, the value of SFR is a function of the scaling relation and could change if a different relation is used. Earlier estimations by Karachentsev & Kaisina (2013a) and Hunter et al. (2010) using GALEX FUV observations are comparable. Though SFR of WLM is less compared to that of Milky way (1.9±0.4 $M_{\odot}/yr$ (Chomiuk & Povich 2011)), the value of specific SFR (sSFR = SFR/Stellar mass of galaxy) of WLM is 16 times higher than that of Milky Way. For the total stellar mass of WLM ($1.6 \times 10^7 M_{\odot}$ (Zhang et al. 2012)) and Milky Way ($(6.4 \pm 0.6) \times 10^{10} M_{\odot}$ (McMillan 2011)), the estimated values of sSFR are 5.0×10^{-10} and 3.0×10^{-11} yr^{-1} respectively. Therefore being a dwarf irregular galaxy, WLM is able to form stars in a relatively higher rate than Milky way (Rubio et al. 2015).

4.6 Summary

The main results of this chapter are summarised below:

1. The UVIT images in FUV and NUV are used to study the demographics of the star forming regions in WLM.
2. The UV emission of WLM is found to be present up to a galactocentric distance of 1.7 kpc, with most of the flux originating within a radius of 1 kpc.

3. We divided the galaxy into 5 different regions to compare the demographics and identify three most luminous and massive star forming complexes, with the largest one extending not more than 50 pc.

4. The hot star forming regions with T > 17500 K (populated with OB stars) have a range in size, with a few tens of regions in the 20-50 pc range and a few hundred regions with < 10 pc size.

5. The hot stellar regions are found to be surrounded by regions with cooler stars, suggesting a hierarchical nature of distribution.

6. The presence of several hot regions suggest that the galaxy underwent a recent star formation $\sim$ 10 Myr ago.

7. We find a good spatial correlation between UV detected hot regions with Hα emitting regions, H I distribution and HST detected massive stars in the galaxy. The western part (R1) of the galaxy is likely to have undergone a vigorous recent star formation.

8. The sizes and masses of isolated star forming regions closely match with those of CO clouds estimated using ALMA observations. WLM is found to have a large number of low mass (M < $10^3 M_\odot$) compact star forming regions.

9. The star formation in the southern part of the galaxy is more active than the northern part. The SFR of the galaxy is $\sim 0.008\ M_\odot/yr$, which is similar to that found in other dwarf galaxies.

Chapter 5

UVIT view of dwarf irregular galaxy IC 2574 : Is the star formation triggered due to expanding H I shells?

5.1 Introduction

IC 2574 (also known as DDO 81 or UGC 5666) is a gas-rich dwarf irregular galaxy in the M81 group, located at a distance of 3.79 Mpc (Dalcanton et al. 2009). It was discovered in 1898 by Edwin Foster Coddington and hence also referred to as Coddington's Nebula. The size of the galaxy is comparatively large (optical disk radius $\sim$ 9 kpc) and it has an absolute magnitude of -17.6 in optical V band. The galaxy, being present $\sim$ 164 kpc away from the brightest group member M81, does not have any signature of interaction (Yun 1999). The galaxy shows a solid

body like rotation curve, which reduces the effect dynamical shear internal to it also. Parameters of this galaxy are listed in Table 5.1.

The SFR of the galaxy is found to have increased during the last 1 Gyr (Walter & Brinks 1999) and hence it is a good candidate to study recent enhancement in the star forming activities. The ISM of this galaxy is very interesting and intriguing. The distribution of H I in this galaxy shows many shell like structures. Using VLA observations, Walter & Brinks (1999) identified 48 H I shells and holes in the galaxy and studied them in detail. In order to understand the connection between H I holes and triggered star formation in the galaxy, they used the catalogue of Hα emitting regions from Miller & Hodge (1994) and defined 40 H II regions, and investigated their connection with the features observed in the H I map. They reported that the Hα emissions, which traces the current star formation, are predominantly found along the rims of larger holes. Pasquali et al. (2008) used optical images taken with Large Binocular Telescope (LBT) to explore the star formation history of the galaxy and reported two recent bursts of star formation in the galaxy. They found an older burst about 100 Myr ago inside 4 kpc radius and another younger burst during last 10 Myr between radius 4 to 8 kpc. They further noticed that the younger burst of star formation is mainly located in the periphery of H I shells. Therefore the galaxy IC 2574 offers a good opportunity for studying nature of star formation triggered due to the expanding H I shells. Pellerin et al. (2012) observed the north-eastern part of the galaxy using HST and detected 75 young stellar groups (age $\sim$ 10 Myr), which again points to the recent star formation in the galaxy.

One of the identified super giant shells (SGSs), located in the north-east of the galaxy, has been studied rigorously in the literature. Using UV observations from UIT, Stewart & Walter (2000) identified a remnant cluster inside the SGS and confirmed a causal relation between the remnant cluster and the triggered star formation seen along the rim of the shell. Cannon et al. (2005) used Spitzer

TABLE 5.1: Properties of IC 2574

Property	Value	Reference
RA	10 28 23.5	Skrutskie et al. (2006)
DEC	+68 24 43.7	Skrutskie et al. (2006)
Distance	3.79 Mpc	Dalcanton et al. (2009)
Metallicity (Z)	0.006	Cannon et al. (2005)
M_V	−17.6	de Vaucouleurs et al. (1991)
Inclination	63°	Pasquali et al. (2008)
PA of major axis	55°	Pasquali et al. (2008)
H I mass	14.8×10^8 $M_\odot$	Walter et al. (2008)

observations to conclude that the triggered star formation detected along the rim of the shell is found to alter the temperature of the dust present around it. An HST study by Weisz et al. (2009) also revealed that star formation happened earlier inside the SGS has triggered further recent star formation along its rim. Yukita & Swartz (2012) identified a luminous X-ray source, which is slightly offset from the remnant cluster, inside the SGS. They also showed GALEX FUV image of the SGS (their Figure 2) where the remnant cluster is shown as C2. Though the SGS located in the north-eastern part of the galaxy is studied in FUV, a detailed investigation of the FUV emission with respect to all the H I holes in IC 2574 has not been performed. Therefore, a study of star formation across the galaxy with FUV observations will be an enriching activity.

In this chapter, we present an FUV imaging study of the galaxy IC 2574 observed with UVIT F148W band (Image - Figure 5.1). The objective is to understand the connection between the recent star formation and the H I holes across the galaxy. We combined the FUV data along with the Hα data from Miller & Hodge (1994) to trace the star formation not only in and around H I holes, but also in the entire galaxy. Details of this study are presented in this chapter.

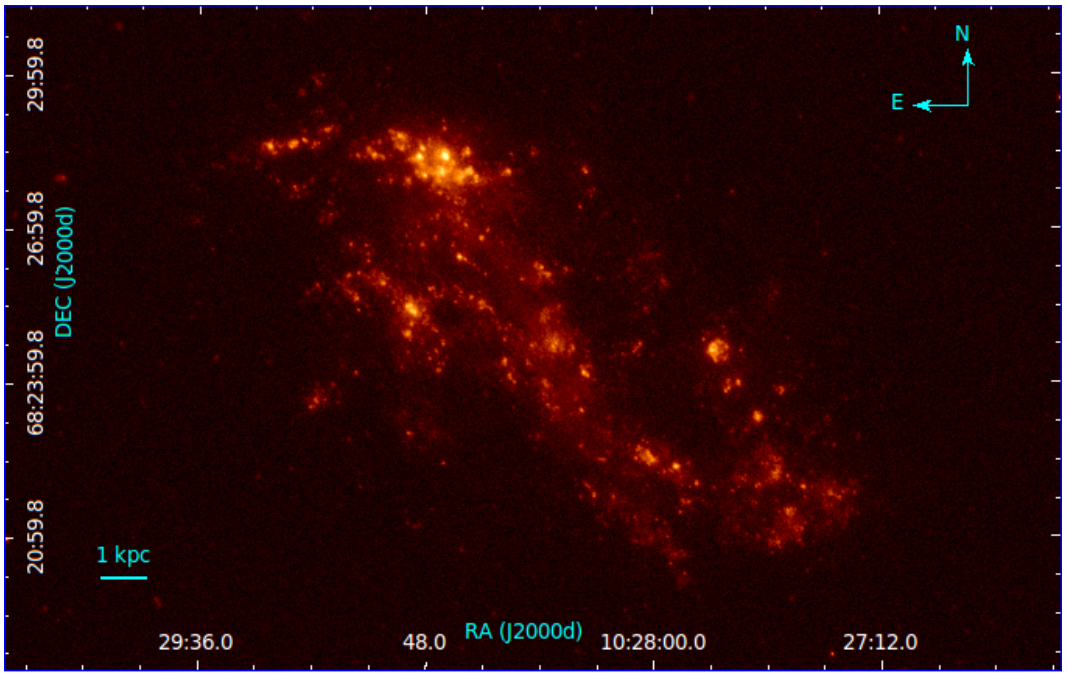

FIGURE 5.1: UVIT F148W band image of the galaxy IC 2574.

5.2 Extinction in UV

The nature of extinction in UV band shows characteristic variation for different external galaxies. Gordon et al. (2003) studied the behaviour of extinction in the LMC, the SMC and the Milky way and found differences specifically in the UV regime. Since FUV radiation is sensitive to extinction, we considered both the Galactic extinction foreground to IC 2574 and interstellar extinction within the galaxy IC 2574 in our study. The E(B−V) values for Galactic foreground reddening and interstellar reddening of the galaxy IC 2574 are reported to be 0.036 and 0.013 mag respectively (Pasquali et al. 2008). The nature of extinction law in IC 2574 was considered to be SMC type in the previous study by Pasquali et al. (2008) and Stewart & Walter (2000). In order to calculate extinction value in F148W filter, we considered Fitzpatrick law (Fitzpatrick 1999) for foreground and SMC bar type extinction law (Gordon et al. 2003) for the interstellar reddening

of the galaxy IC 2574. The extinction coefficients are calculated using extinction law calculator of McCall (2004) available in NED. We considered R_V values as 3.07 and 2.75 respectively for Fitzpatrick and SMC bar type extinction law and estimated the average value of extinction coefficient (R_{F148W}) in F148W band (for the range 1250 - 1750 $\AA$). The estimated values of R_{F148W} are found to be 8.57 and 13.06 respectively for Fitzpatrick and SMC bar type law. We calculated the value of extinction using equation 4.1, where R_{F148W} is the extinction coefficient, and found it as 0.31 mag and 1.70 mag respectively for foreground and interstellar extinction. The observed fluxes are corrected for both these extinctions in our analysis. It is to be noted that the value of interstellar extinction of the galaxy may have spatial variation and that can change the value of some of our estimated parameters.

5.3 Data and Analysis

This study is done primarily based on the UVIT FUV data observed in F148W filter. The UVIT image of the galaxy and the related observation details are given in Section 2.2.1. We further used H I column density map and Hα data of the galaxy, which are described in Chapter 2.

5.3.1 Distribution of FUV emission and H I gas

We considered the FUV image of the galaxy IC 2574 to locate young star forming regions. The distribution of FUV bright regions in the galaxy are mostly found to be clumpy in nature (Figure 5.1). In order to understand the extent and characteristics of these regions more clearly, we generated contours for two different

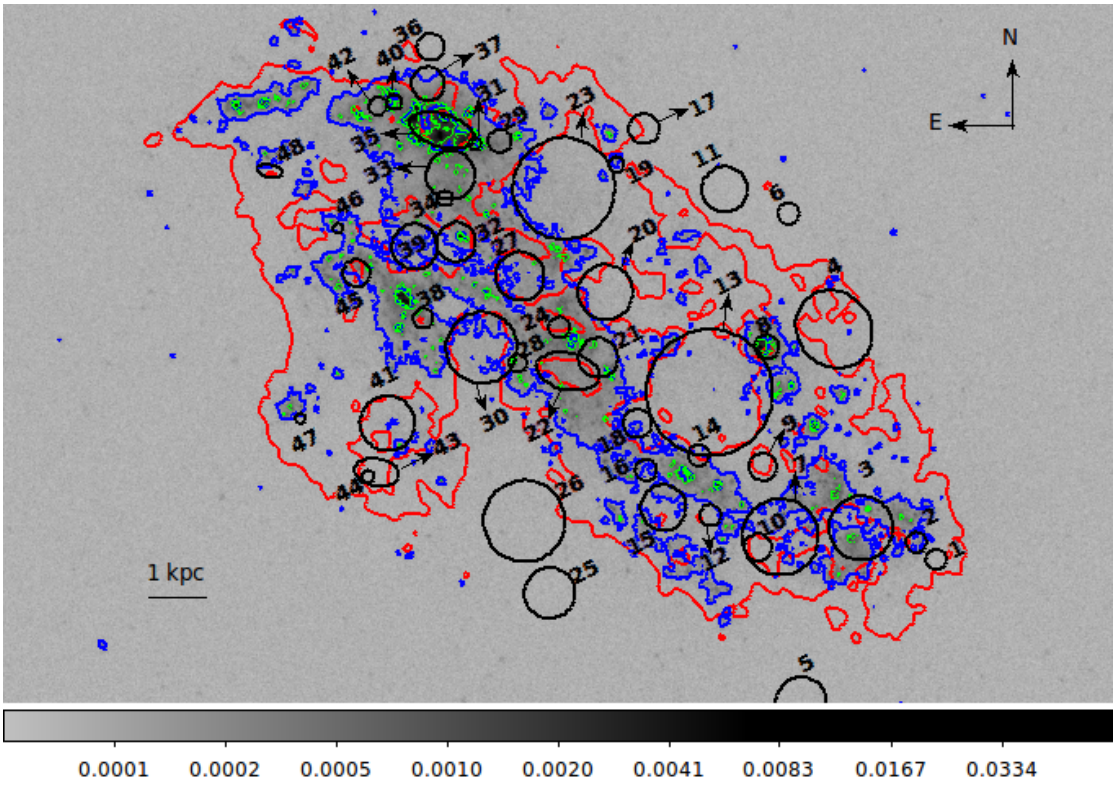

FIGURE 5.2: The background image is the UVIT FUV image of the galaxy IC 2574 observed in F148W filter. The H I holes, as identified by Walter & Brinks (1999), are shown by black circles/ellipses. The number corresponding to each hole is same as assigned by these authors. The green and blue contours signify pixels with FUV flux more than 2.14×10^{-18} and 3.21×10^{-19} $erg/sec/cm^2/\mathring{A}$ respectively. The red contours denote regions with H I column density greater than $1.0 \times 10^{21} cm^{-2}$.

threshold fluxes and displayed them in Figure 5.2. The method to produce contours for different flux levels is explained in Section 3.3.1. The blue and green contours shown in the figure respectively signify threshold value of 3.21×10^{-19} and 2.14×10^{-18} $erg/sec/cm^2/\mathring{A}$, which are respectively equivalent to 3 and 20 times the average background flux. The reason behind choosing these two different values for generating the contours is to trace both the brighter and the fainter features together in the FUV emission profile of IC 2574. By choosing this lower limit, we expect to get rid of the background emission completely and to trace emission region only due to the galaxy. The green contours which trace relatively massive and more active star forming complexes, are found to be more compact in

nature whereas we noticed the blue contours, which trace the overall FUV emission profile of IC 2574, to be more extended around the green contoured regions. Therefore, the star forming regions of the galaxy are found to have an overall patchy distribution with several compact clumps dispersed throughout the disk.

FUV emission, which mimics the current SFR in a galaxy, is found to correlate well with H_2 gas, whereas it does not follow a universal relationship with H I gas throughout the galaxy (Bigiel et al. 2008). In order to check the correlation of identified FUV bright regions with the column density of H I gas, we plotted contours for $n_{HI} > 10^{21} cm^{-2}$ which is shown in red in Figure 5.2. These density contours are generated from the VLA moment 0 H I map of the galaxy available in Walter et al. (2008). The identified FUV bright star forming regions (both green and blue contours) of the galaxy are mostly found to be present within the extent of plotted H I density contour. This simply conveys that star formation is mainly happening in regions with H I column density greater than $10^{21} cm^{-2}$, which is known as the threshold value for star formation in IC 2574 (Walter & Brinks 1999). There is no major star formation found outside the extent of the red contours.

5.3.2 H I shells

The gaseous component of the galaxy IC 2574 has many hole like structures distributed all over its disk. Using VLA H I observations, Walter & Brinks (1999) identified 48 H I shells and holes in the galaxy with radius in the range 100 - 1000 pc. The lower limit of the detected hole size is constrained by the beam size of the instrument. In Figure 5.3, the H I column density map of the galaxy is shown along with these 48 holes. Walter & Brinks (1999) also found $H\alpha$ emission along the rims of larger holes which in other word signifies propagating star formation triggered due to the expansion of these holes. An expanding H I hole can compress

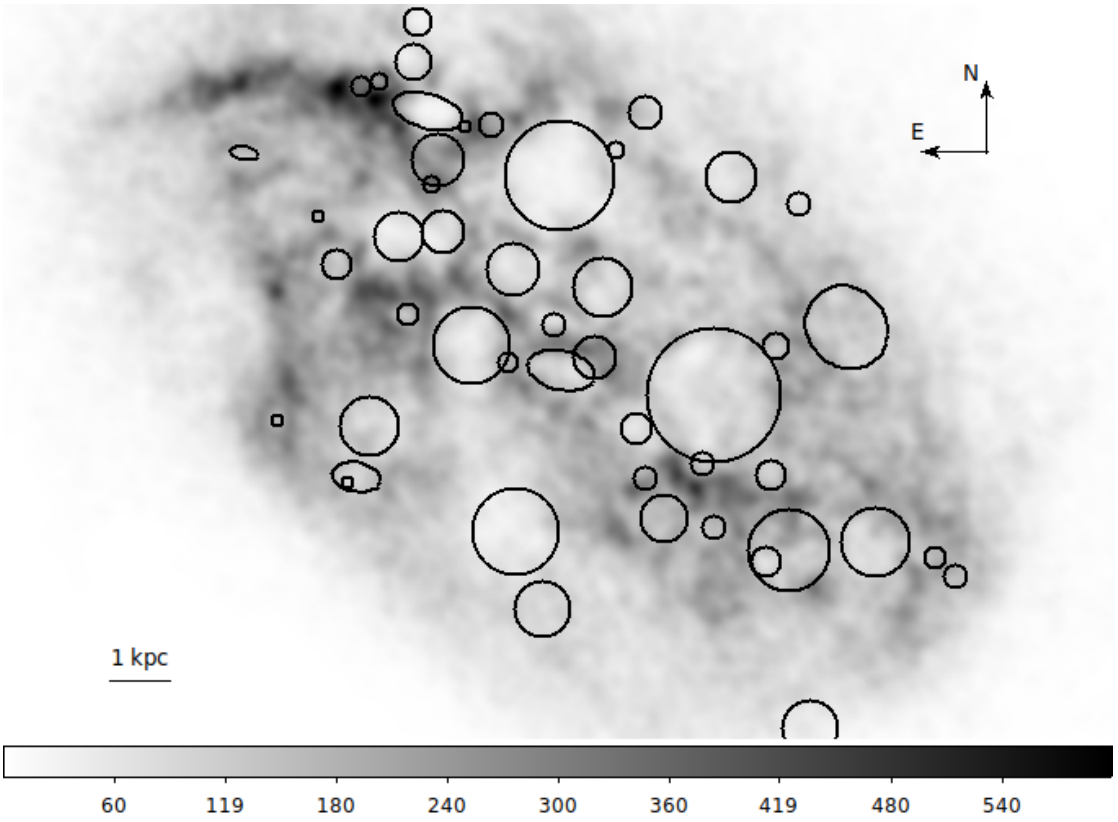

FIGURE 5.3: The H I column density map of the galaxy is shown along with the 48 H I holes (black circles/ellipses) as identified by Walter & Brinks (1999). The grey scale shows flux in JY/B*M/S.

their surrounding ISM to trigger further star formation in a galaxy (Tenorio-Tagle et al. 2005). In order to explore this, we have shown all these 48 holes as identified by Walter & Brinks (1999), overlaid on the FUV image of the galaxy also in Figure 5.2. A careful look reveals that many holes have bright FUV emissions (green contours) in their shells whereas some show signature of FUV emission inside the hole as well. We found 30 holes with FUV emission in their periphery while 15 holes show emission inside them. This signifies that star formation in certain parts of the galaxy could be triggered due to the expansion of H I holes. It is also possible that some of these emissions are actually coming from other parts of the galaxy and they seem to be related to the holes due to projection in the sky plane.

As FUV radiation traces star formation up to a few hundred Myr and the H I holes

of IC 2574 are of $\leq$ 50 Myr (Walter & Brinks 1999), a detection of FUV bright region is not sufficient to confirm the existence of hole driven star formation. In order to verify whether the FUV regions are actually young (age <10 Myr), it is important to check whether they also show Hα emission. We used the catalogue of Hα emitting regions of Miller & Hodge (1994) for cross-identification. This catalogue contains position, $H\alpha$ flux and size information of 289 H II regions detected in the galaxy. About 54% of the FUV bright regions, detected in the shells, are also found to have Hα emission. These are potential locations where star formation could be triggered due to the expanding holes. The emission identified inside the holes (specifically with Hα counter part) can actually be coming from the shell, present either in front or back along the line of sight. We discuss these in detail in the next section. It is further noticed that some of the green contours in different places across the galaxy are present in between multiple holes. This gives an appearance of star formation happening in regions which are surrounded by holes. The feedback from the expanding holes may have compressed the ISM in between to make those sites more favourable for star formation. Both the above scenarios signify the impact of hole expansion in triggering star formation inside the galaxy.

Again, the fact that star forming regions are mostly identified in regions with H I density more than $10^{21} cm^{-2}$ signifies that the mechanism which has shaped the H I distribution inside the galaxy has also triggered secondary star formation in some of those sites. Therefore, in majority of the cases, the FUV emission, H I density and the shell structure are likely to be co-spatial.

5.3.3 FUV bright star forming regions

In order to identify FUV bright star forming regions across the galaxy, we used the Python package *astrodendro*, explained in Section 3.3.3. We considered the

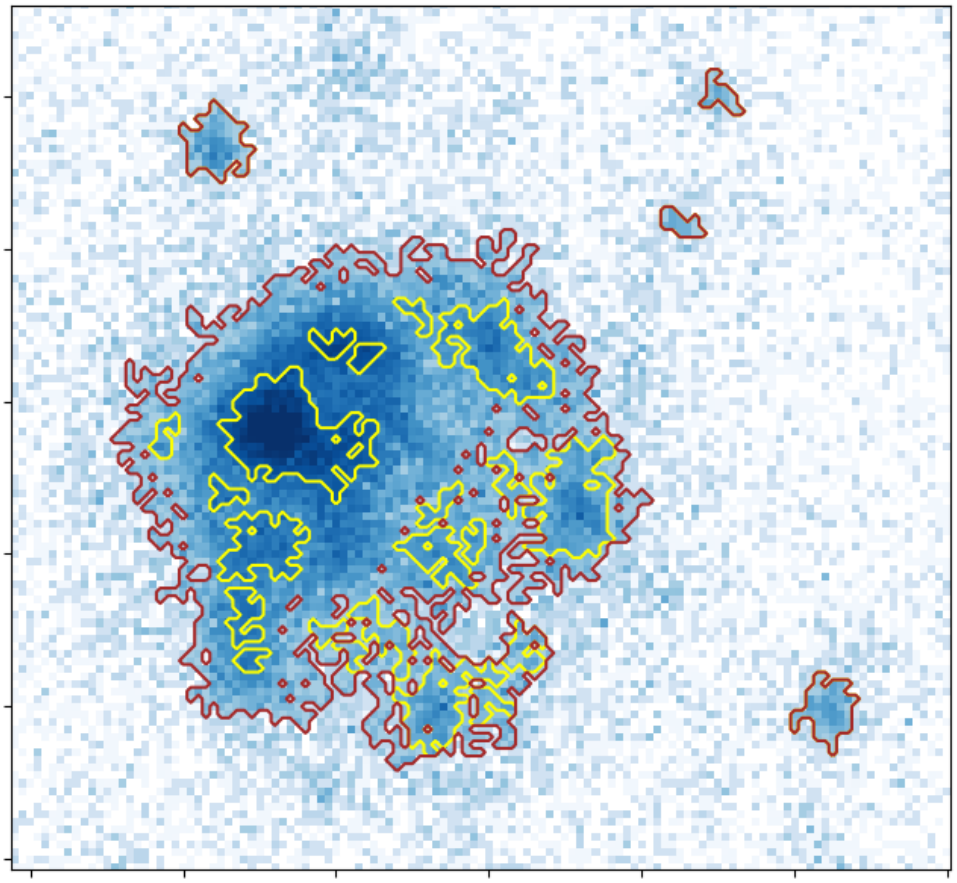

FIGURE 5.4: A smaller part of the galaxy IC 2574 is shown. The brown contour signifies parent structure and the yellow contour is for child structures.

threshold flux as $1.07 \times 10^{-18} erg/sec/cm^2/\mathring{A}$, which is 10 times the average FUV background flux. This threshold corresponds to the flux of a B5 spectral type star at the distance of IC 2574. The minimum number of pixels for the identification of regions is considered as 10, which corresponds to a radius of $\sim$ 15 pc for a circular area. The value of this lower limit is fixed by balancing two facts. One is to resolve the smaller clumps well and other is to avoid identifying a lot of them. With these parameters, we identified a total of 403 parent structures in the galaxy within a galactocentric distance of 10 kpc. These FUV bright regions are likely to be the active star forming regions of the galaxy. In Figure 5.4, we have shown a smaller part of the galaxy and highlighted some of these identified parent and child structures with brown and yellow contours respectively. Four among the five parent structures shown in the figure do not have any sub-structure inside, while

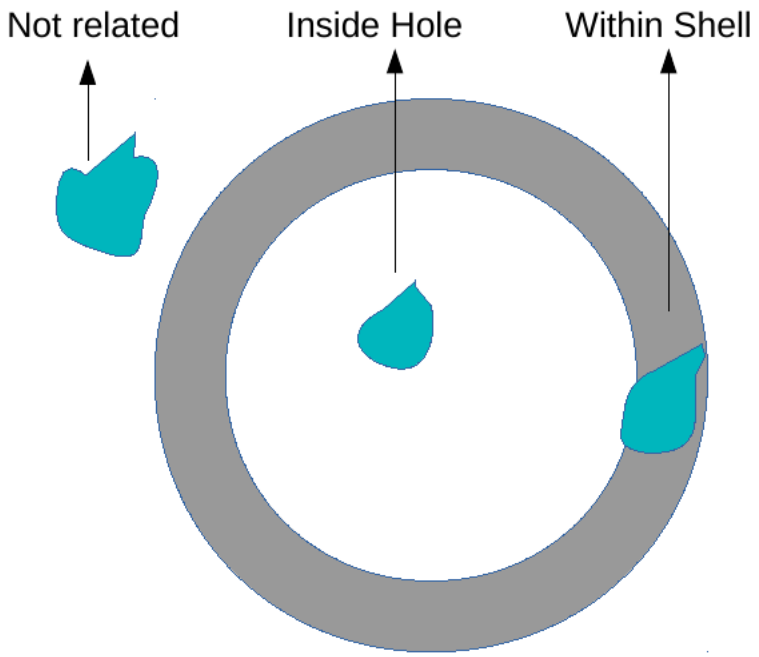

FIGURE 5.5: This is a cartoon image of an H I hole of radius R. The grey annular region is the shell of width R/3. The cyan clumps represent star forming regions in three different scenarios as discussed in the study.

one with the larger size contains multiple sub-structures within it. Out of the total 403 parent clumps, 96 (23.8%) are found to have multiple smaller sub-structures within them whereas the rest 307 (76.2%) clumps show no sub-structures within the detection threshold. Among all the identified parent structures, we found one, located in the north-eastern part of the galaxy, to be exceptionally larger than the rest. This parent structure contains many smaller sub-structures inside it. We selected 17 bright sub-structures instead of this single large structure for our study. Hence we have a total of 419 FUV bright regions, which we considered for the rest of our analysis.

In order to identify an FUV bright region to be formed due to an expanding H I shell, we need to define a thickness to the shell and check for FUV bright regions located within this shell. Here, we considered the width of the shell as R/3 (where R is the radius of the hole), from radii (R−R/6) to (R+R/6) for each hole (Figure 5.6). Implication of this assumption is discussed in section 5.4. If an FUV bright

region (or some part of it) is present within the radii (R−R/6) to (R+R/6) of any hole, then it is considered as part of the shell of that hole. If it is present within radius (R−R/6), then we assume it to be inside the hole. In case the region is located at a distance more than (R+R/6) from the hole centre, we considered it to be not related to that hole. This is highlighted with the help of a cartoon image shown in Figure 5.5. Following this methodology, we identified regions which are connected with holes (either in the shell or inside) and listed them in Table 5.2. Walter & Brinks (1999) estimated the ages of these 48 holes and also classified them in three different types (Type 1, 2, 3) on the basis of their appearance in the p-V diagram. We also noted this information in Table 5.2.

Out of 419 identified regions, we found 120 (28.6%) to be present in shells and 53 (12.6%) to be present inside holes. It is to be noted that the list is made as per their locations in the projected sky plane and hence there can be a possibility to have a slightly different scenario in the galaxy plane. We also found 252 (60.1%) regions as not related to any of the holes. Therefore, 60.1% of the star formation happening in the galaxy has no connection with the holes. In other words, 30 (62.5%) out of 48 holes are found to have FUV emission in their shell whereas 15 (31.2%) holes show emission inside. We noticed 16 (33.3%) holes to have no related FUV emission. There are 13 holes which show FUV emission both in shell and inside them.

In Figure 5.6, we have shown some selected holes of various types along with the identified FUV bright regions. In the case of Hole 3 (top-left of Figure 5.6), we noticed 8 regions (Regions 22, 27, 33, 43, 44, 55, 57, 58) to be present in the shell and 9 regions (Regions 28, 35, 37, 38, 40, 42, 46, 47, 52) are identified inside it (Table 5.2). The regions found inside can actually be present in the shell but it appears to be inside the hole only in the projected plane. The other holes (except Hole 11) are also found to have emissions in their shell. Hole 11 is an example of holes which do not have any related FUV emission. Hole 8 and 32 show strong

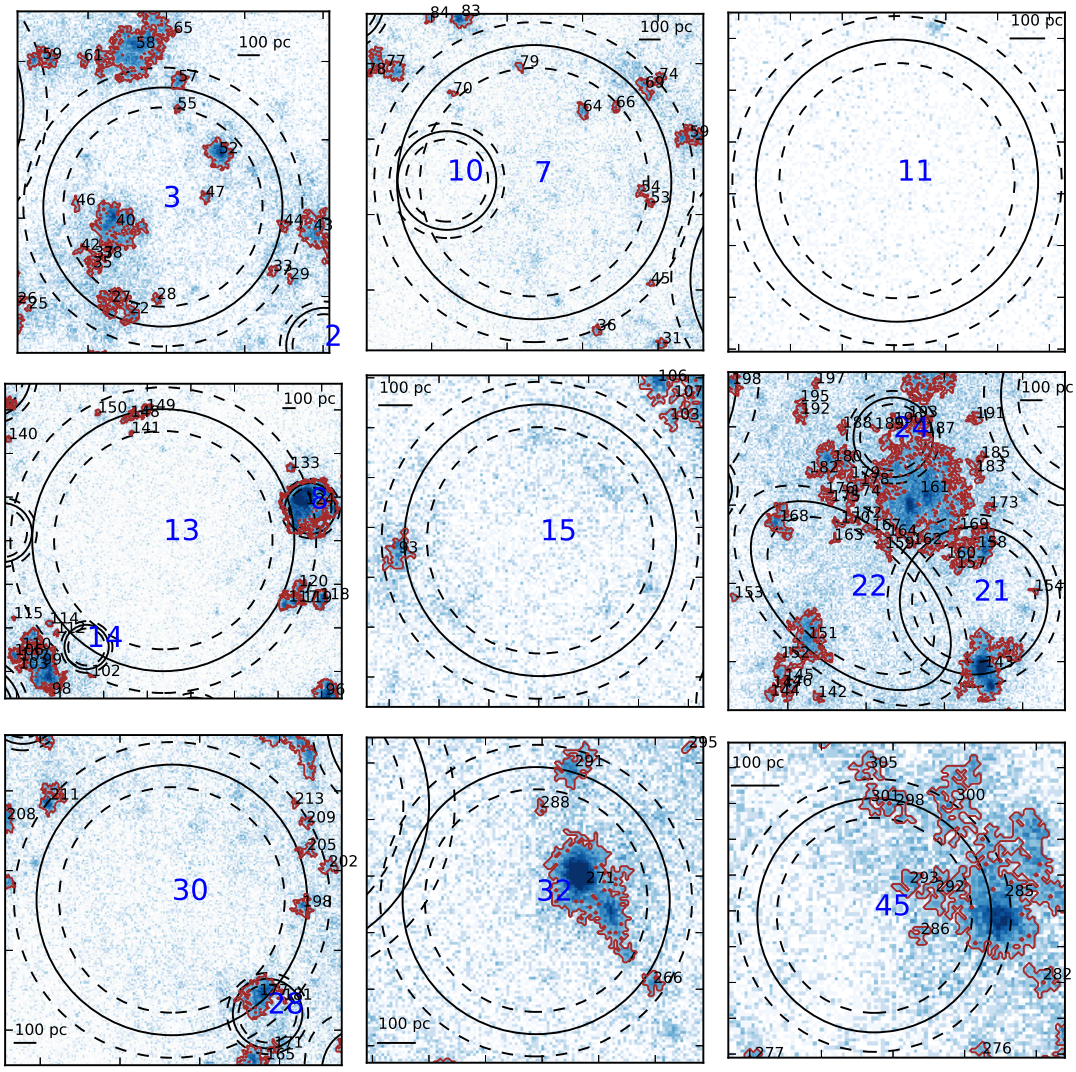

FIGURE 5.6: The figure shows some selected holes along with the identified FUV bright regions. The background image is UVIT FUV image of IC 2574. The black solid circles/ellipses show the holes of radius R, where the shells are defined by black dashed lines of width R/3 between radii (R−R/6) to (R+R/6). A length scale of 100 pc is shown in each image. The brown contours denote the FUV bright regions identified for a threshold flux of 1.07×10^{-18} $erg/sec/cm^2/\mathring{A}$. The numbers shown in blue and black respectively signify the ID for holes and identified regions as given in Table 5.2.

FUV emission inside them. We also noticed FUV emission in region between Hole 21, 22 and 24. This is an example where star formation is possibly triggered due to expansion/collision of multiple holes.

We further checked the Hα counter part for each FUV region from the catalogue of Miller & Hodge (1994). In case there is a cross-match, we mentioned the ID number of the Hα emitting region (from their catalogue) for the corresponding FUV region in parenthesis in Table 5.2. We noticed 65 (15.5% of total) out of 120 regions identified in the shell to have Hα emission also. The detection of Hα emission signifies a recent star forming activity in these regions. Therefore, these are the most possible sites where star formation has been triggered recently due to expanding H I holes. We found 16 out of 53 regions present inside the holes to have Hα detection. These 16 regions therefore have recent star formation and hence it is more possible that they are actually present in shells, but appears to be located inside holes. The same exercise is also performed for the 252 non-related regions and we noticed 106 of them to have Hα counter part. In Table 5.4, we have extracted the summary of Table 5.2 for different types of hole and the identified FUV regions. We found that the number of holes with emission identified in their shells are 12, 5 and 13 respectively for Type 1, Type 2 and Type 3 holes respectively. Among the 15 holes with emission inside, we found 9 of Type 3, 4 of Type 1 and 2 of Type 2. It is noticed that 23 out of 30 holes, which show FUV emission in their shell, also have $H\alpha$ emission. Therefore, 47.9% of the holes show positive signature of triggered star formation in their shell. We did not find any significant correlation between holes with/without triggered star formation and their ages.

To understand the physical properties of these 419 identified regions, we estimated several parameters and listed in Table 5.5. We estimated the radius (R) in pc and the galactocentric distance (R_{gc}) in kpc for each region. The radius, which is estimated by equating the area of the irregular shaped regions to that of a circle,

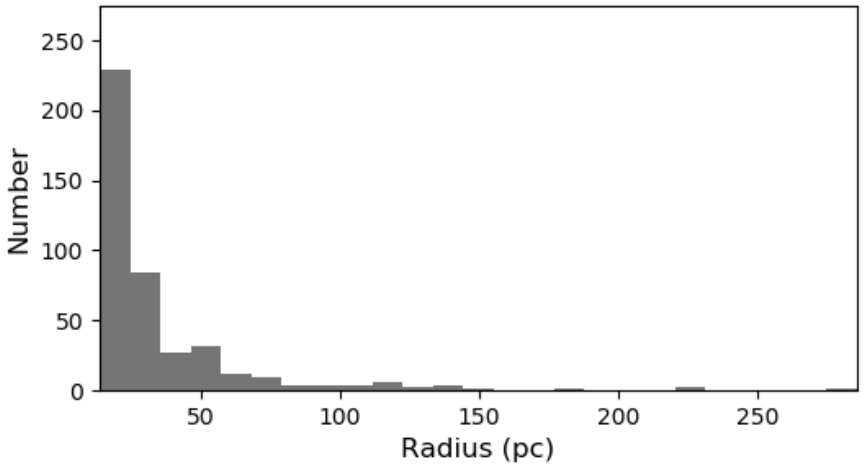

FIGURE 5.7: The histogram of the size of identified parent clumps.

is found to have a range between $\sim$ 15 - 285 pc. 95% of our identified regions have radii smaller than 100 pc. In Figure 5.7, we have plotted one histogram which shows the size of these identified parent clumps. The galactocentric distances are estimated by assuming the galaxy centre, inclination and position angle of IC 2574 from Table 5.1 and using the relation given in section 2.0 of van der Marel & Cioni (2001).

5.3.3.1 Estimation of FUV flux, Luminosity and SFR

The *astrodendro* package also provides area and flux for the identified regions. Considering these two, we measured the background and extinction corrected FUV flux ($erg/sec/cm^2/\mathring{A}$) for the regions. The background flux is estimated from the average flux measured in four different circular regions of radius 1 arcmin present in the galaxy field. We choose the radius to be 1 arcmin as it is around 145 pixels in the image and thus covers a good area for estimating the average background. The circle of 1 arcmin radius also fits well in the space between the edge of the detector and the extent of the galaxy. The corrected fluxes are used to estimate luminosity density ($erg/sec/pc^2$) and SFR density ($M_\odot/yr/kpc^2$) corresponding

to each region. We used the relation given by Karachentsev & Kaisina (2013a) for estimating the SFR from the measured FUV magnitude. The relation is given in equation 7.4, where mag_{FUV} is the apparent FUV magnitude (AB system) and D is the distance to the galaxy in Mpc. The measured value of SFR density shows a range between 0.0238 - 0.5409 $M_{\odot}/yr/kpc^2$ which highlights the diversity of star forming regions in the galaxy.

$$log(SFR_{FUV}(M_{\odot}/yr)) = 2.78 - 0.4 * mag_{FUV} + 2log(D) \tag{5.1}$$

5.3.3.2 Estimation of H I density

As the estimated values of SFR density show a wide range, it will be interesting to correlate it with the average H I column density of these regions. In Figure 5.8, we have shown the H I column density map of the galaxy from Walter et al. (2008) along with 419 FUV bright regions (blue circles). These circles are plotted for the equivalent area of each identified region. The red contours signify regions with H I column density greater than $10^{21} cm^{-2}$. The identified star forming regions are mostly found to be present in locations with dense H I gas. We measured the average column density of neutral hydrogen for the FUV bright regions from the moment 0 H I map. In order to convert the image pixel unit JY/B*M/S to column density, we used equation 2.1. The values of b_{maj} and b_{min} for the observation of IC 2574 were 12.81″ and 11.90″ respectively (Walter et al. 2008). The estimated values of column density show a range between 0.11 - 3.83 $\times 10^{21} cm^{-2}$. In Figure 5.9, we have shown the FUV luminosity density and H I column density for all these 419 regions. The average H I column density is found to be more than $10^{21} cm^{-2}$ for 345 ($\sim$ 82.3%) regions. Out of these 345 regions, 241 have values between $10^{21} cm^{-2}$ and $2 \times 10^{21} cm^{-2}$, 95 between $2 \times 10^{21} cm^{-2}$ and $3 \times 10^{21} cm^{-2}$ and 9 with value greater than $3 \times 10^{21} cm^{-2}$. The rest 74 regions ($\sim$ 17.7%)

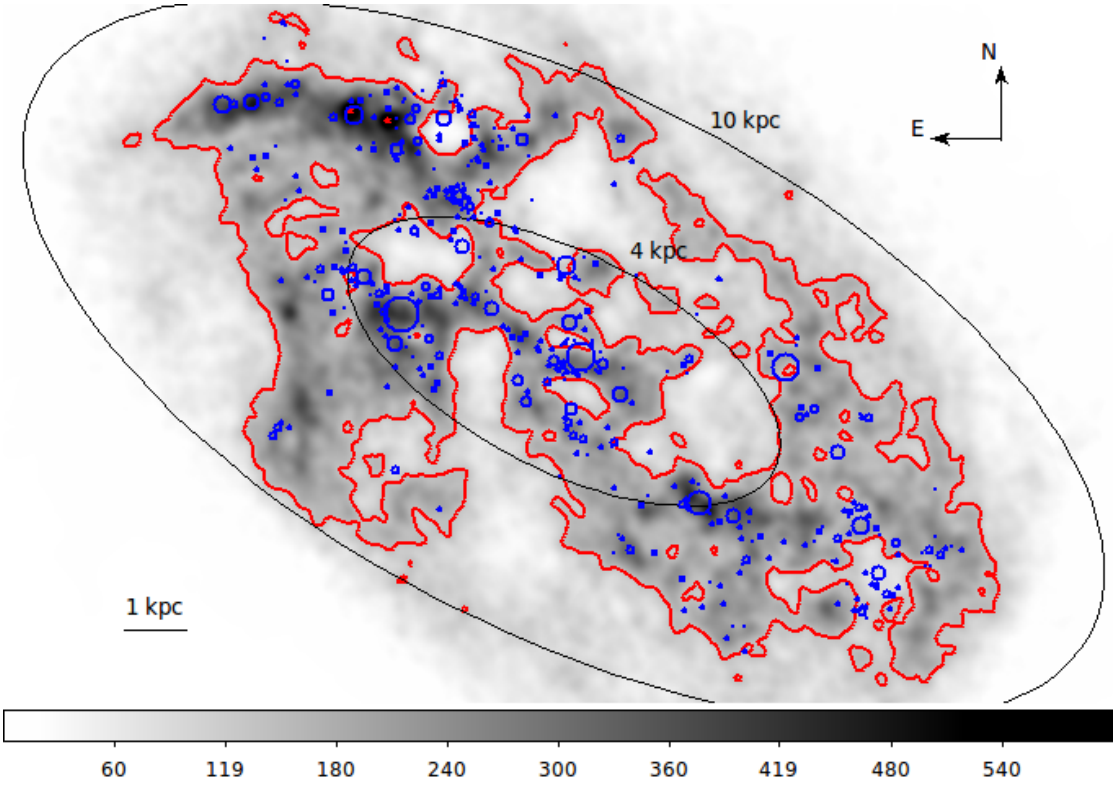

FIGURE 5.8: The background image is H I moment 0 map of IC 2574. The grey scale signifies flux in JY/B*M/S. The red contours signify regions having H I column density more than $10^{21} cm^{-2}$. The identified FUV bright star forming regions are shown as blue circles.

show column density less than $10^{21} cm^{-2}$. The estimated value of the H I column density will differ slightly from the actual value due to the circular approximation of the regions. Similarly for FUV surface luminosity density, we found 347 regions ($\sim$ 82.8%) to have value between 10^{35} and 2×10^{35} $erg/sec/pc^2$ and 72 regions ($\sim$ 17.2%) have value more than 2×10^{35} $erg/sec/pc^2$ with 11 of them brighter than 10×10^{35} $erg/sec/pc^2$.

5.3.4 Structure of star forming regions

Since the structure of star forming regions in galaxies is known to be hierarchical in nature (Elmegreen et al. 2000), we further explored the structural characteristics

TABLE 5.2: Connection between FUV bright star forming regions and the H I holes. This table helps to capture the location of the FUV bright regions with respect to the H I holes. In the second column we listed the regions present in the shell. The regions present inside each hole are shown in column 3. Each region number signifies its ID, listed in Table 5.5. The numbers given within parentheses are the ID of Hα cross-identified region from the catalogue of Miller & Hodge (1994). The age of each hole and their types are given in columns 4 and 5 respectively from Walter & Brinks (1999).

Hole	Region in shell	Region inside hole	Age of hole (Myr)[a]	Hole type[a]
1	–	–	19.6	3
2	–	–	31.3	3
3	22,27,33,43(3),44,55,57(5),58(9)	28,35,37,38,40(6),42, 46,47,52(4)	29	3
4	123(24)	–	42.5	2
5	–	–	43.5	3
6	–	–	20.6	3
7	36(18),45,53,59(16),69,70,74(22),79(42)	54,64,66	–	1
8	–	124(32,34,36,38,39,40,41,44)	12.2	3
9	–	–	30.2	3
10	–	–	–	1
11	–	–	44.1	3
12	–	–	–	1
13	99(57,58,60,63),102,112(61),114, 117(30,33),119,120,124(32,34,36,38,39, 40,41,44),133(45),141,148(66), 149(64),150	–	–	1
14	–	–	–	1
15	93	–	58.7	3
16	116	–	20.6	3
17	–	–	18.1	3
18	–	122	19.9	3
19	281	–	14.7	3
20	199(92)	–	–	1
21	143(80,83,84),154(78),161(94,96, 102,104),162,169	157(89),158(87,90),160(89)	17	3
22	151(103),159,162,164,167,168,170,172, 174(107),175,176	163	28.9	3

[a] From the study of Walter & Brinks (1999)

TABLE 5.3: Table5.2 continued

Hole	Region in shell	Region inside hole	Age of hole (Myr)[a]	Hole type[a]
23	232,235(109),241(109),330	269,287	–	1
24	161(94,96,102,104)	187,189,190,193	–	1
25	–	–	30.1	3
26	–	–	–	1
27	231,249	–	–	1
28	171(115)	177(121),181(121)	23.5	3
29	343(118),356(128),358(128)	346,349,354	18	3
30	177(121),181(121),198(120),202(119), 205,209(124),211(173),213	–	–	1
31	1(133),2(134)	–	–	1
32	266(136),291(165)	271(143,155),288(155)	12.7	3
33	303(144),308,310(151),311,313(144), 314,323,335,340(186),344,348,350,360	318(150),319,320(150),322, 327,328,329,333,334,337, 338,341,355(178)	16.3	2
34	319,327,328	–	13.1	3
35	7(137),8(137),9(138),10(138),14(192), 15(194),16(198,202),17(167),364,365	5(148),6(148),12(172),13	14.3	2
36	–	–	21.1	3
37	386(170),393,396	387,389	–	1
38	226(181),233(193,197,199,203,206, 208,218),234,238	–	–	1
39	263(184),304,306,321	–	–	1
40	3(224)	–	11.7	3
41	156(212)	–	–	1
42	385(235),391(235),403	–	10.8	2
43	–	–	–	2
44	–	–	11.7	3
45	285(236),298,300(241),301,305	286,292,293	30.2	3
46	–	–	19.6	3
47	220	–	9.8	3
48	394	–	17.6	2

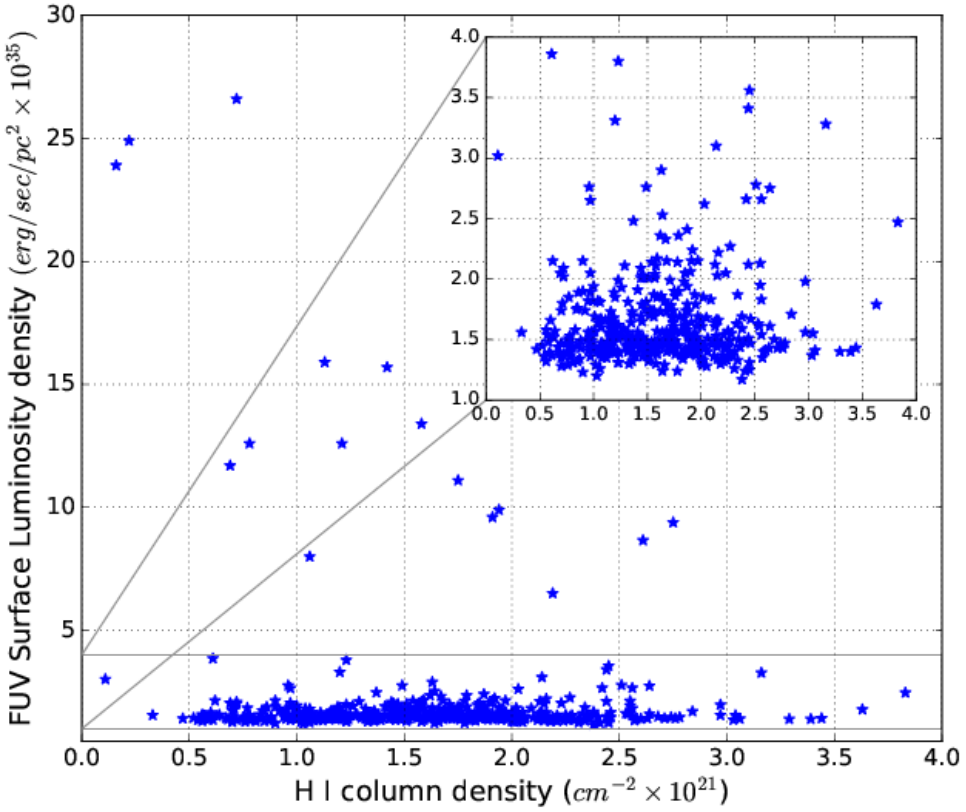

FIGURE 5.9: The measured value of FUV surface luminosity density and H I column density of 419 identified FUV bright regions are shown. The inset shows the zoomed in part for FUV luminosity density between $1-5\times10^{35}$ $erg/sec/pc^2$.

of identified star forming regions as a function of varying flux level. We selected 9 relatively larger parent structures from the list of our identified regions (Section 5.3.3) and shown them in Figure 5.10. Among these, we have also included the largest parent structure (top panel of the figure) identified in the north-eastern part of the galaxy. Each of these parent structure contains multiple sub-structures of different size and flux level inside them. In order to explore the characteristics of sub-structures we have shown dendrogram for each region in the same figure. The definition and details of the algorithm are presented in Section 3.3.3. Each tree present in Figure 5.10 signifies a parent structure whereas the leaves connected to that tree represent child structures present within the parent structure. The selected regions have different significance as per their location in the galaxy.

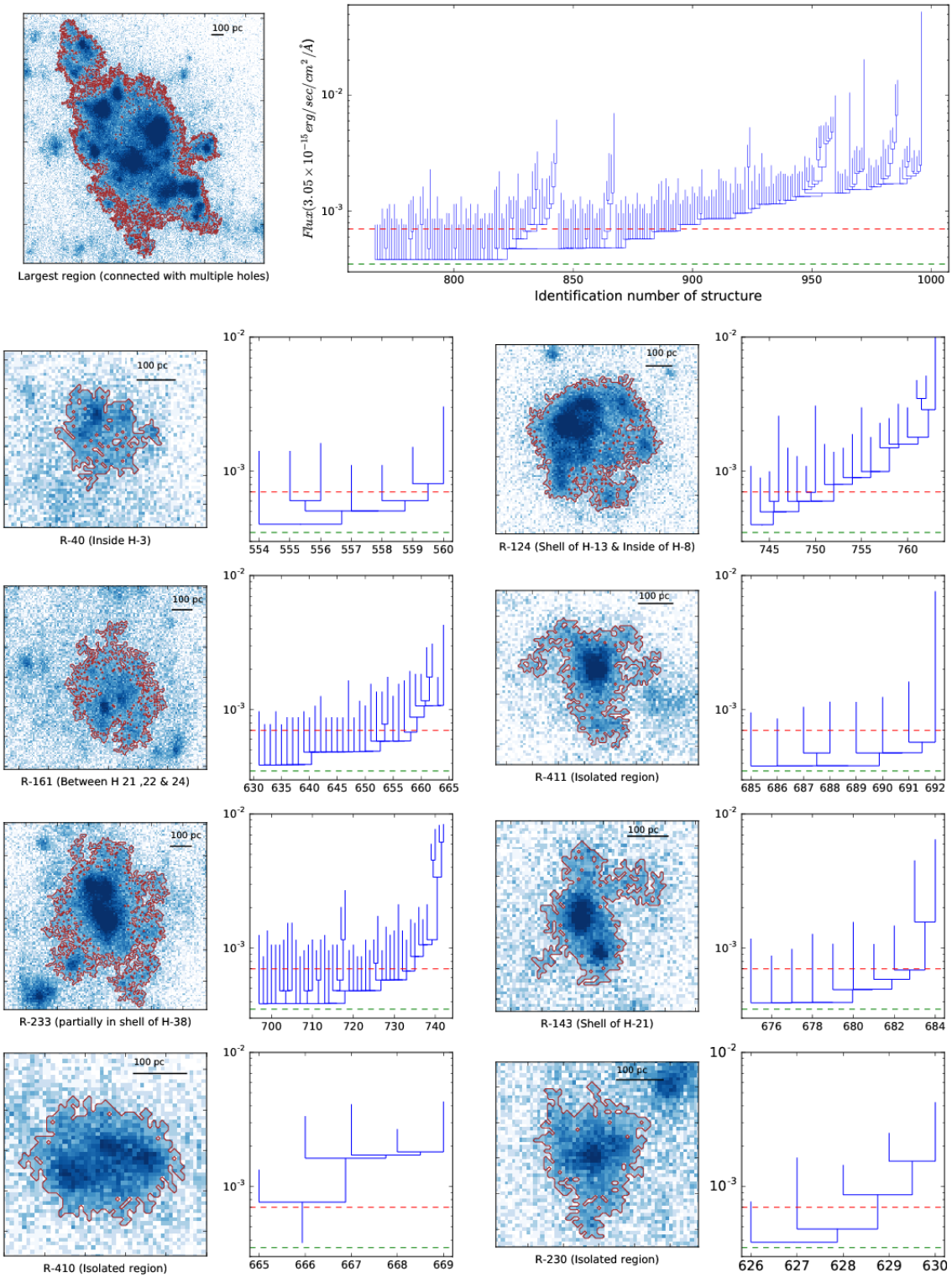

FIGURE 5.10: The figure shows 9 selected parent structures, along with their dendrograms, identified for a threshold flux $1.07 \times 10^{-18} erg/sec/cm^2/\AA$ (green dashed line). The red dashed lines represent flux value of $2.14 \times 10^{-18} erg/sec/cm^2/\AA$. The largest parent structure and its dendrogram are shown in the upper panel of the figure. A length scale of 100 pc is shown for each region in solid black line. The Y axis of dendrogram shows the flux in terms of counts per second while the X axis denotes unique identification number of each structure which is not related to their ID presented in the paper.

TABLE 5.4: Summary of Table 5.2. Column 2 shows the total number for holes (along with three different types) and identified regions. Columns 3 and 4 respectively show the number of holes with FUV emission in shell and inside it. Column 5 lists the number of holes with no related FUV emission. The bottom row of the table denotes the similar statistics with respect to the identified regions. The numbers shown in parenthesis denote the numbers after cross-match with Hα emission.

Hole	Total number	FUV emission in shell	FUV emission inside hole	With no related FUV emission
Total hole	48	30(23)	15(7)	16
Type 1 hole	16	12(11)	4(0)	4
Type 2 hole	6	5(4)	2(2)	1
Type 3 hole	26	13(8)	9(5)	11
	Total number	Present in shell	Present inside hole	Not related with hole
FUV Region	419	120(65)	53(15)	252(106)

They are located either in shell, inside hole, in between multiple holes or away from any hole. The idea is to check the structural nature of star forming regions located in different environments of the galaxy. In the dendrograms, the y axis denotes the FUV flux level of each sub-structure. The dendrogram of the largest parent structure (top panel of the Figure 5.10), which is distinctly different from the rest, shows many leaves with different flux levels. The brightest star forming knots present in the galaxy are actually part of this large region. In case of other parent structures which are much smaller than this large region, we noticed similar nature of dendrogram with much reduced number of leaves, but with different flux levels. The brighter star forming clumps (sub-structure) identified throughout the galaxy are found to be present inside such large complexes (parent structure). Therefore, irrespective of location, the larger star forming complexes have multiple sub-structures inside them.

TABLE 5.5: Properties of FUV bright star forming regions as defined in Figure 5.6. The full table containing all 419 regions is available in electronic format.

Region	RA (J2000) (hh:mm:ss.s)	DEC (J2000) (dd:mm:ss.s)	Radius (pc)	R^a_{gc} (kpc)	Flux[b]	Luminosity density[c]	SFR [d]	Average HI column density[e]
1	10:28:37.1	+68:27:57.1	22.2	5.64	1.70	9.39	0.1910	2.75
2	10:28:37.2	+68:28:1.9	27.4	5.79	2.38	8.66	0.1762	2.61
3	10:28:53.0	+68:28:35.1	29.6	6.25	2.10	6.51	0.1324	2.19
4	10:28:53.4	+68:28:49.8	33.9	6.67	4.70	11.13	0.2263	1.75
5	10:28:40.5	+68:28:1.0	22.6	5.58	2.37	12.61	0.2564	0.78
6	10:28:40.1	+68:28:3.6	25.3	5.69	2.76	11.73	0.2386	0.69
7	10:28:38.8	+68:28:6.7	17.1	5.86	1.35	12.56	0.2554	1.21
8	10:28:38.3	+68:28:6.7	19.1	5.89	1.80	13.41	0.2727	1.58
9	10:28:38.5	+68:28:8.9	14.8	5.95	1.27	15.73	0.3199	1.42
10	10:28:38.9	+68:28:9.4	16.6	5.94	1.60	15.92	0.3238	1.13
11	10:28:39.0	+68:28:30.3	44.9	6.63	5.91	8.00	0.1627	1.06
12	10:28:44.5	+68:28:10.4	24.9	5.72	5.46	23.93	0.4868	0.16
13	10:28:44.4	+68:28:7.0	30.5	5.62	8.52	24.88	0.5061	0.22
14	10:28:48.1	+68:28:4.2	66.9	5.43	15.79	9.60	0.1953	1.91
15	10:28:48.6	+68:28:35.0	66.0	6.35	15.82	9.90	0.2014	1.94
16	10:28:49.2	+68:28:25.0	87.6	6.03	46.57	16.52	0.3361	2.19
17	10:28:43.8	+68:28:26.3	121.2	6.25	143.31	26.59	0.5409	0.72
18	10:27:21.8	+68:18:43.5	32.0	9.79	1.14	3.02	0.0615	0.11
19	10:27:28.7	+68:20:56.3	29.6	6.97	0.52	1.63	0.0331	1.15
20	10:27:32.8	+68:20:48.6	18.6	6.81	0.22	1.76	0.0359	0.85

[a] Galactocentric distance

[b] Total FUV flux in $erg/sec/cm^2/\mathring{A}$ $\times 10^{-15}$

[c] FUV Luminosity in $erg/sec/pc^2$ $\times 10^{35}$.

[d] SFR is in $M_\odot/yr/kpc^2$.

[e] Density is in $cm^{-2} \times 10^{21}$

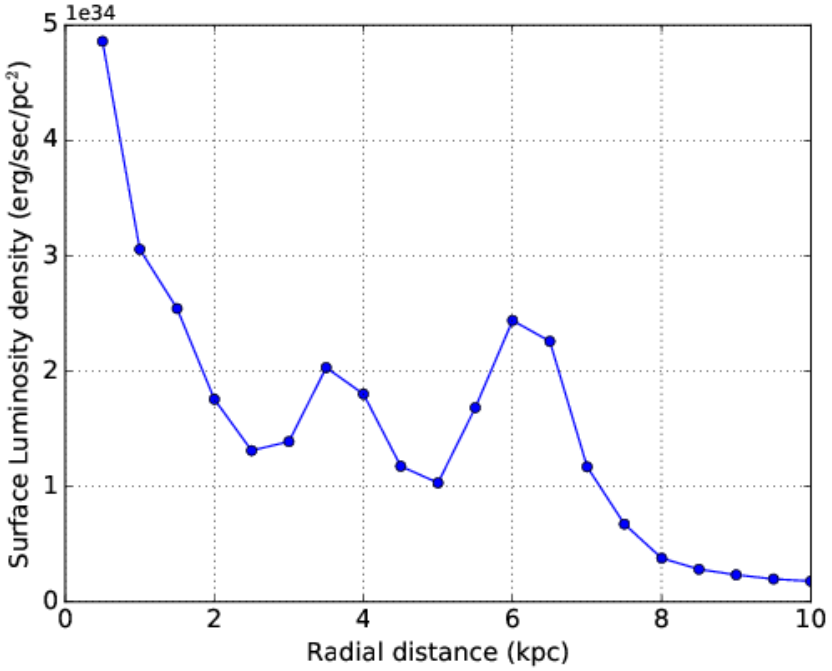

FIGURE 5.11: The radial surface luminosity density ($erg/sec/pc^2$) profile of the galaxy.

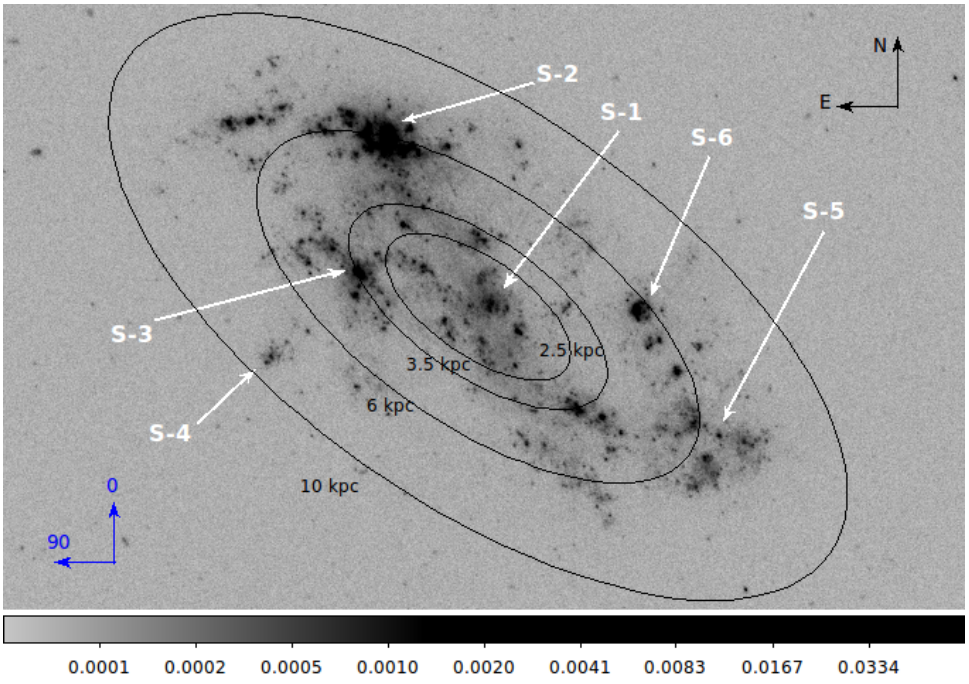

FIGURE 5.12: The FUV image of the galaxy IC 2574. The regions highlighted as S1, S2, S3, S4, S5 and S6 are the active star forming regions of the galaxy.

5.3.5 FUV Luminosity density profile of IC 2574

The H I holes and the bright star forming regions both have a scattered distribution in the galaxy IC 2574. We also noticed the presence of active star formation from inner to far outer part of the galaxy. In order to understand the overall FUV emission profile of the galaxy as a function of galactocentric distance, we plotted radial surface luminosity density ($erg/sec/pc^2$) profile in Figure 5.11. We estimated galactocentric distance to each of the pixel of the FUV image similarly as explained in section 5.3.3. Starting from the galaxy centre, we considered annulus of width 0.5 kpc up to a radius 10 kpc and estimated total flux in each individual annuli. The measured fluxes are then corrected for background and extinction. The background is estimated from an annuli between radius 12 kpc and 13 kpc whereas extinction correction is done similarly as discussed in Section 5.2. The corrected fluxes ($erg/sec/cm^2/\mathring{A}$) are converted to luminosity (erg/sec) by adopting a distance to the galaxy as 3.79 Mpc (Dalcanton et al. 2009) and bandwidth of F148W filter as 500 $\mathring{A}$ (Table 5.1 & 2.2). Then the estimated luminosity values are divided by the area of each individual annuli to calculate surface luminosity density ($erg/sec/pc^2$) at that particular radius and shown in Figure 5.11.

To understand the characteristics of luminosity density profile, we have shown the FUV image of IC 2574 and highlighted the location of six bright star forming regions of the galaxy as S1, S2, S3, S4, S5 and S6 in Figure 5.12. The radial profile shows an exponential decrease up to a radius 2.5 kpc with a central peak which is due to the star forming region S1. Beyond 2.5 kpc, we noticed two peaks, one at 3.5 kpc and another at 6 kpc from the galaxy centre. Emission from the region S3 has major contribution for the peak seen at 3.5 kpc, whereas the peak at 6 kpc is mainly due to S2, the brightest star forming region of the galaxy. The nature of the radial luminosity density profile signifies the presence of active star formation in the outer part of the galaxy also.

TABLE 5.6: Starburst99 model parameters

Parameter	Value
Star formation	Instantaneous
Stellar IMF	Kroupa (1.3, 2.3)
Stellar mass limit	0.1, 0.5, 120 $M_{\odot}$
Total cluster mass	$10^3 M_{\odot}$-$10^6 M_{\odot}$
Stellar evolution track	Geneva (high mass loss)
Metallicity	Z=0.004
Age	10 Myr

We also estimated the background and extinction corrected total flux of the galaxy in F148W filter for a radius of 10 kpc and the value is $3.3{\times}10^{-12}$ $erg/sec/cm^2/\mathring{A}$. The corresponding F148W magnitude and the total SFR (estimated using the relation of Karachentsev & Kaisina (2013a)) of the galaxy are estimated to be 10.45 mag and 0.57 $M_{\odot}/yr$ respectively. It is to be noted that if we use different relations for estimating SFR from the measured FUV flux, we get different values. For example, the relation provided by Murphy et al. (2011) and Hunter et al. (2010) results in a SFR of 0.12 and 0.18 $M_{\odot}/yr$ respectively for the same estimated flux of the galaxy IC 2574.

5.3.6 Remnant cluster of Super Giant Shell

Among the 48 identified shells, there are multiple SGSs present in the galaxy IC 2574 (Walter & Brinks 1999). One of the present SGSs (shell 35 as per Walter & Brinks (1999), Figure 5.2), is studied extensively in literature due to its prominent multi-wavelength characteristics.

In Figure 5.13, we showed the UVIT FUV image of this SGS 35. The presence of remnant cluster as well as star forming regions along the rim are clearly noticed

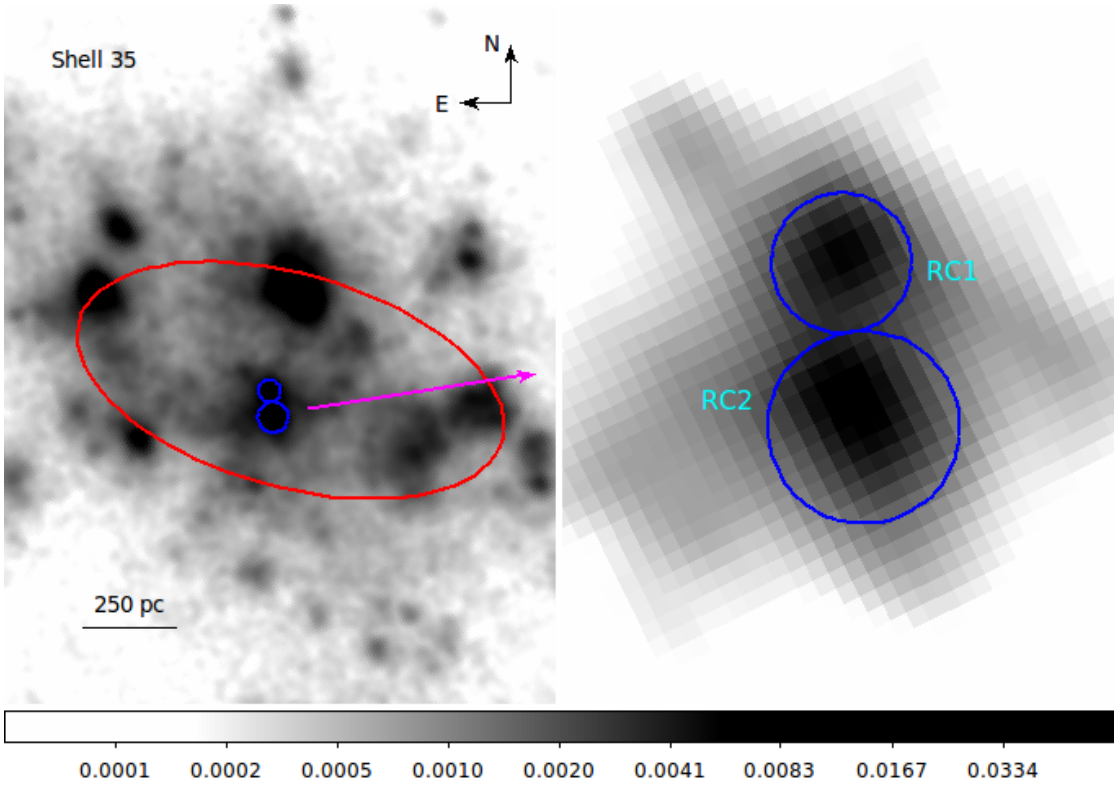

FIGURE 5.13: The FUV image of H I shell 35 (red ellipse) along with the remnant cluster (blue circle) is shown in the left. The zoomed in view of the cluster is shown in right where two resolved components are clearly noticed.

TABLE 5.7: Properties of the remnant cluster

Component	Radius (pc)	FUV Flux (10^{-15} $erg/sec/cm^2/\AA$)	Mass ($10^4 M_\odot$)
RC1	30.3	7.1	4.9
RC2	41.7	13.2	7.3

in the image. With the spatial resolution of UVIT, we identified two resolved components of the remnant cluster (RC1 and RC2 in Figure 5.13) which were not detected earlier by both UIT and GALEX. The individual components are shown in the figure by blue circular apertures. In order to study the remnant cluster, we estimated the background and extinction corrected FUV fluxes for both the components shown in right panel of Figure 5.13. Stewart & Walter (2000) estimated the age and mass of the central cluster and the reported values are 11 Myr and 14.2×10^4 $M_\odot$ respectively. Assuming the age to be 10 Myr, we also estimated the masses for both the components with the help of starburst99 SSP (Leitherer et al. 1999) model. We adopted the method explained in Section 3.2.1 for the mass estimation. The model parameters assumed for this estimation are listed in Table 6.2. All the measured parameters of the cluster are listed in Table 5.7. The added mass of both the components is $12.2\times10^4 M_\odot$ which matches closely with earlier estimate by Stewart & Walter (2000).

5.4 Results and Discussion

Giant H I holes present in some dwarf galaxies represent a prominent feature in their interstellar medium (Egorov et al. (2014) and references therein). The slow solid body-like rotation of the dwarf galaxies and the lack of strong spiral density waves, help in the formation of larger sized and long lived holes in these galaxies. Dwarf galaxies are known to sustain star formation over a very long period. It is thus important to understand how the presence of holes and the sustained star formation go hand in hand in dwarf galaxies. The key aim of this study is to identify young star forming regions in the galaxy IC 2574 and further explore their connection with the H I holes. In order to do that we used deep FUV observations of the galaxy with UVIT F148W filter. A 28′ field of view of

the telescope along with a pixel scale of 0.4″ has helped us to image the whole galaxy with finer details.

In this study, the extinction correction of the FUV data has been performed by assuming an SMC type extinction law for the whole galaxy. It is possible to have a spatial variation in the nature of extinction within the galaxy. Therefore, the values of our estimated parameters, such as FUV flux, luminosity density and SFR will change accordingly.

We noticed a good spatial correlation between the FUV emission and the H I column density throughout the galaxy. The FUV bright regions of the galaxy are mostly found to have H I column density more than $10^{21} cm^{-2}$, which is the reported threshold value for star formation in IC 2574. This signifies star formation, in this gas-rich dwarf galaxy, is mainly happening in regions which have higher gas density. We also noticed some active regions to have H I column density less than $10^{21} cm^{-2}$. As the FUV emission in some of these regions is high, it is possible that the recent star formation has used up or ionised the neutral gas there. It is also possible that a few of these regions are not part of the galaxy and probably some background sources.

We identified 419 star forming regions in the galaxy by fixing the threshold flux as 1.07×10^{-18} $erg/sec/cm^2/\mathring{A}$ (10 times average background flux) and minimum number of pixel to define a region as 10. A threshold flux lower than the selected value will result in identifying more number of regions and also the same regions with a little bigger size. In case of a higher threshold flux, the identified regions will be less in number and smaller in size. In order to keep a balance, we fixed an intermediate value for our analysis. The value of minimum number of pixel for identifying the regions will decide the minimum size of the region we want to detect. The value we adopted for our analysis can detect star forming clumps smallest up to radius $\sim$ 15 pc. The number of identified regions will increase with

decreasing value of the minimum number of pixel and the vice versa. We fixed the value as 10 to identify small star forming clumps and also to avoid detecting very small regions which may not be part of the galaxy.

The nature of star formation shows broad characteristic variation for different dwarf galaxies. Both the external environment and internal feedback play dominant role in regulating star formation in dwarfs. Our study highlights that the expanding H I holes have a major impact in triggering secondary star formation in some part of the galaxy. H I holes are mainly created due to the combined effect of stellar winds and supernova explosions on to the ISM of a galaxy (Tenorio-Tagle & Bodenheimer 1988). Tenorio-Tagle et al. (2005) concluded that the massive and compact super star clusters contribute a positive feedback for triggering further star formation around them. We find that star formation could be started either due to scooping of material by an expanding H I shell and/or collision and compression of matter due to collision of multiple shells. We found that out of 48 holes, 30 show FUV emission in their shells, 15 holes have emission inside and 16 holes do not have any related FUV emission. This denotes that more than half of the holes (30/48) have active star formation in their shells, whereas 16/48 holes do not show any triggered star formation. Our study finds that 28.6% of the identified star forming regions are located in shells while 12.6% are present inside. We also found 60.1% of the regions to be present away from holes and are not related. These numbers are estimated on the basis of our adopted shell width as R/3. The width of the shell can actually be different from our assumed value. This can slightly alter our estimated numbers for each individual holes.

In order to identify the star forming regions younger than 10 Myr we checked for their Hα counter parts. It turns out that 65 of 120 regions present in the shell show both FUV and Hα emission. In other words, 23 holes show both Hα and FUV emission in their shells. Therefore, $\sim$ 48% holes show signature of recently triggered star formation. As per the estimation of Walter & Brinks (1999), these

holes cover an age range of $\sim$ 10 - 40 Myr. If star formation is triggered in some region due the expansion of a hole, then that has to be younger than the age of the hole. As the regions with both FUV and Hα emission are likely to be younger than 10 Myr, the detection of these regions in the shell signify that star formation has been triggered there due to the expansion of holes. The regions present in the shells with only FUV emission may be a little older and hence do not show Hα emission. Among 252 regions, which are not related with the holes, 106 found to have Hα emission also. This means 60.1% of the identified regions in the galaxy are undergoing star formation triggered due to other mechanisms with 25.3% experiencing most recent trigger. Therefore, expansion or collision of H I holes is not the only mechanism to cause recent enhancement of star formation in the galaxy. The cross-identification of Hα emission is done from the available catalogue of Miller & Hodge (1994). The Hα observations have $\sim$ 4 times shallower exposure than that in FUV. In the case of some FUV bright regions, there can be faint Hα emissions which are not detected in this Hα image. Hence, we expect a few more cross-detection with much deeper Hα image. That can slightly change the statistics of our results.

The radius of the identified regions cover a range between 15 - 285 pc, with 95% of them to be smaller than 100 pc. The larger regions are the big parent complexes with smaller sub-structures of size 15 - 100 pc inside. As these clumps are bright in FUV, it is possible that some of them are OB associations. The sizes of OB associations cover a range between 10 - 100 pc for the Milky way and other nearby spiral and dwarf galaxies (Mel'Nik & Efremov 1995; Bresolin et al. 1996; Ivanov 1996; Bresolin et al. 1998; Bastian et al. 2007). Therefore, the galaxy IC 2574 have produced OB associations which are similar in size with those of other nearby galaxies. In order to characterise the star forming regions, we measured their FUV surface luminosity density and the average H I column density. We noticed a clear variation in the properties of these regions across the galaxy. Some regions show very high FUV luminosity with less H I density, signifying vigorous

recent star formation. Majority of the regions have moderate FUV luminosity with H I density above the threshold, whereas we also do notice regions with very high H I density and moderate FUV luminosity. These altogether indicate that the galaxy IC 2574 has a variable star forming environment throughout it.

As it has been suggested that the nature of star forming region is hierarchical from smaller scale to larger scale (Elmegreen et al. 2000; Efremov 1995), we also explored the structural characteristics of star forming regions in the galaxy IC 2574. We noticed that majority of the large star forming complexes in IC 2574 have several smaller sub-structures of different flux levels. It is further observed that the brighter star forming clumps of the galaxy are mostly present inside larger complexes. By analysing the dendrogram of some selected large regions, we understand that in different flux levels, star forming regions form similar structure of different sizes. This highlights the hierarchical nature of these active regions. As the hierarchy is noticed for regions both related and not related to the holes, we speculate turbulence of the ISM as the primary reason behind this (Elmegreen et al. 2000).

We produced the radial surface luminosity density profile of the galaxy and able to trace FUV emission at least up to a radius 10 kpc. The presence of two major bright star forming regions, at radius 3.5 kpc and 6 kpc, are identified in this radial profile. The brightest star forming region which is located at 6 kpc from the centre of the galaxy signifies that the star formation in IC 2574 is not concentrated only in the inner part of the galaxy. The presence of this active region clearly reveals that star formation in dwarfs can be dominant in any part of the galaxy depending upon a favourable star forming environment. We estimated the total FUV flux of the galaxy within 10 kpc radius and found it to be $3.3{\times}10^{-12}$ $erg/sec/cm^2/\mathring{A}$. The measured SFR of the galaxy is 0.57 $M_{\odot}/yr$, which signifies a relatively active nature of IC 2574.

With the help of UVIT's spatial resolution, we identified two resolved components of the remnant cluster of shell 35. Stewart & Walter (2000) reported the discovery of this remnant cluster (single component) using UIT data and derived its properties. We derived the mass for each of the resolved cores by using starburst99 SSP model. The bigger component (M $\sim 7.3 \times 10^4$ $M_\odot$) is found to be 1.5 times massive than the smaller component (M $\sim 4.9 \times 10^4$ $M_\odot$). The added mass (M $\sim 12.2 \times 10^4$ $M_\odot$) of these components matches well with the mass of the remnant cluster measured earlier by Walter et al. (2008).

5.5 Summary

The main results of this chapter are summarised below

1. We identified 419 FUV bright star forming regions in the galaxy IC 2574 with the help of UVIT FUV imaging data.

2. We estimated several parameters, such as size, FUV flux, surface luminosity density, H I column density, SFR density, galactocentric distance for the identified regions.

3. We found 28.6% of the identified regions to be located in H I shells, 12.6% inside holes and 60.1% away from holes.

4. 30 out of the 48 holes show triggered star formation in their shells with 23 of them having more recent trigger, whereas 16 holes do not show any triggered star formation. We also found 15 holes to have FUV emission inside them, with 12 of those having emission in their shells as well.

5. Star formation in 60.1% of the identified regions in IC 2574 has no connection with the H I holes and hence it is possibly triggered due to other mechanisms.

6. The identified regions have radii between 15 - 285 pc, with 95% of them smaller than 100 pc.

7. 82.3% of the identified FUV bright regions have H I column density more than $10^{21} cm^{-2}$.

8. We found sub-structures of different flux levels and sizes inside the larger star forming complexes across the galaxy. We speculate turbulence as one of the dominant drivers to build this hierarchy.

9. The galaxy is found to have active star formation in the outer part beyond 5 kpc also.

10. We resolved two individual components for the remnant cluster of shell 35 and estimated their masses. The added mass of both the component is $\sim 12.2 \times 10^4\ M_\odot$ with the larger one to be 1.5 times more massive than the smaller one.

11. The star formation rate of the galaxy is found to be $\sim$0.57 $M_\odot/yr$.

Chapter 6

Tracing young star forming clumps in the nearby flocculent spiral galaxy NGC 7793

6.1 Introduction

NGC 7793 is a SA(s)d type flocculent spiral galaxy belonging to the nearby sculptor group (de Vaucouleurs et al. 1991). It is located at a distance of 3.4 Mpc and has two nearby dwarf companions (Zgirski et al. 2017; Koribalski et al. 2018). The galaxy has an absolute B band magnitude of −18.31 with a sub-solar metallicity (Carignan 1985; Van Dyk et al. 2012). The optical radius (R_{25}) of the galaxy is around 4.67′ (∼4.62 kpc) (de Vaucouleurs et al. 1991). The galaxy is reported to have a nuclear star cluster at the centre (Walcher et al. 2006; Kacharov et al. 2018).

Several observational studies have explored the disk properties of the galaxy in various wavebands. Carignan (1985) studied the H I disk of the galaxy and found it to be extended up to 1.5 times the optical diameter of the galaxy. They also noticed the galaxy rotation curve to be declining in nature in the outer part. A recent H I study by Koribalski et al. (2018) traced the H I disk further out, along with a significant wrap in the outer disk. Dicaire et al. (2008) identified signature of Hα emission up to the extent of the H I disk which suggested an ongoing star formation across the galaxy. Apart from these, several studies have been done with HST observations to understand the star formation history, hierarchy of star forming regions and the interplay between young star clusters and giant molecular clouds in this galaxy (Elmegreen et al. 2014; Radburn-Smith et al. 2012; Grasha et al. 2018; Sacchi et al. 2019). These observations cover a wide wavelength range from near-UV to infrared. The results conclude that the disk of NGC 7793 supports a inside-out growth scenario. The outer disk of the galaxy beyond $\sim$ 3 kpc is mostly populated with younger populations which show an abrupt break at radius $\sim$ 5 kpc. Hermanowicz et al. (2013) used GALEX FUV data to identify several star forming regions and compared their FUV flux with that of Hα. Though the disk properties of NGC 7793 have been explored in different wavebands, a detail study has not been done by combining the data from FUV and NUV band together, which has the potential of age-dating the stellar population.

In this chapter, we primarily aim to identify young star forming regions throughout the galaxy using FUV and NUV broad band observations from the UVIT (Image - Figure 6.1). We used starburst99 SSP models to characterise the properties of identified clumps in terms of their age and mass. We explored the spatial distribution of these clumps as a function of age and mass. The details of this study are presented in this chapter.

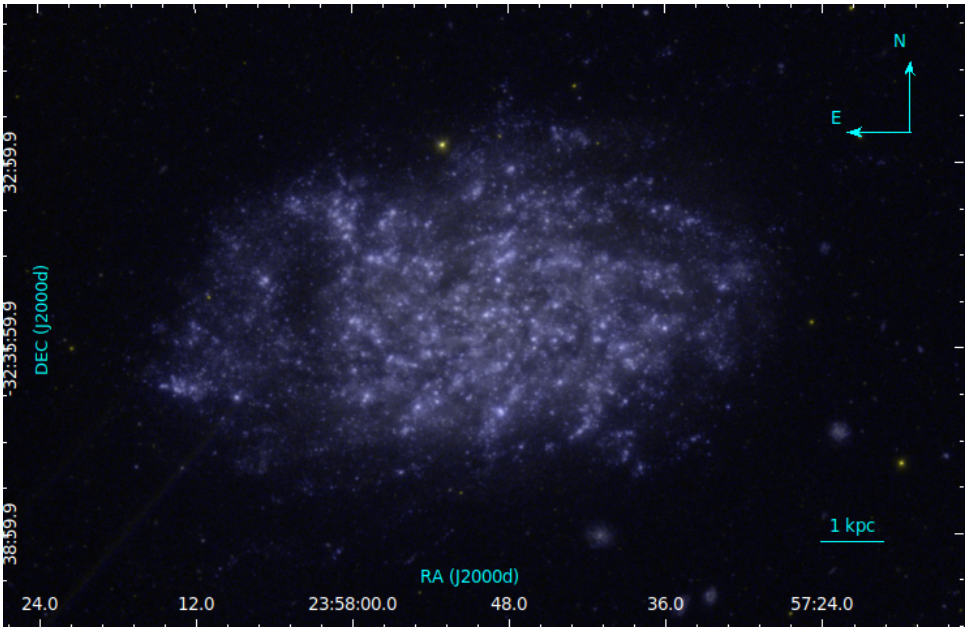

FIGURE 6.1: False colour composite image of the galaxy NGC 7793. The galaxy is observed in two UVIT filters F148W and N242W which are represented by blue and yellow colours respectively.

TABLE 6.1: Properties of NGC 7793

Property	Value	Reference
Morphological type	SA(s)d	de Vaucouleurs et al. (1991)
RA	23 57 49.7	Skrutskie et al. (2006)
DEC	-32 35 27.6	Skrutskie et al. (2006)
Distance	3.4 Mpc	Zgirski et al. (2017)
R_{25}	4.62 kpc	de Vaucouleurs et al. (1991)
Metallicity (Z)	$0.6Z_{\odot}$	Van Dyk et al. (2012)
Inclination	53.7°	Carignan (1985)
PA of major axis	279.3°	Carignan (1985)

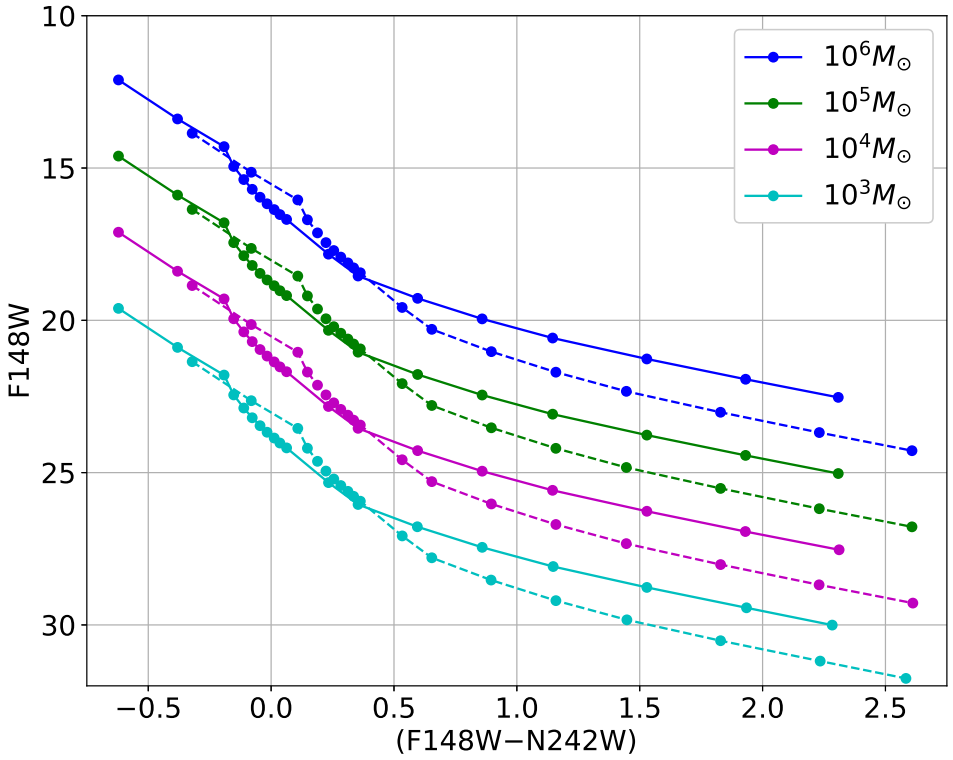

FIGURE 6.2: The Figure shows F148W vs (F148W−N242W) colour-magnitude plot, simulated with the data from starburst99 SSP model. Different curves (continuous line) signify four different total cluster masses ($10^6 M_\odot$, $10^5 M_\odot$, $10^4 M_\odot$, $10^3 M_\odot$). The dashed lines are plotted by considering the extinction and reddening of the galaxy. The points shown in each curve are for different ages starting from 1 Myr to 900 Myr (increasing along the colour axis) with age interval 10 Myr for 1 to 100 Myr range and 100 Myr for 100 to 900 Myr. The values of model input parameters are listed in Table 6.2.

6.2 Theoretical models

In order to characterise the star forming regions in the galaxy NGC 7793, we used starburst99 SSP model, explained in Chapter 3. We exploited starburst99 model data and produced Figure 6.2 to estimate the age and mass of the identified star forming clumps in the galaxy. The method to simulate this figure is demonstrated in Chapter 3. The adopted values of model parameters are listed in Table 6.2. The metallicity is assumed to be 0.006, which is closest to that reported by Van

TABLE 6.2: Starburst99 model parameters

Parameter	Value
Star formation	Instantaneous
Stellar IMF	Kroupa (1.3, 2.3)
Stellar mass limit	0.1, 0.5, 120 $M_{\odot}$
Total cluster mass	$10^3 M_{\odot}$-$10^6 M_{\odot}$
Stellar evolution track	Geneva (high mass loss)
Metallicity	Z=0.006
Age range	1-900 Myr

Dyk et al. (2012), among the available model values.

6.3 Extinction in UV

The importance of extinction in ultra-violet has already been discussed in Chapter 4. In a similar approach, we addressed the effect of extinction in NGC 7793 also. In order to estimate the extinction value in observed UVIT filters, we adopted the value of $E(B-V) = 0.179$ from the study of Bibby & Crowther (2010). As the metallicity of the galaxy is similar to that of LMC, we assumed the extinction law to be average LMC type as modelled by Gordon et al. (2003). We used the extinction law calculator of McCall (2004) supplied in NED to estimate the value of extinction coefficients (R_{λ}) in F148W and N242W bands of UVIT. The values of R_{F148W} and R_{N242W} are found to be 9.78 and 8.12 respectively. Using the value of R_{λ} and $E(B-V)$ in equation 4.1, we estimated the values of extinction (A_{λ}) in both the bands. The values of A_{F148W} and A_{N242W} are found to be 1.75 mag and 1.45 mag respectively. We used these values to correct the observed flux values in our study.

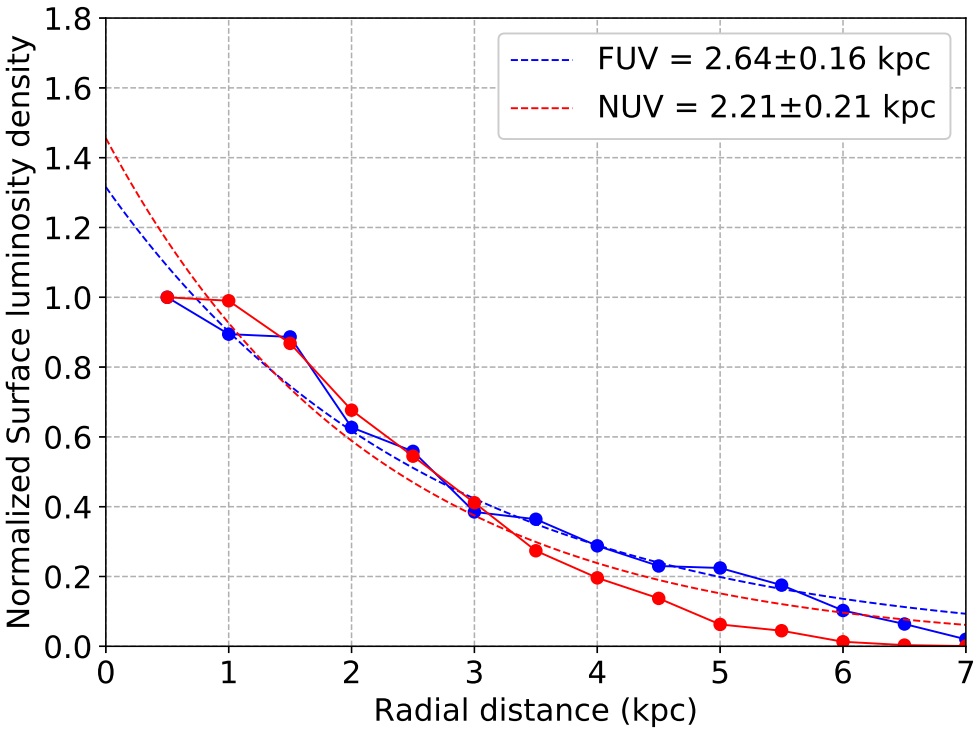

FIGURE 6.3: The FUV and NUV radial luminosity density profiles of NGC 7793 are respectively shown in solid blue and red lines. Each profile is normalised with respect to the maximum of the respective curve. The dashed lines are the exponential fits for each observed profiles. The values of the estimated disk scale-length in FUV and NUV are 2.64±0.16 kpc and 2.21±0.21 kpc respectively.

6.4 Data and Analysis

In this study, we primarily used UV data observed in two broad band filters F148W and N242W of UVIT. The colour composite UVIT image of the galaxy is shown in Figure 6.1. The observation details are given in Chapter 3. We have also used H I moment 0 map of the galaxy from VLA observations (Walter et al. 2008).

6.4.1 UV disk profile of NGC 7793

The FUV and NUV emission in a galaxy primarily trace stellar population of age up to 100 and 200 Myr respectively (Kennicutt & Evans 2012). In order to understand the characteristics of UV emission in the galaxy NGC 7793, we produced radial luminosity density profiles in both FUV and NUV. The nature of these profiles are expected to highlight the distribution of younger star forming regions across the galaxy. We assumed the distance, galaxy centre, inclination and position angle of the galaxy from Table 6.1 and used the equation given in section 2 of van der Marel & Cioni (2001) to estimate galactocentric distance in kpc for each image pixel. Starting from the galaxy centre, we considered concentric annuli of width 0.5 kpc and estimated the value of luminosity density in each annulus from the measured flux. We normalised the measured luminosity values with respect to the maximum of respective curve and plotted the profiles for both FUV and NUV in Figure 7.11. Both the profiles show exponential nature.

In order to estimate the disk parameters, we fitted exponential curves to these observed profiles and estimated the values of disk-scale length (R_d) in FUV and NUV. The values of R_d are found to be 2.64±0.16 kpc and 2.21±0.21 kpc respectively in FUV and NUV. The optical disk scale-length of the galaxy is reported to be 1.08 kpc by Carignan (1985). This signifies that the disk of NGC 7793 is more extended towards shorter wavelengths. We noticed both the observed profiles in Figure 7.11 to follow each other up to radius 3 kpc. Beyond this, the FUV luminosity dominates over the NUV in the outer disk. These together signify that the stellar populations in the outer disk beyond 3 kpc are mostly younger. Our result satisfies the similar profiles derived from the HST observations by Radburn-Smith et al. (2012). We further noticed that the observed FUV luminosity density profile has a break at a radius around 5 kpc, which is also noticed in Figure 6 of Radburn-Smith et al. (2012) for the younger populations.

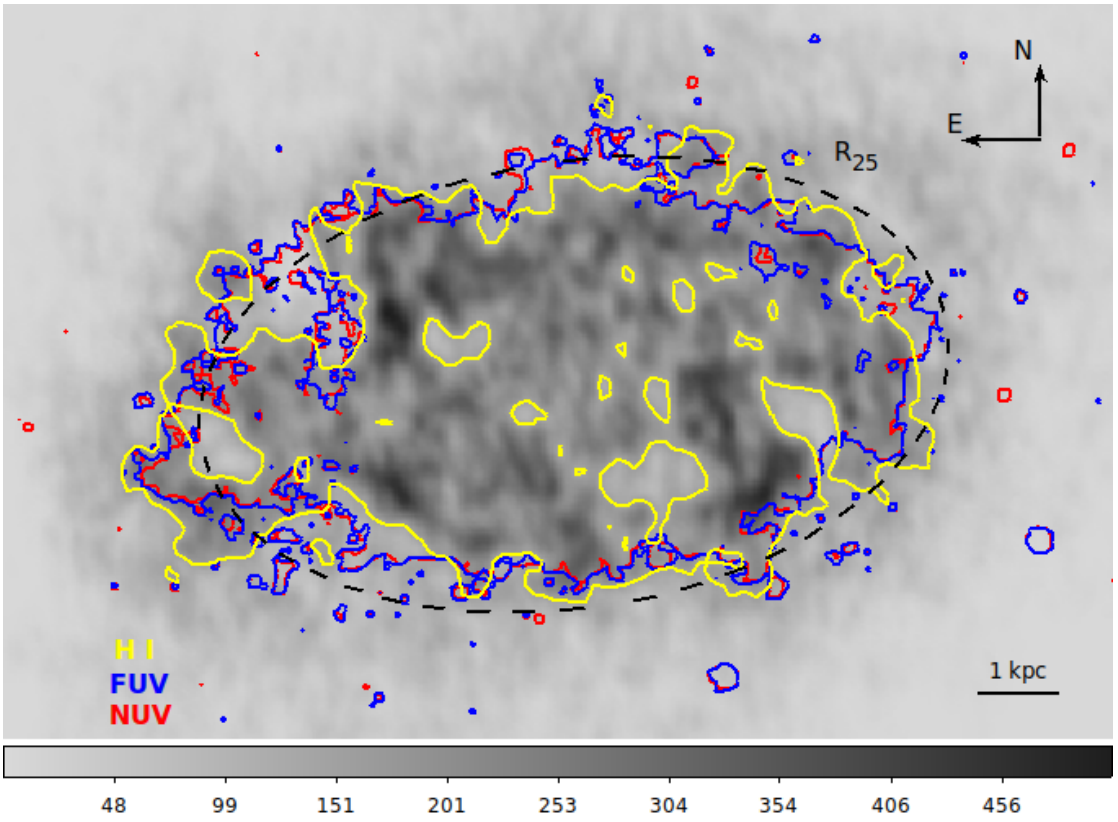

FIGURE 6.4: The figure shows the H I moment 0 map of the galaxy NGC 7793. The grey scale is in Jy/B*M/S. The yellow contours show regions with H I column density more than $10^{21} cm^{-2}$. The blue and red contours respectively represent FUV and NUV emission profile. These are generated for a threshold flux of 5 times the average background value measured in each respective band. The black dashed ellipse shows the R_{25} boundary of the galaxy.

6.4.2 Correlation with H I column density

The H I column density is known to have a threshold value of $\sim 10^{21} cm^{-2}$ for star formation in galaxies (Skillman 1987; Clark & Glover 2014). Carignan & Puche (1990) observed the galaxy NGC 7793 with VLA and found H I gas with column density $5 \times 10^{19} cm^{-2}$ up to $1.5 R_{25}$ radius of the galaxy. As the FUV and NUV disk emission profiles trace the distribution of young star forming regions, we compare those with H I gas density profile to understand the relation between gas and star formation. In Figure 6.4, we have shown the moment 0 H I map of the galaxy, observed with VLA by Walter et al. (2008). In order to compare the emission profiles in FUV, NUV and H I, we plotted contours as displayed in

Figure 6.4. The yellow contour signify the extent of the H I disk with column density more than $10^{21} cm^{-2}$. To trace the extent of the disk in FUV and NUV, we adopted the threshold as 5 times the average background flux in each respective band and created contours. The contours are shown in blue and red respectively for FUV and NUV in the same figure. The extent of the disk emission in both FUV and NUV is found to be almost similar for the adopted thresholds. Also, the H I disk with column density more than $10^{21} cm^{-2}$ closely matches with both the UV profiles. In some regions along the east and western part, we noticed H I contours to be little more extended than the UV. While in northern part, we found a part UV contours to extend outside the H I contour. The overall good spatial correlation between UV and H I profiles signify that star formation is happening in NGC 7793 up to the extent where H I column density is more than the threshold value $10^{21} cm^{-2}$.

6.4.3 Identification of young star forming clumps

As the FUV emission is predominantly contributed by massive young OB stars, imaging in FUV will eventually help to trace the young star forming regions hosting massive stars in a galaxy. In order to identify young star forming clumps in NGC 7793, we utilised UVIT FUV image. We used *astrodendro*[*] python package to locate bright star forming clumps in the FUV image. The detail algorithm of this package is discussed in Chapter 3. We fixed the minimum number of pixel value as 10, which corresponds to a radius of $\sim$ 12 pc ($\sim$ 1.8 pixel) at the distance of the galaxy. This value is chosen such that the size of the smallest region matches with the FWHM of the PSF, which is $\sim$ 3.5 pixel in the observed field. In order to fix the threshold flux, we started with a value 5 times the average FUV background flux ($\log[\text{flux}(erg/sec/cm^2/\mathring{A})] = -18.40$) and increased it with 0.2 interval in logarithmic scale up to $\log(\text{flux}) = -16.20$. For each threshold,

[*]http://www.dendrograms.org/

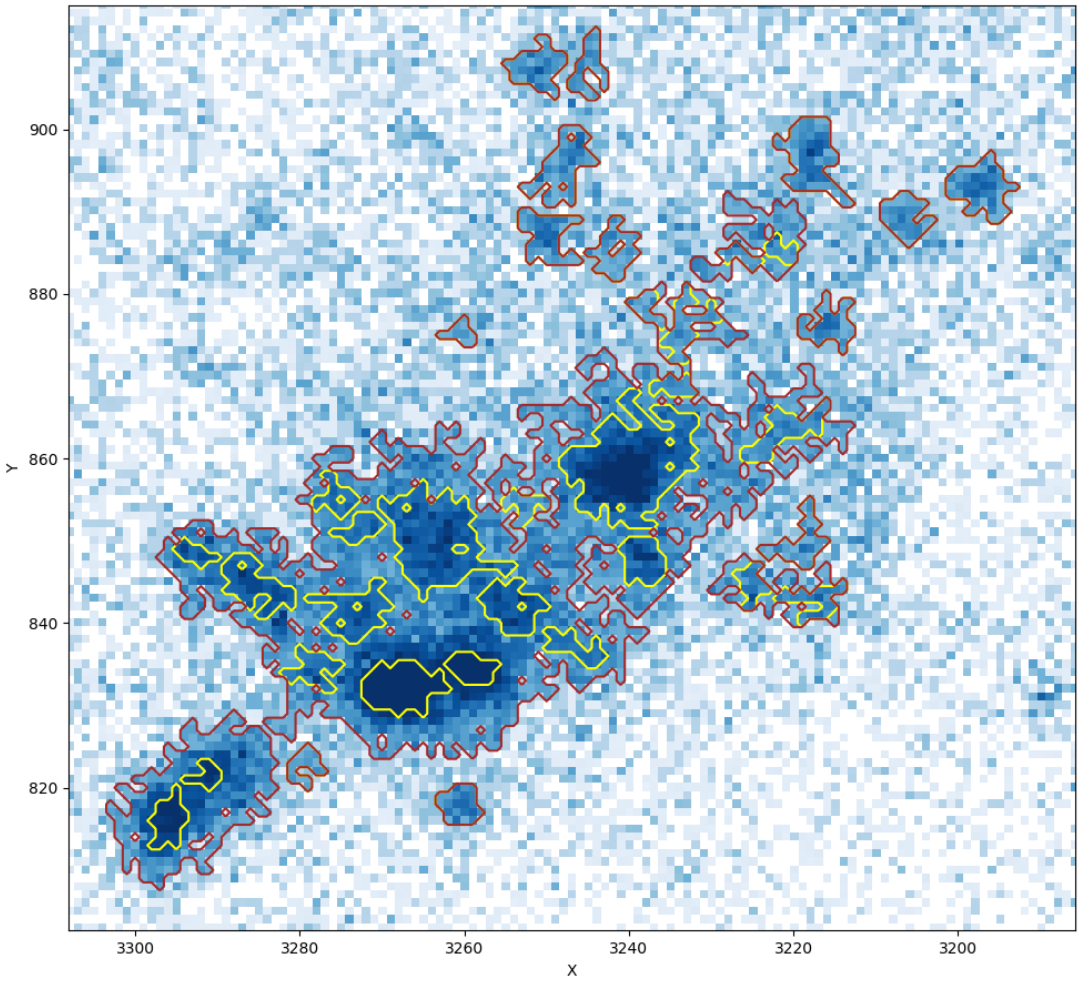

FIGURE 6.5: A selected star forming region of the galaxy is shown along with the contour of parent (brown) and child (yellow) structures. The background shows UVIT F148W band image. The value of the adopted threshold flux is $\log[\text{flux}(erg/sec/cm^2/\mathring{A})] = -17.80$.

we counted the number of identified parent and child structures and plotted in Figure 6.6. The individual structures with no sub-structure inside are counted as both parent and child structure in *astrodendro*. The ratio of the child and parent structures, represented by the black line, shows an increasing trend with decreasing threshold flux and becomes nearly constant after the value $\log(\text{flux}) = -17.80$. This flux value also corresponds to the flux of a B5 spectral type star at the distance of the galaxy NGC 7793. As stars with spectral type cooler than B type does not

contribute much of FUV flux, we fixed this value ($\log[\text{flux}(erg/sec/cm^2/\mathring{A})] = -17.80$) to be the threshold flux. For this threshold, the numbers of identified parent and child structure are found to be 835 and 3266 respectively within the galactocentric radius of 7 kpc. We considered 7 kpc as the outer boundary, as this value is equivalent to $\sim 1.5R_{25}$, up to which Carignan & Puche (1990) traced the H I disk. Again, as per the study of Radburn-Smith et al. (2012), the signature of younger population has been traced up to this radius with HST observations. In Figure 6.5, we have shown an example of parent and child structures identified at a particular star forming region of the galaxy for the chosen threshold flux.

As the larger parent structures contain multiple unresolved clumps inside, we considered the child structures, which are identified as individual star forming clumps in UVIT image, for our further analysis. The output of *astrodendro* provides position, area and flux of each identified clumps. We considered the area of these irregular shaped clumps and estimated the equivalent radius, which shows a range between $\sim$ 12 - 70 pc. The histogram of the size is shown in Figure 6.7. This matches well with the size of the GMCs detected in the galaxy (Grasha et al. 2018). We used the position and area equivalent radius of these identified clumps as measured in the FUV image and estimated FUV and NUV fluxes from each respective images for the same calculated aperture size. This provides both FUV and NUV magnitudes of the clumps. We corrected these magnitudes for background and extinction. The average background in each individual image is estimated by considering four circular regions, each of radius 1 arcmin, in the observed field located away from the galaxy. The extinction correction is done as explained in section 6.3.

In order to avoid clumps with relatively larger photometric error ($\gtrsim$0.1 mag), we considered only those clumps with corrected FUV magnitude brighter than 21 mag in our analysis. This results in 2046 number of individual star forming clumps. We showed the histogram of (F148W−N242W) colour of these clumps

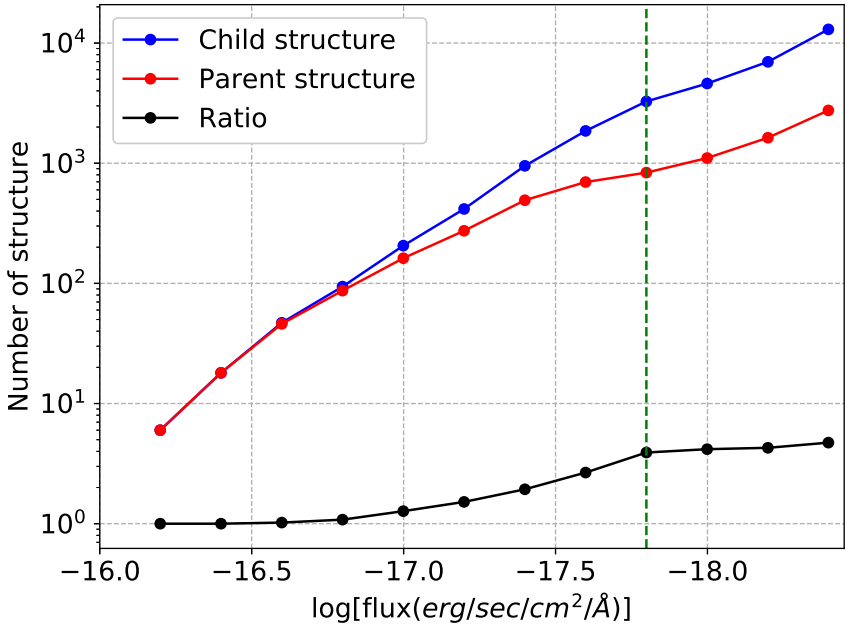

FIGURE 6.6: The number of identified parent and child structures are shown as a function of varying threshold flux. The black line shows the ratio of the number of child and parent structures. The vertical green dashed line represents the threshold flux (log(flux) = −17.80) selected for our analysis.

in the top panel of Figure 6.8. The distribution shows a gaussian nature with a peak around (F148W−N242W) = −0.25. We also estimated the galactocentric distance for each clump by adopting the method as explained in Section 6.4.1. The (F148W−N242W) colours of the clumps are plotted as a function of galactocentric distance in the bottom panel of Figure 6.8. The distribution shows a flat nature for the inner 3 kpc radius of the galaxy whereas most of the clumps identified in the outer part beyond 3 kpc have relatively bluer colour. This signifies that the outer part of the galaxy mostly have younger sources while the inner part shows a uniform distribution.

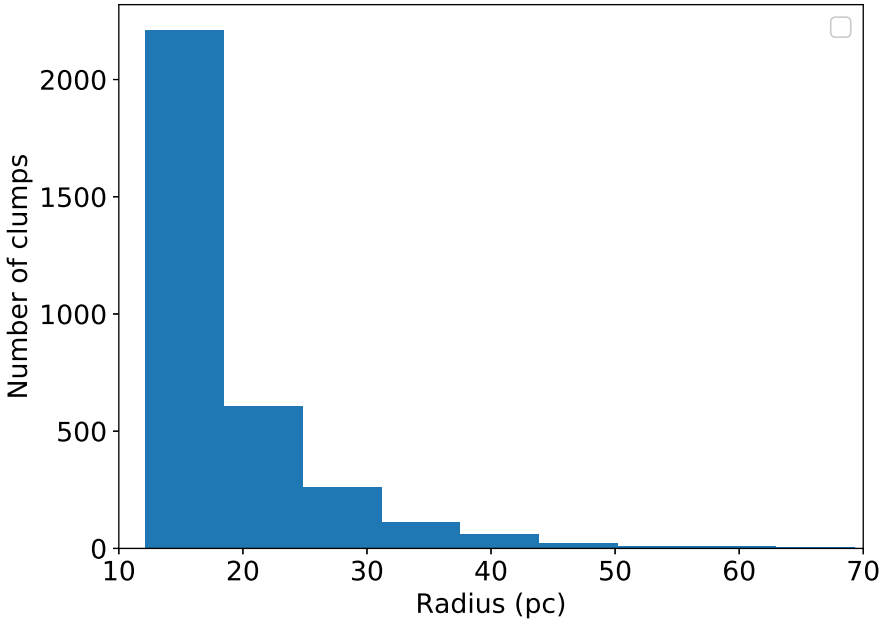

FIGURE 6.7: The histogram shows the size of identified clumps (child structure) for the selected values of threshold flux and minimum number of pixel.

6.4.4 Age estimation

As discussed in Section 6.2, the age of an unresolved star cluster can be estimated from its observed (F148W−N242W) colour. The child structures identified in the FUV image are likely to be the unresolved FUV bright star forming clumps of the galaxy. Among all, the smaller clumps are mostly composed of a single entity whereas the larger ones can be stellar associations or combination of multiple clumps, which could not be resolved further with UVIT. In order to apply SSP model to these clumps, we assumed each of them as single entities. We estimated the background and extinction corrected F148W magnitude and (F148W−N242W) colour of these identified clumps and shown them in Figure 7.15 (grey points) along with the model curves of Figure 6.2. Only a few observed points are lying outside the model colour range in the bluer side. We have excluded these points from our analysis. We considered (F148W−N242W) colour for rest of the clumps and performed linear interpolation along the colour axis to estimate

age of each clump. The histogram of the estimated ages is shown in Figure 7.13. We noticed a richness of younger clumps with age less than 20 Myr. This suggests that the stellar populations identified in the FUV image are mostly younger and the galaxy NGC 7793 has undergone an enhanced phase of star formation in the last 20 Myr.

6.4.5 Age distribution

The spatial distribution of star forming clumps as a function of age conveys the star formation history across a galaxy. As star formation in a galaxy can be triggered by multiple mechanisms, the spatial age map of star forming clumps is important to draw conclusion about the impact of local environment and also the possible triggering activities. In order to visualise the spatial distribution of these star forming clumps as a function of age, we divided them in four different groups between the age range 1 - 400 Myr. The age ranges of the groups are 1 - 10 Myr, 10 - 20 Myr, 20 - 50 Myr and 50 - 400 Myr. The bin size of the groups are chosen on the basis of age histogram shown in Figure 7.13. We fixed the interval to be more smaller where there are more number of clumps and to be more wider where there are less number of clumps. Also, for each selected bin, the value of mean error in the estimated ages is less when compared to the bin size.

The locations of the clumps identified in each age group are shown on the galaxy image in Figure 6.11. The youngest star forming clumps (age group : 1 - 10 Myr) are mostly found to be located along the flocculent arms in the outer part of the galaxy. The distribution of these clumps are also more compact in nature. In the case of clumps with age between 10 -20 Myr, we notice a similar pattern with a predominant distribution along the arms. We find an overall scattered distribution of clumps in the age range 20 -50 Myr across the galaxy. These are preferably found away from the arms. Beyond the age 50 Myr, the clumps are

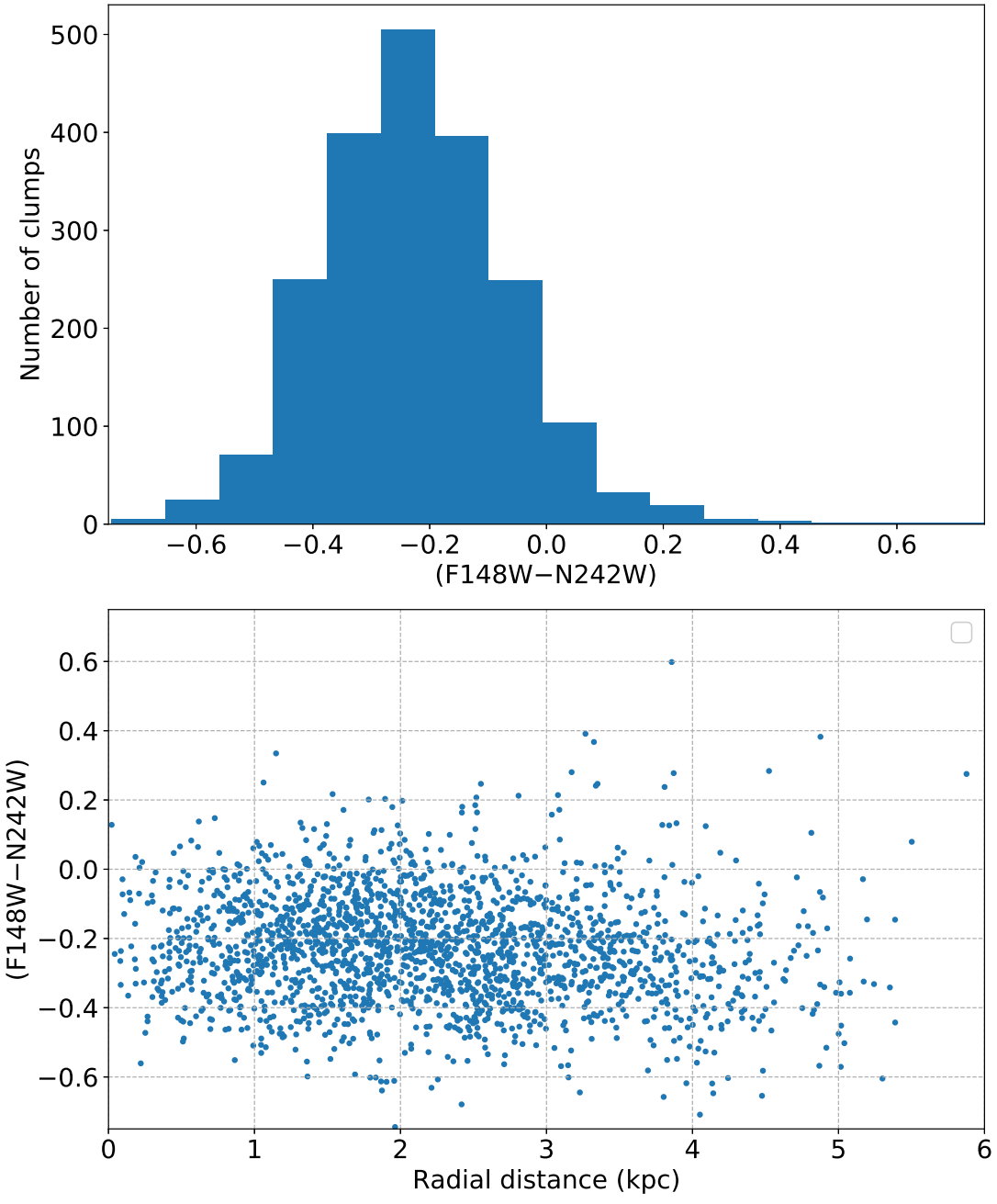

FIGURE 6.8: The histogram of (F148W−N242W) colour of the clumps brighter than 21 mag in F148W band is shown in the upper panel. In the lower panel, we have shown their distribution as a function of radial distance from the galaxy centre.

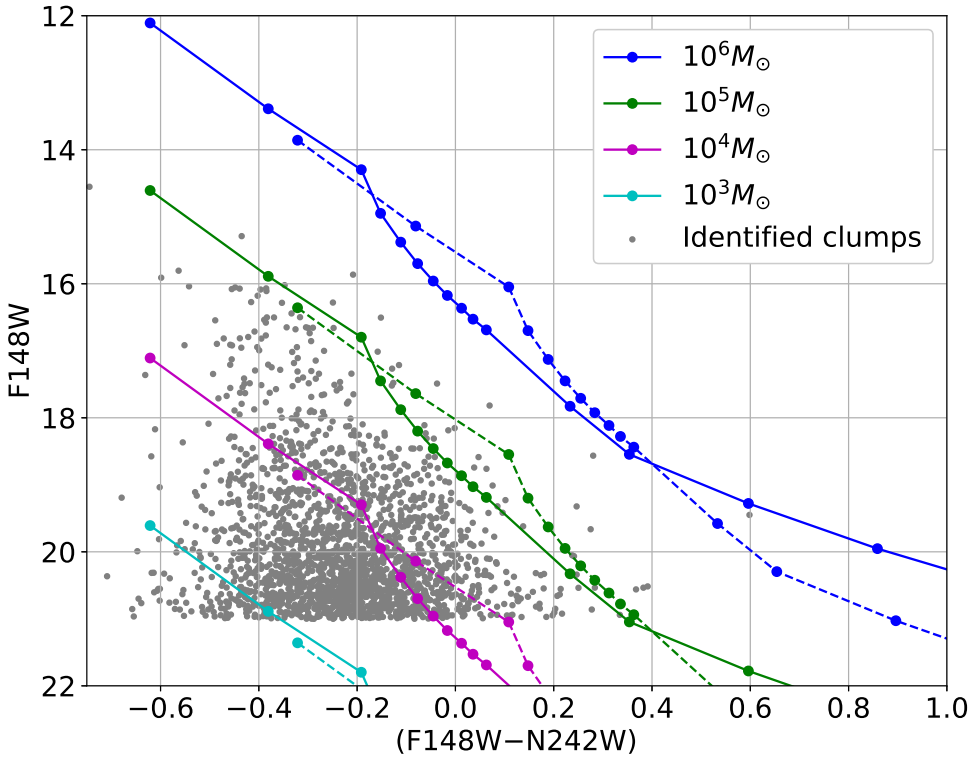

FIGURE 6.9: The identified star forming clumps are over plotted (grey filled circles) on the simulated model curves as shown in Figure 6.2.

noticed to be present more in the inner part of the galaxy. The regions between two arms are mostly populated by clumps older than 20 Myr. The overall picture thus suggests that star formation in the last 20 Myr are taking place mostly along the flocculent arms of the galaxy. The star forming regions located in the far outer part in the east direction are found to be populated with clumps younger than 20 Myr.

6.4.6 Mass estimation

We also estimated mass of each clump from its observed F148W magnitude. For the known value of (F148W−N242W) colour of each clump, we used the F148W

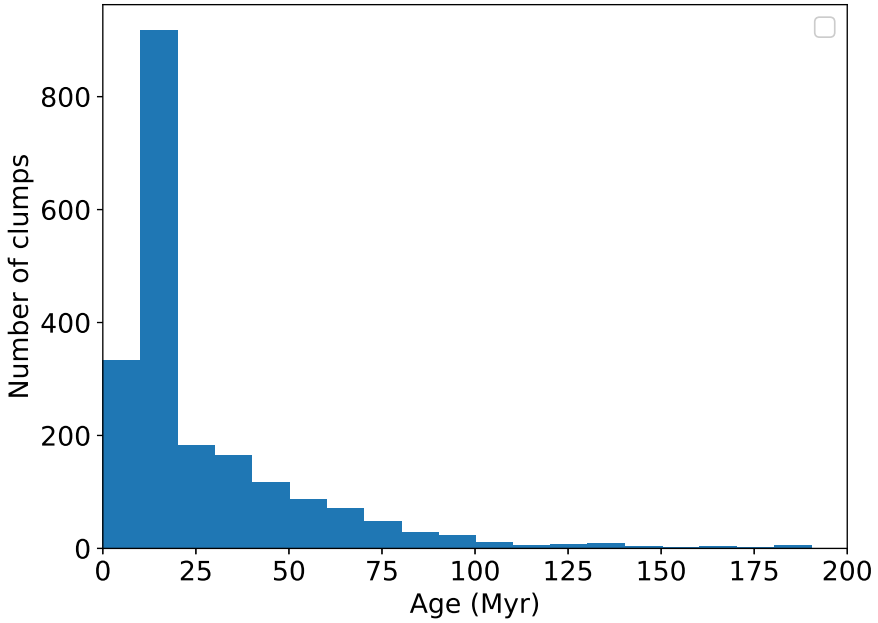

FIGURE 6.10: The age histogram of the identified star forming clumps.

band observed magnitude and performed a linear interpolation along the magnitude axis of Figure 7.15 to estimate mass. The histogram for the estimated masses is shown in Figure 7.16. It shows that the identified clumps have a mass range between $3 \times 10^2 M_\odot$ - $10^6 M_\odot$ with a peak around $10^4 M_\odot$. The GMCs identified in this galaxy also have a similar mass range (Grasha et al. 2018). The estimation of masses below $10^3 M_\odot$ is not accurate due to the lower limit of model mass range. Majority of the clumps are found to have intermediate mass between $10^3 M_\odot$ - $10^4 M_\odot$. The number of clumps with mass greater than $10^5 M_\odot$ is relatively small in number. This might indicate that the galaxy has not formed much of massive complexes in recent times.

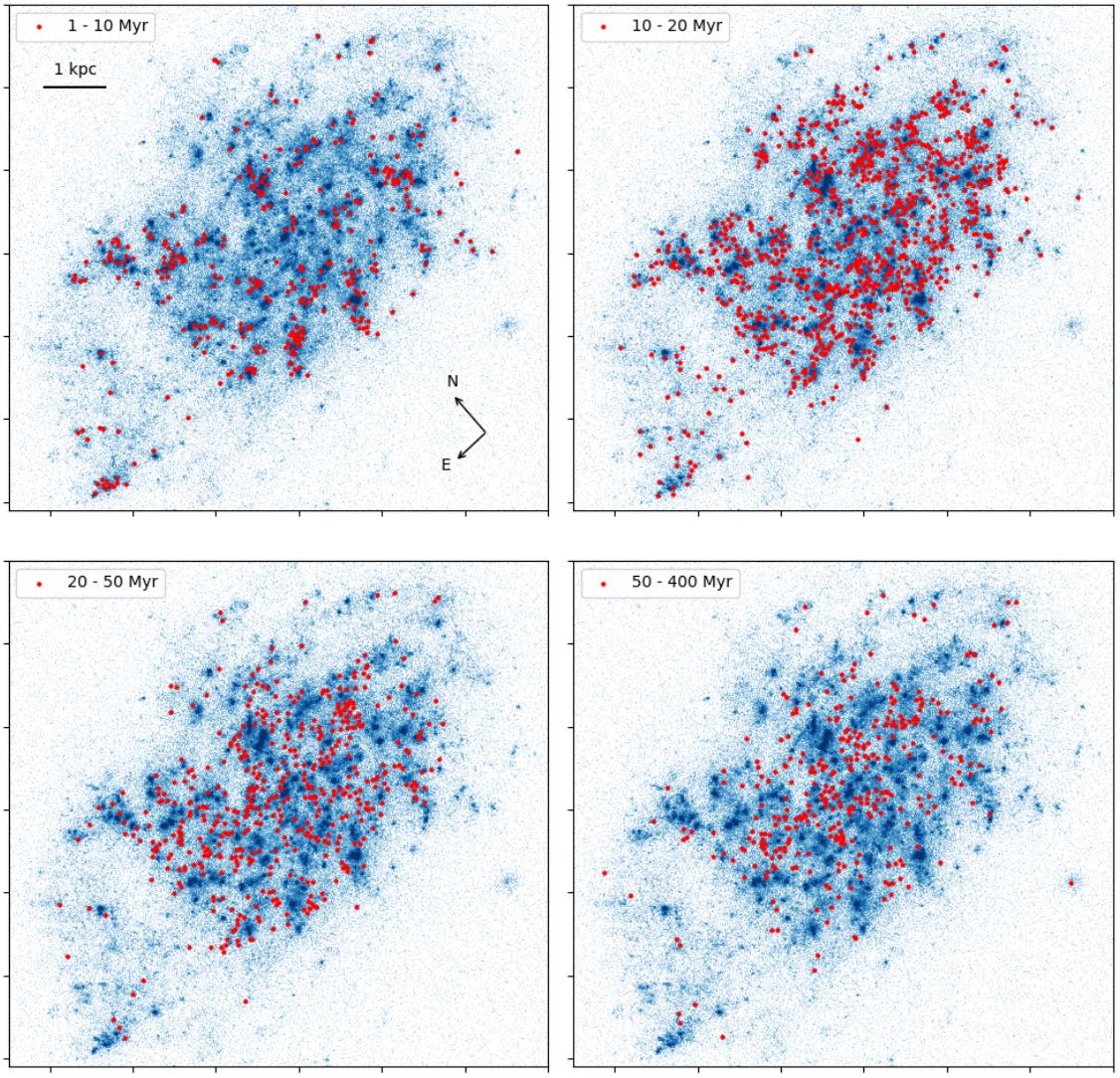

FIGURE 6.11: Spatial distribution of clumps (red points) as a function of their estimated age between the range 1 - 400 Myr. The figures represent four different age groups as mentioned in the text. The age range of the group is mentioned in the corresponding panel.

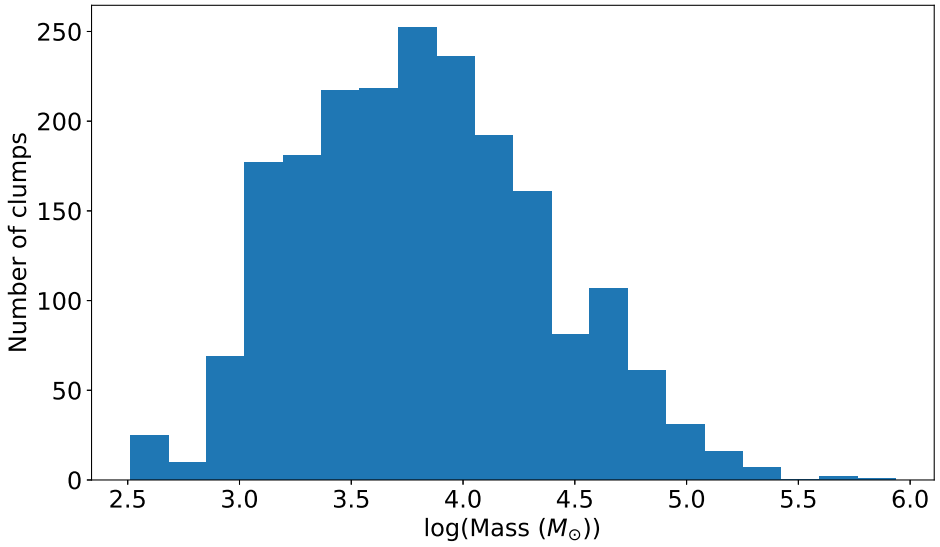

FIGURE 6.12: The mass histogram of the identified star forming clumps.

6.4.7 Mass distribution

The mass of a star forming clump primarily depends on the mass of the parent molecular cloud from where it is formed. The massive clumps generally form from giant molecular clouds, whereas low mass clumps can be produced from molecular cloud of relatively smaller mass. It is thus important to know the mass distribution of clumps to explore the star forming environment across a galaxy. In order to understand the mass distribution of identified clumps across the galaxy NGC 7793, we made four groups for different mass ranges. The mass ranges of the groups are $log(M) < 3.5$, $3.5 < log(M) < 4.0$, $4.0 < log(M) < 4.5$ and $4.5 < log(M) < 6.0$. The bins are fixed by following the same steps as mentioned in Section 6.4.5. In Figure 6.13, we have shown the position of these clumps on the FUV image of the galaxy. We noticed a hierarchical distribution of star forming clumps as a function of mass. The low mass clumps ($log(M) < 3.5$) are mostly distributed along the flocculent arms. The central region of the galaxy has a few of these low mass clumps. The clumps, with mass in the range $3.5 < log(M) < 4.0$, show similar distribution with relatively less number. These clumps are seen more in the inner part of the arms than its outer part. The distribution of more massive clumps with

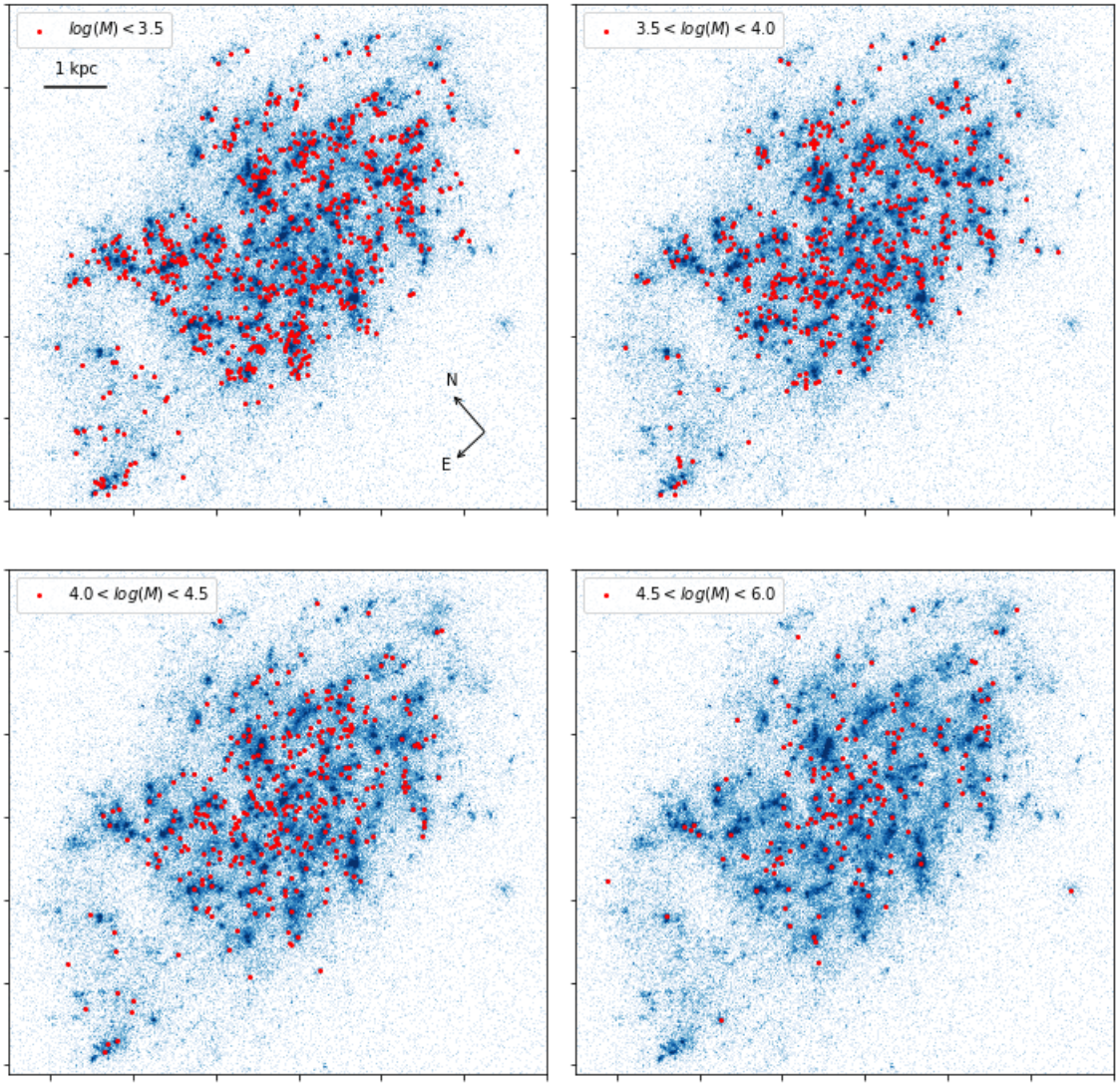

FIGURE 6.13: Spatial distribution of clumps (red points) as a function of their estimated mass between the range $3 \times 10^2 - 10^6 M_{\odot}$. The figures represent four different mass groups as mentioned in the text. The mass range of the group is mentioned in the corresponding panel.

mass between $4.0 < log(M) < 4.5$ gradually shrink towards the inner part. These are also seen in between the arms. The most massive clumps ($4.5 < log(M) < 6.0$) of the galaxy are distributed more in the central part of the galaxy. The overall scenario portrayed is that the inner part of the flocculent arms contain both low and high mass clumps whereas the outer part of these arms are populated with more of low mass clumps with mass $log(M) < 3.5$. This brings out the hierarchical distribution of star forming clumps along the spiral arms.

6.4.8 Nuclear star cluster

Nuclear star cluster is know to be a dense stellar system which is mostly seen in the dynamical centre of disk galaxies. The sizes of these objects are quite similar to those of globular clusters. It has been found that more than 75% of nearby late-type spiral galaxies have nuclear star cluster at their centre (Böker et al. 2002). The galaxy NGC 7793 is also reported to have nuclear star cluster (Walcher et al. 2006; Carson et al. 2015; Kacharov et al. 2018). This cluster has an effective radius of 12.45 pc, measured in the HST F275W band (Carson et al. 2015). Carson et al. (2015) studied this cluster with multi-band HST data and reported that the size of the cluster is bigger in U band than in optical. The SFH of the cluster shows a complex nature. The VLT spectroscopic observations by Kacharov et al. (2018) found that the cluster contains stellar population of four different age ranges. The majority of the cluster populations are older than 10 Gyr, whereas some have age around 2 Gyr, some between 200 - 600 Myr and some are very young with age $\sim$ 10 Myr.

In this study, we used UVIT FUV and NUV observations to characterise the nuclear cluster. In order to check the properties in UV, we considered both FUV and NUV images and defined multiple apertures centred on the reported cluster position. The radius of the smallest aperture is considered as 1.5 pixel ($\sim 0.6''$,

i.e. diameter of the aperture $\sim$ FWHM of PSF) and further increased with an increment of 3 pixel to define four more apertures (Figure 6.14a). Each pixel of the UVIT image corresponds to $\sim 0.4''$. We measured fluxes in both F148W and N242W bands in each defined annulus and estimated extinction and background corrected (F148W$-$N242W) colour and are plotted as a function of aperture radius in Figure 6.14b. The (F148W$-$N242W) colour gradually becomes bluer with increasing radius and flattens beyond a radius of 10 pixels. This signifies that the stellar populations present in the outskirts of the nuclear cluster are more younger than the inner part, which indirectly supports the earlier conclusion of circumnuclear star formation by Carson et al. (2015). This can also happen due to the accretion of younger population from the nearby stellar groups to the nuclear cluster. We also identified this cluster as a single star forming clump with the method as discussed in section 6.4.3. The estimated values of cluster age and mass are found to be 19.1$\pm$0.8 Myr and $2.3\times10^5 M_\odot$ respectively. As FUV emission traces the younger populations, this age and mass values therefore sample the properties of the stellar populations which are youngest among the four different types as found by Kacharov et al. (2018).

6.5 Results and Discussion

The primary aim of this study is to identify young star forming clumps in the galaxy NGC 7793 and then estimate their ages and masses. In order to do that, we used FUV and NUV imaging data of the galaxy, observed with F148W and N242W filters of UVIT. The spatial resolution of UVIT has helped to identify clumps of radii $\sim$ 12 pc. The fluxes measured in FUV and NUV bands are compared with the model values to estimate ages and masses of the clumps.

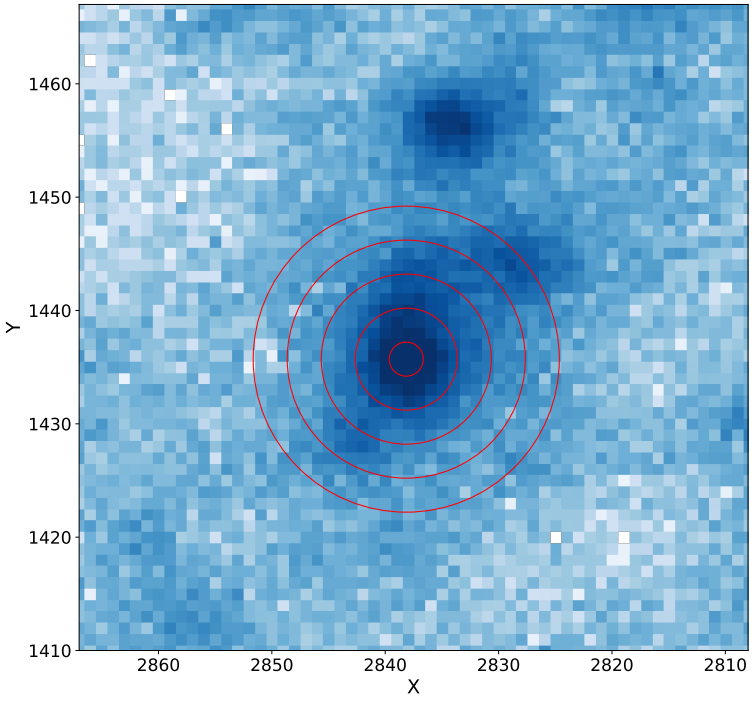

(a)

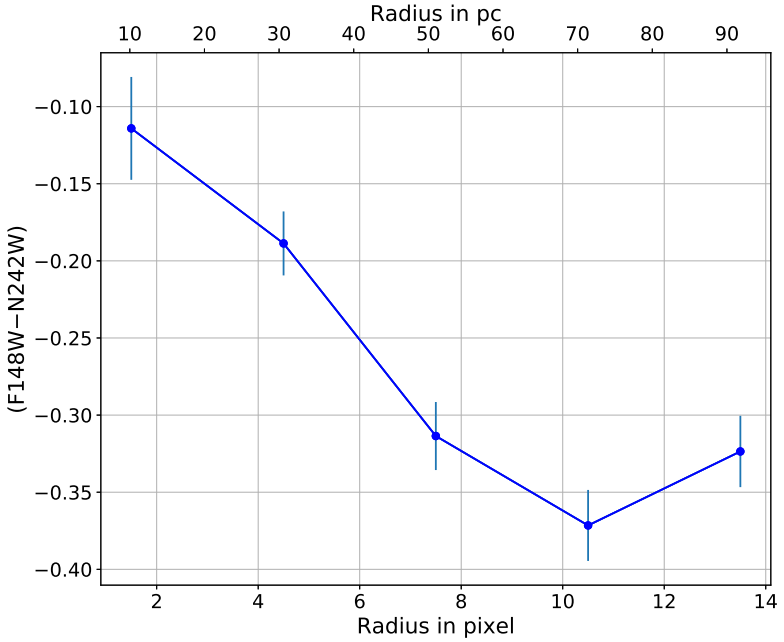

(b)

FIGURE 6.14: The upper panel (a) shows the nuclear star cluster as seen in the UVIT FUV image. The red circles represent five different apertures with radius starting from 1.5 pixel to 13.5 pixel. The lower panel (b) shows the extinction and background corrected (F148W−N242W) colour profile of the object as measured from the annuli displayed above.

We used starburst99 model data to simulate diagnostic plot which helped us estimating age and mass of the clumps from their observed F148W magnitude and (F148W−N242W) colour. Therefore, error in the measurements of magnitude and colour will reflect in the estimated values of age and mass. The photometric error in both F148W and N242W bands lie within a range between $\sim$ 0.01 - 0.1 mag. The corresponding error in age has a range between $\sim$ 1 - 80 Myr. The younger clumps have less error in age while the older clumps have relatively large error. The mean error value for each of the four age groups defined in our study have value smaller than the bin size. For example, the group containing clumps with age between 1 - 10 Myr has a mean error of $\sim$ 3 Myr. Similarly, the error in F148W magnitudes results in $\sim$ 1 - 15% error in the estimated mass values. Another parameter which can change the measured age and mass values of the clumps is the adopted value of E(B−V). A larger reddening will make the clumps more younger and massive and vice versa. We adopted the extinction law to be average LMC type for dealing the interstellar extinction in NGC 7793. A change in extinction law will also affect the estimated age and mass values accordingly.

Several studies have been done with observations in different bands to understand the disk properties of the galaxy NGC 7793. Vlajić et al. (2011) observed two fields in the extended outer part of the galaxy with Gemini Multi Object Spectrograph (GMOS) and reported that the galaxy disk beyond $\sim$ 5 kpc is mostly populated with older red giant branch (RGB) stars. They could trace the stellar disk up to $\sim$ 10 kpc. With HST observations, Radburn-Smith et al. (2012) studied a part of the galaxy disk in the eastern side and found that the surface density of older population in the outer disk between 3 - 5 kpc decreases gradually while it remains almost constant in the case of younger population. They also noticed an abrupt break in the distribution of younger stars at a radius of 5 kpc. The FUV and NUV luminosity density profiles presented in our study support the earlier results. We noticed the FUV profile to take over NUV at 3 kpc radius and remains flat up to 5 kpc radius. We also found that the clumps identified between radii 3 -5 kpc

are more blue. This signifies that the stellar populations present in the outer disk between 3 - 5 kpc are mostly younger. It is also possible that the outer disk of the galaxy has relatively low reddening than the adopted value. A decrease in the E(B−V) value will make the clumps more redder, which will make the distribution of clumps in the outer disk, between radii 3 - 5 kpc, flatter.

The drop in the FUV luminosity beyond 5 kpc conveys that the disk outside this radius has less number of younger and/or less massive population. Both the work by Vlajić et al. (2011) and Radburn-Smith et al. (2012) studied a limited part of the disk, whereas our study covered the entire galaxy disk from centre to outside. Therefore, the radial nature of the disk, derived from a limited region in the eastern side by HST, remains similar when averaged over the entire disk. This conveys that the enhancement in the recent star formation between radius 3 - 5 kpc has happened mostly along all azimuthal directions. Sacchi et al. (2019) performed a more comprehensive study by almost covering the entire disk with HST observations to understand the radial star formation history in the galaxy. Their study reported an inside-out growth for the galaxy disk. The SFR in the outer part of the galaxy has been enhanced in more recent times while the inner part is mostly populated with population older than 1 Gyr. We measured the values of disk scale-length in FUV and NUV as 2.64±0.16 kpc and 2.21±0.21 kpc respectively. The optical scale-length of the galaxy is reported as 1.08 kpc by Carignan (1985). These together signify that the disk becomes extended in shorter wavelengths. This in other word means that the older populations are more centrally concentrated, which also portray an inside-out growth scenario for the disk of NGC 7793.

An HST study done by Grasha et al. (2018) covered almost the entire galaxy disk up to radius of around 5 kpc and identified 293 young star clusters, with 65% of them to be younger than 10 Myr. Bibby & Crowther (2010) identified 74 emission line regions across the galaxy disk using imaging observation from Very

Large Telescop (VLT)/FOcal Reducer and Spectrograph (FORS1). Dicaire et al. (2008) detected Hα emission up to the edge of the H I gas disk of the galaxy and speculated massive stars as the source of this emission. These all together convey an enhancement in the recent star formation across the galaxy. In our study, we found around 61% of the 2046 identified clumps to be younger than 20 Myr. This also signifies recent star forming activities during the last 20 Myr.

The impact of density wave to trigger star formation in spiral galaxies was first proposed by Roberts (1969). Although, Elmegreen & Elmegreen (1986) reported only a small difference between the average SFR in grand design and flocculent spiral galaxies. This indirectly says that spiral density wave does not have stronger impact to trigger star formation in galaxies. Several observational studies (for example, Seigar & James (2002)) have supported the idea of Roberts (1969) for triggered star formation in spirals. Our study found that the distribution of youngest star forming clumps (Age $<$ 10 Myr) of the galaxy are more compact in nature and they trace the flocculent arms of the galaxy. This signifies that the enhancement of star formation during last 10 Myr has specifically happened along the arms. A recent study by Sacchi et al. (2019) found that the presence of spiral density wave is not clearly seen in the distribution of stellar populations older than 1 Gyr in NGC 7793, whereas the younger populations were mostly seen along the flocculent arms. Therefore, these results offer a scenario to test the impact of density wave to trigger star formation in such flocculent galaxies.

Elmegreen et al. (2014) studied the star forming regions of the galaxy NGC 7793 as a part of HST Legacy UV survey and reported a hierarchical nature of star forming regions with a range of size between $\sim$ 1 - 70 pc. The star forming clumps identified in our study found to have radius in the range 12 - 70 pc. The clumps with radii smaller than 12 pc could not be resolved in our study due to the resolution limit of UVIT. It is also possible that the larger clumps identified by UVIT are actually combination of multiple smaller clumps, which appear as a

single clump in the UVIT images. Grasha et al. (2018) reported a similar range for the radius of GMCs identified in the galaxy. They further concluded that the younger clusters are more closely associated with GMCs while the older one are found to be more dispersed away from the natal cloud. This along with the similarity in size further strengthens the connection between star forming clumps and the molecular clouds in the galaxy.

The star forming clumps identified in our study mostly cover a mass range between $10^3 - 10^5 M_\odot$. We noticed only a few clumps more massive than $10^5 M_\odot$. This picture matches with the mass of GMCs identified in the galaxy (Grasha et al. 2018). The clumps with relatively more mass ($4 < log(M) < 6$) are mostly seen in the inner part of the galaxy disk. This can be due to the massive molecular clouds, which are preferably seen in the inner part. Also, this can be the result of an artefact due to crowding. The inner part of a disk galaxy has more crowded environment than the outer part, and therefore, it is possible that some of the massive clumps identified in the inner disk are actually group of multiple clumps which could not be resolved by UVIT. The other interesting result is the distribution of clumps along the flocculent arms. We noticed that the ends of the arms are populated with more low mass clumps ($log(M) < 3.5$), whereas the inner part of arms have low as well as more massive clumps. This portrays a gradient in the mass distribution from inner to outer part along the arms.

We have also characterised the nuclear star cluster of the galaxy with UV observations. Carson et al. (2015) reported that the nuclear cluster of NGC 7793 has decreasing effective radius with increasing wavelength, which signifies a recent circum-nuclear star formation. Walcher et al. (2006) found stellar population younger than 100 Myr in the nucleus of the galaxy. Kacharov et al. (2018) reported a complex star formation history for this cluster. They noticed stellar population of different ages staring from $\sim$ 10 Myr to $>$ 10 Gyr as part of the cluster. They concluded that merging of multiple clusters with different ages can

give rise to the observed properties of the nuclear cluster. The (F148W−N242W) colour profile of the cluster, derived in our study, found to become more blue with increasing aperture size. This further supports the possibility of circum-nuclear star formation or accretion of young stellar population from nearby stellar groups to the nuclear cluster. The effective radius of the cluster is reported to be 12.45 pc in HST F275W band Carson et al. (2015). Considering the limit of UVIT resolution, the smallest aperture we could define is around this value. Therefore, the apertures larger than the effective radius of the cluster basically trace stellar population in the cluster outskirts or those which are in the process to be accreted by the nuclear cluster. We estimated the age and mass of the cluster as 19.1±0.8 Myr and $2.3\times10^5 M_\odot$ respectively. As FUV and NUV emission primarily trace stellar population of age up to a few hundred Myr, the estimated age of the cluster, which reported to have stellar populations of a wide age range, characterises the younger populations. Similarly the estimated mass of the cluster signifies the amount of mass contributed by younger populations present in the cluster.

The H I disk of the galaxy also shows some noticeable characteristics. Carignan & Puche (1990) noticed non-circular motion in the northern part of the galaxy and speculated the possibility of past interactions with a nearby companion of the sculptor group. Along the north and north-eastern part, we noticed some parts of the star forming UV disk to extend outside the extent of H I gas having density more than $10^{21} cm^{-2}$. The recent star formation could have used up the H I gas. Thus these features could be a result of a recent interaction which resulted in the enhancement of star formation in the outer part of the galaxy.

6.6 Summary

The main results of this study are summarised below.

1. We used UVIT FUV and NUV observations to understand the UV disk emission profile and to identify young star forming clumps in the galaxy NGC 7793.

2. The value of the galaxy disk scale-length (R_d) is found to increase towards shorter wavelength from optical to FUV. We estimated the value R_d to be 2.64±0.16 kpc and 2.21±0.21 kpc in FUV and NUV respectively.

3. Relative to the inner part, we noticed FUV emission to be more dominant than the NUV emission in the outer part of the galaxy (between radius 3 - 5 kpc).

4. We identified 2046 young star forming clumps in the galaxy with radius ranging between $\sim$ 12 - 70 pc.

5. The majority of the clumps were found to have age younger than 20 Myr, which signifies enhancement in recent star formation across the galaxy.

6. The youngest clumps (age $<$ 10 Myr) are specifically found along the flocculent arms of the galaxy.

7. The identified clumps mostly cover a mass range between $10^3 M_\odot - 10^5 M_\odot$.

8. We noticed a hierarchical mass distribution of the clumps along the flocculent arms. The end of the flocculent arms have more low mass clumps whereas the inner part of those arms contain low as well as more massive clumps.

9. The extent of the star forming UV disk of NGC 7793 closely matches with the extent of H I disk with column density more than $10^{21} cm^{-2}$.

10. The stellar population in the outskirts of the the nuclear star cluster are found to be younger compared to the inner part. This signifies a possibility of circum-nuclear star formation or accretion of younger stellar population from nearby stellar groups to the nuclear cluster.

Chapter 7

Tracing the outer disk of NGC 300: An ultraviolet view[†]

7.1 Introduction

NGC 300 is a nearby SA(s)d type spiral galaxy located at distance of 1.9 Mpc (de Vaucouleurs et al. 1991). It has an absolute B band magnitude of -17.66 and a metallicity around the solar value. Due to various similarities, this galaxy is also known as the near-optical twin of the local group galaxy M33 (Gogarten et al. 2010; Dalcanton et al. 2009). NGC 300 is also the brightest member of the sculptor group with a nearly isolated location (Tully et al. 2006; Karachentsev et al. 2003). The Sculptor group, with a span between 2 to 5 Mpc, is among the nearest galaxy groups beyond the Local Group (Jerjen et al. 1998).

Several studies have been done to understand the disk properties of NGC 300 from

[†]Results of this chapter are published in Mondal et al. (2019)

inner to outer part of the galaxy. Bland-Hawthorn et al. (2005) reported a pure exponential stellar disk up to $\sim$ 14.4 kpc ($\sim 2.2R_{25}$), which is about 10 disk scale length for NGC 300 while M33 has a disk break at $\sim$8 kpc (Ferguson et al. 2007; Barker et al. 2011). Present star formation rate (SFR) in the disk of NGC 300 has been measured and a relatively low value of $\sim$ 0.08 - 0.30 $M_{\odot}$ yr^{-1} is estimated by different tracers like Hα emission (Helou et al. 2004; Karachentsev & Kaisina 2013b), FUV luminosity (Karachentsev & Kaisina 2013b), mid-IR (Helou et al. 2004) and X-ray (Binder et al. 2012). The standard model of disk galaxy evolution suggests an inside-out growth of the disk, i.e. the inner part of the disk forming earlier than the outer part. Using HST observation of individual stars up to 5.4 kpc, Gogarten et al. (2010) concluded an inside-out disk growth in NGC 300 in the last 10 Gyr. Vlajić et al. (2009) found an extended stellar disk and an upturn in metallicity gradient at a radius of $\sim$10 kpc in NGC 300 and concluded that radial mixing or accretion in the outer disk may be the reason behind this change in the metallicity gradient. Gogarten et al. (2010) also found a similar metallicity gradient in the inner disk of the galaxy through HST observation and suggested that the probability of radial mixing is very less in NGC 300 because of its low mass. Using HST observation, Hillis et al. (2016) studied the star formation history in the past 200 Myr in four different regions of NGC 300 and identified an unbroken young stellar disk at least up to 8 disk scale length. In another study, Rodríguez et al. (2016) identified 1147 young stellar groups by studying six different regions in the galaxy and noticed that these groups are mostly present along the spiral arm of the galaxy.

H I disk of this galaxy is well studied and found to show some noticeable structures. Puche et al. (1990) reported a warp in the H I disk just outside the optical disk. Westmeier et al. (2011) used ATCA radio observation and mapped the H I disk of NGC 300 outward to a larger extent. They found a dense inner disk and an extended outer disk of 35 kpc in diameter along the major axis of the galaxy. They also observed an asymmetry in the outer disk, which they speculated to be as due

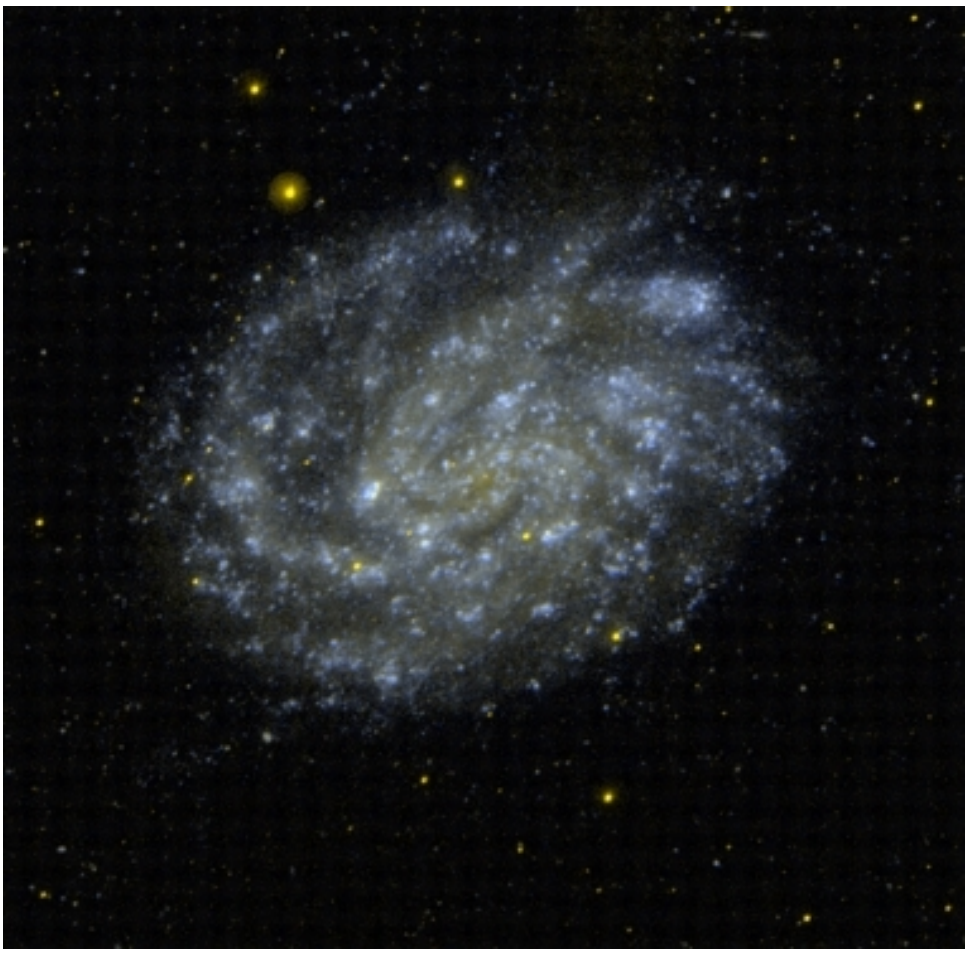

FIGURE 7.1: False colour composite GALEX image of the galaxy NGC 300 where FUV and NUV are represented by blue and yellow colour respectively. Image courtesy : NED Database.

to ram pressure caused by the interaction between the galaxy and surrounding inter-galactic medium (IGM).

In this chapter, we present an ultra-violet study of the galaxy NGC 300 using GALEX far-UV (FUV) and near-UV (NUV) observations (Image - Figure 7.1). The aim is to study the nature of UV emission in the galaxy and correlate it with optical, H I and mid-infrared (3.6 μm) wavelengths.

TABLE 7.1: Properties of NGC 300

Property	Value	Reference
RA	00:54:53.4	Skrutskie et al. (2006)
DEC	-37:41:03.7	Skrutskie et al. (2006)
Morphological type	SA(s)d	de Vaucouleurs et al. (1991)
Distance	1.9 Mpc	Rizzi et al. (2006)
Inclination	42.3°	Puche et al. (1990)
PA of major axis	109°	de Vaucouleurs & Page (1962)
Mass	$2.9 \times 10^{10} M_{\odot}$	Westmeier et al. (2011)
R_{25}	5.3 kpc	Faesi et al. (2014)
Optical scale-length (R_d)	2.1 kpc	Carignan (1985)

7.2 Theoretical models

We used starburst99 SSP model (Leitherer et al. 1999) to generate diagnostic diagrams for studying the young star forming regions of the galaxy NGC 300. The starburst99 model data are acquired for the chosen set of parameters given in Table 7.2. We simulated two plots, shown in Figure 7.2 and 7.3, to estimate age and mass of clusters present in the galaxy. The method to generate these diagrams are explained in Section 3.2.1. In order to estimate age from the observed (FUV−NUV) colour, we used blue curve (Z = 0.02) of Figure 7.2. Mass of the clumps are estimated with the help of the model grids shown in Figure 7.3.

7.3 Data and Analysis

This study primarily used FUV and NUV imaging data of NGC 300 from the observation of GALEX. We used images as well as the catalogue of sources produced by GALEX data pipeline (Morrissey et al. 2007) for the whole 1.25° field

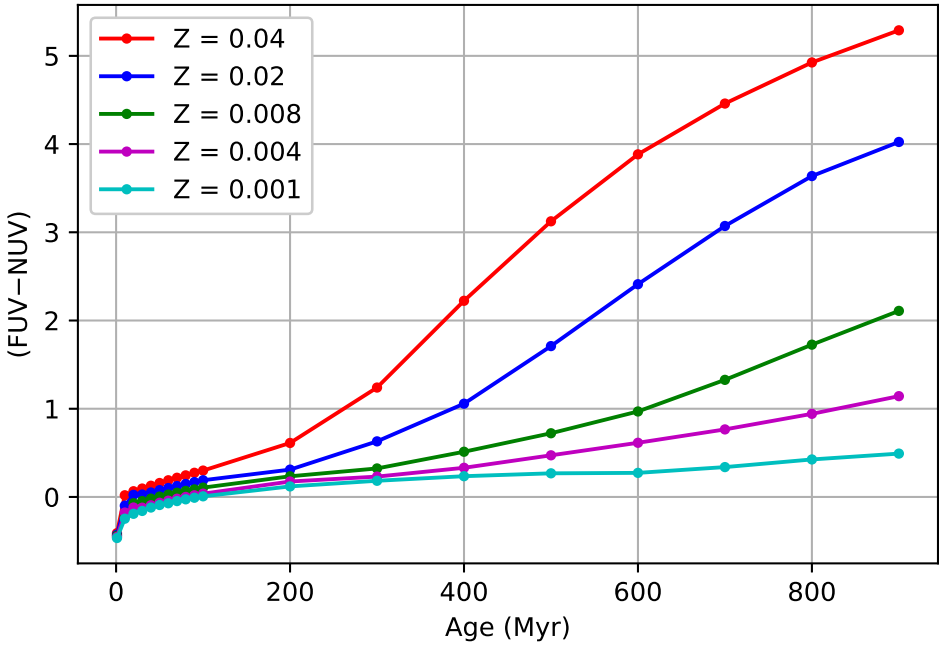

FIGURE 7.2: Starburst99 model generated (FUV−NUV) colour as a function of age (Myr). Different curves are for five different metallicities (Z). For 1-100 Myr range, age interval is 10 Myr and after that interval is 100 Myr for age up to 900 Myr. The cluster mass considered is $10^6 M_\odot$.

TABLE 7.2: Starburst99 model parameters

Parameter	Value
Star formation	Instantaneous
Stellar IMF	Kroupa (1.3, 2.3)
Stellar mass limit	0.1, 0.5, 120 $M_\odot$
Cluster mass range	$10^3 M_\odot$-$10^7 M_\odot$
Stellar evolution track	Geneva (high mass loss)
Metallicity	Z=0.04, 0.02, 0.008, 0.004, 0.001
Age range	1-900 Myr

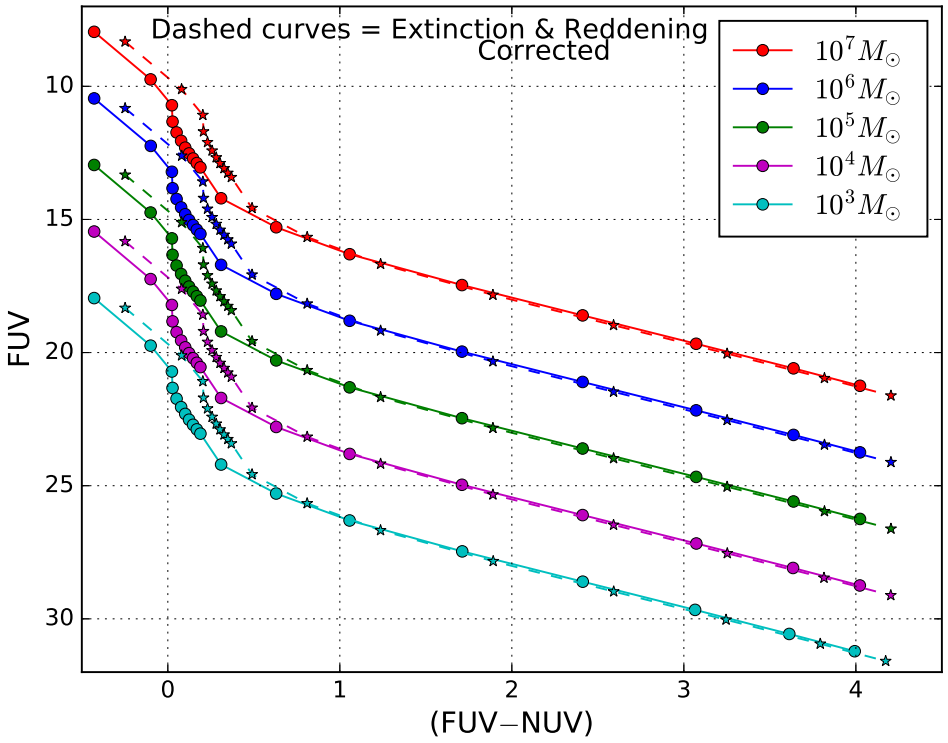

FIGURE 7.3: Starburst99 model generated FUV vs (FUV−NUV) CMD for simple stellar population. Different curves signify five different total cluster mass ($10^7 M_\odot$, $10^6 M_\odot$, $10^5 M_\odot$, $10^4 M_\odot$, $10^3 M_\odot$). The points shown in each curve are for different ages starting from 1 Myr to 900 Myr (increasing along the colour axis) with the same age interval chosen in Figure 7.2.

of view. The catalogue contains 19289 identified sources within the total field of view. Out of these, we found 6554 sources to have both FUV and NUV detection. The catalogue provides apparent magnitudes of sources in both FUV and NUV band along with their RA and DEC. We have also used optical, infra-red and H I data of the galaxy for correlating the results obtained from UV data. The details of all the data utilised in this work are described in Chapter 2.

7.3.1 Background and foreground sources

It is very important to exclude background galaxies and foreground stars from the identified source catalogue. Since the galaxy NGC 300 is located at a high galactic latitude ($b \approx -79°$) (Vlajić et al. 2009), very less number of foreground stars are expected to be present in the field. In order to remove background sources, we divided the whole GALEX tile into two regions having equal area which are shown in Figure 7.4. One is the inner circular region (i.e. galaxy region) having a radius of $25.8'$ and another is the outer annular region (i.e. field region) with an inner and outer radii of $25.8'$ and $36.5'$ respectively. We assumed all the sources present in the outer annular region as background contaminants and used them to remove background sources present in the inner circular region by a statistical technique. We constructed FUV vs (FUV−NUV) colour magnitude diagrams (CMD) for sources present in both the galaxy region and the field region (Figure 7.5). We considered each source in the field CMD and identified its nearest counterpart in the galaxy CMD and then removed it from the inner circular region. In order to do this, we constructed a grid of [magnitude, colour] bins with different sizes, starting from [$\triangle$FUV, $\triangle$(FUV − NUV)] = [0.01, 0.01] and reaching up to a maximum of [0.5, 0.5]. The number of sources present in the inner region and field region are 3880 and 2674 respectively.

Following the above mentioned technique, we removed 2507 number of sources from the galaxy region as background contamination and are left with 1373 sources. We have shown the CMD for 1373 sources in Figure 7.6a. Since the fraction of background contaminants increases with decreasing brightness value, we have further excluded sources fainter than 23 mag in FUV band assuming them to be background galaxies. The foreground stars are expected to have a larger (FUV−NUV) colour. In the study of extended disks of several nearby galaxies using GALEX data, Goddard et al. (2010) considered only sources with (FUV−NUV) < 1.5 to exclude foreground and background sources. We treated sources with (FUV−NUV)

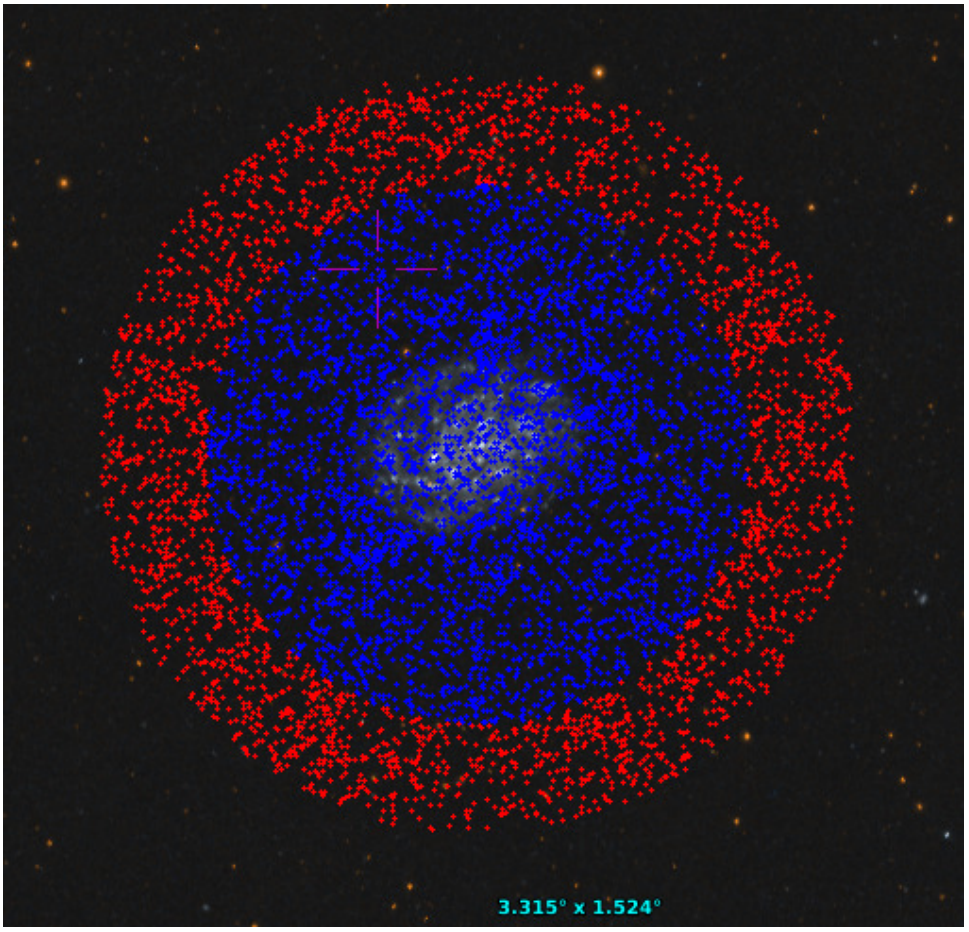

FIGURE 7.4: The identified sources (detected in both FUV and NUV bands) are over plotted on GALEX image of NGC 300. The inner circular region, containing the blue points, is considered as the galaxy and outer annular region with red points is assumed as field region.

> 1.0 as not part of the galaxy and excluded them. The remaining sources are corrected for reddening and extinction (discussed in Section 7.3.2). The sources with corrected (FUV−NUV) < -0.43 ($\sim 7\%$ of the remaining sources) are also excluded since their colour value is outside the model range. Finally, we are left with 742 sources in the galaxy region and considered them as candidate UV sources of the galaxy. The reddening and extinction corrected CMD for these 742 selected UV sources are shown in Figure 7.6b. Since our main interest is to study the outer disk of the galaxy, out of these 742 UV sources we selected 261 sources, which are present between the radii 5.3 kpc (optical radius of NGC 300 (Faesi et al. 2014)) to 10 kpc, for our analysis. These 261 sources are shown in red in Figure 7.6b.

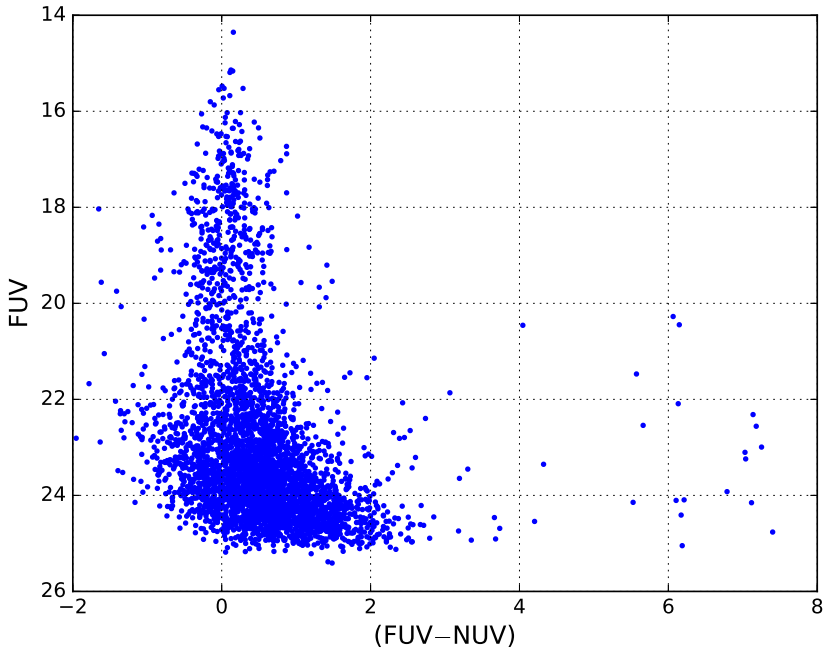

(a)

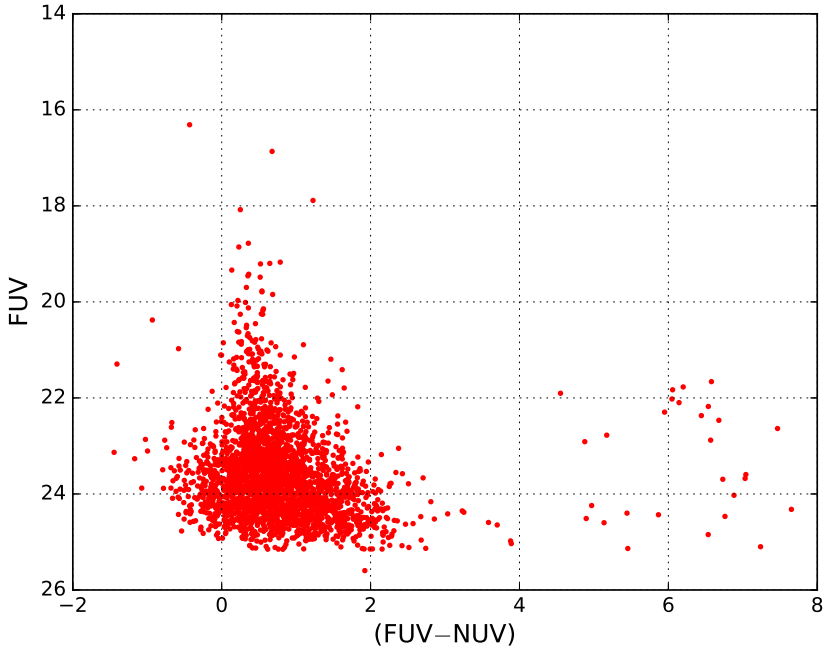

(b)

FIGURE 7.5: Figure (a) shows the FUV vs (FUV−NUV) CMD for galaxy region (blue points in Figure 7.4) and Figure (b) shows the CMD for outer field region (red points in Figure 7.4).

We have also estimated the number of background galaxies in both GALEX FUV and NUV filters following the study of Xu et al. (2005). For the magnitude range 14.2 to 23.7, the estimated number of background galaxies are 0.7/arcmin^2 and 1.4/arcmin^2 respectively in FUV and NUV bands. Through our statistical method, we have excluded 2507 sources ($\sim$ 93% of the total field sources) from the galaxy region, which corresponds to a density of $\sim$ 1.2/arcmin^2, similar to the numbers provided above. We therefore conclude that our sample has negligible contamination due to background as well as foreground sources.

7.3.2 Reddening and Metallicity

We corrected reddening and extinction to estimate the intrinsic (FUV−NUV) colour and both FUV and NUV magnitude for all selected sources. To study the outer stellar disk of NGC 300, Vlajić et al. (2009) considered a foreground reddening E(B−V) = 0.011-0.014 mag. The foreground reddening given in the GALEX catalogue for the field of NGC 300 is also very low (E(B−V) $\approx$ 0.01). Apart from this, interstellar extinction also contributes to reddening inside the disk of a galaxy. Using HST observation, Rodríguez et al. (2016) studied different regions (from inner to outer disk) of NGC 300 by considering a constant reddening of E(B−V) = 0.075 mag. In our study, we also adopted this reddening value throughout the galaxy. Following conversion rules are used to calculate E(FUV−NUV), A(FUV) and A(NUV) from E(B−V).

$$E(FUV - NUV) = R(FUV - NUV)E(B - V) \tag{7.1}$$

$$A(FUV) = R(FUV)E(B - V) \tag{7.2}$$

$$A(NUV) = R(NUV)E(B - V) \tag{7.3}$$

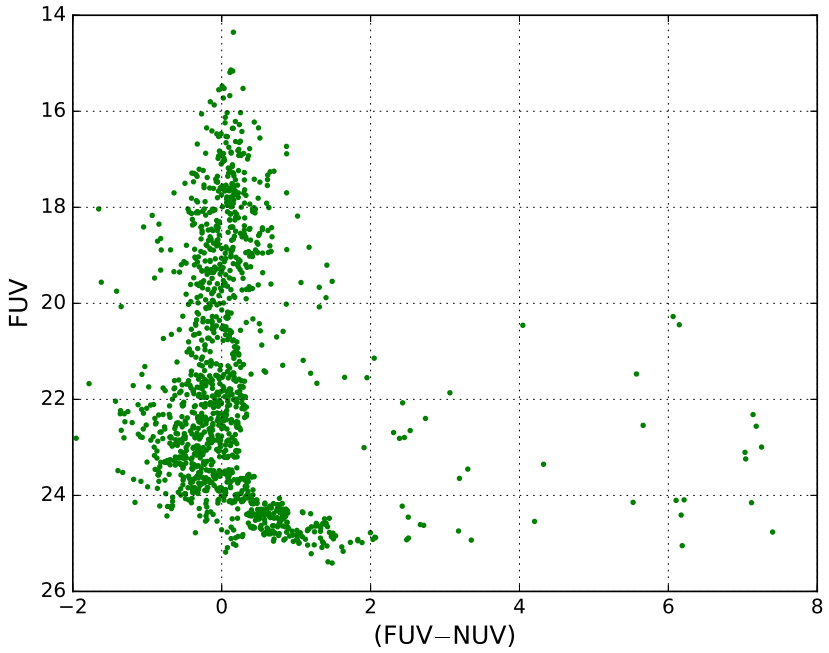

(a)

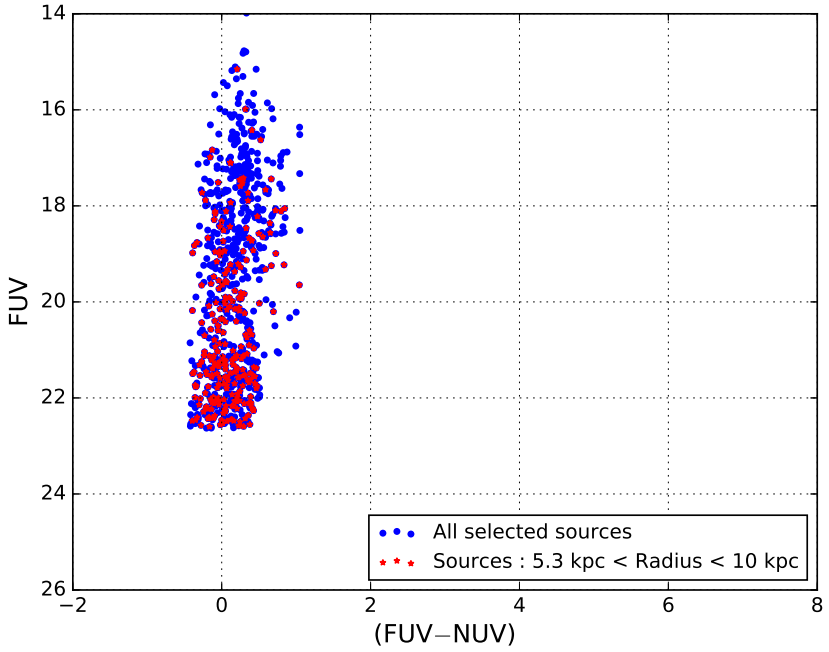

(b)

FIGURE 7.6: Figure (a) shows the FUV vs (FUV−NUV) CMD of sources remaining in the galaxy region after performing background subtraction. Figure (b) shows the CMD of 742 UV sources (reddening and extinction corrected) which are finally considered as part of the galaxy. The sources marked with red star are present in the outer disk between radius 5.3 kpc to 10 kpc.

TABLE 7.3: Details of flux and magnitudes for contours in the FUV map shown in Figure 7.7.

FUV magnitude range (extinction corrected)	$Flux_{FUV}$ $(erg/sec/cm^2/\AA)$ (extinction uncorrected)	Contour colour
< 20	$> 33.6 \times 10^{-15}$	Blue
> 20 & < 21	$13.3 - 33.6 \times 10^{-15}$	Green
> 21 & < 23	$0.21 - 13.3 \times 10^{-15}$	Red

We adopted the value of reddening coefficients from Yuan et al. (2013). Using standard pair technique over a large sample of galactic stars, they estimated the values of R(FUV−NUV), R(FUV) and R(NUV) to be −2.35, 4.89 and 7.24 respectively for GALEX filters. The estimated values of E(FUV−NUV), A(FUV) and A(NUV) are −0.18 mag, 0.37 mag and 0.54 mag respectively. These are used to correct colour and magnitude of all the sources. We used the reddening corrected colour (FUV−NUV) and extinction corrected magnitude (FUV, NUV) throughout our analysis. In order to estimate different parameters of the detected sources, we adopted Z=0.02 as the present day metallicity of star forming regions from the study of supergiant stars in NGC 300 done by Gazak et al. (2015) and Kudritzki et al. (2008).

The parameters of the galaxy are presented in Table 1. We used the relations given in section 2 of van der Marel & Cioni (2001) and calculated the inclination-corrected galactocentric distance (in kpc) for each source by considering the galaxy centre as $\alpha_0 = 13.722833$, $\delta_0 = -37.684389$, distance d = 1.9 Mpc, inclination i = 42.3° and position angle (PA) of major axis $\theta = 109°$.

7.3.3 FUV Disk of NGC 300

In order to identify large massive star forming complex of NGC 300, we produced a 960×960 pixel image from the 3840×3840 pixel GALEX FUV image by binning 4×4 pixels of original image as one single pixel. Each pixel of the binned image has an area coverage of $\sim$ 6×6 arcsec^2 ($\sim$ 55×55 pc^2). The resolution of the image is degraded such that the pixel size becomes comparable to the average size of young stellar groups in NGC 300 identified by Rodríguez et al. (2016). Since far-UV radiation is mainly contributed by massive young stars, we considered the image in FUV filter for this purpose. To understand the distribution of star forming regions, we created different contours by fixing the lower and upper limit of fluxes which are given in Table 7.3. The FUV image with different contours is shown in Figure 7.7.

The massive star forming complexes of NGC 300 are picked up by the blue contours created for pixel brighter than 20 magnitude (i.e. $Flux_{FUV} > 33.6 \times 10^{-15}$ $erg/sec/cm^2/\mathring{A}$). The two main spiral arms of the galaxy, one along north-west (NW) and another along east to north-east (NE), are found to have massive star forming complexes which all together follow the spiral structure. Almost all of these complexes are found to be present within the optical radius (R_{25}) of the galaxy. The green contours, signifying relatively less bright regions, are found around each of the blue contoured regions. The red contours, generated for pixels fainter than 21 magnitude and brighter than 23 magnitude, trace the extended structure of the FUV disk nearly up to a radius 7 kpc. The north-eastern spiral arm, which do not have much massive complexes, is mainly covered by this red contour. We do see two extended structures along the major axis (south-east (SE) to NW) of the galaxy which are mainly picked up by the red contours. The regions covered by red contour in the east and northern part, extend beyond the optical radius (R_{25}) of the galaxy. Therefore, NGC 300 has an extended UV disk with relatively less massive star forming complexes when compared to the inner disk.

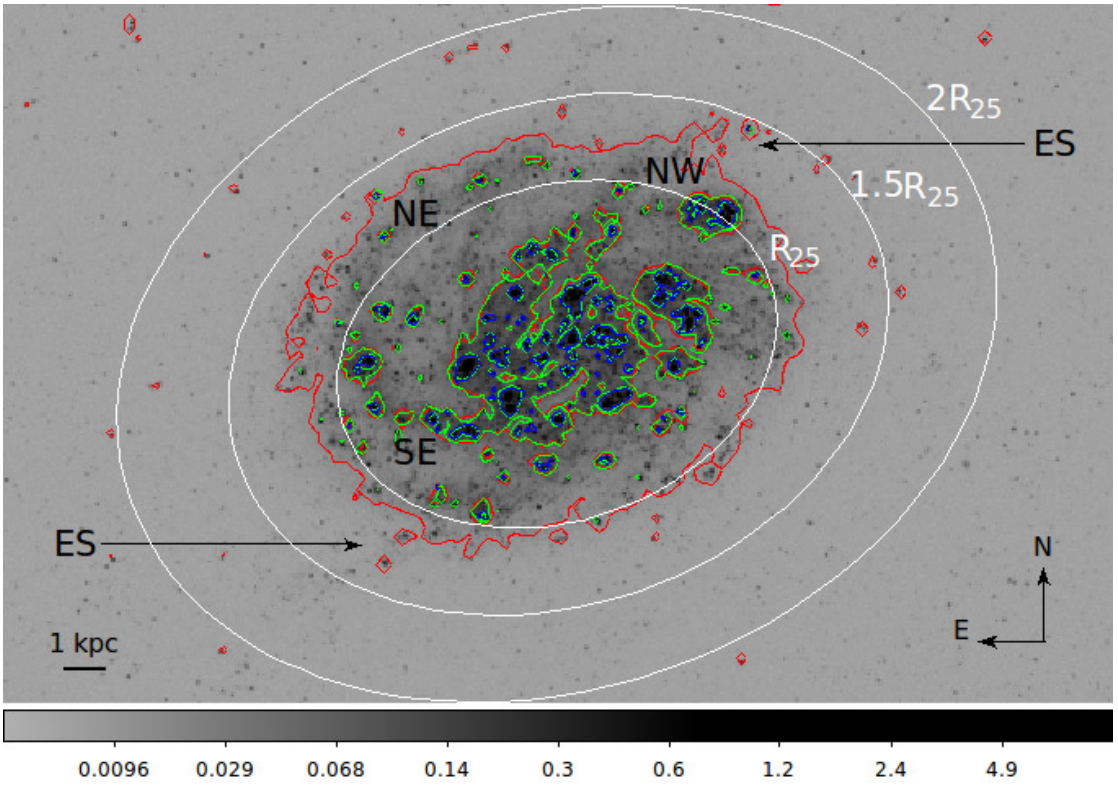

FIGURE 7.7: The background figure is the binned 960×960 pixel FUV image of NGC 300 with different contours plotted for different limits of FUV flux value as mentioned in Table 7.3. The blue contours represent the brightest (hence massive) regions of the galaxy. The grey scale of the image denotes counts per second per pixel. The ellipses shown in the figure signify R_{25}, $1.5R_{25}$ and $2R_{25}$ galactocentric distance respectively. Two extended structures (ES) are also shown by arrow.

7.3.4 Correlation with optical image

As the young massive stars have a large continuum flux in UV, when compared to optical, a correlation between UV and optical emission will eventually help to trace the young star forming regions. In order to correlate the FUV disk of NGC 300 with the optical disk, we have over plotted the blue and green contours of Figure 7.7 on the DSS optical image of the galaxy in Figure 7.8. The yellow contour in Figure 7.8 displays the main part of the optical disk of the galaxy. It is noticed that the massive complexes identified in the GALEX FUV image of NGC 300 (blue and green contour) correlate well with the optical disk structure

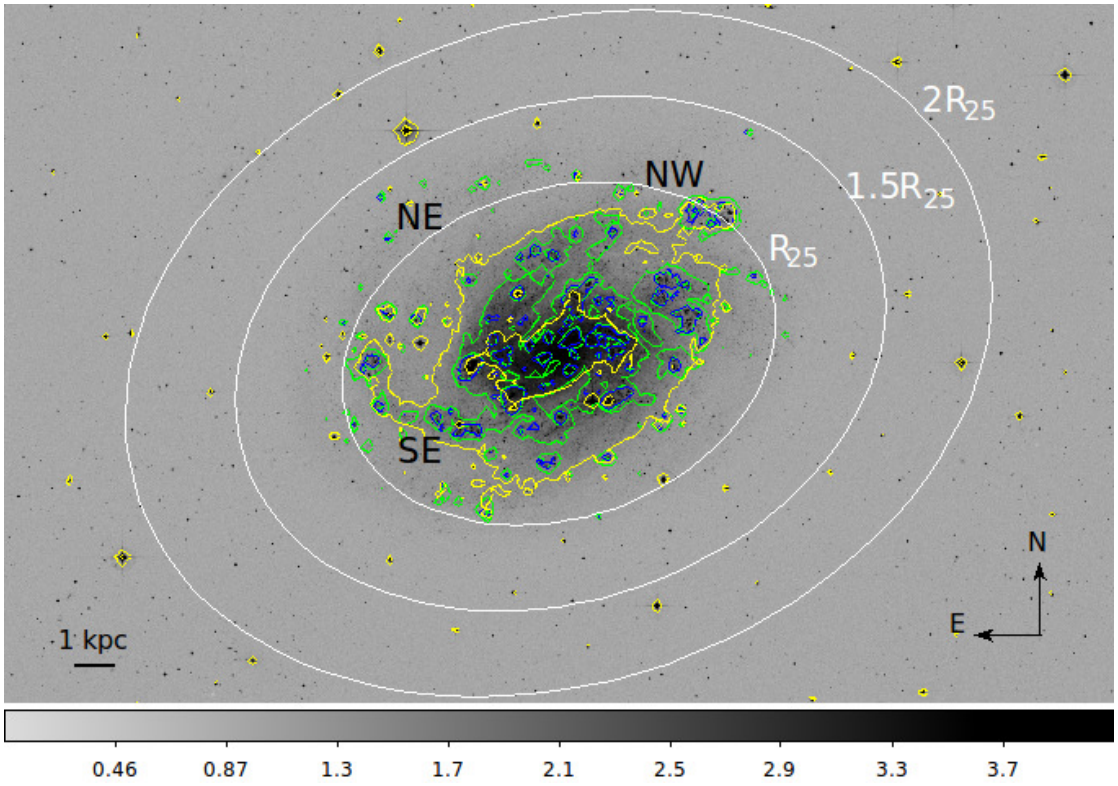

FIGURE 7.8: The background figure shows the DSS optical image of NGC 300. The yellow contoured region represents the main optical disk of the galaxy. Blue and green contours are same as shown in Figure 7.7.

(yellow contour) of the galaxy. It is to be noted that, the optical emission arising from the north-eastern spiral arm of the galaxy is very low compared to other regions of the galaxy, whereas in the FUV image (Figure 7.7), we can clearly notice the spiral arms and the extended structures present in the outer disk of the galaxy. Therefore, the extended disk, identified in UV, is not easily noticeable in the optical image of the galaxy.

7.3.5 Correlation with H I

In order to correlate the distribution of young star forming regions and H I column density of the galaxy, we over plotted the FUV contours of Figure 7.7 on the H I

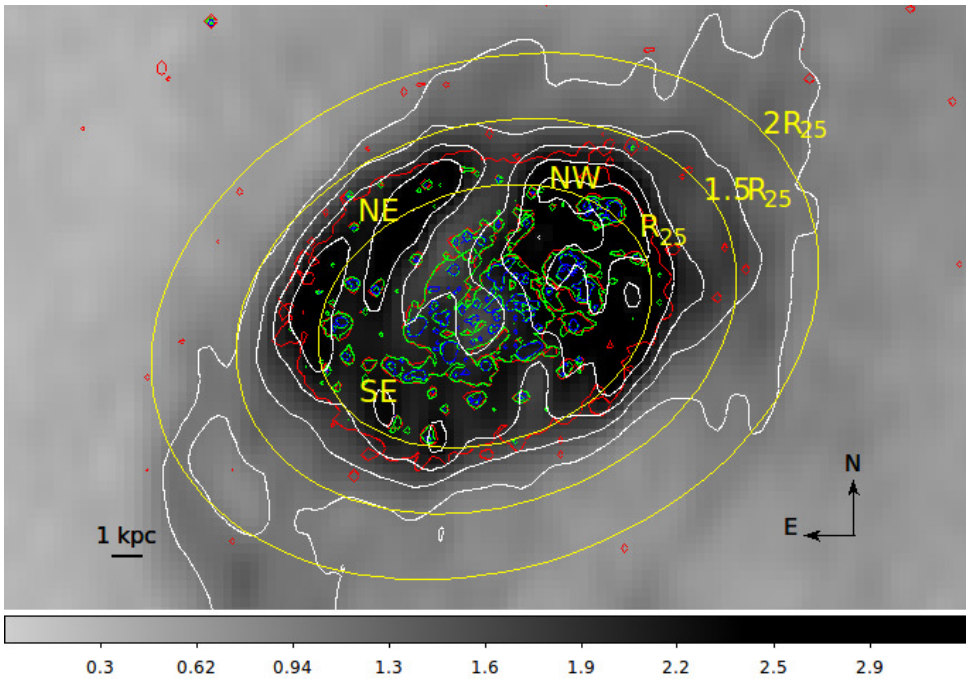

(a)

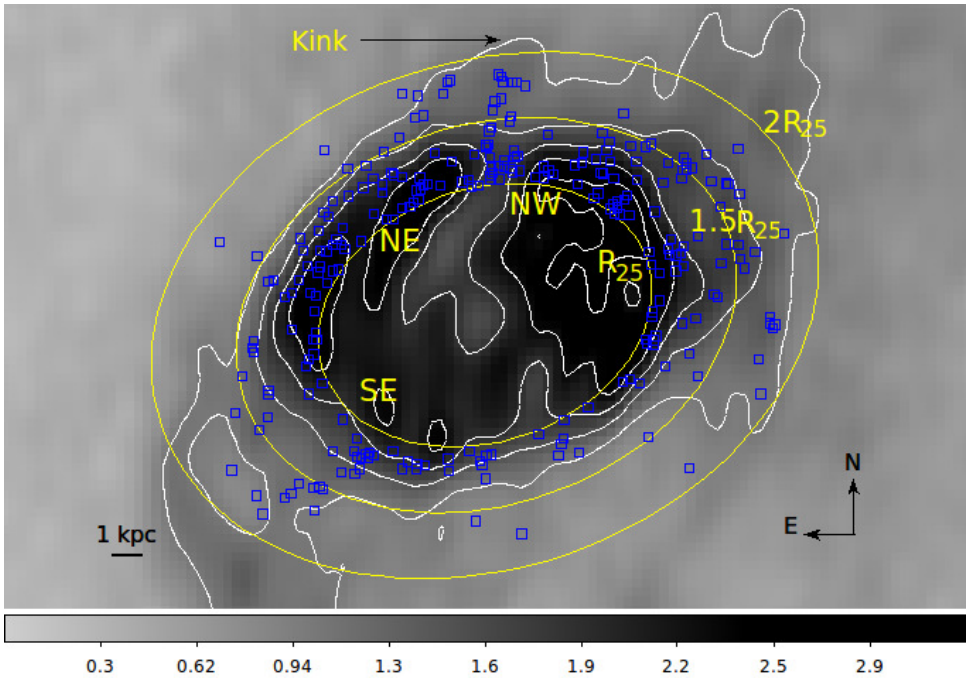

(b)

FIGURE 7.9: The H I density contours are shown in white on the background H I density map of NGC 300 in both figures. The unit of the grey scale is Jy/beam. The blue, green and red contours shown in Figure (a) are the same as Figure 7.7. In Figure (b) we have shown the distribution of UV sources (blue points) present in the outer disk (between 5.3 kpc and 10 kpc) of NGC 300.

map in Figure 7.9a. The H I density contours, generated for a higher threshold value, are shown in white in the same figure. It is noticed that the extent of the detected FUV disk of the galaxy is well within the dense H I disk. H I contour map shows a large compression of gas in the south-eastern part of the galaxy. Westmeier et al. (2011) found that the south-eastern side showed a distinctive plateau, followed by a sudden and steep drop in the column density of the H I disk, which is not found in the north-western side. The UV sources which are present along the north-eastern spiral arm of the galaxy are also found to coincide with the dense H I contours (Figure 7.9b). A kink in the density contour is also seen in the northern direction and it coincides with the extended structure identified in the source distribution. The extended features noticed along south-east and north-west direction also follow the extended density contour of H I.

7.3.6 Correlation with 24 μm infrared image

The star forming regions of the galaxy NGC 300 are found to have strong 24 μm infrared emission (Helou et al. 2004). Since the dust present in the star forming regions gets heated by the FUV photons originating from the massive stars which in turn produces radiation in 24 μm, it is expected that the massive star forming complexes detected in FUV image of NGC 300 should also show emission in 24 μm. In order to verify this, we over plotted the blue contour (of Figure 7.7), signifying massive star forming complex, on the infrared 24 μm image of the galaxy in Figure 7.10. The red contours shown in the figure indicate the regions with intense 24 μm emission. It is noticed that for the inner disk both the blue and red contours show a good spatial correlation which signifies the location of active star forming regions in NGC 300. We also note that a few FUV emission regions located within R_{25}, do not have corresponding 24 μm emission. This may be due to a variety of reasons such as, difference in resolution and sensitivity of the detections in

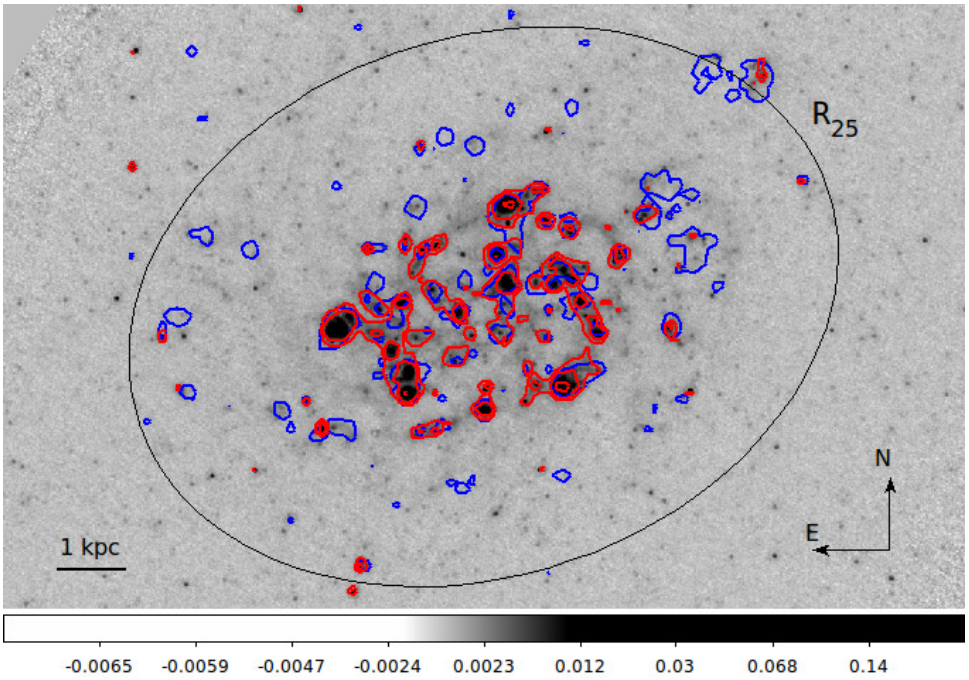

FIGURE 7.10: The MIPS 24 μm image of NGC 300 is shown in the background with red contours indicating regions with intense infrared emission. The same blue contours of Figure 7.7 are also shown. The unit of the grey scale is MJy/sr.

these wavelengths, reduced dust in the outer regions, presence of a few possible not-so-young star forming regions without dust etc.

7.3.7 Luminosity density profile

The emission from stellar population of different ages peaks in different wavelengths. The older populations show significant emission in optical and infrared bands whereas emission from younger populations mainly peak in UV. In order to trace the disk of NGC 300 in different wavelengths, we produced normalised surface luminosity density profiles of the galaxy in different wavebands which are shown in Figure 7.11. These profiles depict the nature of the galaxy disk in different wavelengths. The disk scale-length (R_d) of NGC 300 is reported to be 2.10 kpc and 1.47 kpc respectively in optical B band and infrared I band (Carignan 1985;

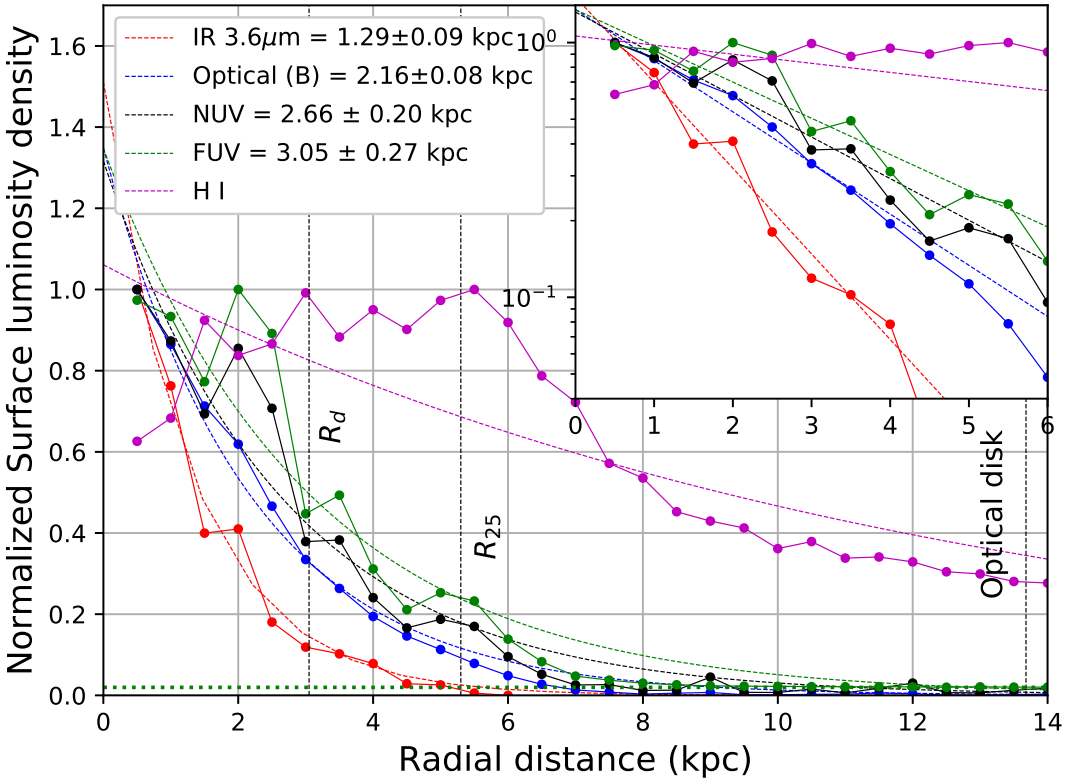

FIGURE 7.11: The normalised surface luminosity density profiles of NGC 300 in different wavebands are shown in different colours. The solid lines denote the observed profiles whereas dashed lines of the same colour show the fitted exponential profiles. Three vertical black dashed lines are plotted to show the FUV scale-length (R_d) (our study), optical radius (R_{25}) and the extend of optical disk of the galaxy from Bland-Hawthorn et al. (2005). The horizontal dotted green line represents the FUV background. In inset, we have shown all the observed and fitted profiles in logarithmic scale up to radial distance of 6 kpc.

Kim et al. 2004). These two independent measurements highlight that the disk is more extended in shorter wavelengths. We used GALEX FUV and NUV, DSS optical B band and infrared 3.6 μm IRAC images to estimate disk scale-length by fitting an exponential curve to each of the observed profiles, shown in Figure 7.11 in different colours. The measured values of scale-length are 1.29±0.09 kpc, 2.16±0.08 kpc, 2.66±0.20 kpc and 3.05±0.27 kpc respectively for infrared, optical B band, NUV and FUV respectively. This suggests that the disk of NGC 300 gradually extends to larger radii from longer to shorter wavelengths. The distribution of younger populations, traced by the FUV disk, is found to be more

extended than the rest. This thus confirms the presence of XUV disk in the galaxy NGC 300.

The average FUV background, estimated from the flux measured between radii 14 and 15 kpc, is shown in green dotted line. The observed FUV luminosity density profile nearly converges to background level at radius $\sim$ 12 kpc. Therefore, we conclude that the disk of NGC 300 is extended at least up to $\sim$ 12 kpc. We have also shown the radial H I column density profile of the galaxy in the same figure. The behaviour of this profile is found to be different than the rest. Instead of an exponential nature like other bands, it shows a dip in the central part with gradual increase up to a radius $\sim$ 5.5 kpc. Beyond this radius the profile drops down slowly in the outer disk. We did not show the Hα profile because the image available for that in NED has a radial coverage of around 4 kpc, which is less than the optical radius of the galaxy.

7.3.8 Star formation rate

To estimate the SFR of NGC 300, we considered a radius of 10 kpc (1 $\sim$ 2 R_{25}) and measured the total flux within that from the GALEX FUV image. This flux is corrected for extinction and background as discussed in previous section and further converted to magnitude. We used equation 7.4 from Karachentsev & Kaisina (2013b), where mag_{FUV} denotes the background and extinction corrected magnitude and D is the distance to the galaxy in Mpc, to calculate the SFR ($M_{\odot}/yr$) of the galaxy. The total SFR integrated up to a radius 10 kpc for NGC 300 is found to be 0.46 $M_{\odot}/yr$, which nearly matches with the earlier estimate of 0.30 $M_{\odot}/yr$ by Karachentsev & Kaisina (2013b). To generate the radial profile of SFR density ($M_{\odot}/yr/kpc^2$), we similarly considered annuli of width 0.5 kpc from the centre to a radius 10 kpc and measured the background and extinction corrected FUV magnitude per kpc^2 in each individual annuli. We used equation 7.4 to estimated

the SFR for each annuli and plotted radially in Figure 7.12. The profile shows that the central 2 kpc of the galaxy shows high SFR density. After that it starts decreasing and becomes little stable inside the radius 5.5 kpc. Beyond this radius the SFR density becomes very small compared to the inner disk.

In a study of NGC 300 using HST data, Gogarten et al. (2010) calculated the radial SFR density ($M_{\odot}/yr/kpc^2$) for different age ranges. They used three HST ACS fields oriented as a radial strip from centre to outside of the galaxy in the western part. These fields thus cover a limited part of the galaxy's inner disk. Our study instead considered the whole galaxy disk observed by GALEX to estimate the azimuthally averaged radial SFR density profile of NGC 300. Both of these measurements have different area coverage and hence values are expected to be different. In order to check only the nature of radial profile from both the studies, we have plotted the values from Gogarten et al. (2010) for the age range 4-80 Myr (Figure 7.12 (red curve)), after scaling it to our estimations. The plot highlights that though HST covers a specific part of the disk, the nature of radial profile closely follows that estimated for the whole disk with GALEX in this study.

$$log(SFR_{FUV}(M_{\odot}/yr)) = 2.78 - 0.4 * mag_{FUV} + 2log(D) \tag{7.4}$$

7.3.9 Age estimation of UV sources

The diagnostic diagram shown in Figure 7.2 can be used to estimate the age of a source from its (FUV−NUV) colour for a given metallicity. As NGC 300 is observed to have solar metallicity, we considered the blue curve (Z=0.02) in Figure 7.2 to estimate the age of identified UV sources. The sources detected in the inner disk have crowding issue. Because of the poor spatial resolution of GALEX, a

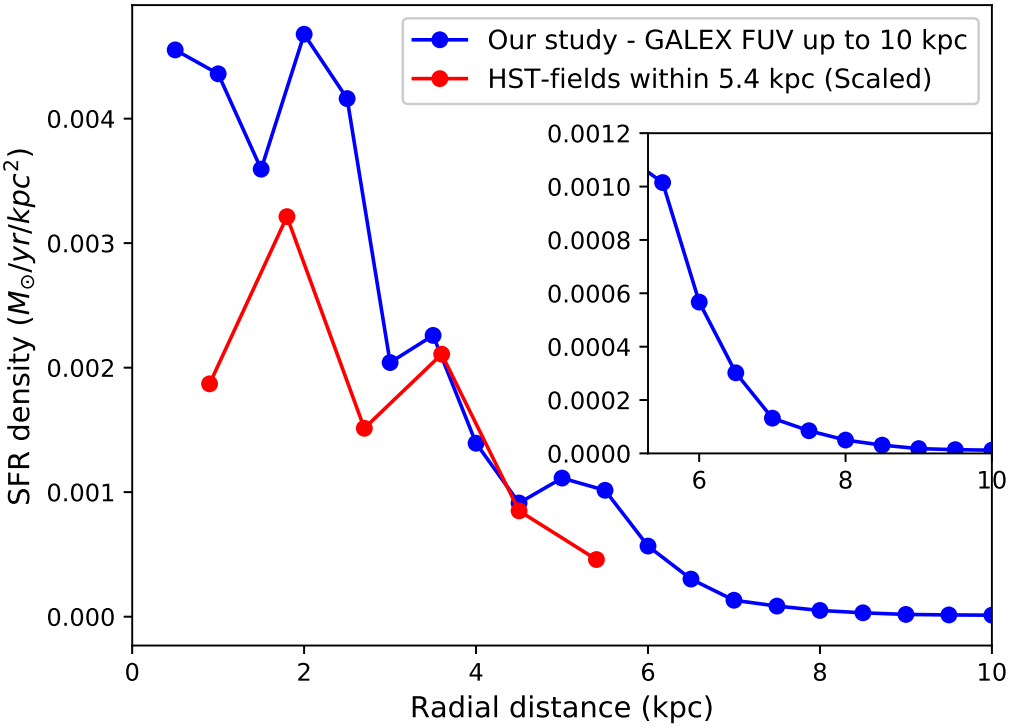

FIGURE 7.12: The radial profile of SFR density ($M_\odot/yr/kpc^2$) is shown up to a radius 10 kpc (blue curve). The red curve shows the scaled value of SFR density ($M_\odot/yr/kpc^2$) as calculated through an HST study by Gogarten et al. (2010). The radial profile of SFR density between radii 5.3 kpc and 10 kpc is shown in the inset.

combination of multiple sources in the inner disk can appear like a single source. Whereas in the outer disk of the galaxy, artefact due to crowding is much reduced. Also, out of 742 we selected 261 sources having galactocentric distance greater than 5.3 kpc and less than 10 kpc for our study. We do not consider sources beyond 10 kpc for contaminants might be more in the far outer disk. We used the reddening corrected observed colour of these 261 UV sources and interpolated it with the model data (blue curve) to estimate their ages within the range 1 to 400 Myr. In Figure 7.13, we have shown the age histogram for these selected UV sources. The figure signifies that the outer disk of NGC 300 has a large number of young sources with age less than 25 Myr.

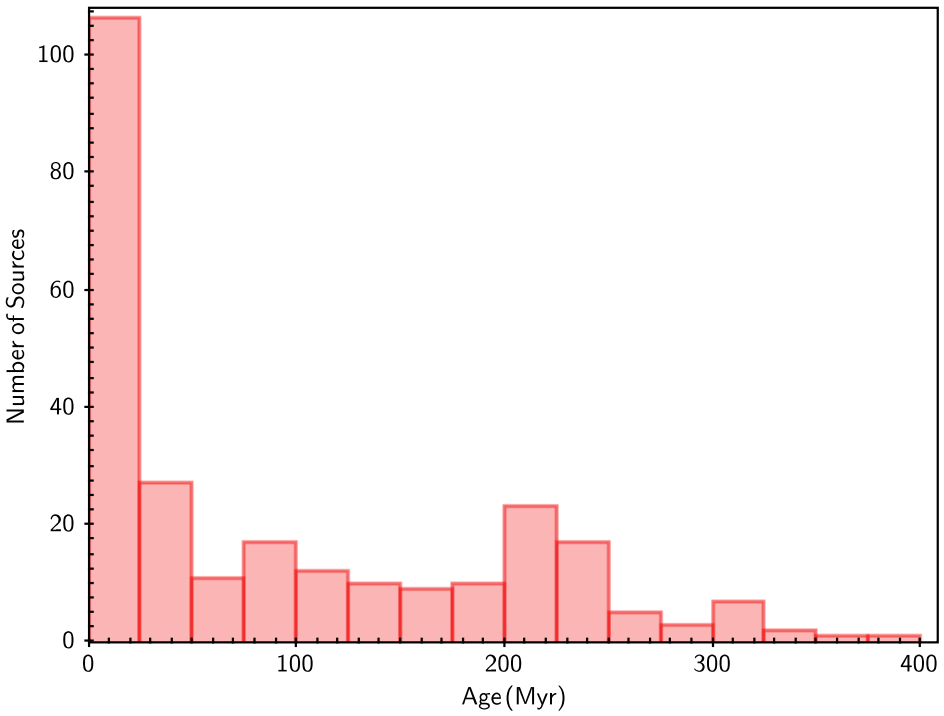

FIGURE 7.13: Age histogram of all the selected UV sources between radius 5.3 kpc and 10 kpc.

7.3.10 Spatial age distribution of UV sources

In order to visualise the spatial age distribution of these 261 selected UV sources, we separated them into two groups, one as the young group (Age $<$ 25 Myr) and another one as relatively older group (Age $>$ 25 Myr). The sources in each groups are then over plotted on the GALEX FUV image in Figure 7.14. 60% of the sources with age $<$ 25 Myr are found to be present between PA 0 - 180° whereas 40% are present between PA 181-360°. In case of sources older than 25 Myr, the scenario is exactly opposite to this. Majority of the younger sources (Age $<$ 25 Myr) are found to be present along the north-eastern spiral arm of the galaxy (Figure 7.14a). The extended part of a spiral arm seen in the western part of the galaxy are found to be populated by most of the older sources (Figure 7.14b). The elongated distribution of sources along the major axis of the galaxy (south-east to north-west) is seen only for the older sources.

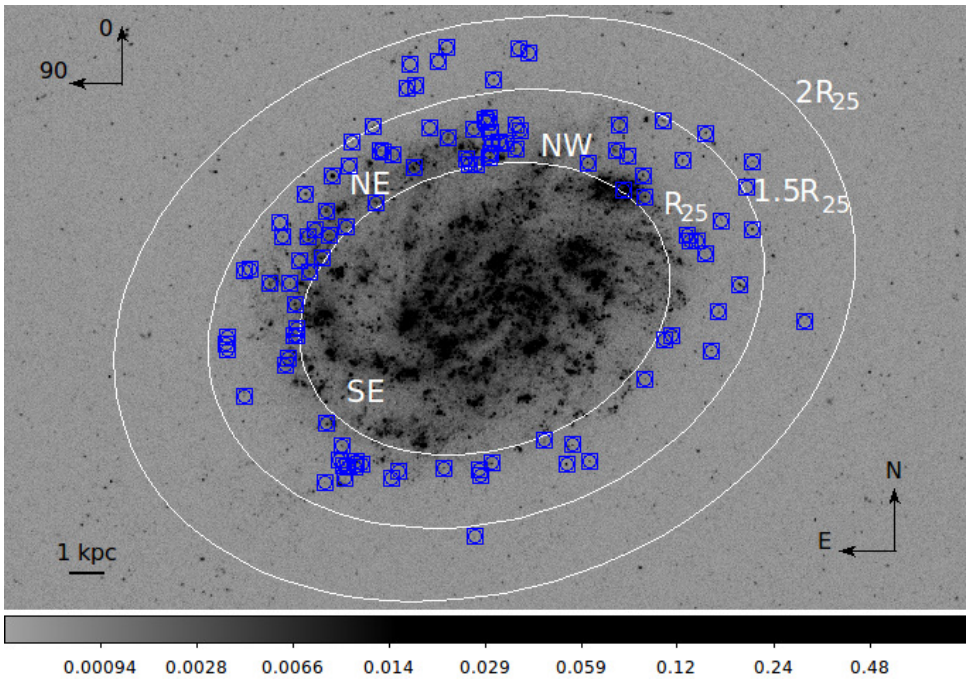

(a)

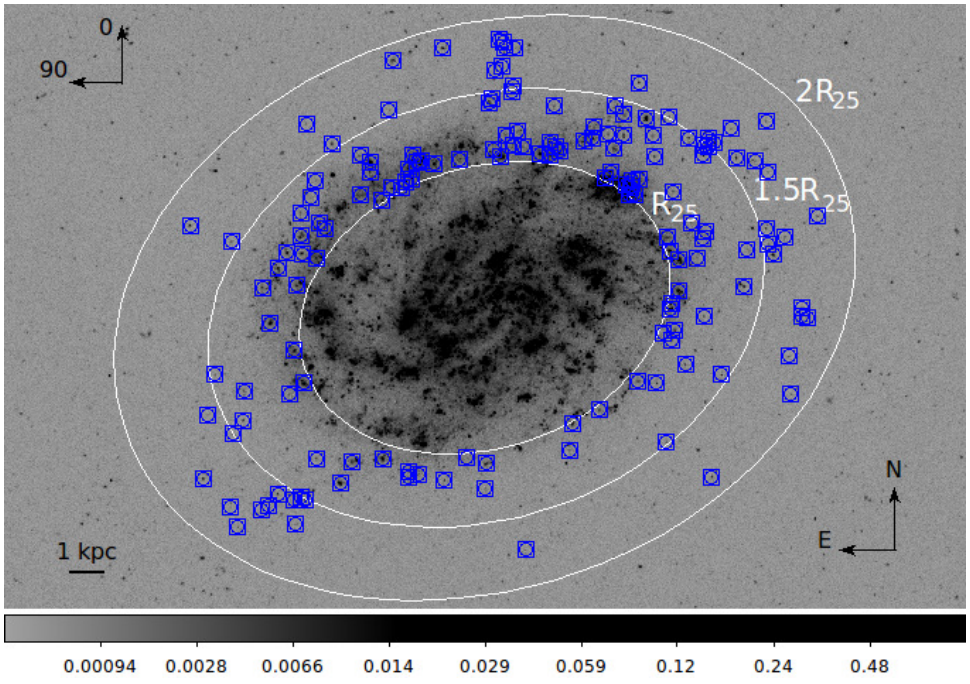

(b)

FIGURE 7.14: The selected UV sources (blue square) in the outer disk are overplotted on the GALEX FUV image of the galaxy. Figure (a) shows the spatial position of younger sources (Age $<$ 25 Myr) and the relatively older sources (Age $>$ 25 Myr) are shown in Figure (b). The reference PA is shown in the top left corner.

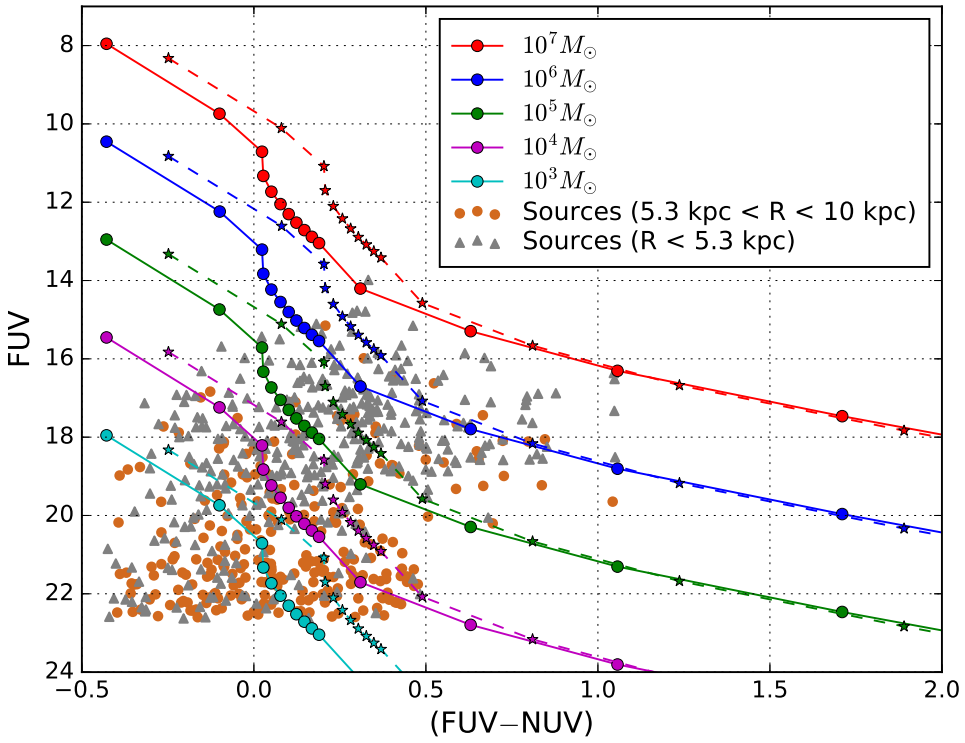

FIGURE 7.15: The selected UV sources are shown on the simulated plot presented in Figure 7.3. The sources present in the outer disk between radii 5.3 kpc to 10 kpc are shown in brown circles whereas grey diamonds represent the sources in the inner disk within radius 5.3 kpc.

7.3.11 Mass estimation of UV sources

The SSP models as shown in Figure 7.3 suggest that for a given colour (equivalently age), FUV magnitude changes with cluster mass. We plotted 742 selected sources on the simulated figure shown in Figure 7.3 and displayed it in Figure 7.15. This figure helps us to estimate mass for each selected source. We performed a linear interpolation between the two nearest model generated magnitude values to estimate the mass of a source corresponding to the observed extinction corrected magnitude. As our study aims to explore the outer disk only, we estimated mass for 261 sources present between radii 5.3 kpc to 10 kpc ($1 \sim 2$ R_{25}) of the galaxy. The histogram of the estimated masses of all these 261 sources is shown in Figure

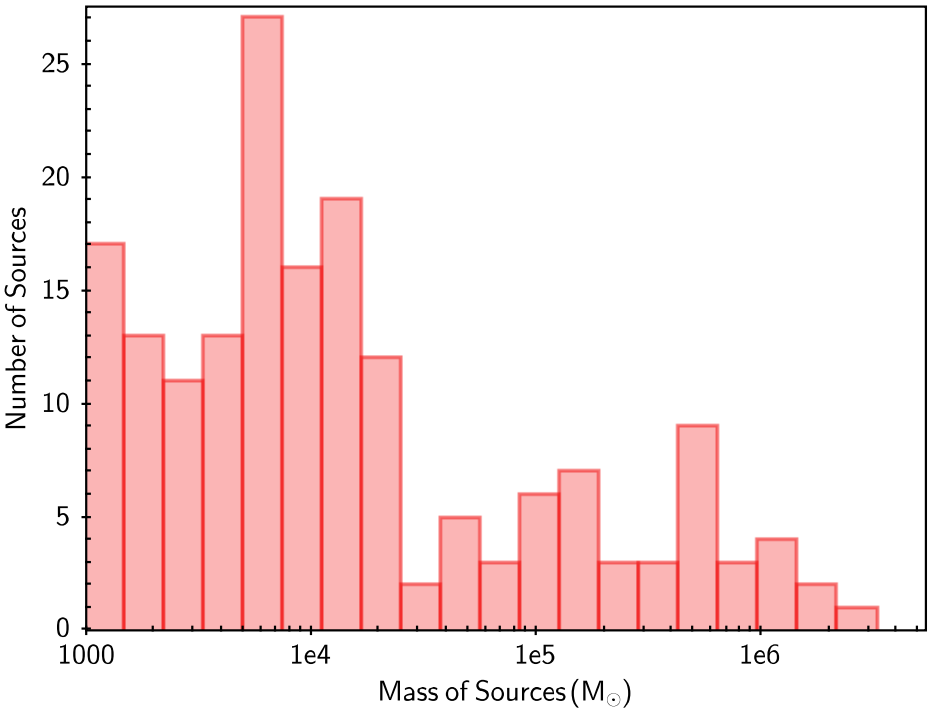

FIGURE 7.16: Mass histogram of the detected UV sources present between radius 5.3 kpc and 10 kpc is shown. Sources with mass below $10^3 M_\odot$ are not displayed in the figure.

7.16. The figure clearly shows that majority of the sources present in the outer disk of the galaxy have mass less than $10^5 M_\odot$. The sources with masses below $10^3 M_\odot$ are not shown in Figure 7.16 as their measured value is not accurate due to the lower limit of model mass range (Figure 7.3). The sources identified in the inner disk are relatively more massive. There can be an artefact of assuming multiple sources as single one due to the crowding in the inner disk.

7.3.12 Spatial mass distribution of UV sources

In order to map the mass distribution of UV sources in the outer disk we have separated the selected sources in three groups, such as high mass (M $> 10^5 M_\odot$), intermediate mass ($10^3 M_\odot$ <M< $10^5 M_\odot$) and low mass (M $< 10^3 M_\odot$) and over

plotted them on GALEX FUV image in Figure 7.17. The massive sources are small in number and are mainly found near to the inner disk of the galaxy (Figure 7.17a). The extended arm in the north-west direction is found to have a few massive sources. We see this arm to be extended more in the outer disk in Figure 7.17b, where it is populated by intermediate mass sources. The inner part of north-eastern spiral arm is also found to have intermediate mass sources. The low mass sources, which are not shown in Figure 7.16, are mostly seen in the outer part of the north-eastern spiral arm (Figure 7.17c). We also noticed two clumps of low mass UV sources, one in the northern part and another in the south-eastern part of the galaxy. Figure 7.17 conveys that the outer disk of NGC 300 has mostly formed low and intermediate mass sources ($\sim$ 86% of the selected sample), in the last few hundred Myr.

7.4 Results and Discussion

Understanding the nature of star formation in the outer part of disk galaxies is important ingredient to the evolution of the galaxy (Barnes et al. 2011). As the outer disks of galaxies have lower gas density, lower metallicity and lower dust content, altogether it offers an extreme environment to explore the characteristics of star formation (Zaritsky & Christlein 2007; Barnes et al. 2011). Detection of young star forming complex in the outer disk is also important to test the star formation threshold. The young and massive OB stars contribute a substantial amount of far-UV radiation which can trace the location of young star forming regions in a galaxy. The key aim of this study was to decipher the FUV disk properties of NGC 300 and to understand the age and mass distribution of UV sources in the outer disk of the galaxy.

The detection of several extended structures in the FUV image strongly validates

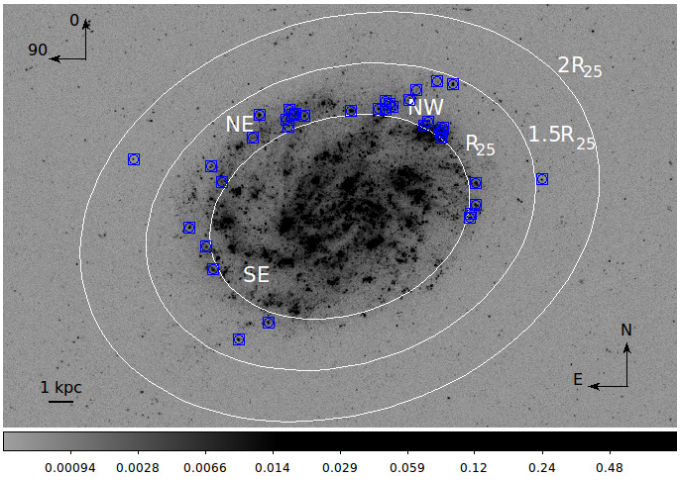

(a)

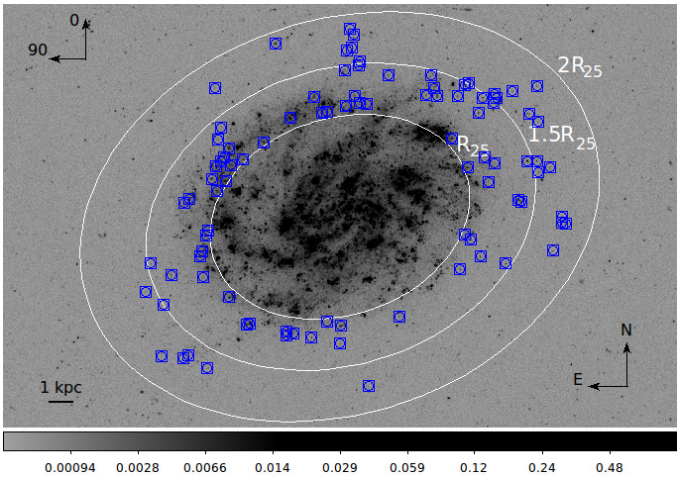

(b)

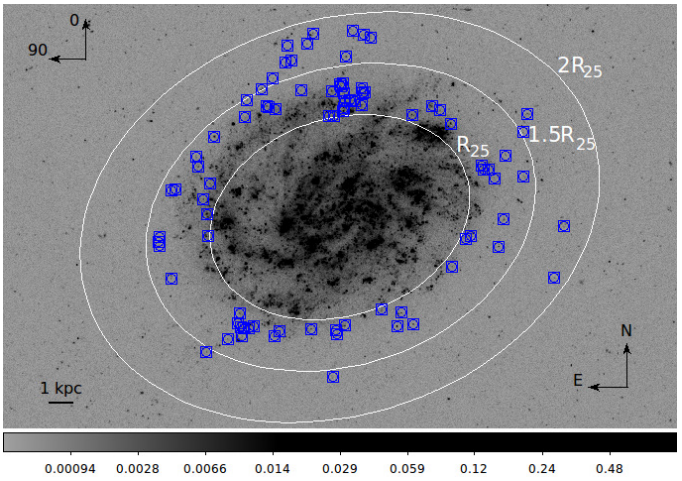

(c)

FIGURE 7.17: The figures show the mass distribution of UV sources in the outer disk of the galaxy. Figure (a) shows the high mass (M> $10^5 M_\odot$) sources, Figure (b) shows intermediate mass ($10^3 M_\odot$ <M< $10^5 M_\odot$) sources and low mass sources (M< $10^3 M_\odot$) are shown in Figure (c).

the presence of an outer disk in NGC 300. The galaxy is found to form substantially large number of objects during the last 25 Myr in its outer disk. The spiral arm present in the north-eastern direction is mainly populated by these young sources. Though we see a low level optical emission from this region of the galaxy, the detection of significant number of young sources in the UV image conveys that star formation in the north-eastern spiral arm is a recent phenomenon. Rodríguez et al. (2016) identified 1147 young stellar groups by studying six different regions of NGC 300 through HST observations. They reported an age range from 1 to 235 Myr for all the stars present in the blue bright groups. Using another HST observation, Hillis et al. (2016) identified 576 stars with an age between 10 to 200 Myr in one of their chosen fields. We are also obtaining an age range of 1-300 Myr for the selected sources in our study.

The radial luminosity density profiles in different wavebands suggest that the disk of NGC 300 gradually becomes more extended from longer to shorter wavelengths. The scale-length estimated in FUV is found to be 2.3 times larger than that in infrared. This signifies that the older populations are more centrally concentrated in the galaxy disk whereas the younger ones show more extended distribution. This also confirms the presence of XUV disk in NGC 300. The radial profile of the H I column density show a relatively flatter profile which suggests that star formation can trigger in the outer disk of the galaxy under favourable conditions.

Another important finding is the correlation between the H I map and the identified young UV sources. The north-eastern spiral arm, prominently seen in the UV image, is found to coincide with dense H I gas. A large fraction of the young sources are also identified along this arm. The galaxy is believed to move in the south-east direction (Westmeier et al. 2011), which has caused the compression of H I gas in the south-east part of the disk. The H I contour map also shows a compression in the north-eastern direction, followed by dense H I gas. The star formation in the north-east region is likely to be due to this compression. We also

detect a clump of low mass sources at the base of northern extended structure.

With the help of starburst99 SSP model, we have analysed the GALEX photometric data of the galaxy, NGC 300, and estimated the age and mass of identified sources present in the outer disk. As these sources are likely to be star clusters, we derive the recent cluster formation history of the galaxy. As the formation of clusters is closely related to the formation of stars in general, the cluster formation episodes are likely to suggest star formation episodes as well.

The parameters estimated in this study are based on the SSP model. We have assumed instantaneous star formation and stellar IMF as Kroupa, which is appropriate to study star formation in nearby galaxies. The errors of the estimated parameters (age and mass) are calculated from the photometric errors of both FUV and NUV magnitudes. The range of photometric error for the (FUV−NUV) colour is 0.01 - 0.10. This error will reflect in the estimated age of the sources. The error in age for most of the sources present in the outer disk is less than 20 Myr. Some of the young sources (age $<$ 150 Myr) show larger error whereas sources older than 200 Myr have less error in estimated age. The photometric error in FUV magnitude will contribute to the error in the estimation of mass. This error also has a range 0.01 - 0.10, which corresponds to 0.5 - 5 % error in the estimated mass for all the sources. The estimation of age has a dependency on reddening and metallicity. We have assumed moderate reddening and any decreased reddening will make the ages younger. The metallicity for the entire disk is assumed to be Solar. If there is a significant gradient in the metallicity, the age estimation will be affected by the dependency as can be seen in Figure 7.2. The estimation of mass also has a dependence on the adopted extinction correction. As our study primarily explores the recent star forming regions, we have assumed a moderate value of reddening and thus extinction. Any reduction in the assumed reddening will increase the FUV magnitude and the mass of a source and vice versa.

The outer disk of NGC 300 shows low level UV luminosity whereas optical studies indicate the presence of an unbroken stellar disk (Bland-Hawthorn et al. 2005). We detect several low mass sources in the outer disk of the galaxy. We found that the wispy extension of inner disk identified by Thilker et al. (2007) is due to these low mass young sources and slightly older intermediate mass sources. The low level star formation in the outer disk of NGC 300 may happen because of the less-availability of H I. Mild perturbation due to the motion of the galaxy and ram pressure of the sculptor group medium could be causing the star formation in the outer disk. Therefore, this may be the process with which the outer disk is built in this galaxy.

The mass distribution of selected UV sources suggests that the outer disk has predominantly formed low and intermediate mass sources (M$< 10^5 M_\odot$). Majority of the young sources (age < 25 Myr) detected along the north-eastern spiral arm are found to have low mass which signifies a low level recent star formation in the galaxy. We considered Kroupa IMF to estimate mass of UV sources with the help of SSP model. Keeping other parameters as same (Table 7.2), we changed the IMF value to 2.35 (classical value, Salpeter (1955)) with a stellar mass range from 0.1 - 120 $M_\odot$ and estimated the mass of the sources. The estimated masses were 1.3 - 1.8 times the mass estimated using kroupa IMF. The regions with intense 24 μm infrared emission in the galaxy spatially correlate with the massive star forming complexes detected in the inner disk of NGC 300. Faesi et al. (2014) studied 76 H II regions in the disk of NGC 300 and estimated the stellar mass associated with each region. They found a range of mass from $10^3 M_\odot$ to $4 \times 10^4 M_\odot$. The young stellar groups, identified by Rodríguez et al. (2016), with substantially large number of stars are also likely to have total mass greater than $10^3 M_\odot$. In our study, we obtained a mass range from $10^3 M_\odot$ to $10^6 M_\odot$ (with some below $10^3 M_\odot$) for the sources present in the outer disk between 5.3 kpc and 10 kpc.

The nature of FUV luminosity density profile of NGC 300 points to the presence

of an inner disk up to 5.5 kpc and an extended outer disk at least up to 12 kpc. The SFR of NGC 300 is found to be $\sim 0.46\ M_{\odot}/yr$. Considering the GALEX FUV data Verley et al. (2009) reported a SFR of 0.55 $M_{\odot}/yr$ for the galaxy M33. M33 is considered as the near optical twin of NGC 300 and they both have similar H I mass. Therefore, the comparable values of SFR observed in both the galaxies signifies that they are undergoing a similar state of star formation.

7.5 Summary

The main results of this study are summarised below:

1. Using GALEX UV data, we identified several extended structures in the outer part of the galaxy and confirmed the presence of an XUV disk in NGC 300.

2. The inner disk of the galaxy has a radius of 5.5 kpc whereas we detect an outer disk at least up to radius 12 kpc.

3. The disk scale-length, which found to increase gradually from longer to shorter wavelength, is estimated to be 2.66±0.20 kpc in NUV and 3.05±0.27 kpc in FUV.

4. We identified 261 candidate UV sources in the outer disk between radius 5.3 kpc to 10 kpc (1∼2 R_{25}) and estimated their age and mass by applying SSP models.

5. We noticed a richness of younger (Age $<$ 25 Myr) as well as low and intermediate mass (M $< 10^5 M_{\odot}$) sources in the outer disk of the galaxy.

6. The star formation in the north-eastern spiral arm of the galaxy is a recent phenomenon, consisting of low mass sources with age $<$ 25 Myr.

7. The distribution of UV sources identified in the outer disk correlates well with the features of H I density map.

8. Presently, the galaxy is undergoing a low level recent star formation in the outer disk ($\geq$ R_{25}), which may be due to its motion in the Sculptor group.

9. The SFR of NGC 300 ($\sim$0.46 $M_{\odot}/yr$) is found to be comparable with its near optical twin M33.

Chapter 8

Conclusions and Future Work

In this thesis, we present an observational study of star forming regions in four nearby galaxies. The key aim is to understand the distribution of young star forming regions in each galaxy and further explore their characteristics. Nearby galaxies serve as an excellent laboratory for understanding the details of star formation and its impact on galactic evolution. Due to their proximity to us, these galaxies offer a unique opportunity to resolve star forming regions into smaller components and study their properties. Among the four galaxies discussed in this thesis, two are dwarf irregular type and the other two are spiral galaxies. The motivation behind choosing different types of galaxies is to expand our understanding regarding recent star formation in various environments. In this chapter, we summarise our results and present the conclusions from our study, followed by a discussion on related future work.

8.1 Summary

Dwarf irregular galaxies -

In chapter 4, we presented a study on the nearby dwarf irregular galaxy WLM with multi-band UVIT observations. The galaxy WLM is a small (radius $\sim$ 1.7 kpc), low mass, metal poor gas-rich system. Our study investigated the recent star forming sites of this galaxy with FUV and NUV imaging observations from UVIT. We identified several possible OB associations with sizes between 4 - 50 pc in the galaxy. This pointed to the enhancement in star formation during the last 10 Myr. We explored the demographics of these young hot regions and noticed a hierarchical nature in their structure. The CO molecular clouds identified by Rubio et al. (2015) in this galaxy have masses around $\sim 10^3 M_{\odot}$. The smaller size of the galaxy and the reported mass of these CO clouds together signify that the star forming clumps will also be less massive. By agreeing with this, our study also found that the identified compact star forming regions of this galaxy are mostly less massive (M $< 10^3 M_{\odot}$). We also used Hα and H I observations to understand the properties of neutral and ionised ISM of the galaxy. With the help of full field observation of the galaxy by UVIT, we traced the extent of UV emission up to a radius 1.7 kpc. The SFR, estimated from the measured FUV flux, is found to be 0.008 $M_{\odot}/yr$. Though this value is similar to that of other nearby dwarf galaxies, the specific SFR of WLM is almost 16 times higher than that of the Milky Way. Therefore, being a small low mass dwarf galaxy, WLM is able to form stars at a higher rate. As this galaxy is known to be isolated, the stellar feedback internal to the galaxy may be playing an important role in triggering a recent star formation.

In chapter 5, we presented a study on another nearby dwarf irregular galaxy IC 2574. This is also a gas-rich system with relatively larger size (radius $\sim$ 10 kpc) and sub-solar metallicity. This study was primarily done with UVIT FUV observations performed with F148W filter. Our study identified FUV bright young

star forming clumps and investigated their connection with the H I holes. We identified a total of 419 star forming regions and found that 28.6% of those were located in shells, 12.6% inside holes and 60.1% away from holes. This indicated that star formation in the galaxy IC 2574 was only partly triggered due to the expansion of H I holes. The identification of 60.1% regions away from the holes also signified that expanding H I holes was not the only mechanism which triggered star formation in this galaxy. In order to verify whether the FUV bright regions were actually younger than 10 Myr, we checked their Hα emission. We noticed 30 out of the 48 holes have FUV emissions in their shells with 23 of them having both FUV and Hα emission signifying more recent triggers. We found 15 holes to have FUV emission inside them, with 12 of those having emission in their shells as well. Another 16 holes were found to have no related FUV emission. As dwarf galaxies are the ideal place where such H I holes can be sustained longer and grow larger, our study delivers a general path to understand the connection between star formation and expanding H I holes in such dwarf systems.

We further characterised the identified regions by estimating their size, SFR density, and H I column density. We noticed that 95% of the regions have radius smaller than 100 pc, which is similar to those identified in other nearby dwarf and spiral galaxies. The average H I column density is found to be more than $10^{21} cm^{-2}$ for 82.3% of the identified regions. This highlighted that star formation in this gas-rich system is mainly happening in those regions where gas density is more than the threshold value. We also noticed that the star forming regions have a hierarchical nature as a function of varying flux levels. We speculate that turbulence could be the main driver for creating this hierarchy. The spatial resolution of UVIT helped us to resolve two individual components of a well studied remnant cluster for the first time in UV and further to estimate their mass. The estimated value of SFR ($\sim$0.57 $M_{\odot}/yr$) signifies that this dwarf galaxy was quite active in forming stars during the last 100 Myr.

Spiral galaxies -

In chapter6, we present an ultra-violet imaging study of the nearby flocculent spiral galaxy NGC 7793, observed in F148W and N242W UVIT filters. Our study covers the entire disk of the galaxy in both FUV and NUV. We find that the disk scale-length estimated in FUV (2.64±0.16 kpc) is more than that in NUV (2.21±0.21 kpc) and optical (1.08 kpc). The FUV and NUV luminosity density profiles of the galaxy convey that between radius 3 - 5 kpc in the outer disk, the FUV emission is more dominant than the NUV. These together support the inside-out growth scenario of the disk. The star forming UV disk also found to closely follow the extent of H I disk having density more than $10^{21} cm^{-2}$. With the spatial resolution of UVIT (1 pixel $\sim$ 6.8 pc), we identified 2046 young star forming regions in the galaxy with radius between $\sim$ 12 - 70 pc, which matches well with the sizes of GMC detected in the galaxy. Around 61% of the regions, identified in our study, have age younger than 20 Myr, which points to a recent enhancement of star formation across the galaxy.

We also noticed that the youngest star forming regions, with age $<$ 10 Myr, distinctly trace the flocculent arms of the galaxy. This can be due to the impact of density wave which could have triggered recent star formation along the arms. The estimated masses of the regions mostly have a value between $10^3 - 10^5 M_{\odot}$. We noticed a hierarchical distribution of the recent star forming regions along the flocculent arms as per their masses. The inner parts of the arms have clumps of different masses whereas the tips of the arms mainly contain low mass clumps. We have also studied the nuclear star cluster of the galaxy. The nature of the (F148W−N242W) colour profile of the cluster indicates that the outskirts of the cluster have a younger population than the inner part. This strengthens the earlier speculation of circum-nuclear star formation or accretion of younger population to the nucleus of the galaxy. In summary, we noticed that the recent star formation in the galaxy NGC 7793 is mostly taking place along the flocculent arms.

In chapter 7, we present a UV imaging study of a nearby spiral galaxy NGC 300 with GALEX FUV and NUV observations. NGC 300 is a late-type spiral with no signature of bar. In this study, we discuss the stellar populations located in the outer disk of the galaxy. Using multi-wavelength imaging data, we find that the disk scale-length of the galaxy increases gradually from longer to shorter wavelengths and thus confirms the presence of an XUV disk. The FUV disk scale-length is found to be 3.05±0.27 kpc, which is 2.3 times larger than that at 3.6 μm. The UV disk emission profile is compared with that in optical, H I and 24μm infra-red. Using the GALEX source catalogue, we have identified 261 unresolved UV sources in the outer disk of the galaxy between radii 5.3 kpc to 10 kpc (1 $\sim$ 2 R_{25}). We have estimated the age and mass of these UV sources with the help of starburst99 SSP model. They are found to have an age range between 1 - 300 Myr and a mass range between $10^3 M_\odot$ to $10^6 M_\odot$. We notice a richness of younger sources (Age $<$ 25 Myr) in the outer disk. The majority of these sources also have low and intermediate mass. These young low mass sources are specifically found to populate the north-eastern part of a spiral arm which is not clearly seen in optical image. Our study thus found a low level recent star formation happening in the outer disk of the galaxy. This could be because of the ram-pressure originating from the motion of the galaxy through the IGM. We conclude that the XUV disk of this galaxy is mainly populated by these young and low mass UV sources. Our study thus shows a way to investigate the outer part of such nearby galaxies having an XUV disk.

8.2 Conclusion

We have used UV, 21 cm radio and other related multi-wavelength imaging data to study star formation in four nearby galaxies. We adopted several methods to

analyse the data and implemented theoretical models to extract results out of it. From the obtained results, we conclude the following:

1. This is one of the first studies which highlights the capability of UVIT in identifying smaller star forming regions in nearby galaxies and probes the nature of star formation up to a smaller length scale ($\sim$ 10 pc for distance up to 4 Mpc).

2. Our study demonstrates that the FUV and NUV fluxes together can help to characterise unresolved single stellar population of nearby galaxies up to a few hundred Myr age.

3. We have identified several possible OB associations of size 4 - 50 pc in the galaxy WLM. Being a small isolated dwarf irregular galaxy, WLM is found to have vigorous star formation in the recent past. This also conveys that internal stellar feedback could be the major driver to trigger star formation in such systems.

4. In another dwarf irregular galaxy IC 2574, almost one third of the recent star formation is found to be triggered by expanding H I holes. We understood that expansion of H I holes is only one of the mechanisms which can alter the internal gas distribution and drive further star formation in such dwarf systems, but it is an important mechanism.

5. In both of the studied dwarf irregular galaxies, the spatial distribution of enhanced star forming sites does not have a preferred location. Some active regions are identified in the outer part of the galaxy as well. This signifies the local impact of internal feedback to trigger star formation in such galaxies.

6. In the case of both the spiral galaxies, we noticed that the value of the disk scale-length gradually increases towards shorter wavelength. In other words, this signifies that the outer part of the disk contains a younger population. This can also be a clue for the inside-out disk growth scenario in disk galaxies.

7. In the flocculent spiral galaxy NGC 7793, we noticed the majority of the clumps younger than 10 Myr are located along the flocculent arms of the galaxy. This signifies the possible impact of spiral density wave to trigger star formation in spiral galaxies.

8. In another spiral galaxy NGC 300, we noticed the signature of recent star formation both in the inner and outer disk of the galaxy. We identified 261 young UV sources in the extended UV disk and found the majority of them to be young (age < 25 Myr) and less massive than $10^5 M_{\odot}$. There can be multiple reasons to have this sustained star formation in such a low gas density environment of the galaxy. In the case of NGC 300, we speculate that it may be because of the ram pressure originating from its motion through the IGM.

9. The regions with higher H I column density show a good spatial correlation with the sites of enhanced star formation in all these galaxies. This highlights that star formation in galaxies is favoured in locations with higher gas densities.

10. The sizes of the unresolved star forming regions detected by UVIT in different galaxies are almost similar and range between $\sim$ 15 - 100 pc, which is similar to the sizes of OB association in nearby dwarf and spiral galaxies.

11. The masses of the identified compact star forming regions in the dwarf irregular galaxy WLM are found to be less compared to those detected in the spiral galaxies NGC 7793 and NGC 300. We compared the mass range of these regions with the mass of detected molecular clouds for the galaxy WLM and NGC 7793 and found these to match for each respective galaxy.

8.3 Future Work

In this thesis, we have developed methods to identify and study unresolved star forming regions in nearby galaxies using FUV and NUV imaging data. We have explored several aspects of starburst99 SSP model and used it to estimate age and mass of the identified clumps. With this understanding, we plan to carry out a few related studies in the future with UVIT multi-band imaging data. Our primary aim is to expand our understanding of star forming regions in nearby galaxies by studying a number of samples with different varieties of morphology.

One of the planed studies is to understand the properties of star forming clumps in NGC 2403, a SAB(s)cd type nearby spiral galaxy (de Vaucouleurs et al. 1991). This galaxy stands for one of the three nearby (D $<$ 4 Mpc) bulgeless disk systems and thus offers an unique environment to study star formation. Williams et al. (2013) reported the presence of an undisturbed exponential disk up to 11 disk scale-length in NGC 2403. The H I velocity field of the galaxy is found to be the most symmetric one among the THINGS sample (Walter et al. 2008). Therefore, it provides an ideal scope to study the impact of spiral density wave to induce star formation in the absence of bulge and other external perturbations. The galaxy has already been observed with two broad band filters F148W and N242W of UVIT. We plan to use the observed deep UVIT images to identify young star forming regions in the galaxy. The (F148W$-$N242W) colour and F148W magnitude of these regions will be used to estimate their age and mass with the help of starburst99 SSP model. We will explore the age and mass gradient of star forming regions identified along the arms. This will help to understand (i) the impact of spiral density wave to trigger star formation and (ii) the nature of stellar population identified in the outer disk of the galaxy. This can also give us important clues to understand the mechanism which can sustain star formation in such extreme environments.

Another study is planned for NGC 1313, a nearby late-type spiral galaxy (SBd) with a strong bar and two main spiral arms. The bar is visible in both UV and IR observations (Suzuki et al. 2013). The impact of a stellar bar can be to make the gas flow inside and trigger star formation in the central region and also along the bar (Athanassoula 1992; Sheth et al. 2005; Coelho & Gadotti 2011). An enhancement of star formation is also expected along the spiral arms due to the impact of spiral density wave (Roberts 1969). Apart from the bar and spiral arms, the galaxy also has one giant super-shell and two satellite components (Ryder et al. 1995; Marcelin & Gondoin 1983). An expanding super-shell can trigger star formation in its periphery due to the accumulation of swept out material (Tenorio-Tagle et al. 2005). In Chapter 5, we presented a related study on the star formation triggered due to expanding shells. In this scenario, the important thing will be to study the properties of star forming regions across the galaxy and explore their possible connection with spiral arms or bar or the giant super shell. The proposal to observe the galaxy with UVIT has been accepted. Due to the unavailability of UVIT NUV channel, we propose to observe the galaxy in two FUV filters F148W and F169M. With these observations we plan to (i) build the spatial map of SFR and explore the impact of spiral density wave, bar and expanding giant super shell, (ii) trace the features of extended spiral arms in FUV. This study will give an idea about the impact of different mechanism to trigger star formation inside a single system.

We also have a plan to study a sample of interacting dwarf galaxies in Lynx-Cancer Void to understand galaxy interaction processes on smaller scales. Voids are low density regions of galaxies surrounded by walls and filaments. Observations suggest that the interiors of these void regions are mostly dominated by bluer dwarf galaxies with high specific SFR (Rojas et al. 2005; Liu et al. 2015). Due to the low density, structure formation within voids is similar to that in the early universe. Thus, dwarf galaxies in voids provide an opportunity to study galaxy interactions/assembly process on smaller scales, triggered star formation, as well as

early stages of structure formation. In this context, we propose UVIT observations of three such star forming dwarf galaxy pairs, UGC 3672, DDO 68, UGC 5272 in Lynx-Cancer Void region. Two of the proposed samples are already observed with F148W and F169M filters. From UVIT observations, we plan to (i) identify the star forming regions, estimate their sizes and explore their spatial distribution and (ii) trace tidal features around these systems. These metal-poor and gas-rich dwarf systems which resemble systems with high redshift will also provide valuable insights to our understanding of how star formation proceeded in the early universe.

Bibliography

Astropy Collaboration, Robitaille, T. P., Tollerud, E. J., et al. 2013, *Astron. Astrophys.*, 558, A33

Astropy Collaboration, Price-Whelan, A. M., Sipőcz, B. M., et al. 2018, *Astron. J.*, 156, 123

Athanassoula, E. 1992, *Mon. Not. Roy. Astron. Soc.*, 259, 345

—. 2005, *Mon. Not. Roy. Astron. Soc.*, 358, 1477

Azzollini, R., Trujillo, I., & Beckman, J. E. 2008, *Astrophys. J.*, 684, 1026

Bacon, R., Accardo, M., Adjali, L., et al. 2010, in Society of Photo-Optical Instrumentation Engineers (SPIE) Conference Series, Vol. 7735, *Proc. SPIE*, 773508

Baldry, I. K., Glazebrook, K., Brinkmann, J., et al. 2004, *Astrophys. J.*, 600, 681

Barker, M. K., Ferguson, A. M. N., Cole, A. A., et al. 2011, *Mon. Not. Roy. Astron. Soc.*, 410, 504

Barnes, K. L., van Zee, L., & Skillman, E. D. 2011, *Astrophys. J.*, 743, 137

Bastian, N., Ercolano, B., Gieles, M., et al. 2007, *Mon. Not. Roy. Astron. Soc.*, 379, 1302

Basu, S., & Mouschovias, T. C. 1994, *Astrophys. J.*, 432, 720

Beckwith, S. V. W., Stiavelli, M., Koekemoer, A. M., et al. 2006, *Astron. J.*, 132, 1729

Bertin, E., & Arnouts, S. 1996, *Astron. Astrophys. Suppl.*, 117, 393

Bianchi, L. 2011, *Astrophys. Space Sci.*, 335, 51

Bianchi, L., Efremova, B., Hodge, P., Massey, P., & Olsen, K. A. G. 2012, *Astron. J.*, 143, 74

Bibby, J. L., & Crowther, P. A. 2010, *Mon. Not. Roy. Astron. Soc.*, 405, 2737

Bigiel, F., Leroy, A., Walter, F., et al. 2008, *Astron. J.*, 136, 2846

Binder, B., Williams, B. F., Eracleous, M., et al. 2012, *Astrophys. J.*, 758, 15

Bland-Hawthorn, J., Vlajić, M., Freeman, K. C., & Draine, B. T. 2005, *Astrophys. J.*, 629, 239

Blanton, M. R., & Moustakas, J. 2009, *Ann. Rev. Astron. Astrophys.*, 47, 159

Blanton, M. R., Hogg, D. W., Bahcall, N. A., et al. 2003, *Astrophys. J.*, 594, 186

Blumenthal, G. R., Faber, S. M., Primack, J. R., & Rees, M. J. 1984, *Nature*, 311, 517

Bodenheimer, P. H. 2011, Principles of Star Formation, doi:10.1007/978-3-642-15063-0

Boggess, A., Bohlin, R. C., Evans, D. C., et al. 1978, *Nature*, 275, 377

Böker, T., Laine, S., van der Marel, R. P., et al. 2002, *Astron. J.*, 123, 1389

Boss, A. P. 1995, *Astrophys. J.*, 439, 224

Bresolin, F., Kennicutt, Jr., R. C., & Stetson, P. B. 1996, *Astron. J.*, 112, 1009

Bresolin, F., Kennicutt, Jr., R. C., Ferrarese, L., et al. 1998, *Astron. J.*, 116, 119

Bromm, V., Yoshida, N., Hernquist, L., & McKee, C. F. 2009, *Nature*, 459, 49

Brook, C. B., Kawata, D., Martel, H., Gibson, B. K., & Bailin, J. 2006, *Astrophys. J.*, 639, 126

Calzetti, D., Kinney, A. L., & Storchi-Bergmann, T. 1994, *Astrophys. J.*, 429, 582

Calzetti, D., Kennicutt, R. C., Engelbracht, C. W., et al. 2007, *Astrophys. J.*, 666, 870

Calzetti, D., Lee, J. C., Sabbi, E., et al. 2015, *Astron. J.*, 149, 51

Cameron, A. G. W., & Truran, J. W. 1977, *Icarus*, 30, 447

Cannon, J. M., Walter, F., Bendo, G. J., et al. 2005, *Astrophys. J. Lett.*, 630, L37

Carignan, C. 1985, *Astrophys. J. Suppl.*, 58, 107

Carignan, C., & Puche, D. 1990, The Astronomical Journal, 100, 394

Carson, D. J., Barth, A. J., Seth, A. C., et al. 2015, The Astronomical Journal, 149, 170

Castelli, F., & Kurucz, R. L. 2004, ArXiv Astrophysics e-prints, astro-ph/0405087

Chomiuk, L., & Povich, M. S. 2011, *Astron. J.*, 142, 197

Cignoni, M., & Tosi, M. 2010, Advances in Astronomy, 2010, 158568

Cignoni, M., Sacchi, E., Aloisi, A., et al. 2018, *Astrophys. J.*, 856, 62

Clark, P. C., & Glover, S. C. O. 2014, *Mon. Not. Roy. Astron. Soc.*, 444, 2396

Coelho, P., & Gadotti, D. A. 2011, *Astrophys. J. Lett.*, 743, L13

Courteau, S., Dutton, A. A., van den Bosch, F. C., et al. 2007, *Astrophys. J.*, 671, 203

Dalcanton, J. J., Williams, B. F., Seth, A. C., et al. 2009, *Astrophys. J. Suppl.*, 183, 67

Dale, J. E., Ercolano, B., & Bonnell, I. A. 2012, *Mon. Not. Roy. Astron. Soc.*, 424, 377

de Jong, R. S. 1996, *Astron. Astrophys.*, 313, 377

de Vaucouleurs, G. 1959, Handbuch der Physik, 53, 275

de Vaucouleurs, G., de Vaucouleurs, A., Corwin, Jr., H. G., et al. 1991, Third Reference Catalogue of Bright Galaxies. Volume I: Explanations and references. Volume II: Data for galaxies between 0^h and 12^h. Volume III: Data for galaxies between 12^h and 24^h.

de Vaucouleurs, G., & Page, J. 1962, *Astrophys. J.*, 136, 107

de Vaucouleurs, G. H., de Vaucouleurs, A., & Shapley, H. 1964, Reference catalogue of bright galaxies

Deharveng, L., Lefloch, B., Zavagno, A., et al. 2003, *Astron. Astrophys.*, 408, L25

Di Matteo, P., Combes, F., Melchior, A. L., & Semelin, B. 2007, *Astron. Astrophys.*, 468, 61

Dicaire, I., Carignan, C., Amram, P., et al. 2008, The Astronomical Journal, 135, 2038

Dohm-Palmer, R. C., Skillman, E. D., Saha, A., et al. 1997, *Astron. J.*, 114, 2527

Dolphin, A. E. 2000, *Astrophys. J.*, 531, 804

—. 2002, *Mon. Not. Roy. Astron. Soc.*, 332, 91

Draine, B. T. 2011, Physics of the Interstellar and Intergalactic Medium

Dressler, A. 1980, *Astrophys. J.*, 236, 351

Efremov, Y. N. 1995, *Astron. J.*, 110, 2757

Efremov, Y. N., & Elmegreen, B. G. 1998, *Mon. Not. Roy. Astron. Soc.*, 299, 588

Egorov, O. V., Lozinskaya, T. A., Moiseev, A. V., & Smirnov-Pinchukov, G. V. 2014, *Mon. Not. Roy. Astron. Soc.*, 444, 376

Elmegreen, B. G., Efremov, Y., Pudritz, R. E., & Zinnecker, H. 2000, Protostars and Planets IV, 179

Elmegreen, B. G., & Elmegreen, D. M. 1986, *Astrophys. J.*, 311, 554

Elmegreen, B. G., & Lada, C. J. 1977, *Astrophys. J.*, 214, 725

Elmegreen, D. M., Elmegreen, B. G., Adamo, A., et al. 2014, *Astrophys. J. Lett.*, 787, L15

Eskridge, P. B., Frogel, J. A., Pogge, R. W., et al. 2000, *Astron. J.*, 119, 536

Faesi, C. M., Lada, C. J., Forbrich, J., Menten, K. M., & Bouy, H. 2014, *Astrophys. J.*, 789, 81

Fazio, G. G., Hora, J. L., Allen, L. E., et al. 2004, *Astrophys. J. Suppl.*, 154, 10

Ferguson, A., Irwin2, M., Chapman, S., et al. 2007, Astrophysics and Space Science Proceedings, 3, 239

Ferguson, H. C., & Binggeli, B. 1994, *Astron. Astrophys. Rev.*, 6, 67

Ferraro, F. R., Fusi Pecci, F., Tosi, M., & Buonanno, R. 1989, *Mon. Not. Roy. Astron. Soc.*, 241, 433

Fitzpatrick, E. L. 1999, *Pub. Astron. Soc. Pac.*, 111, 63

Frater, R. H., Brooks, J. W., & Whiteoak, J. B. 1992, Journal of Electrical and Electronics Engineering Australia, 12, 103

Gallagher, J. S., I., Hunter, D. A., & Tutukov, A. V. 1984, *Astrophys. J.*, 284, 544

Gallart, C., Aparicio, A., Bertelli, G., & Chiosi, C. 1996, *Astron. J.*, 112, 2596

Gallazzi, A., Charlot, S., Brinchmann, J., & White, S. D. M. 2006, *Mon. Not. Roy. Astron. Soc.*, 370, 1106

Gallouet, L., Heidmann, N., & Dampierre, F. 1975, *Astron. Astrophys. Suppl.*, 19, 1

Garcia, M., Herrero, A., Castro, N., Corral, L., & Rosenberg, A. 2010, *Astron. Astrophys.*, 523, A23

Gazak, J. Z., Kudritzki, R., Evans, C., et al. 2015, *Astrophys. J.*, 805, 182

Gieren, W., Pietrzyński, G., Szewczyk, O., et al. 2008, *Astrophys. J.*, 683, 611

Gil de Paz, A., Madore, B. F., Boissier, S., et al. 2005, *Astrophys. J. Lett.*, 627, L29

Gil de Paz, A., Boissier, S., Madore, B. F., et al. 2007, *Astrophys. J. Suppl.*, 173, 185

Girish, V., Tandon, S. N., Sriram, S., Kumar, A., & Postma, J. 2017, Experimental Astronomy, 43, 59

Goddard, Q. E., Kennicutt, R. C., & Ryan-Weber, E. V. 2010, *Mon. Not. Roy. Astron. Soc.*, 405, 2791

Gogarten, S. M., Dalcanton, J. J., Williams, B. F., et al. 2010, *Astrophys. J.*, 712, 858

González Delgado, R. M., Cid Fernandes, R., Pérez, E., et al. 2016, *Astron. Astrophys.*, 590, A44

González Delgado, R. M., Pérez, E., Cid Fernandes, R., et al. 2017, *Astron. Astrophys.*, 607, A128

Gordon, K. D., Clayton, G. C., Misselt, K. A., Landolt, A. U., & Wolff, M. J. 2003, *Astrophys. J.*, 594, 279

Gordon, K. D., Clayton, G. C., Witt, A. N., & Misselt, K. A. 2000, *Astrophys. J.*, 533, 236

Grasha, K., Calzetti, D., Adamo, A., et al. 2017, *Astrophys. J.*, 840, 113

Grasha, K., Calzetti, D., Bittle, L., et al. 2018, *Mon. Not. Roy. Astron. Soc.*, 481, 1016

Grasha, K., Calzetti, D., Adamo, A., et al. 2019, *Mon. Not. Roy. Astron. Soc.*, 483, 4707

Grebel, E. K., Gallagher, John S., I., & Harbeck, D. 2003, *Astron. J.*, 125, 1926

Helou, G. 1986, *Astrophys. J. Lett.*, 311, L33

Helou, G., Roussel, H., Appleton, P., et al. 2004, *Astrophys. J. Suppl.*, 154, 253

Hermanowicz, M. T., Kennicutt, R. C., & Eldridge, J. J. 2013, Monthly Notices of the Royal Astronomical Society, 432, 3097

Hillis, T. J., Williams, B. F., Dolphin, A. E., Dalcanton, J. J., & Skillman, E. D. 2016, ArXiv e-prints, arXiv:1609.02106

Hodge, P. W. 1971, *Ann. Rev. Astron. Astrophys.*, 9, 35

Hopkins, P. F., Cox, T. J., Hernquist, L., et al. 2013, *Mon. Not. Roy. Astron. Soc.*, 430, 1901

Hubble, E., & Humason, M. L. 1931, *Astrophys. J.*, 74, 43

Hubble, E. P. 1926, *Astrophys. J.*, 64, doi:10.1086/143018

Huchra, J. P., Geller, M. J., Gallagher, J., et al. 1983, *Astrophys. J.*, 274, 125

Hunter, D. 1997, *Pub. Astron. Soc. Pac.*, 109, 937

Hunter, D. A., & Elmegreen, B. G. 2004, *Astron. J.*, 128, 2170

Hunter, D. A., Elmegreen, B. G., & Ludka, B. C. 2010, *Astron. J.*, 139, 447

Hunter, D. A., Gillett, F. C., Gallagher, III, J. S., Rice, W. L., & Low, F. J. 1986, *Astrophys. J.*, 303, 171

Hunter, J. D. 2007, Computing In Science & Engineering, 9, 90

Hutchings, J. B., Postma, J., Asquin, D., & Leahy, D. 2007, *Pub. Astron. Soc. Pac.*, 119, 1152

Impey, C., & Bothun, G. 1997, *Ann. Rev. Astron. Astrophys.*, 35, 267

Ivanov, G. R. 1996, *Astron. Astrophys.*, 305, 708

Jeans, J. H. 1928, Astronomy and cosmogony

Jerjen, H., Freeman, K. C., & Binggeli, B. 1998, *Astron. J.*, 116, 2873

Joye, W. A., & Mandel, E. 2003, in Astronomical Society of the Pacific Conference Series, Vol. 295, Astronomical Data Analysis Software and Systems XII, ed. H. E. Payne, R. I. Jedrzejewski, & R. N. Hook, 489

Kacharov, N., Neumayer, N., Seth, A. C., et al. 2018, *Mon. Not. Roy. Astron. Soc.*, 480, 1973

Kaisina, E. I., Makarov, D. I., Karachentsev, I. D., & Kaisin, S. S. 2012, Astrophysical Bulletin, 67, 115

Karachentsev, I. D. 2005, *Astron. J.*, 129, 178

Karachentsev, I. D., & Kaisina, E. I. 2013a, *Astron. J.*, 146, 46

—. 2013b, *Astron. J.*, 146, 46

—. 2019, Astrophysical Bulletin, 74, 111

Karachentsev, I. D., Karachentseva, V. E., Huchtmeier, W. K., & Makarov, D. I. 2004, *Astron. J.*, 127, 2031

Karachentsev, I. D., Makarov, D. I., & Kaisina, E. I. 2013, *Astron. J.*, 145, 101

Karachentsev, I. D., Grebel, E. K., Sharina, M. E., et al. 2003, *Astron. Astrophys.*, 404, 93

Kennicutt, R. C., J. 1983, *Astrophys. J.*, 272, 54

Kennicutt, Robert C., J., Calzetti, D., Walter, F., et al. 2007, *Astrophys. J.*, 671, 333

Kennicutt, R. C., & Evans, N. J. 2012, *Ann. Rev. Astron. Astrophys.*, 50, 531

Kennicutt, Jr., R. C. 1998, *Astrophys. J.*, 498, 541

Kennicutt, Jr., R. C., Armus, L., Bendo, G., et al. 2003, *Pub. Astron. Soc. Pac.*, 115, 928

Kepley, A. A., Wilcots, E. M., Hunter, D. A., & Nordgren, T. 2007, *Astron. J.*, 133, 2242

Kewley, L. J., Rupke, D., Zahid, H. J., Geller, M. J., & Barton, E. J. 2010, *Astrophys. J. Lett.*, 721, L48

Kim, S. C., Sung, H., Park, H. S., & Sung, E.-C. 2004, *Chin. J. Astron. Astrophys.*, 4, 299

Koribalski, B. S., Wang, J., Kamphuis, P., et al. 2018, *Mon. Not. Roy. Astron. Soc.*, 478, 1611

Kormendy, J., & Kennicutt, Jr., R. C. 2004, *Ann. Rev. Astron. Astrophys.*, 42, 603

Kraan-Korteweg, R. C., & Tammann, G. A. 1979, Astronomische Nachrichten, 300, 181

Kreckel, K., Faesi, C., Kruijssen, J. M. D., et al. 2018, *Astrophys. J. Lett.*, 863, L21

Kroupa, P. 2001, *Mon. Not. Roy. Astron. Soc.*, 322, 231

Kudritzki, R.-P., Urbaneja, M. A., Bresolin, F., et al. 2008, *Astrophys. J.*, 681, 269

Kumar, A., Ghosh, S. K., Hutchings, J., et al. 2012, in *Proc. SPIE*, Vol. 8443, Space Telescopes and Instrumentation 2012: Ultraviolet to Gamma Ray, 84431N

Larson, R. B. 1981, *Mon. Not. Roy. Astron. Soc.*, 194, 809

Larson, R. B., & Tinsley, B. M. 1978, *Astrophys. J.*, 219, 46

Leaman, R., Venn, K. A., Brooks, A. M., et al. 2012, *Astrophys. J.*, 750, 33

Lee, T., Papanastassiou, D. A., & Wasserburg, G. J. 1977, *Astrophys. J. Lett.*, 211, L107

Leisawitz, D., Bash, F. N., & Thaddeus, P. 1989, *Astrophys. J. Suppl.*, 70, 731

Leitherer, C., Schaerer, D., Goldader, J. D., et al. 1999, *Astrophys. J. Suppl.*, 123, 3

Leroy, A. K., Walter, F., Brinks, E., et al. 2008, *Astron. J.*, 136, 2782

Leroy, A. K., Schinnerer, E., Hughes, A., et al. 2017, *Astrophys. J.*, 846, 71

Li, A., & Draine, B. T. 2001, *Astrophys. J.*, 554, 778

Lin, C. C., & Shu, F. H. 1966, Proceedings of the National Academy of Science, 55, 229

Liu, C.-X., Pan, D. C., Hao, L., et al. 2015, *Astrophys. J.*, 810, 165

Longair, M. S. 2008, Galaxy Formation

Marcelin, M., & Gondoin, P. 1983, *Astron. Astrophys. Suppl.*, 51, 353

Marinova, I., & Jogee, S. 2007, *Astrophys. J.*, 659, 1176

Martin, D. C., Fanson, J., Schiminovich, D., et al. 2005, *Astrophys. J. Lett.*, 619, L1

Mason, K. O., Breeveld, A., Much, R., et al. 2001, *Astron. Astrophys.*, 365, L36

Massey, P., McNeill, R. T., Olsen, K. A. G., et al. 2007, *Astron. J.*, 134, 2474

Mayer, L., Governato, F., Colpi, M., et al. 2001, *Astrophys. J. Lett.*, 547, L123

McCall, M. L. 2004, *Astron. J.*, 128, 2144

McKee, C. F., & Ostriker, E. C. 2007, *Ann. Rev. Astron. Astrophys.*, 45, 565

McMillan, P. J. 2011, *Mon. Not. Roy. Astron. Soc.*, 414, 2446

McQuinn, K. B. W., Skillman, E. D., Dolphin, A. E., & Mitchell, N. P. 2015, *Astrophys. J.*, 808, 109

McQuinn, K. B. W., Skillman, E. D., Cannon, J. M., et al. 2010a, *Astrophys. J.*, 721, 297

McQuinn, K. B. W., Skillman, E. D., Cannon, J. M., et al. 2010b, *Astrophys. J.*, 721, 297

—. 2010c, *Astrophys. J.*, 724, 49

Melena, N. W., Elmegreen, B. G., Hunter, D. A., & Zernow, L. 2009, *Astron. J.*, 138, 1203

Melnick, J., & Sargent, W. L. W. 1977, *Astrophys. J.*, 215, 401

Mel'Nik, A. M., & Efremov, Y. N. 1995, Astronomy Letters, 21, 10

Meyer, M. J., Zwaan, M. A., Webster, R. L., et al. 2004, *Mon. Not. Roy. Astron. Soc.*, 350, 1195

Miller, B. W., & Hodge, P. 1994, *Astrophys. J.*, 427, 656

Minniti, D., & Zijlstra, A. A. 1997, *Astron. J.*, 114, 147

Mo, H., van den Bosch, F. C., & White, S. 2010, Galaxy Formation and Evolution

Mo, H. J., Mao, S., & White, S. D. M. 1998, *Mon. Not. Roy. Astron. Soc.*, 295, 319

Mondal, C., Subramaniam, A., & George, K. 2018, *Astron. J.*, 156, 109

—. 2019, Journal of Astrophysics and Astronomy, 40, 35

Moos, H. W., Cash, W. C., Cowie, L. L., et al. 2000, *Astrophys. J. Lett.*, 538, L1

Morgan, W. W., & Osterbrock, D. E. 1969, *Astron. J.*, 74, 515

Morrissey, P., Conrow, T., Barlow, T. A., et al. 2007, *Astrophys. J. Suppl.*, 173, 682

Muñoz-Mateos, J. C., Gil de Paz, A., Boissier, S., et al. 2007, *Astrophys. J.*, 658, 1006

Murphy, E. J., Condon, J. J., Schinnerer, E., et al. 2011, *Astrophys. J.*, 737, 67

Nagakura, T., Hosokawa, T., & Omukai, K. 2009, *Mon. Not. Roy. Astron. Soc.*, 399, 2183

Oemler, Augustus, J. 1974, *Astrophys. J.*, 194, 1

Ott, J., Stilp, A. M., Warren, S. R., et al. 2012, *Astron. J.*, 144, 123

Panter, B., Jimenez, R., Heavens, A. F., & Charlot, S. 2007, *Mon. Not. Roy. Astron. Soc.*, 378, 1550

Pasquali, A., Leroy, A., Rix, H.-W., et al. 2008, *Astrophys. J.*, 687, 1004

Pellerin, A., Meyer, M. M., Calzetti, D., & Harris, J. 2012, *Astron. J.*, 144, 182

Phillipps, S., & Edmunds, M. G. 1991, *Mon. Not. Roy. Astron. Soc.*, 251, 84

Pilkington, K., Few, C. G., Gibson, B. K., et al. 2012, *Astron. Astrophys.*, 540, A56

Postma, J. E., & Leahy, D. 2017, *Pub. Astron. Soc. Pac.*, 129, 115002

Powell, L. C., Bournaud, F., Chapon, D., & Teyssier, R. 2013, *Mon. Not. Roy. Astron. Soc.*, 434, 1028

Preibisch, T., Brown, A. G. A., Bridges, T., Guenther, E., & Zinnecker, H. 2002, *Astron. J.*, 124, 404

Puche, D., Carignan, C., & Bosma, A. 1990, *Astron. J.*, 100, 1468

Radburn-Smith, D. J., Roškar, R., Debattista, V. P., et al. 2012, *Astrophys. J.*, 753, 138

Rejkuba, M., Minniti, D., Gregg, M. D., et al. 2000, *Astron. J.*, 120, 801

Revaz, Y., & Jablonka, P. 2018, *Astron. Astrophys.*, 616, A96

Rieke, G. H., Young, E. T., Engelbracht, C. W., et al. 2004, *Astrophys. J. Suppl.*, 154, 25

Rizzi, L., Bresolin, F., Kudritzki, R.-P., Gieren, W., & Pietrzyński, G. 2006, *Astrophys. J.*, 638, 766

Roberts, W. W., J., Roberts, M. S., & Shu, F. H. 1975, *Astrophys. J.*, 196, 381

Roberts, M. S., & Haynes, M. P. 1994, *Ann. Rev. Astron. Astrophys.*, 32, 115

Roberts, W. W. 1969, *Astrophys. J.*, 158, 123

Rodríguez, M. J., Baume, G., & Feinstein, C. 2016, *Astron. Astrophys.*, 594, A34

Rogers, H., & Pittard, J. M. 2013, *Mon. Not. Roy. Astron. Soc.*, 431, 1337

Rogerson, J. B. 1963, *Space Sci. Rev.*, 2, 621

Rojas, R. R., Vogeley, M. S., Hoyle, F., & Brinkmann, J. 2005, *Astrophys. J.*, 624, 571

Roming, P. W. A., Kennedy, T. E., Mason, K. O., et al. 2005, *Space Sci. Rev.*, 120, 95

Roškar, R., Debattista, V. P., Stinson, G. S., et al. 2008, *Astrophys. J. Lett.*, 675, L65

Rowan-Robinson, M. 1986, *Mon. Not. Roy. Astron. Soc.*, 219, 737

—. 1992, *Mon. Not. Roy. Astron. Soc.*, 258, 787

Rubio, M., Elmegreen, B. G., Hunter, D. A., et al. 2015, *Nature*, 525, 218

Ryder, S. D., Staveley-Smith, L., Malin, D., & Walsh, W. 1995, *Astron. J.*, 109, 1592

Sacchi, E., Cignoni, M., Aloisi, A., et al. 2019, The Astrophysical Journal, 878, 1

Salpeter, E. E. 1955, *Astrophys. J.*, 121, 161

Sánchez-Blázquez, P., Ocvirk, P., Gibson, B. K., Pérez, I., & Peletier, R. F. 2011, *Mon. Not. Roy. Astron. Soc.*, 415, 709

Sandage, A. 1961, The Hubble Atlas of Galaxies

Sandage, A., & Tammann, G. A. 1981, A Revised Shapley-Ames Catalog of Bright Galaxies

Schaye, J. 2004, *Astrophys. J.*, 609, 667

Schechter, P. 1976, *Astrophys. J.*, 203, 297

Schinnerer, E., Meidt, S. E., Pety, J., et al. 2013, *Astrophys. J.*, 779, 42

Schmidt, M. 1959, *Astrophys. J.*, 129, 243

Searle, L., Sargent, W. L. W., & Bagnuolo, W. G. 1973, *Astrophys. J.*, 179, 427

Seigar, M. S., & James, P. A. 2002, *Mon. Not. Roy. Astron. Soc.*, 337, 1113

Shapley, H., & Ames, A. 1932, Annals of Harvard College Observatory, 88, 41

Sheth, K., Vogel, S. N., Regan, M. W., Thornley, M. D., & Teuben, P. J. 2005, *Astrophys. J.*, 632, 217

Singh, K. P., Tandon, S. N., Agrawal, P. C., et al. 2014, in Society of Photo-Optical Instrumentation Engineers (SPIE) Conference Series, Vol. 9144, *Proc. SPIE*, 91441S

Skillman, E. D. 1987, in NASA Conference Publication, Vol. 2466, NASA Conference Publication, ed. C. J. Lonsdale Persson

Skrutskie, M. F., Cutri, R. M., Stiening, R., et al. 2006, *Astron. J.*, 131, 1163

Stecher, T. P., Cornett, R. H., Greason, M. R., et al. 1997, *Pub. Astron. Soc. Pac.*, 109, 584

Stewart, S. G., & Walter, F. 2000, *Astron. J.*, 120, 1794

Stone, J. M., & Norman, M. L. 1992, *Astrophys. J. Lett.*, 390, L17

Sun, J., Leroy, A. K., Schruba, A., et al. 2018a, *Astrophys. J.*, 860, 172

Sun, N.-C., de Grijs, R., Cioni, M.-R. L., et al. 2018b, *Astrophys. J.*, 858, 31

Suzuki, T., Kaneda, H., & Onaka, T. 2013, *Astron. Astrophys.*, 554, A8

Tan, J. C. 2000, *Astrophys. J.*, 536, 173

Tandon, S. N., Subramaniam, A., Girish, V., et al. 2017, *Astron. J.*, 154, 128

Taylor, M. B. 2005, in Astronomical Society of the Pacific Conference Series, Vol. 347, Astronomical Data Analysis Software and Systems XIV, ed. P. Shopbell, M. Britton, & R. Ebert, 29

Taylor, V. A., Jansen, R. A., Windhorst, R. A., Odewahn, S. C., & Hibbard, J. E. 2005, *Astrophys. J.*, 630, 784

Tenorio-Tagle, G., & Bodenheimer, P. 1988, *Ann. Rev. Astron. Astrophys.*, 26, 145

Tenorio-Tagle, G., Silich, S., Rodríguez-González, A., & Muñoz-Tuñón, C. 2005, *Astrophys. J. Lett.*, 628, L13

Thilker, D. A., Bianchi, L., Meurer, G., et al. 2005a, in Bulletin of the American Astronomical Society, Vol. 37, American Astronomical Society Meeting Abstracts, 1500

Thilker, D. A., Bianchi, L., Boissier, S., et al. 2005b, *Astrophys. J. Lett.*, 619, L79

Thilker, D. A., Bianchi, L., Meurer, G., et al. 2007, *Astrophys. J. Suppl.*, 173, 538

Thompson, A. R., Clark, B. G., Wade, C. M., & Napier, P. J. 1980, *Astrophys. J. Suppl.*, 44, 151

Thuan, T. X., & Izotov, Y. I. 2005, *Astrophys. J. Suppl.*, 161, 240

Thuan, T. X., & Martin, G. E. 1981, *Astrophys. J.*, 247, 823

Tolstoy, E., Hill, V., & Tosi, M. 2009, *Ann. Rev. Astron. Astrophys.*, 47, 371

Toomre, A. 1964, *Astrophys. J.*, 139, 1217

Tosi, M., Greggio, L., Marconi, G., & Focardi, P. 1991, *Astron. J.*, 102, 951

Tully, R. B. 2015, *Astron. J.*, 149, 54

Tully, R. B., Rizzi, L., Dolphin, A. E., et al. 2006, *Astron. J.*, 132, 729

Urbaneja, M. A., Kudritzki, R.-P., Bresolin, F., et al. 2008, *Astrophys. J.*, 684, 118

van den Bergh, S. 1976, *Astrophys. J.*, 206, 883

—. 1994, *Astron. J.*, 107, 1328

—. 2000, The Galaxies of the Local Group

van der Marel, R. P., & Cioni, M.-R. L. 2001, *Astron. J.*, 122, 1807

Van Dyk, S. D., Davidge, T. J., Elias-Rosa, N., et al. 2012, The Astronomical Journal, 143, 19

Verley, S., Corbelli, E., Giovanardi, C., & Hunt, L. K. 2009, *Astron. Astrophys.*, 493, 453

Vlajić, M., Bland-Hawthorn, J., & Freeman, K. C. 2009, *Astrophys. J.*, 697, 361

—. 2011, The Astrophysical Journal, 732, 7

Walcher, C. J., Böker, T., Charlot, S., et al. 2006, *Astrophys. J.*, 649, 692

Walter, F., & Brinks, E. 1999, *Astron. J.*, 118, 273

Walter, F., Brinks, E., de Blok, W. J. G., et al. 2008, *Astron. J.*, 136, 2563

Weisz, D. R., Dolphin, A. E., Skillman, E. D., et al. 2014, *Astrophys. J.*, 789, 147

Weisz, D. R., Skillman, E. D., Cannon, J. M., et al. 2009, *Astrophys. J. Lett.*, 691, L59

Weisz, D. R., Dalcanton, J. J., Williams, B. F., et al. 2011, *Astrophys. J.*, 739, 5

Westmeier, T., Braun, R., & Koribalski, B. S. 2011, *Mon. Not. Roy. Astron. Soc.*, 410, 2217

White, S. D. M., & Frenk, C. S. 1991, *Astrophys. J.*, 379, 52

Whiting, A. B., Hau, G. K. T., & Irwin, M. 1999, *Astron. J.*, 118, 2767

Whitworth, A. P., Bhattal, A. S., Chapman, S. J., Disney, M. J., & Turner, J. A. 1994, *Mon. Not. Roy. Astron. Soc.*, 268, 291

Williams, B. F., Dalcanton, J. J., Stilp, A., et al. 2013, *Astrophys. J.*, 765, 120

Williams, J. P., Blitz, L., & McKee, C. F. 2000, in Protostars and Planets IV, ed. V. Mannings, A. P. Boss, & S. S. Russell, 97

Wilsey, N., & Hunter, D. 2010, in Bulletin of the American Astronomical Society, Vol. 42, American Astronomical Society Meeting Abstracts #215, 481

Woods, D. F., Geller, M. J., & Barton, E. J. 2006, *Astron. J.*, 132, 197

Xu, C. K., Donas, J., Arnouts, S., et al. 2005, *Astrophys. J. Lett.*, 619, L11

York, D. G., Adelman, J., Anderson, Jr., J. E., et al. 2000, *Astron. J.*, 120, 1579

Young, J. S., Xie, S., Tacconi, L., et al. 1995, *Astrophys. J. Suppl.*, 98, 219

Yuan, H. B., Liu, X. W., & Xiang, M. S. 2013, *Mon. Not. Roy. Astron. Soc.*, 430, 2188

Yukita, M., & Swartz, D. A. 2012, *Astrophys. J. Lett.*, 750, L16

Yun, M. S. 1999, in IAU Symposium, Vol. 186, Galaxy Interactions at Low and High Redshift, ed. J. E. Barnes & D. B. Sanders, 81

Zaritsky, D., & Christlein, D. 2007, *Astron. J.*, 134, 135

Zavagno, A., Deharveng, L., Comerón, F., et al. 2006, *Astron. Astrophys.*, 446, 171

Zgirski, B., Gieren, W., Pietrzyński, G., et al. 2017, *Astrophys. J.*, 847, 88

Zhang, H.-X., Hunter, D. A., Elmegreen, B. G., Gao, Y., & Schruba, A. 2012, *Astron. J.*, 143, 47